EFFECT OF COLD WORK ON THE AGEING AND FORMABILITY OF A Cu 1.8wt% Be 0.25wt% Co ALLOY

by

AHMET SELÇUK, B.Sc. (Eng), M.Sc.

THESIS SUBMITTED
FOR THE DEGREE OF DOCTOR OF PHILOSOPHY
OF THE UNIVERSITY OF LONDON
AND
FOR THE DIPLOMA OF MEMBERSHIP OF
THE IMPERIAL COLLEGE OF SCIENCE, TECHNOLOGY AND MEDICINE

APRIL 1989

DEPARTMENT OF MATERIALS, ROYAL SCHOOL OF MINES,
IMPERIAL COLLEGE OF SCIENCE, TECHNOLOGY AND MEDICINE,
LONDON SW7 2BP

ABSTRACT

The aim of the present work was to:
(i) investigate the precipitation processes in Cu 1.8wt.%Be 0.25wt.%Co strip alloy, (a) undeformed and (b) prior cold rolled in the range 5 to 41% reduction in thickness (RT), during ageing at temperatures in the range 300 to 500°C, and
(ii) select heat treatments (at temperatures in the range 350 to 420°C) which give the optimum formability and strength for various commercial grades of the alloys, such as WM, W1/4HM, W1/2HM, etc.; the objective was to assist industry in producing fully heat treated alloys in a continuous strip process, which are still formable enough for fabricating into the required shape.

As regards (i), the microstructural changes during ageing of the undeformed and deformed alloys were studied by isothermal and non-isothermal differential thermal analysis techniques, complemented by transmission electron microscopy, X-ray diffraction, and hardness and electrical resistivity measurements. The results were used to construct temperature-time-transformation (TTT) diagrams for both deformed and undeformed alloys. The precipitation sequence and mechanisms of the various metastable phases, namely G.P. zones, γ'', and γ''_D, as well as the recrystallisation processes have been discussed in relation to the TTT diagrams. The activation energies and time exponent (n) values for the formation of the γ'' and γ''_D phases were calculated using the thermal analysis data and the results interpreted in terms of the precipitation kinetics. The crystallographic texture orientations in (i) undeformed, (ii) cold rolled and (iii) cold rolled and aged alloys were determined by X-ray texture analysis.

In order to assess the formability of the alloys a cantilever-type bend test rig was designed and constructed; the bend performance was characterised by "the maximum bendability angle", θ_M, at which the bend sample cracks. The values of θ_M and hardness as a function of ageing time, temperature, and the degree of prior cold work were used, via a combined hardness/bendability function (F_{NORM}), to select the thermal and/or thermo-mechanical treatments which produce an optimum hardness/bendability combination for each commercial grade of the alloy. These treatments were correlated with the available microstructural data. The best treatments corresponded mostly to peak- and/or over-ageing of the alloys cold worked to less than 32% RT.

ACKNOWLEDGEMENTS

I would like to thank my supervisor, Dr R.D. Rawlings, for his invaluable advice, guidance, and constant encouragement during the course of this research. I would also like to express my gratitude to Professor D.W. Pashley for the provision of laboratory facilities.

Thanks are also due to Dr T.J. Baker for his interest and help in the interpretation of deformation phenomena in bending of strip materials, and to Dr C.B. Ponton for many valuable discussions and proof-reading some parts of this thesis, as well as to my colleagues in the Structural Materials research group for much stimulating discussion and also for their co-operation. I am also grateful to the technical and workshop staff for their assistance.

Finally, I am indebted to the Turkish Government for providing, through the Ministry of Education, the scholarship for this research, and to Telcon Metals Ltd. for supplying the strip materials used in this study.

CONTENTS

CHAPTER 1 : INTRODUCTION 10

CHAPTER 2 : REVIEW OF THE LITERATURE 15

2.1 The Cu-Be Phase Diagram 15

2.2 Structure of Supersaturated Solid Solution ... 15

2.3 Precipitation Sequence 21

2.4 Continuous Precipitation 22

2.4.1 Precursor phase 22

2.4.2 G.P. zones 23

2.4.3 γ'' phase 26

2.4.4 γ' phase 29

2.4.5 γ phase 31

2.5 Discontinuous Precipitation 32

2.5.1 Occurrence of discontinuous precipitation 32

2.5.2 Initiation mechanisms 35

2.5.3 Growth mechanisms 39

2.5.4 Phases involved in discontinuous precipitation 40

2.5.5 Effects of prior continuous precipitation 44

2.6 Thermodynamics and Kinetics of Precipitation in Cu-Be Alloys 49

2.6.1 Continuous precipitation 49

2.6.2 Discontinuous precipitation 53

2.7 Effect of Prior Deformation on Ageing Kinetics 57

2.7.1 Effect of cold work on continuous precipitation 58

2.7.2 Effect of cold work on discontinuous precipitation 59

2.8 Recovery and Recrystallisation 64

2.9 Effect of Ternary Additions on Precipitation . 66

2.9.1 Effects of ternary elements on continuous precipitation 67

2.9.2 Effects of ternary elements on discontinuous precipitation 70

CHAPTER 3 : EXPERIMENTAL PROCEDURE AND TECHNIQUES 73

3.1 Materials 73

3.2 Heat Treatments 73

3.3 Mechanical Tests 74

3.3.1 Hardness measurements 74

3.3.2 Tensile tests 78

3.3.3 Conventional 90° bend tests 78

3.3.4 Cantilever-type bend tests 80

3.3.4.1 Preparation of specimens for cantilever-type bend tests 85

3.3.4.2 Test method for cantilever-type bend tests ... 85

3.3.5 Fractography 87

3.4 Thermal Analysis 87

3.4.1 Background 87

3.4.2 Differential thermal analysis (DTA) 88

3.4.3 Differential scanning calorimetry (DSC) 91

3.5 Microstructural Analysis 91

3.6 X-ray Diffractometry 91

3.7 X-ray Texture Determination 92

3.8 Electrical Resistivity 93

CHAPTER 4 : EXPERIMENTAL RESULTS 95

4.1 The Hardening of Copper-Beryllium-Cobalt Alloys 95

4.1.1 Hardening in the solution treated alloy 95

4.1.2 Hardening after prior cold work 96

4.2	TEM Analysis of Decomposition Reactions	103
4.2.1	Structure of as-received alloys	103
4.2.2	Precipitation in the solution treated alloy ..	103
(1)	Ageing at 350°C	103
(2)	Ageing at 400°C	105
4.2.3	Precipitation in prior cold worked alloys	110
(1)	Ageing at 350°C	110
(2)	Ageing at 400°C	113
(3)	Ageing at 500°C	114
4.3	X-ray Diffraction Data Analysis	124
4.3.1	Evolution of X-ray diffraction peaks	124
4.3.2	Change in lattice parameter of the α-matrix ..	130
4.3.3	Half-breath measurements for cold worked alloys	137
4.4	Non-Isothermal Differential Thermal Analysis .	137
4.5	Isothermal Differential Thermal Analysis	149
4.6	Analysis of 90° Bend Test Data	158
4.7	Use of AC Potential Drop Method on 90° Bend Tests	159
4.8	Cantilever-Type Bend Test Results	162
4.8.1	Remarks on "maximum bendability angle, θ_M	162
4.8.2	Corrected bendability data for Cu-Be-Co alloys	163
4.8.3	Fractography of tested samples	170
4.9	Texture Determination for Cu-Be-Co Alloys	178
4.9.1	Recrystallisation texture	179
4.9.2	Rolling texture	179
4.9.3	Annealing texture of prior cold worked alloys	181
4.10	Electrical Resistivity Measurements	187

CHAPTER 5 : DISCUSSION 189

5.1 Precipitation Hardening in the Solution Treated Alloy 190

5.1.1 The microstructure after isothermal treatments 190

5.1.2 Change in the features of diffraction lines during ageing 195

5.1.3 Hardening response during ageing 197

5.1.4 Current TTT diagrams proposed for Cu-Be alloys 200

5.1.5 The present TTT diagrams for the solution treated alloys 201

5.1.6 TTT curves for continuous precipitation 203

5.1.7 TTT curves for discontinuous precipitation ... 205

5.1.7.1 Kinetics of discontinuous precipitation in the solution treated alloy 208

5.1.7.2 Upper and lower "C" curves for discontinuous reaction 211

5.2 Precipitation Hardening in Prior Cold Worked Alloys 215

5.2.1 TTT diagrams for prior cold worked alloys 216

5.2.1.1 "C" curves for alloys D5, D10, and D24 216

5.2.1.2 "C" curves for alloys D32 and D41 222

5.2.2 Hardening response of prior cold worked alloys during ageing 230

5.2.3 Kinetic parameters determined by isothermal and non-isothermal DTA techniques 232

5.2.4 Analysis of the kinetic parameters for deformed and undeformed states 236

5.3 Textural Changes in Cu-Be-Co Alloys 241

5.3.1 Texture after the solution treatment 242

5.3.1.1 The (225)<73$\bar{4}$> plus (522)<$\bar{4}$55> orientations .. 245

5.3.1.2 The (210)<001> orientation 246

5.3.2 Texture after cold rolling 246

5.3.3 Texture after annealing cold worked alloys ... 251

5.4 Formability of Cu-Be-Co Strip Alloys 254

5.4.1 A thickness correction factor for cantilever-type bend tests 256

5.4.1.1 Analytical model 256

(1) Purely elastic bending 256

(2) Inelastic bending 258

5.4.1.2 Correlation of the analytical model by experimental results 265

(1) Sample preparation and testing 265

(2) Analysis of the experimental data 266

5.4.2 The use of three dimensional plots to follow changes in hardness and bendability 268

5.4.3 The combined 3D graphs of normalised bendability and normalised hardness 276

5.4.4 Selection of the best thermal/thermo-mechanical treatments for optimum values of F_{NORM} 278

5.4.4.1 The solution treated alloy 290

5.4.4.2 Prior cold worked alloys 292

5.4.5 Microstructure for selected treatments 297

5.5 Fracture Behaviour of Bend Samples 299

CHAPTER 6 : CONCLUSIONS AND SUGGESTIONS FOR FURTHER WORK 301

6.1 Conclusions 301

6.1.1 Decomposition of the supersaturated solid solution 301

6.1.2 Hardening response of deformed and undeformed alloys 303

6.1.3 Texture of deformed and undeformed alloys 303

6.1.4 The use of a cantilever-type bend test technique 304

6.1.5 Selection of the best thermal/thermo-mechanical treatments for different commercial grades of Cu-Be-Co alloys 304

6.2 Suggestion for Further Work 306

APPENDIX A : Kinetic Methods for DTA and DSC Analysis . 308

A.1 Isothermal Transformation Kinetics 310

A.2 Non-Isothermal Transformation Kinetics 310

APPENDIX B : Hardness and Bendability Results 315

REFERENCES 318

CHAPTER 1

INTRODUCTION

Cu-Be alloys containing small additions of cobalt have a unique combination of high hardness and strength, good formability, good electrical and thermal conduc--tivities; in the fully age hardened condition, the alloys exhibit tensile strengths between 70 MPa and 125 MPa and Vickers hardness numbers between 200 and 400. Also, in comparison to alloy steels of similar strength and hardness Cu-Be alloys show non-sparking characteristics and greater resistance to corrosion. They are therefore used in a variety of applications, including contacts in electronics and electrical engineering, springs, parts required for high wear resistance, and non-sparking tools.

The characteristic properties of Cu-Be alloys are obtained by a two stage heat treatment schedule, namely; (i) solution treating at an elevated temperature and quenching into water to produce a single phase metastable solid solution, and (ii) ageing at a temperature in the range 300 to 500° C in order to induce precipitation of various intermediate metastable phases, such as G.P. zones, γ'', and γ', prior to the formation of the equilibrium γ phase.

Heat treatment is often carried out by a component manufacturer after fabricating the material, i.e. stamping and forming into the required shape. However, component manufacturers would prefer to obtain Cu-Be alloys in sheet form in the fully heat treated condition, but which is formable enough for required shaping, for the following reasons:

(i) when heat treating Cu-Be alloys at high temperatures there is a health hazard if beryllium, or certain of its compounds, is released into the atmosphere,

(ii) any heat treatment increases the production cost,

(iii) optimum properties may not be fully obtained due to failing to comply with the recommended heat treatment conditions.

It is clear that if Cu-Be alloys are to be used more widely than at present, they will have to be supplied to the component manufacturer in the heat treated conditions. Furthermore, they will have to be produced at the suppliers with similar or better properties allied with the ease of formability to those obtained by heat treating at the component manufacturers. In an attempt to achieve this, the supplier cold works the solution treated alloys and then heat treats in a continuous strip process. This procedure is called "mill-hardening", and depending on the amount of cold work, commercial mill-hardened Cu-Be alloys are avai--lable in six age hardenable tempers as shown in Table 1.1.

In terms of ageing response of mill-hardened alloys, there are three approaches to achieving the required mechanical properties as shown in Figure 1.1 (Harkness, 1980), namely:

(i) high temperature-short time underageing,

(ii) high temperature-long time overageing, and

(iii) low temperature-long time underageing.

There is considerable discussion as to the relative merits of these three approaches. The changes in the structure due to plastic deformation affect the precipita--tion kinetics during subsequent ageing, and hence alter the mechanical properties. While it is easy to increase the strength and the hardness by prior cold work and an appropriate ageing treatment of solution treated alloys, it is unfortunately more difficult to obtain a concomitant improvement in formability. Furthermore, there are problems in assessing formability quantitatively. However, the effectiveness of any mill-hardening cold work-heat treat--ment regime must be measured by the ease of formability and the increased hardness and strength obtained compared

to that from the standard commercial practice of heat treatment subsequent to component forming.

Although the ageing kinetics and microstructures developed during the decomposition of supersaturated Cu-Be solid solutions have been extensively studied, much of the work is not directly applicable to mill-hardening as:

(i) Many alloys previously studied are binary and small quantities of the additional elements, such as cobalt, found in commercial alloys have a marked effect on the precipitation process.

(ii) It is desirable to keep mill-hardening ageing times relatively short whereas much of the published literature is concerned with long periods of ageing.

(iii) Prior cold work is an important variable in mill-hardening, but to date the effect of cold work on the precipitation processes in Cu-Be based alloys has only received a limited amount of attention.

For these reasons, it was appropriate to investigate the effect of differing degrees of prior cold work (up to 41% reduction in thickess) and ageing treatments on the precipitation process and properties of a commercial Cu-Be-Co alloy. The properties of concern were the mechanical properties and formability, with particular emphasis being placed on determining the latter in a quantitative manner.

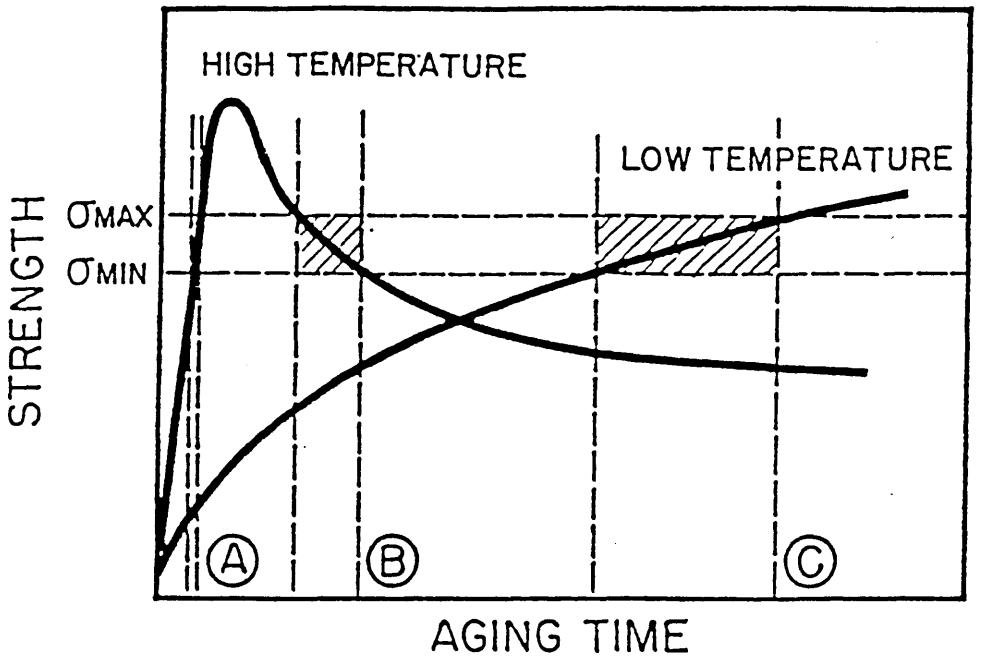


Figure 1.1- Schematic ageing response curves for copper-beryllium alloys and approaches to less-than-peak properties (Harkness, 1979).

A = Short time, high temperature under-ageing.
B = Long time, high temperature over-ageing.
C = Long time, low temperature under-ageing.

Table 1.1

Mechanical properties of mill-hardened Cu 1.7-1.9 wt% Be alloys, containing 0.05-0.4 wt% Ni plus Co (British Standard, 2870:1980)

Material (§)	Tensile strength (MN/m^2)	Elongation (%)	90° bend test		Vickers Hardness	
			T(*)	L(*)	min.	max.
WM	70	18	t	t	210	250
W1/4HM	76	14	2t	2t	240	280
W1/2HM	83	10	2t	2t	260	310
WHM	93	8	3t	3t	295	345
WEHM	104	4	6t	3t	330	380
WESHM	117	2	-	-	360	415

(*) T (transverse) and L (longitudinal) indicates the 90° bend tests carried out on samples with the bending direc--tion perpendicular or parallel to the rolling direction, respectively. Also t, which is the thickness of samples, indicates the relative safe bending radius at the inner fibre of a sample, as a measure of formability.

(§) M, HM, EHM, or ESHM indicates various thermo-mechanical treatments, i.e. degree of prior cold work and ageing time and temperature, which are classified for different hardening conditions in standards.

CHAPTER 2

REVIEW OF THE LITERATURE

2.1 The Cu-Be Phase Diagram

Experimental data on the Cu-Be phase diagram has recently been reviewed by Chakrabarti et al. (1987), and the Cu-rich side of the proposed phase diagram is given in Figure 2.1-a. According to the phase diagram in Figure 2.1-a, the maximum solubility of Be in Cu is 16.5 at.% (2.73 wt%) at 866°C, and the solute solubility temperature for 1.7-1.9 wt.% Be content is about 700°C. In order to obtain a proper supersaturated solid solution, the Cu-Be alloy must be quenched from the solution treatment tempera--ture to room temperature with a cooling rate of more than 60°C/s (Toda, 1970). The decomposition of supersaturated solid solution, α_s, passes through the precipitation of several metastable phases prior to the formation of the equilibrum phase, and may be summarised as follows:

$$\alpha_s \longrightarrow \alpha + \text{G.P. zone} \longrightarrow \alpha + \gamma'' \longrightarrow \alpha + \gamma' \longrightarrow \alpha + \gamma$$

although not all workers have detected the γ'' phase. The solvi for these metastable phases have been determined (see Figure 1.2.b) by reversion experiments in conjunction with TEM metallography and hardness measurements (Laughlin and Tanner, 1981; Shiromizu and Mishima, 1971). Further discussions on the phase transformation sequence and the associated metastable phases will be presented in the following sections.

2.2 Structure of Supersaturated Solid Solution

When a solute atom is added to a solvent lattice, the following phenomena may occur (Hume-Rothery et al., 1969; Sivertsen and Nicholson,1961; Massalski,1983):

(i) uniform lattice expansion or contraction,

(ii) change in atom size,

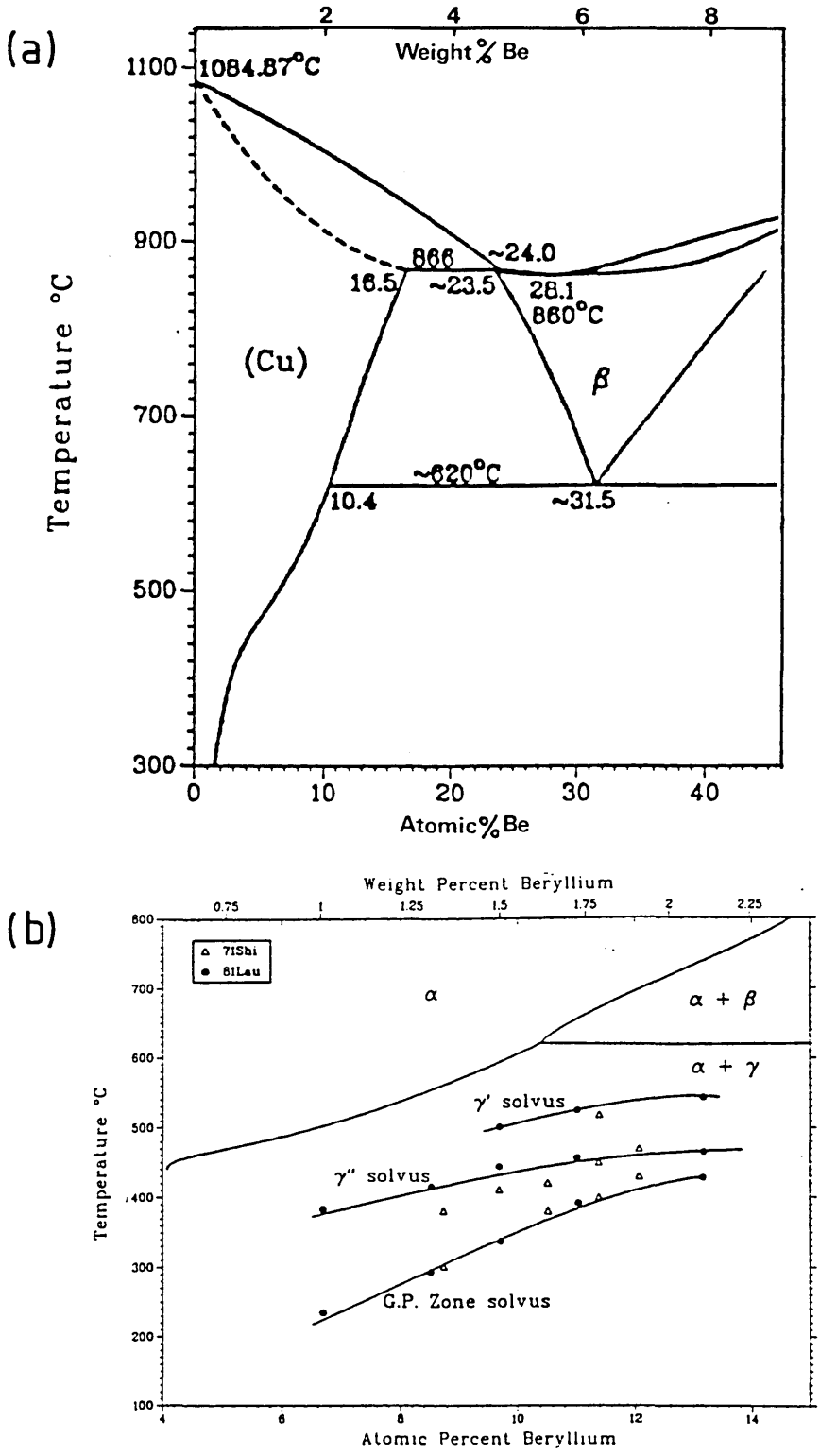


Figure 2.1- (a) Copper-rich section of the Cu-Be phase diagram (Chakrabarti et al., 1986).
(b) Solvi of metastable phases, G.P. zones, δ'', and δ' (Chakrabarti et al., 1987).

(iii) change in the electronic energy, ΔE, due to the change in the electronic structure of the solid solution,

(iv) local static displacement of the mean atomic positions of the lattice arising from the difference in size of solute and solvent atoms.

These factors are considered to be responsible for microstructural changes in solid solutions, such as the formation of lattice defects and their interactions with solute atoms, and change in the properties, e.g. lattice parameter, resistivity or conductivity, stacking fault energy, crystallographic order, and heat capacity.

In the literature, the change in lattice parameter in an alloy system is explained by a number of factors, namely the difference in atomic sizes of solute and solvent atoms, the change in the number of valence electrons due to the replacement of solvent atoms by solute atoms, and the change in the number of solute atoms per unit cell (Massalski, 1983; Sivertsen and Nicholson, 1961).

The Cu lattice parameter is reduced by the addition of 3 to 15 at.% Be as shown in Figure 2.2 (Nakagawa, 1965; Tanimura et al., 1933, as cited in Chakrabarti et al., 1987; Armitage, 1963; Wilkes and Barrand, 1968). Thus, the contraction of Cu lattice by the addition of Be atoms may be explained mainly by Be atoms being smaller than Cu atoms; atomic radii for Be and Cu are 0.089 nm and 0.117 nm respectively. There is no valence effect on the contrac--tion of the lattice in Cu-Be alloys because the addition of Be into Cu does not change the nominal electron concen--tration, both elements being two-valent. Armitage (1963) noted that the lattice parameter reduction in Cu-Be alloys closely obeys the relationship proposed by Miyatani (1949) (cited in Armitage, 1963) as shown in Figure 2.2:

$$A_s = (A_{Cu} - 0.003\ C)\ nm \qquad [2.1]$$

where A_s and A_{Cu} are the lattice parameters of the solid solution and pure copper respectively, and C is the atomic concentration of Be in solution. Armitage (1963) also proposed that 1.8 wt. % Be addition to copper lowers the

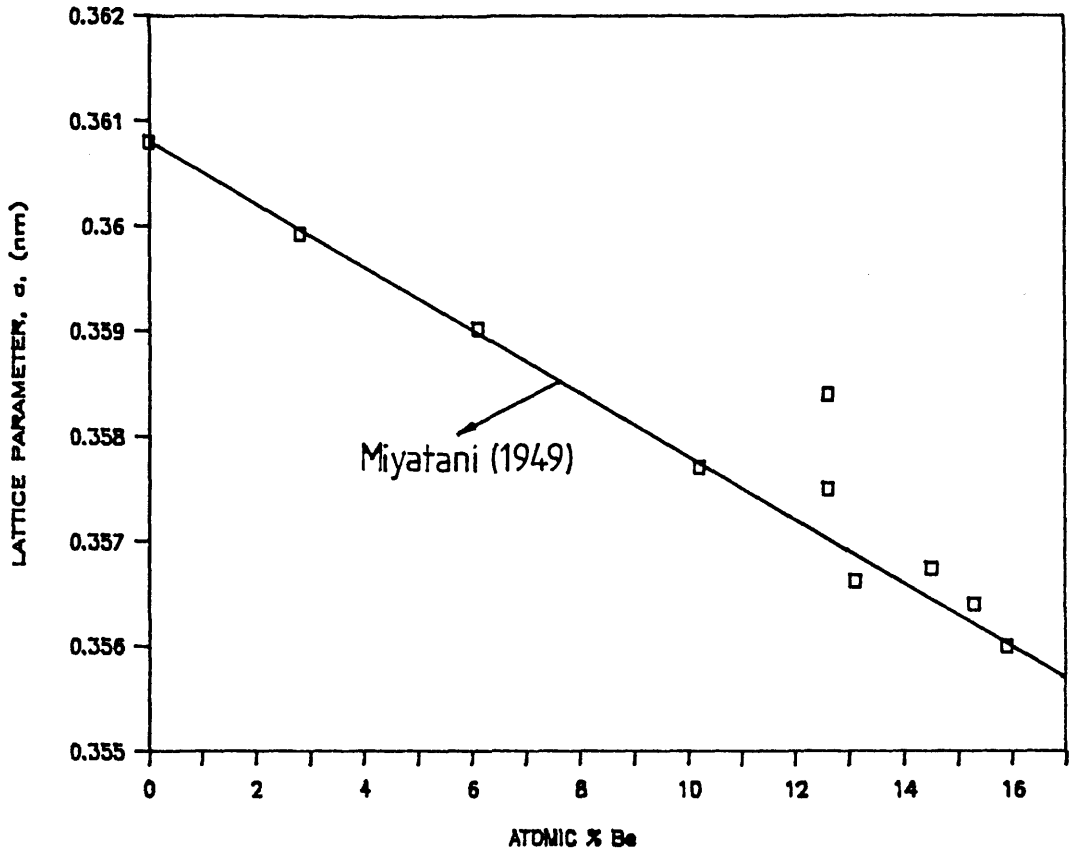


Figure 2.2- Change in the lattice parameter of Cu-Be alloys with increase in Be content. The straight line is according to equation [2.1], proposed by Miyatani (1949), and the data points are from data, reported in the literature and which have been recently summarised by Chakrabarti et al. (1987).

stacking fault energy to 30 mJm^{-2}, and thus increases the number of annealing twins.

It is evident from the data presented by Miki et al. (1983) that during the precipitation of metastable phases, Be atoms will diffuse to the nuclei of precipitates, and thus the lattice spacing of the solid solution will gradually increase as the Be concentration of the matrix falls. Thus the change in lattice parameter may be employed to follow precipitation.

During the solution treatment of Cu-Be alloys, the clustering or ordering of Be atoms, which indicates the departure from randomness, as well as the formation of defects, such as vacancies, various types of dislocations, stacking faults, and small-angle boundaries, may occur. Occurrence of these features depends on the nature of the solid solution (Massalski, 1983). Also, it has been established for many alloy systems that quenching from a single phase field gives rise to an excess vacancy concentration. During the quenching, these vacancies may

(i) condense into dislocation loops,

(ii) induce climbing to give helical dislocations, or

(iii) remain in the solid solution, probably associated with the solute atoms (Yamamoto et al.1971; Thomas and Whelan, 1959; Thomas, 1959; Smallman et al. 1959; Nicholson and Nutting, 1961; Embury and Nicholson, 1965).

Significant number of dislocation loops and helical dislocations are not observed in quenched Cu-Be alloys. A typical equilibrium room temperature vacancy concentration is of the order of 10^{-8}-10^{-7}, but during quenching the high temperature vacancy concentration, which may be of the order of 10^{-5}-10^{-4}, can be retained. (Bonfield and Edwards, 1974; Nutting, 1971). Also, the prior plastic deformation after the solid solution treatment introduces a vacancy concentration of 10^{-6} (Bonfield and Edwards, 1974). It has therefore been concluded that most of the quenched-in vacancies are held in supersaturation, and probably some association occurs between the Be atoms and quenched-in vacancies (Wilkes, 1968).

It has been suggested that, in Cu-Be alloys, the clustering for later precipitation occurs during quenching and vacancies are trapped at the clusters due to a high binding energy ($E_B \approx 0.35 \times 10^{-19}$ J) between vacancies and Be atoms (Lawley et al., 1965; Wilkes and Barrand, 1968; Wilkes, 1968). A consequence of the binding energy between solute atoms and vacancies is believed to be an increase in the concentration of vacancies around the solute atoms relative to the concentration of vacancies in the lattice (Lawley, 1967). Therefore, during the annealing treatment, the Be atom clusters may act as nuclei for the formation of G.P. zones by the transport of solute atoms to these nuclei by vacancies (Wilkes, 1968; Wilkes and Barrand, 1968).

Lawley et al. (1965) used the equation due to Lomer for the vacancy concentration, C_V, in dilute alloys to calculate the energy to form a vacancy in Cu 0.5-2.0 wt% Be alloys:

$$C_V = \exp(\Delta S/R)\exp(-E_F'/RT) \qquad [2.2]$$

where E_F' is apparent vacancy formation energy, ΔS is the entropy of the vacancy formation, and R and T have their usual meanings. But, due to the high concentrations of Be (up to 2 wt% = 12.6 at.%) equation [2.2] becomes:

$$C_V \approx \exp(S/R)\exp(-E_F/RT) \times \{1 - 12c + 12c[\exp(\Delta S_B/R)\exp(E_B/RT)]\} \qquad [2.3]$$

where S is the entropy associated with a vacancy in the pure metal, ΔS_B is the binding entropy, E_F is vacancy formation energy in pure solvent, and E_B is the binding energy. Thus, according to equation [2.3] the energy required to form vacancies and the binding energy between solute atoms and vacancies in Cu 1.5-2wt%Be alloys are $1.4\text{-}1.6 \times 10^{-19}$ J and $\approx 0.32 \times 10^{-19}$ J, respectively (Wilkes, 1968).

The addition of about 0.2-0.3 wt% Co to the binary Cu-Be alloy modifies the grain boundary step density and hence reduces the grain boundary mobility (Bonfield and Edwards, 1974). It is well documented that not only does Co segregate at grain boundaries and refine the grain size, but also localizes in cuboidal particles in the matrix during solid solution treatment (Nourbakhsh and Nutting,

1979; Tsubakino et al., 1980; Williams, 1978; Baumann and Williams, 1980; Mishima et al. 1969). It has been suggested that cuboidal particles contain both Co and Cu in addition to Fe and Si trace impurities and probably some Be (Williams, 1978). If these particles contain some Be, they would deplete the solid solution of beryllium (Entwisle and Wynn, 1960).

2.3 Precipitation Sequence

Precipitation hardening can be understood as the rearrangement of individual solute atoms to form precipi--tates during the ageing of solution treated alloys at a specified temperature for a specified time. As stated previously, three metastable phases form in succession prior to the equilibrum γ phase in Cu-Be alloys, namely, G.P. zones, γ'', and then γ'. In addition, the existence of a precursor to G.P. zones, i.e. an extremely fine dispersed structure, has also been proposed (Phillips and Tanner, 1973; Rioja and Laughlin, 1980). It should be noted that some of the information available in the literature has been obtained from Cu-Be binary and some from Cu-Be-Co ternary alloys with various Be contents (0.5-2 wt.% Be). This may explain the confusion in the literature regarding the interpretation of the precipitation mechanisms, morphology, and crystallography of metastable phases; these matters will be presented and discussed in the following sections.

Because of the distinct differences in the nuclea--tion and growth mechanisms of phases forming in the matrix and at grain boundaries and twin boundaries, the precipita--tion sequence will be summarised and discussed under two headings, namely "continuous precipitation" and "disconti--nuous precipitation".

2.4 Continuous Precipitation

2.4.1 Precursor phase

As mentioned earlier, in solution treated Cu-Be alloys containing a large vacancy supersaturation, the solute Be atoms coalesce, which is consistent with an association of Be atoms with vacancies, to form small coherent clusters during or immediately after quenching from the solution temperature (Wilkes,1968; Wilkes and Barrand,1968; Yamamoto et al.,1971; Murakami et al.,1968 Lawley et al., 1967). Such clusters therefore indicate the departure from a random distribution of solute atoms in solid solution. During ageing at room temperature (for durations up to one month), an increase in either the density or the size of clusters (or both) has been noticed in experiments based on resistivity and thermoelectric power measurements (Pelletier et al., 1983; Wilkes,1968). However, it is not clear whether these clusters form the precursor phase prior to G.P. zones. Phillips and Tanner, (1973) suggested that an intermediate state may exist between a random solid solution and the development of monolayer zones because they observed diffuse <110> scattering in the diffraction pattern of electron microscopy samples.

On the other hand, the X-ray diffraction results of Tyapkin (1966) suggest that small nuclei of an ordered phase form on ageing Cu 2 wt.% Be alloys at 200°C for up to 5 hours; these nuclei would be almost equiaxial (d=2-3 nm). Furthermore, Armitage (1963) proposed that the first indication of the decomposition of a supersaturated solid solution is the formation of solute clusters (which act as the nuclei of G.P. zones) on ageing a Cu 1.77 wt.% Be 0.24 wt.% Co alloy at 200°C up to 4 hours. These clusters would cause the short streaks (called relrods) along <110> in electron diffraction patterns, observed in conjunction with the mottled structure in the grains. However, these clusters could not be resolved by electron microscopy, presumably because the clusters would not have sharp

boundaries. On the other hand, Kainuma and Watanabe (1971) attributed the <110> relrods to the elastic strain effects induced by the formation of G.P. zones.

Neverthless, Rioja and Laughlin, (1980) claimed to have observed by electron microscopy the growth of clusters which subsequently formed the precursor phase of "equiaxed Be clusters" when a Cu 2 wt.%Be alloy is naturally aged at room temperature. They suggested that initially these clusters have equiaxed or spherical shape to minimise both surface and strain energy, but the lattice mismatch (≈12%) limits the growth of these morphologies beyond 5nm, at which the clusters probably become more plate-like to minimise the strain energy as proposed by Lee et al.(1977); as platelets they may play a role in the nucleation of G.P. zones.

2.4.2 G.P. zones

In several studies it has been shown that the process of continuous precipitation begins with the formation of metastable plate-like precipitates within the matrix, which are referred to as Guinier-Preston zones, or G.P. zones. The presence of such platelets is usually recognised by the regularly oriented streaks in electron diffraction patterns and the tweed-like structure having striations in the bright field mode in the transmission electron microscope. The striations are due to the distor--tion on the planes where solute atoms coagulate to form platelets.

In agreement with the early work of Guinier and Jacquet (1944) and Guy et al.(1948), many investigators have reported that G.P. zones form as plate-like monolayers of Be atoms which form coherently along the traces of {100} planes in the Cu-Be matrix (Figure 2.3) at temperatures below the G.P. solvus; the solvus curve for G.P. zones is shown in Figure 2.1. This phase has been characterised by both X-ray diffraction (Tyapkin and Gavrilova, 1964; Tyapkin, 1966; Geisler, 1952) and electron microscopy studies which are based on the explanation of the charac-

-teristic continuous <100> streaks and <110> relrods in the electron diffraction patterns. These features have been explained in terms of localised elastic stresses around the zones in the <100> directions, and elastic deformations along <110> (Tanaka et al., 1963; Armitage, 1963 Pfeiffer, 1965; Sorokin, 1967; Price and Kelly, 1963; Yamamoto and Murakami, 1969; Tanner, 1966; Wilkes and Jackson, 1969; Phillips and Tanner, 1973).

Electrical resistivity measurements have also shown that a maximum in resistivity occurs in the early stages of ageing in Cu-Be alloys, which is consistent with the formation of plate-like G.P. zones (Wilkes 1968; Thomas and Dorfurt, 1959; Murakami et al. 1968; Lawley et al.1967)

It has been suggested that the platelets of G.P. zones have a superlattice structure with a=0.253 nm and c=0.322 nm, (Figure 2.4.a) and an orientation relationship with the matrix of (Bonfield and Edwards, 1974):

$$(111)_{\alpha} \;//\; (110)_{G.P.} \;;\; [110]_{\alpha} \;//\; [001]_{G.P.}$$

However, many workers believe this orientation relationship applies to the more stable body-centred tetragonal γ'' phase, nucleated by the G.P. zones (Geisler et al., 1952; Zhu et al., 1986; Shimizu et al., 1971) (Figure 2.4.b).

As ageing proceeds, the G.P. zones grow in size until it is energetically favourable for the zones to lose coherency and transform to a more stable form, denoted as γ'' or γ', in the literature. It has been found that both the growth and transformation processes of G.P. zones are strongly temperature dependant, supporting the existence of the solvus for G.P. zones.

The solvi for the metastable phases in Cu-Be alloys have been determined by reversion experiments, and are given in Figure 2.1. (Laughlin and Tanner, 1981; Mishima et al., 1969; Shiromizu and Mishima, 1971). In addition, some other data in the literature for the solvus of G.P. zones in Cu 1.8-1.9 wt.% Be alloys give solvus temperatures between 320°C and 450°C (Wilkes and Jackson, 1969; Djuric and Jovanovic, 1980; Bonfield and Edwards, 1974). It must be noted that the difference in the solvus temperature may arise from discrepancies in the solution treatments and/or

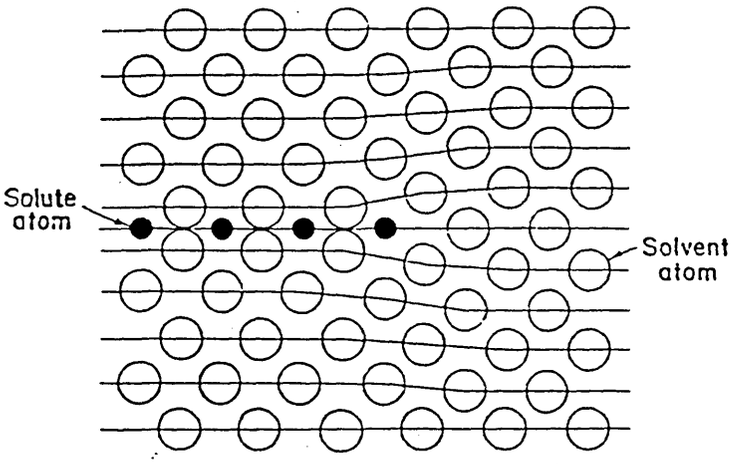
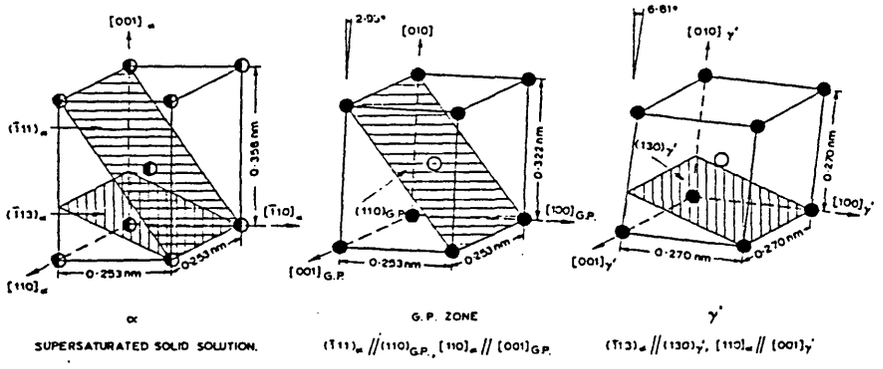


Figure 2.3- Schematic representation of G.P. zones according to Tanner (1966).

(a)



(b)

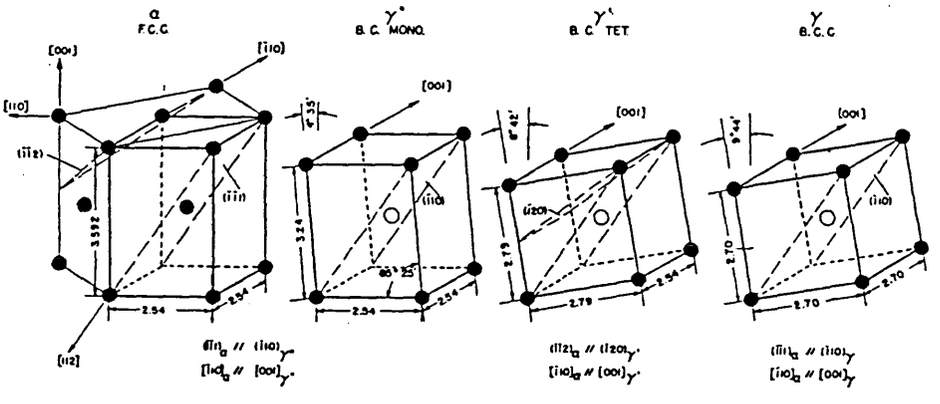


Figure 2.4- The unit cells and the relative orientations of the preci-pitates involved in the continuous precipitation sequence of Cu-Be alloys (● - Cu atom; O=Be atom; ◐=Cu or Be atom), proposed by (a) Bonfield and Edwards (1974) and (b) Geisler et al. (1952).

minor compositional differences between the alloys studied by various workers. It was found (Bonfield and Edwards, 1974) that G.P. zones may form during heating to 425°C, but there is a possibility that only zones below a critical size dissolved on heating above the "solvus", and that the remainder nucleated the subsequent more stable phase. Therefore, the reported solvus temperature above 400°C may not necessarily be correct.

2.4.3 γ'' phase

The occurrence and structure of γ'' phase in Cu-Be alloys is under debate in the literature. The γ'' phase has not been observed in all investigations and when it is observed there are differences in the proposed structure. However, as will be seen in the following detailed discussion of this phase, the general consensus is that the γ'' phase may be considered as a stack of G.P. zones on parallel planes.

According to Geisler et al. (1952), on ageing a Cu 2 wt.% Be alloy at 300°C, the γ'' phase forms coherently on $(100)_\alpha$ habit planes as shown in Figure 2.4-b. Their work, which is based on X-ray diffraction, indicated that the γ'' phase has a body centred monoclinic structure with $\beta=85°25'$, a=b= 0.254 nm and c=0.324 nm, and the following crystallographic orientation relationship:

$$(111)_\alpha \;//\; (110)_{\gamma''} \;;\; [110]_\alpha \;//\; [001]_{\gamma''}$$

Bonfield and Edwards, (1974) reported a G.P. zone with above orientation relationship, but with a body centred tetragonal structure (Figure 2.4-a), and hence there is the possibility that one of these groups has incorrectly identified the precipitate phase.

Yamamoto et al. (1971) and Yamamoto and Murakami, (1969) observed extra reflections of {110} indices, and attributed these to a coherent ordered phase, γ'', formed on $(100)_\alpha$ planes with a lattice parameter about three times that of the original solid solution. This structure may be viewed as the result of the stacking of G.P. zones such that Be atoms occupy alternate $\{100\}_\alpha$ layers.

For a Cu 2 wt.% Be alloy, Shimizu et al. (1971) reported the appearance of both 2/3{200} and 1/3{200} reflections, and attributed 1/3{200} reflections to double diffraction. The 2/3{200} reflections were assigned to the stacking of G.P. zones on alternate $\{100\}_\alpha$ planes in the manner also described by Yamamoto et al. (1971) (Figure 2.5). Shimizu et al. (1971) reported that this phase would have a body centered tetragonal structure with

$$a_{\gamma''}=a_\alpha/\sqrt{2}=0.253 \text{ nm} \; ; \; c_{\gamma''}=0.290 \text{ nm}$$

with the crystallographic orientation relationship:

$$(001)_{\gamma''}//(001)_\alpha \; ; \; [100]_{\gamma''}//[110]_\alpha$$

Similarly, Baburaj et al., (1979) reported the formation of a phase after G.P. zones, having the above structure and crystallographic orientation relationship that cause 2/3{200} reflections, however, they did not refer to this phase as the γ'' phase. Zhu et al. (1986) also observed the γ'' phase described as a body-centred tetragonal lattice having a Be atom at the centre with the c-axis contracted to 0.29 nm. They suggested that this phase is formed by the stacking of parallel G.P. zones with the distance of two lattice parameters of the matrix, containing 50 at.% Be. Also, Henmi and Nagai (1969) proposed a γ'' phase formed by the stacking of G.P. zones on about every sixth $(200)_\alpha$ atom planes.

Most studies are carried out on samples which have been quenched directly into iced water or brine and then up-quenching into a bath/furnace at the ageing temperature. However, Rioja and Laughlin (1980) have investigated the effect of two quenching conditions, namely: (a) quenching directly into a bath at ageing temperature (termed "down quenching") and (b) the conventional "up-quenching". They found that the γ'' phase is formed by the stacking of G.P. zones in the up-quenched alloys regardless of the ageing temperature, whereas, in the down-quenched alloys, the γ'' phase forms only on ageing at 300°C and below. This phenomenon was explained by reference to a schematic TTT diagram in which the curves for the G.P. zone, γ'', and γ' phases are shifted to the left by prior quenching to room temperature (Figure 2.6). The shifting of the curves to the

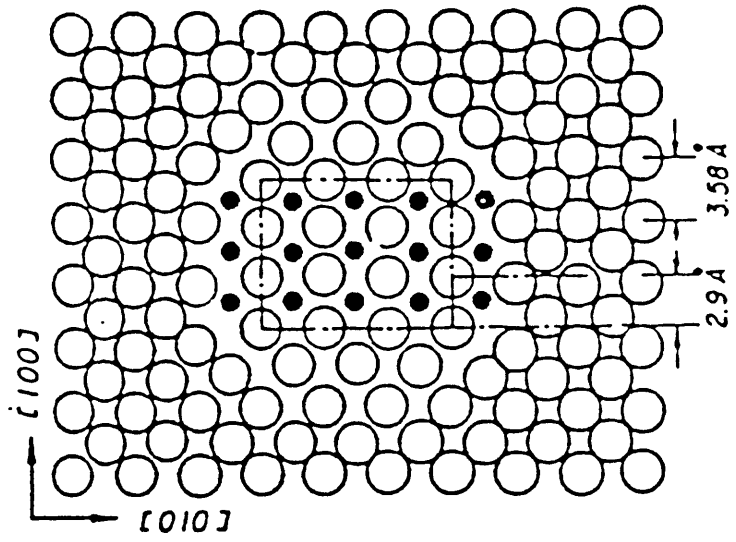


Figure 2.5- Schematic representation of the γ" phase according to Shimizu et al. (1971).

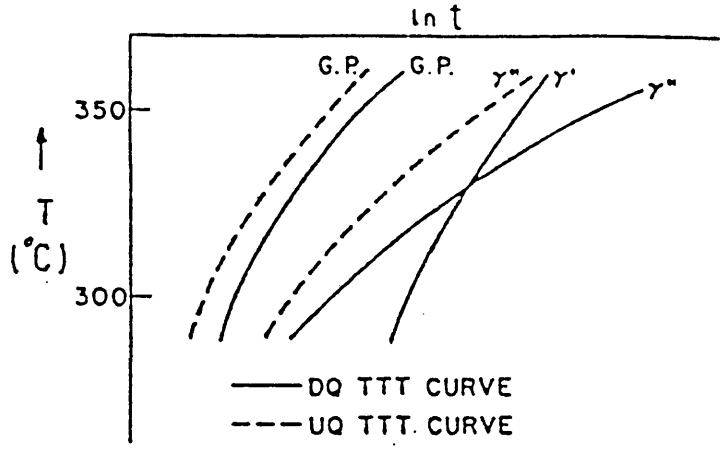


Figure 2.6- Schematic TTT curves of G.P. zones, γ", and γ' in Cu-Be, shown as a function of the type of quench (Rioja and Laughlin, 1980).

left was attributed to enhanced vacancy diffusion and cluster formation during and after the quench, so allowing the γ'' phase to form. In contrast, in samples that are "down-quenched" to ageing temperatures above 300°C, γ' forms before the G.P. zones grow to the critical size necessary to transform into the γ'' phase.

2.4.4 γ' phase

On further ageing, a second type of partially coherent plate-like precipitate, which is designated as the γ' phase, forms semicoherently in the α-matrix. Various formation mechanisms for the γ' phase have been proposed in the literature, namely:

(i) It has been suggested the formation of the 2/3{200} reflections on <100> streaks in the electron diffraction patterns indicates γ' precipitation on the $(100)_\alpha$ habit planes by a transformation process from G.P. zones; the G.P. zones formed on alternate $(100)_\alpha$ planes serve as favourable nucleation sites for the γ' precipitates, and the precipitates grow in size by the diffusion of solute Be atoms (Armitage, 1963; Pfeiffer, 1965; Bonfield and Edwards 1974). As the γ' precipitates continue to grow, the habit plane changes from the $(100)_\alpha$ to $(113)_\alpha$ planes, suggesting that the transformation to the γ' phase is completed. For the final form, the γ' phase has an ordered cubic crystal structure (B2 superlattice structure containing 50 at % Be) with a=0.27 nm as shown in Figure 2.4-a, and the crystal-lographic orientation relationship (Bonfield and Edwards, 1974; Djuric et al., 1980; Jovanovic et al., 1986):

$$(113)_\alpha \;//\; (130)_{\gamma'} \;;\; [110]_\alpha \;//\; [001]_{\gamma'}$$

(ii) The γ' phase is, however, not always nucleated by G.P. zones. As mentioned in Section 2.4.3, Rioja and Laughlin (1980) reported that in Cu 2 wt.% Be alloys quenched from the solution temperature, G.P. zones trans-form to the γ'' precipitates on ageing at any temperature. Since the γ'' phase causes a large contraction (20%) in the

G.P. zone c-axis to retain coherency within the α-matrix, on further ageing it becomes unstable and dissolves in to the matrix, rather than nucleating the γ' phase (Shimizu et al., 1971; Rioja and Lauglin, 1980). With regard to the formation of the γ' precipitates, the resistivity and microhardness studies of Sachslehner et al. (1984) are consistent with the work of Shimizu et al. (1971) and Rioja and Laughlin (1980) in that they have proposed that G.P. zones do not transform into γ' precipitates However, the γ' phase will nucleate between G.P. zones where the zone density is greatest and the matrix solute concentration is lower. As the γ' nuclei grow between the G.P. zones, they stop the formation of the zones and the Be atoms of the zones will be integrated into the γ' phase. On the basis of the electron microscopy work of Nakagawa (1965), Shimizu et al. (1971), and Yamamoto et al. (1971), it may be concluded that the γ" phase, causing the 2/3{200} reflections in electron diffraction patterns, dissolves into the α-matrix, and the "arrowhead-like" intensity maxima near the 2/3{200} reciprocal lattice positions appear, suggesting that a phase distinct from the γ" phase forms on $\{112\}_\alpha$ habit planes. This phase, which is considered to be γ', has a=0.279 nm and c=0.254 nm and the following crystall--ographic orientation relationship:

$$(112)_\alpha \;//\; (120)_{\gamma'} \;;\; [110]_\alpha \;//\; [001]_{\gamma'}$$

Rioja and Laughlin (1980) also suggested that in the early stages of development, the γ' phase has the $(112)_\alpha$ habit plane, but as the plate-like γ' precipitates grow in size, the habit plane changes from the $\{112\}_\alpha$ to the $\{113\}_\alpha$ planes, and hence the orientation relationship becomes:

$$(113)_\alpha \;//\; (130)_{\gamma'} \;;\; [110]_\alpha \;//\; [001]_{\gamma'}$$

which is the same as that determined for the γ' phase by Bonfield and Edwards (1974) and that for the γ' phase erroneously reported as γ by Shimizu et al. (1971).

(iii) Baburaj et al. (1979) reported that the equilibrium γ phase is the final product of a continuous ordering of the supersaturated solid solution, which is initiated by the formation of G.P. zones, and the compositional changes

of precipitates rather than the nucleation of different metastable precipitates. In this continuous ordering process, they describe a stage where there are intensity maxima at about 2/3{200} in electron diffraction patterns, corresponding to a body centred tetragonal cell with lattice parameters a=0.254 nm and c=0.279 nm. This stage would appear to be analogous to the γ'' phase.

Temperature has a marked effect on the nucleation of the γ' phase. On ageing Cu 1.8-2.0 wt.% Be 0.20-0.24 wt.% Co alloys at low temperatures i.e. T<380°C (Pfeiffer, 1965; Bonfield and Edwards, 1974; Jovanovic et al., 1986), and T<≈325°C (Djuric et al., 1980; Wilkes and Jackson, 1969), the γ' phase is formed continuously in the matrix by one of above processes. But, on ageing at high temperatures, the γ' precipitates are nucleated at grain boundaries, and grow into the adjoining grains. These precipitates, designated for convenience as γ'_D, have the same structure, lattice parameter, and orientation to the continuous γ' phase (Bonfield and Edwards,1974). The γ'_D will be discussed further in Section 2.5.

2.4.5 γ phase

With prolonged ageing times, the equilibrum γ phase forms; it has the B2 structure (Figure 2.4-b) and lattice parameter a=0.27 nm (Geisler et al., 1952). Some investiga--tors consider that the equilibrum γ phase is nucleated only by the γ'_D phase in a discontinuous reaction at grain and twin boundaries (Pfeiffer, 1965; Bonfield and Edwards, 1974; Wilkes and Jackson, 1969; Armitage, 1963). However, others have proposed that after long ageing treatments the γ phase forms directly in the matrix with the Kurdjumov-Sachs orientation relationship (Rioja and Laughlin, 1980; Baburaj et al., 1979):

$$(111)_\alpha \;//\; (101)_\gamma \;;\; [110]_\alpha \;//\; [111]_\gamma$$

It has been suggested (Nakagawa, 1965; Geisler et al. 1952) that the ageing temperature determines whether the γ phase is nucleated in the matrix or by the γ'_D phase. Ageing at low temperatures (T<400°C) results in the form-

-ation of the nodular γ phase in a discontinuous cellular reaction, whereas on ageing at high temperatures i.e at 400 °C (Nakagawa,1965), at 425°C (Price and Kelly,1963), or at 500°C (Sorokin,1967), a Widmannstätten arrangement of the equilibrum γ precipitates is observed within the matrix. The orientation relationship for the continuous γ precipi--tates, determined by electron microscopy, was:

$$(111)_\alpha \;//\; (110)_\gamma \;;\; [110]_\alpha \;//\; [001]_\gamma$$

2.5 Discontinuous Precipitation

Discontinuous precipitation, which may be described as (i) heterogeneous boundary nucleation and (ii) concur--rent boundary migration, has been explained by several models as recently reviewed by Williams and Butler (1981). The two critical steps result in a lamellar precipitate advancing into a supersaturated solid solution which may contain a prior metastable phase. The models proposed in the literature for the occurrence of these steps in Cu-Be alloys as well as in other alloy systems and their overall reaction kinetics will be summarised and discussed in the following subsections.

2.5.1 Occurrence of discontinuous precipitation

In the preceding Sections, continuous precipitation in Cu-Be alloys has been described as the nucleation and growth of precipitates in the matrix with certain orientation relationships and structures. However, under certain conditions, the discontinuous precipitation is the favoured mode of decomposition in the Cu-Be alloy system.

The nucleation of semicoherent or incoherent precipitates in the matrix usually involves a large volume strain around the nuclei (Christian, 1975). In the absence of sufficient defects in the matrix to accommodate the strain, these phases nucleate preferentially at grain boundaries, since grain boundaries contribute significantly to a reduction in the interfacial free energy and the elastic strain energy, resulting in a smaller critical free

energy for the nucleation of precipitates at grain boundaries (Russel and Aaronson, 1975; Kelly and Nicholson, 1963).

Various interpretations have been put forward in the literature concerning the factors governing grain boundary precipitation, such as the energy of the precipitate/matrix interface (Unvin and Nicholson, 1969), the relationship between grain boundary misorientation and boundary migra--tion energy (Rutter and Aust, 1965), impurity-segregation level (Gleiter, 1970), step density and mobility (Gleiter, 1971), and grain boundary diffusivity (Rutter and Aust, 1965). It has also been shown (Butler and Swann, 1976) that the existence of grain boundary steps and ledges, as well as relative orientation of the boundary to the habit plane of precipitates, greatly influences the precipitation at grain boundaries.

Alternatively, Meyrick (1976) considered the occur--rence of the discontinuous precipitation in relation to the driving force to move the grain boundary, which derives from the reduction of the grain boundary energy as the degree of solute segregation decreases. Both the decrease in the segregated solute population at boundaries due to precipitation and the acting of these precipitates as pinning points can provide a driving force for the boundary to migrate. The main criterion in this model is whether sufficient solute atoms are incorporated into the boundary during its initial motion for the reaction to be energetically favourable.

Discontinuous precipitation at grain boundaries also depends on the particle/matrix misfit parameter (Williams and Butler, 1981). The misfit strain arising from the semicoherent or incoherent interfaces of precipitates, can be better accommodated at grain boundaries and therefore the higher the misfit strain, the more favourable is the discontinuous precipitation in the absence of a reasonable number of lattice defects in the matrix. According to the work of Kunze and Wincierz (1965), Williams and Butler (1981) concluded that, in Cu-based alloys, the volume change, Δv, accompanied by precipitation in the matrix

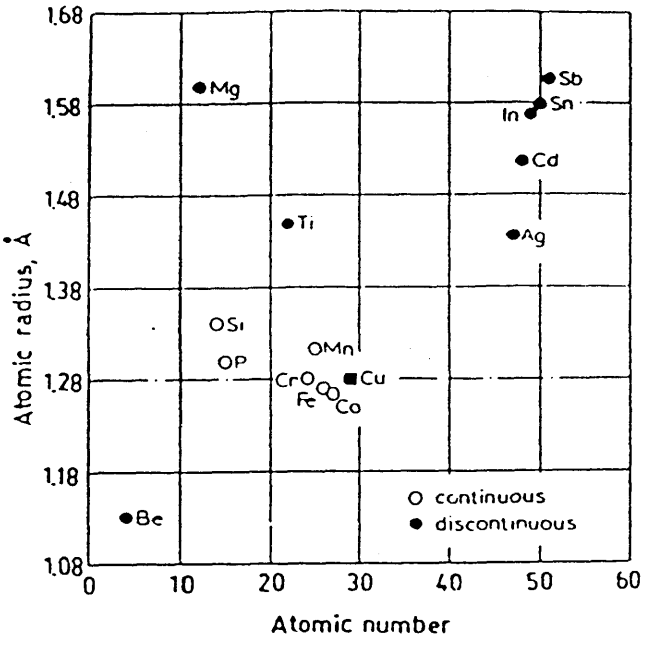


Figure 2.7- The occurrence of continuous and discontinuous precipita-tion in copper-base alloys, according to Böhm (1981).

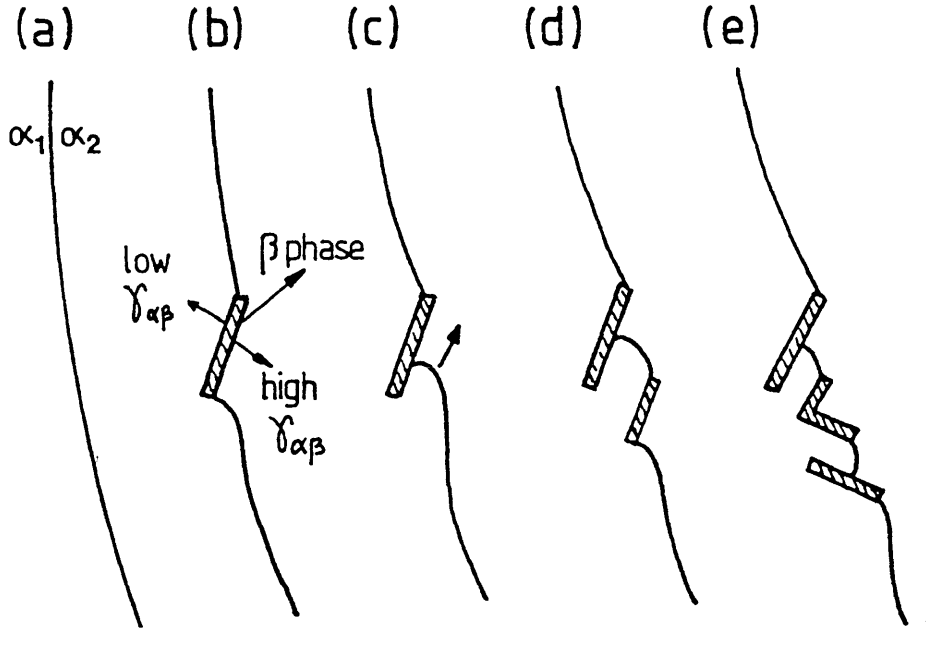


Figure 2.8- Discontinuous cell generation from a single precipitate at a grain boundary, according to "Pucker-type" mechanism (after Tu and Turnbull 1967).

should be between 0.3 and 0.9 %. Hagel and Beattie (1959) suggested that a minimum particle/matrix misfit parameter (≈1%) is necessary to start the discontinuous reaction. To the author's knowledge, the misfit parameter for Cu-Be alloys has not been determined. However, Yamamoto et al. (1971) reported a 10% contraction of the matrix surrounding G.P. zones in the direction normal to the plane of the zones, and the formation of large elastic strain fields associated with the formation of the γ' and γ phases. Similarly, Geisler et al. (1952) found that the γ'', γ', and γ phases formed in a Cu 2 wt% Be alloy involve strains of 3/4-1% in the matrix, suggesting that a large misfit exists between the precipitates and the matrix.

Another criterion for the occurrence of the discon--tinuous reaction in Cu-base binary alloys, is the atomic mismatch, that is the difference in the size of the solute and solvent atoms (Böhm, 1961). As shown in Figure 2.7, when the difference in the size of solute and solvent atoms Δr is larger than 11%, discontinuous precipitation is the favoured mode of reaction while it is suppressed when Δr is $<$ 11%. The value of Δr for Cu and Be atoms is 12.5%, and hence discontinuous precipitation occurs in Cu-Be alloys.

Clearly, there are a number of conditions which favour, to varying degrees, the process of discontinuous precipitation. In turn, these conditions are a function of many factors, e.g. ageing temperature, minor alloying additions etc, all of which may have to be considered. Because of these complications a number of models are available which may or may not be appropriate for a particular alloy system.

2.5.2 Initiation mechanisms

Three distinct mechanisms have been proposed for the initiation of discontinuous precipitation in alloys; namely

(i) Precipitate induced grain boundary migration: Tu and Turnbull (1967) proposed a "pucker" type mechanism for the initiation of discontinuous precipitation. They proposed

that the discontinuous reaction is initiated by the nucleation of a disc or plate-like precipitate on one side of a grain boundary, having a characteristic orientation relationship with the matrix; the implicit assumption in this model is that the boundary would be effectively immobile before precipitation. The precipitate has a high-energy (incoherent) interface along the grain boundary and a low-energy (coherent or semicoherent) interface with the matrix. It was assumed that in order to bring the boundary into alignment with a low energy habit plane, precipitates cause a local deflection of the boundary into the puckered condition, as shown in Figure 2.8-b. To eliminate the imbalance in interfacial energy between the two broad faces of the precipitate, the grain boundary migrates along the high energy interface and leaves the precipitate embedded in the grain. But, the tip of the precipitate is still attached to the grain boundary. This process is repeated to build up a series of parallel precipitates (Figure 2.8-d).

(ii) Precipitation on migrating boundaries: Fournelle and Clark (1972) assumed that thermally induced grain boundary movement over a short distance takes place prior to the nucleation of precipitates (Figure 2.9-a). The movement of the boundary results in the accumulation of solute atoms which nucleate precipitates and hence pin the boundary (Figure 2.9-b). Further movement of the boundary is favoured by the compositional gradient of the solute across the grain boundary and results in the growth of precipita--tes as the boundary bows between the precipitates (Figure 2.9-c and d). Branching may occur to give the final lamellae structure shown in Figure 2.9-e. Thus, the cellular colonies at grain boundaries are formed by boundary migration maintained by the solute transfer to the growing precipitates. In contrast to the pucker-type preci--pitation, no characteristic orientation relationship is required for this mechanism.

(iii) If there are prior coherent or semicoherent matrix precipitates, discontinuous precipitation is initiated by the boundary straightening as the small precipitates on one side of the boundary dissolve. Solute redistribution aids the localised coarsening of the large particles touching the other side of the grain boundary in the manner shown in Figure 2.10 (Williams and Edington, 1976).

It must be noted that the work of Tu and Turnbull (1967) was on ageing Pb-Sn alloys at $T<T_M/2$, where Tm is the melting temperature of the alloy, while Fournelle and Clark (1972) investigated the discontinuous precipitation on ageing Cu-In alloys at $T>T_M/2$. It is therefore possible that the different initiating mechanisms observed by many investigators arise from the effect of temperature on the reaction mechanism. The observations on Cu-Be alloys support the view that the initiation of discontinuous precipitates depends on the ageing temperature. Baumann et al. (1981) proposed that there are two temperature regions which induce different nucleation processes:

(a) At high temperatures ($T > T_M/2 \cong 500$ °C) the thermally activated grain boundary migration precedes the precipita-tion step, and then precipitates nucleate at the boundary. As stated by Fournelle and Clark (1972), the boundary will move towards its centre of curvature before precipitation occurs if there is no prior deformation. As the migration proceeds, some of the precipitates start dissolving while the others continue to grow, which is similar to the process proposed for the initiation of the discontinuous coarsening reaction in the presence of the matrix precipitates in Al-Li alloys (Williams and Edington 1976).

(b) At low temperatures ($T < T_M/2 \cong 500$ °C), discontinuous precipitates form prior to any significant grain boundary migration, which then induces boundary migration by a pucker type process as shown in Figure 2.11. As the boundary moves between precipitates, the precipitates are embedded in the grain in a low energy orientation

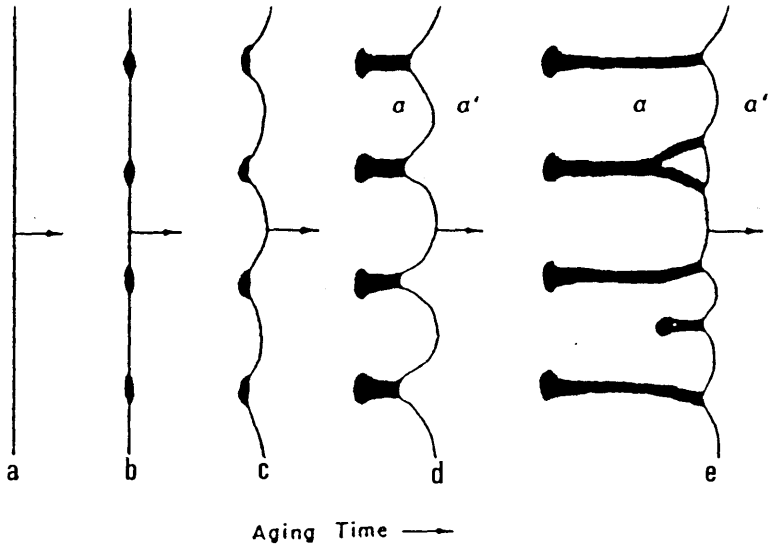


Figure 2.9- Diagram showing the morphological development of cellular structure from an originally unoccupied moving grain boundary (after Fournelle and Clark, 1972).

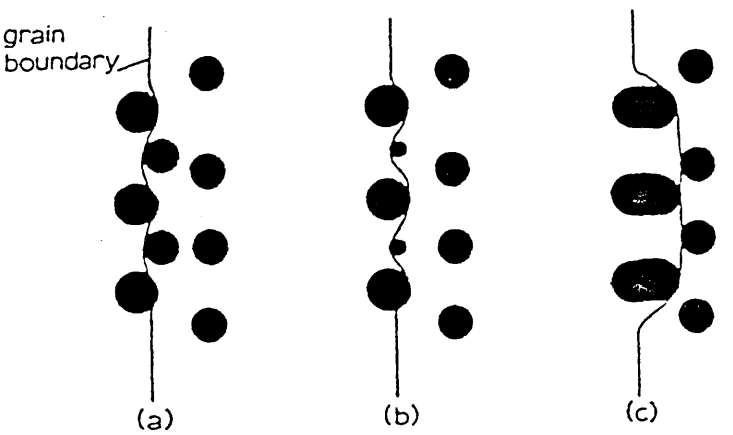


Figure 2.10- Mechanisms for the initiation of discontinuous precipita-tion by competitive coarsening of the matrix precipitates, proposed by Williams and Edington (1976).

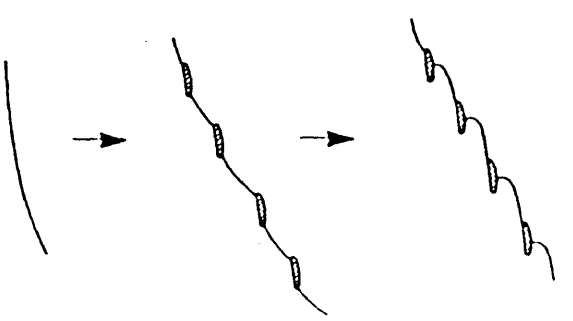


Figure 2.11- Grain boundary precipitation followed by the boundary migration as observed in Cu-Be alloys (Baumann et al., 1981).

relationship with the matrix. This mechanism is similar to that proposed by Tu and Turnbull (1967). However, Baumann et al. (1981) noted a different sequence of events in Cu-Be alloys, namely that multiple precipitate nucleation occurs before any significant grain boundary migration, whilst Tu and Turnbull (1967), based on observations on Cu-In alloys, suggested that the formation of a single precipitate induces the grain boundary migration, which brings the boundary into the favoured orientation for subsequent precipitation.

2.5.3 Growth mechanisms

The growth mechanism of discontinuous precipitates depends on the specific nucleation mechanism that initiated the reaction. The mechanisms proposed in the literature for the growth of precipitates may be classified in two groups, namely; (a) growth in one direction and (b) growth in two directions (Williams and Butler, 1981).

It has been suggested (Williams and Edington, 1976; Butler and Williams, 1982) that growth in one direction takes place when ageing at a temperature at which thermally activated grain boundary migration can occur. The litera-ture reviewed by Williams and Butler (1981) indicates that $T_M/2$ is the minimum temperature for thermally activated boundary migration. Thus, the boundary migration results in concurrent boundary precipitation on one side of the boundary as described by Fournelle and Clark (1972).

When $T<T_M/2$, only precipitate-induced grain boundary migration can occur since the boundary is unable to move through thermal activation, and hence the growth direction depends on the characteristics of the nucleation of preci-pitates (Butler and Williams, 1982). At $T<T_M/2$, the most commonly reported initiation mechanism is that initial precipitation occurs on both sides of the grain boundary (Williams and Butler, 1981). Tu and Turnbull (1967) described the first stage of the discontinuous growth as the formation of a cell structure while the boundary is misoriented (Figure 2.12). The development of "S" shaped

discontinuous cells has been reported by Fournelle (1979) (Figure 2.13) to describe the morphology of discontinuous precipitates in Fe-Ni-Ti alloys . Frebel and Schenk (1979) proposed the development of a "double seam" morphology via an "S" mechanism (Figure 2.14) to explain the growth of discontinuous aggregates in two directions in Au-Fe alloys.

The growth mechanisms in Cu-Be alloys have been investigated in detail by Baumannet al. (1981). They proposed three different growth morphologies on ageing Cu 1.8 wt% Be 0.25 wt% Co alloy, namely, single seam formation (Figure 2.9), which agrees with the definition of Frebel and Schenk (1979), "S" type morphology (Figure 2.15-a,b), and double seam formation (Figure 2.15-c,d). They also reported that the occurrence of these three morphologies depends on the ageing temperature:

(i) At high temperatures ($T>T_M/2$), thermally activated grain boundary migration is predominant, and the direction of nucleus growth is controlled by this factor. Thus, the nucleation and growth of precipitates occurs on one side of the grain boundary, opposite to the migration direction, giving rise to a single seam.

(ii) At low temperatures ($T<T_M/2$), initially the discon--tinuous precipitation occurs on both sides of the boundary that results in an "S" morphology (Figure 2.15-a and b). Then, the cellular growth on both side of the boundary produces a double seam of precipitates, as shown schemati--cally in Figure 2.15-c and d.

2.5.4 Phases involved in discontinuous precipitation

As mentioned earlier, the discontinuous reaction in Cu-Be alloys starts with the nucleation of γ'_D phase at grain boundaries, followed by the growth of duplex cellular precipitates and a reoriented matrix into the adjoining grains (Wilkes and Jackson, 1969; Entwisle and Wynn, 1961; Bonfield and Edwards, 1974). On ageing Cu 1.8 wt% Be 0.28 wt% Co alloys in the temperature range 200 to 425°C,

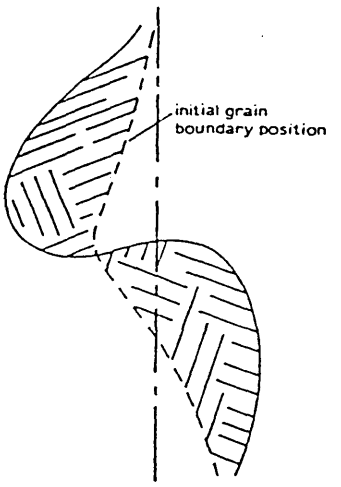


Figure 2.12- Growth of discontinuous precipitates in two directions from an initially curved grain boundary (after Tu and Turnbull, 1967).

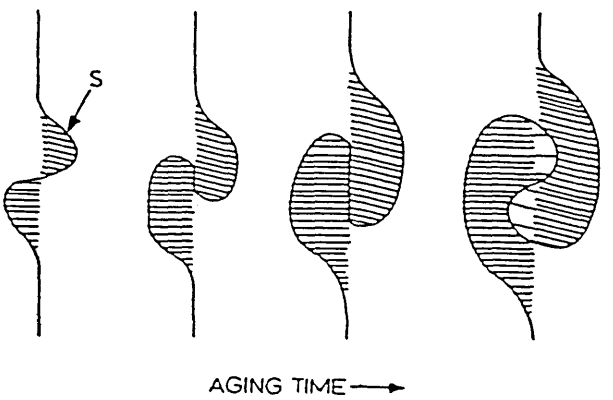


Figure 2.13- Schematic diagram of "S" mechanism according to Fournelle (1979).

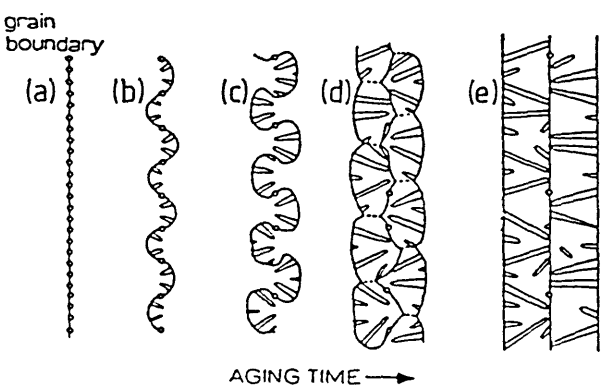


Figure 2.14- Schematic representation of the development of double seam morphology through the "S" mechanism (after Frebel and Schenk, 1979).

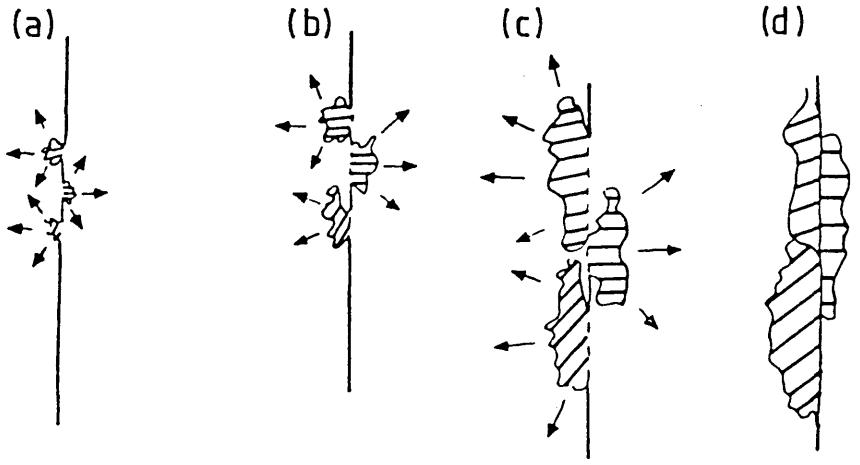


Figure 2.15- Schematic display of "double seam" development from the "S" mechanism, as observed in Cu-Be alloys (Baumann et al., 1981).

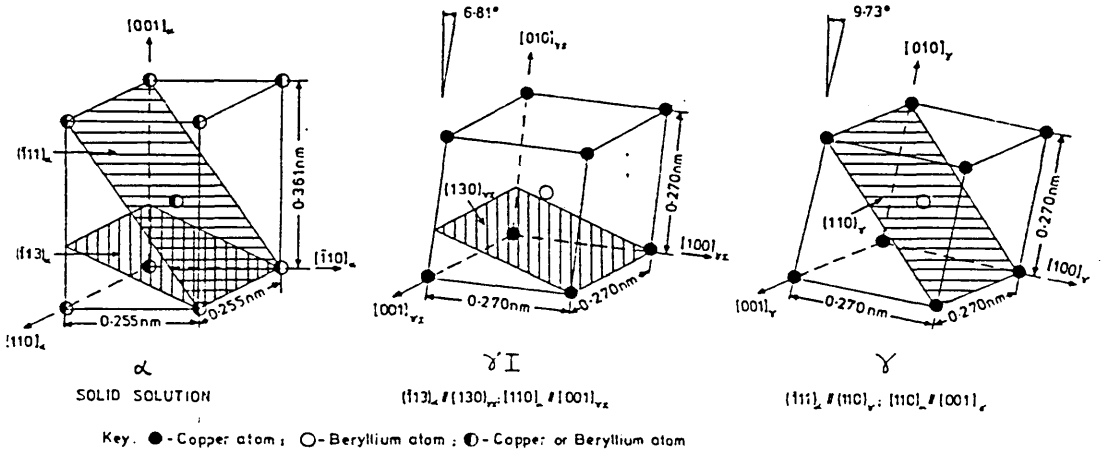


Figure 2.16- The unit cells and relative orientations of the γ'_D and γ_D precipitates (after Bonfield and Edwards, 1974).

Bonfield and Edwards (1974) found that the γ'_D phase has a habit plane close to $(113)_\alpha$, a B2 superlattice structure with a=0.27 nm, and the following crystallographic orientation relationship with the matrix:

$$(113)_\alpha \;//\; (130)_{\gamma'_D} \;;\; [110]_\alpha \;//\; [001]_{\gamma'_D}$$

They also concluded that this phase is the same as the continuously precipitated γ' phase which was described in Section 2.4.4. However, Baumann et al. (1981) proposed that the discontinuous precipitation involved the equilibrum γ phase (designated as γ_D), not the γ'_D phase. They reported that the γ_D phase has the same orientation relationship as the γ'_D phase presented above, but with a $(225)_\alpha$ habit plane.

According to the convergent beam electron microscopy work of Williams (1978) the γ'_D phase has a B2 superlattice structure with a=0.27 nm, agreeing with previous work; however, the orientation relationship was found to be

$$(110)_\alpha \;//\; (001)_{\gamma'_D} \;;\; [112]_\alpha \;//\; [110]_{\gamma'_D}$$

which differs from the other relationships determined.

Bonfield and Edwards (1974) reported that, in the later stages of ageing at 425 °C, the γ'_D precipitates approach equilibrum by a slow lattice diffusion process and transform to the equilibrum γ_D phase. Their analysis has shown that the equilibrum γ_D phase (CuBe) has a B2 superlattice structure with a=0.27nm (Figure 2.16) and the orientation relationship:

$$(111)_\alpha \;//\; (110)_{\gamma_D} \;;\; [110]_\alpha \;//\; [001]_{\gamma_D}$$

However, the electron microdiffraction analysis of Sorokin (1967) on Cu 2 wt% Be alloys suggests that on ageing at 500 °C, the γ_D phase has an orientation relationship:

$$(011)_\alpha \;//\; (100)_{\gamma_D} \;;\; [111]_\alpha \;//\; [001]_{\gamma_D}$$

Thus, although there is some disagreement over the details in the literature, it would appear that the discontinuous reaction at grain boundaries in Cu-Be alloys may be summarised as $\alpha + \gamma'_D \rightarrow \alpha + \gamma_D$, in which the metastable γ'_D phase at grain boundaries transforms to the equilibrium γ_D phase.

2.5.5 Effects of prior continuous precipitation

In many alloys, the formation of metastable phases in the matrix occurs before the reaction front of discontinuous precipitates moves across the matrix. Many factors, such as (a) the interaction of the discontinuous reaction front with precipitates in the matrix, (b) the driving force required to replace the continuous precipitates in the matrix with more stable precipitates in a discontinuous reaction, and (c) the reduction in solute concentration in the matrix by continuous precipitation, effectively slow down the discontinuous reaction kinetics (Hornbogen, 1972; Williams and Butler, 1981). The discontinuous precipitation in Cu-Be alloys must, therefore, be considered with the nucleation and growth of continuous precipitates in the matrix.

The literature suggests that, in the ageing of Cu-Be alloys, two distinct modes of precipitation, namely continuous and discontinuous precipitation, are in competition. The predominant mode depends on the quenching temperature from the solution treatment and the ageing temperature (Tsubakino and Nozato, 1978; Bonfield and Edwards, 1974; Entwisle and Wynn, 1961). The presence of additional elements and the degree of prior cold deformation of the alloy also influence the precipitation mode in Cu-Be alloys; these factors will be discussed in Section 2.7. This section will concentrate on the effect of temperature on the interrelation between continuous and discontinuous precipitation.

During quenching a Cu-Be alloy from the solution treatment temperature, a high vacancy concentration is achieved, which ensures the extensive volume diffusion of the Be atoms during subsequent ageing, and also assists the formation of metastable precipitates in the matrix (Wilkes and Barrand, 1968). Rakhshtadt and Tkhagapsoyev (1975) proposed that, on ageing Cu 1.9 wt% Be alloys, the γ' precipitates formed in the matrix provide an effective physical barrier against the movement of the discontinuous reaction front as well as reducing the Be concentration in

the solid solution, which will consequently reduce the driving force for the discontinuous reaction. They suggested that an increase in the quenching temperature results in the formation of coarser γ' precipitates in the matrix because of the increased rate of decomposition resulting from the increased vacancy concentration. These matrix precipitates pin the discontinuous reaction front more effectively, and hence reduce the rate of discontinu--ous precipitation. Alexander et al. (1982) and Borchers and Schuls (1976) also support this view.

Various explanations have been put forward in the literature for the effect of ageing temperature, T_A, on the precipitation mode in Cu-Be alloys; the main propositions are summarised in Table 2.1. The data cover three tempera--ture ranges, namely $T_A<T_2$, $T_2<T_A<T_1$, and $T_A>T_1$, each with different modes of precipitation. It can be seen that not all investigators have investigated the three ranges and that there is a spread of values for T_1 and T_2. These discrepancies, which in most cases are not significant, may be attributed to differences in composition. The precipita--tion phenomena in the three ranges may be summarised as follows:

(i) Below T_2, the γ' precipitates form after G.P. zones in the matrix, but prior to the discontinuous precipita--tion. Discontinuous precipitates then appear and grow very slowly on further ageing. Values for T_2 vary from 275°C to 400°C with most in the range 350 to 400°C.

(ii) Between T_1 and T_2, the discontinuous precipitation of γ'_D precedes the formation of the γ' phase in the matrix; later, however, the growth of γ' phase in the matrix slows down the discontinuous reaction through the pinning effect. In this temperature range, both continuous and discontinuous precipitates form more rapidly than that at $T_A<T_2$. Values for T_1 range from 415°C to 550°C.

(iii) Above T_1, the discontinuous precipitation (with a lamellar structure) initially appears at the grain

Table 2.1

The change in the mode of precipitation in Cu-Be alloys in relation to ageing temperature and time and compositional changes as observed by various authors.

Composition	Temperature range, (°C)	Observed phenomena
Cu 0.9 wt% Be	$T_A<T_2=275$	Tsubakino and Nozato (1978): Continuous γ' precipitates form after G.P. zones prior to the discontinuous precipitation (cellular reaction). The precipitation of fine γ' phase has no effect on the cellular growth.
" "	$T_2<T_A<T_1=415$ ...	Discontinuous precipitates, γ'_D, form prior to the continuously precipi--tated γ' phase, and later the growth of γ' precipitates in the matrix results in a decrease in the cellular growth rate.
	$T_A>T_1=415$	Discontinuous precipitates (equilibrum γ phase, called γ_D) form with a lamellar structure, prior to the formation of continuous precipitates (equilibrum γ phase). When the γ precipitates form in the matrix, they effectively reduce the cellular growth rate. But, during later stages of ageing, the γ precipitates in the matrix become part of the cellular reaction, and the interface of the cells continue to advance.
Cu 1.4 wt% Be (*)	$T_A<T_2=325$ $T_2<T_A<T_1=450$ $T_A>T_1=450$	Tsubakino and Nozato (1978): observed the same phenomena as above, but the temperature ranges differed slightly.
Cu 1.5 wt% Be	$T_A<T_2=300$	Jovanovic et al. (1986): The age hardening starts with the formation of G.P. zones, followed by the formation of the γ' phase in the matrix. At the same time small lamellar precipitates are formed at grain boundaries.
" "	$T_A>T_2=300$	The start of hardening is related to the discontinuous precipitation of γ'_D phase, as a predominant mode of decomposition. On further ageing, the γ'_D phase transforms to the equilibrum phase γ_D.

CONTD...

Table 2.1 Continued.

Composition	Temperature range, (°C)	Observed phenomena
Cu 1.8 wt% Be 0.28 wt% Co (x)	$T_A<T_2=380$	Bonfield and Edwards (1974): Continuous precipitation is the major mode (G.P. zones⟶γ' phase), and the discontinuous precipitation is limited to small areas around the grain boundaries.
	$T_A>T_2=380$	Discontinuous precipitation (γ'_D phase⟶ β_D phase) is the major mode mode while a considerable amount of continuous precipitates forms.
Cu 1.7 wt% Be 0.24 wt% Co (x)	$T_A<T_2=380$	Entwisle and Wynn (1961): observed the same phenomena as Bonfield and Edwards (1974).
	$T_2<T_A<T_1=500$	
	$T_A>T_1=500$	observed the same phenomena as Tsubakino and Nozato (1978).
Cu 2.0 wt% Be 0.1 wt% Co (x)	$T_A<T_2=380$	Entwisle and Wynn (1961): The same phenomena as those summarised for Cu 1.7 wt% Be 0.24 wt% Co alloys.
	$T_2<T_A<T_1=550$	
	$T_A>T_2=550$	
Cu 2.0 wt% Be	$T_A<T_2=350$	Tsubakino et al. (1981): G.P. zones⟶ γ' phase transformation in the matrix precedes the discontinuous precipitation. The γ' precipitates do not influence the cellular growth.
	$T_A>T_2=350$	Discontinuous precipitation takes place first, and then continuous preci--pitates (plate-like γ' precipitates) appear in the grains where the cellular structure has not developed. Wilkes and Jackson (1969) supported this view, but proposed $T_2=320$ °C.

CONTD...

Table 2.1 Continued.

Composition	Temperature range, (°C)	Observed phenomena
Cu 2.0 wt% Be	$T_A<T_2=400$	Nakagawa (1965): In the early stages of ageing, G.P. zones and grain boundary precipitates, γ, coexist, but later the γ precipitates at the boundaries grow by the process of Be diffusion from the matrix γ' phase.
	$T_A>T_2=400$	The γ' precipitates in the matrix and the γ_D at grain boundaries coexist; the γ' precipitates limit the mobility of the grain boundaries.
Cu 2.0 wt% Be	$T_A<T_2=320$	Wilkes and Jackson (1969): The γ' precipitates are nucleated by G.P. zones in the matrix.
	$T_A>T_2=320$	The γ' precipitates are nucleated inhomogeneously at grain boundaries, accompanied by occasional discontinuous precipitation of the γ_D phase.

(*) An increase in Be content of the alloy increases both T_1 and T_2.
(x) Note that the Co addition increases T_2, and possibly T_1.

boundaries and advances into the grains. This is followed by the formation and growth of the γ' precipitates in the matrix, which slows down the lamellar growth. Nevertheless, on further ageing the discontinuous reaction completely transforms the grains to γ'_D precipitates in a reoriented α-matrix. Finally, although there is some doubt regarding the exact sequence of events on further ageing, i.e. whether γ'_D transforms directly to γ_D, or whether γ_D precipitates and γ'_D dissolves, it is clear that the final microstructure consists of spheroidised γ_D precipitates.

2.6 Thermodynamics and Kinetics of Precipitation in Cu-Be Alloys

2.6.1 Continuous precipitation

In many alloys, it has been found that the precipi--tation sequence follows initially the path of minimum activation energy (minimum critical free energy). The G.P. zones are generally treated as the homogeneous nucleation of a second phase without the aid of pre-existing heteroge--neties in the matrix (Lorimer, 1982). Thus, the coherent G.P. zones are the first phase formed in the matrix, and subsequently they will dissolve due to the formation of a metastable phase with a lower free energy but a higher activation energy (Kelly and Nicholson, 1963).

Rioja and Laughlin (1980) have investigated the nature of sequential precipitate nucleation in Cu-Be alloys by extending the work of Russel and Aaronson (1975) explaining the kinetic theory of nucleation. Russel and Aaronson gave the following equation for the nucleation rate, J:

$$J = Z\beta^* N \exp(-\Delta G^*/kT) \qquad [2.4]$$

where $Z \approx 10^{-2}$, β^* is the rate at which solute atoms join the critical nucleus, N is the number of atomic nucleation sites per unit volume, k and T have their usual meanings, and ΔG^* is the free energy of activation to form a critical nucleus, given by:

$$\Delta G^* = (16\pi\sigma^3_{\alpha/\beta})(1 - 2f[\alpha]) \,/\, 3(\Delta G_V + W)^2 \qquad [2.5]$$

where $f\{\alpha\} = (2 - 3\cos\alpha + \cos^3\alpha)/4$, $\alpha = \cos^{-1}(\sigma^c_{\alpha\beta}/\sigma_\beta)$, $\sigma_{\alpha\beta}$ is interfacial energy of a spherically curved α/β boundary, $\sigma^c_{\alpha\beta}$ is interfacial energy of a partially or fully coherent interface, ΔG_v is the volume free energy change during the nucleation, and W is the volume strain energy for the formation of a critical nucleus.

According to equation [2.5], Rioja and Laughlin assumed that for the nucleation of a disc of radius r and half thickness c, ΔG^*_i is:

$$\Delta G^*_i \propto \{\sigma_{i(1)}\sigma^2_{i(2)}\} / \{\Delta G^V_i + W_i\}^2 \qquad [2.6]$$

where $\sigma_{i(1)}$=the surface energy of the flat surface of the ith phase, $\sigma_{i(2)}$ the surface energy of the edge of the ith phase, ΔG^V_i=the volume free energy change accompanying the formation of the critical nucleus of the ith phase, and W_i=the volume strain energy change due to the the formation of a coherent or semicoherent nucleus of the ith phase. For an incoherent phase W_i=0.

Considering that the requirement for the nucleation of a phase is $\Delta G^V_i + W_i < 0$, the temperature must be below the solvus for a phase to form, and the phase with the lowest ΔG^*_i will be formed fastest, Rioja and Laughlin (1980) explained the variation in the precipitation sequence with ageing temperature by comparing the magnitudes of ΔG^*_i for each phase, as follows:

(i) at 300°C: The sequence of precipitation may imply:

$$\Delta G^*_{GP} < \Delta G^*_{\gamma''} < \Delta G^*_{\gamma'} \qquad [2.7]$$

or

$$\frac{\sigma_{GP(1)}\sigma^2_{GP(2)}}{(\Delta G^V_{GP} + W_{GP})^2} < \frac{\sigma_{\gamma''(1)}\sigma^2_{\gamma''(2)}}{(\Delta G^V_{\gamma''} + W_{\gamma''})^2} < \frac{\sigma_{\gamma'(1)}\sigma^2_{\gamma'(2)}}{(\Delta G^V_{\gamma'} + W_{\gamma'})^2} \qquad [2.8]$$

The G.P. zones having coherent interfaces with the matrix have the lowest surface energy, and hence ΔG^*_{GP} is the lowest. Both the γ'' and γ' phases have incoherent edges, and thus $\sigma_{\gamma''(2)} \approx \sigma_{\gamma'(2)}$. Since the γ'' phase is coherent on the face while the γ' phase has semicoherent faces, $\sigma_{\gamma''(1)} < \sigma_{\gamma'(1)}$; hence $\Delta G^*_{\gamma''} < \Delta G^*_{\gamma'}$. Thus, the sequence of

precipitation at 300°C occurs without missing any phase, in increasing order of free energy.

(ii) at 350°C and above:

$$\Delta G^{*}_{GP} < \Delta G^{*}_{\gamma'} < \Delta G^{*}_{\gamma''} \qquad [2.9]$$

or $$\frac{\sigma_{GP(1)}\sigma^{2}_{GP(2)}}{(\Delta G^{V}_{GP} + W_{GP})^{2}} < \frac{\sigma_{\gamma'(1)}\sigma^{2}_{\gamma'(2)}}{(\Delta G^{V}_{\gamma'} + W_{\gamma'})^{2}} < \frac{\sigma_{\gamma''(1)}\sigma^{2}_{\gamma''(2)}}{(\Delta G^{V}_{\gamma''} + W_{\gamma''})^{2}} \qquad [2.10]$$

The γ'' phase is absent at 350°C because the degree of supersaturation is too low for it to nucleate. Also, in samples which are down-quenched to the ageing temperature, the γ' phase forms before the G.P. zones grow large enough to transform into the γ'' phase, and hence $\Delta G^{V}_{\gamma''} > \Delta G^{V}_{\gamma'}$, which indicates that it would not be possible for γ'' to form without γ' also forming (Figure 2.17). The G.P. zones are not affected by the lack of supersaturation at tempera--tures up to the G.P. zone-solvus since $\Delta G^{*}_{GP} >> \Delta G^{*}_{\gamma''}$, as shown in Figure 2.17. But, at temperatures close to the zone-solvus, G.P. zones do not form for the same reason.

Tsubakino and Nozato (1978) explained the nature of continuous and discontinuous precipitation in Cu 0.9-1.4 wt%Be alloys using isothermal transformation curves (Figure 2.18) produced according to microhardness measurements. They proposed that T_1 and T_2, as indicated with arrows in Figure 2.18-a and b, are the upper temperatures for the formation of the continuous γ' phase and G.P. zones, respectively. On these plots, each C-shaped curve of t_2 above T_1, between T_1 and T_2, and below T_2 corresponds to the formation of the equilibrum γ phase, the metastable γ' phase, and G.P. zones respectively. Thus, according to these plots, on ageing below T_2, the decomposition reaction starts with the formation of G.P. zones, followed by the precipitation of γ', and above T_1, only the γ phase forms. However, the information on the precipitation sequence obtained from "C" curves of this type is limited and cannot quantitatively explain the precipitation kinetics of the γ''

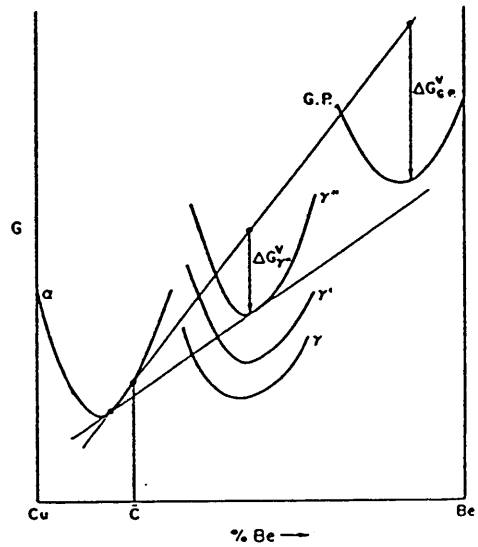
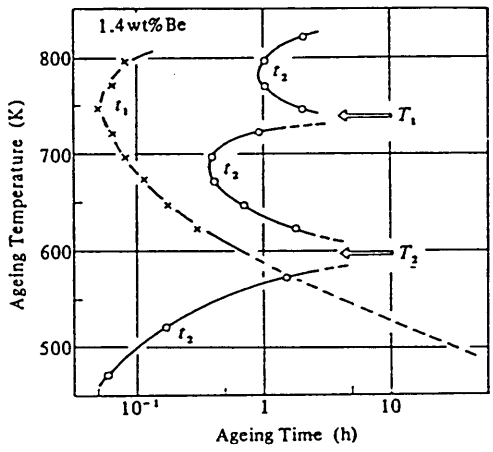


Figure 2.17- Schematic of the free energy curves for the various stable and metastable phases present in Cu-Be alloys.

(a)



(b)

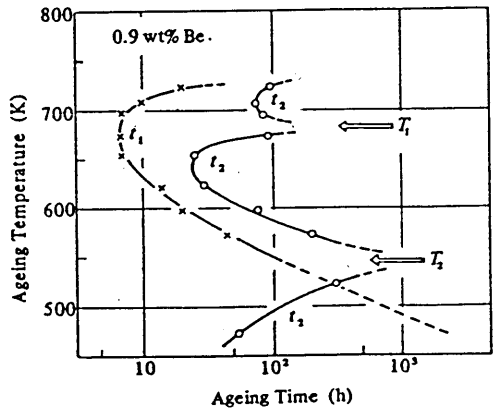


Figure 2.18- Relationship between ageing temperature and time for beginning of age hardening of (a) Cu 0.9wt% Be alloy (b) Cu 1.4wt% Be alloy, obtained from micro-Vickers hardness measurements. t_1 and t_2 indicates the onset of hardening in grain boundary and grain centre regions, respectively (after Tsubakino and Nozato, 1978).

phase and the reactions at temperatures between T_1 and T_2, quantitatively.

2.6.2 Discontinuous precipitation

According to the classical theory of nucleation, it may be concluded (Doherty, 1983) that the driving force for precipitation is proportional to the reduction in free energy, ΔG, which is:

$$\Delta G_{TOT} = \underset{(-)}{\Delta G_V} + \underset{(+)}{\Delta G_S} + \underset{(+)}{\Delta G_{ST}} \qquad [2.11]$$

where ΔG_V, ΔG_S, and ΔG_{ST} are the volume, surface, and strain energy terms, respectively.

A grain boundary has a higher free energy than the matrix; thus, for precipitation governed by the terms ΔG_S and ΔG_{ST}, the energy of the boundary region, where a precipitate nucleus is formed, is available to reduce the surface and possibly the strain energy terms for grain boundary nucleation (Martin, 1980; Pumphrey, 1973).

So, grain boundaries are effective in increasing the nucleation rate, J, in equation [2.4], by reducing the critical free energy, ΔG^*, for nucleation. It has also been proposed (Russell and Aaranson, 1975) that ΔG^* is reduced further if the grain boundary is characteristically oriented relative to the nucleus/matrix boundary. If not, the "pucker" mechanism operates in such a manner that the path of the grain boundary is altered (tilted) so that the grain boundary plane is locally parallel to a nucleus/matrix habit plane as shown for a disc-shaped nucleus in Figure 2.19. In this case, Aaranson and Aaron (1972) proposed that the largest reduction in ΔG^* occurs when the nucleus/matrix habit plane is nearly parallel to the grain boundary or the boundary-tilt angle, ϕ, approaches zero (Figure 2.20); ΔG^* rises rapidly with increasing tilt angle ϕ for such a nucleus. This type of mechanism has been also observed in Cu-Be alloys (Baumann et al., 1981), and has been explained only qualitatively (see section 2.5.2).

Tsubakino et al. (1981) and Borchers and Schulz (1976) have discussed the discontinuous precipitation in Cu-Be alloys by considering that the time dependency of the volume fraction of precipitation, X, at a given temperature is expressed by the following equation (Johnson and Mehl, 1939; Avrami, 1941):

$$X=1-\exp(-kt^n) \qquad [2.12]$$

where X is the volume fraction of the alloy which undergoes discontinuous decomposition during the time t, k is a kinetic constant, and n is called the time exponent or Avrami constant. The equation [2.12] was then written in the form

$$\log\log\{1/(1-X)\}=n\log t+\log(k/2.3) \qquad [2.13]$$

They have used the relationship between $\log\log\{1/(1-X)\}$ and $\log t$ (Figure 2.21) to determine n for discontinuous precipitation as a function of ageing temperature (Table 2.2).

Following the proposition of Cahn (1957) that the values of n in equation [2.12] depend on the nucleation sites of cells, Tsubakino et al. (1981) proposed that the values of n are ≈ 1 at $T_A \leq T_2$ and ≈ 2 at $T_A > T_2$, and thus correspond to grain boundary nucleation and grain edge nucleation respectively. If the following criterion is satisfied:

$$0.1 < Gt_{0.5}/(1.67D) < 0.5 \qquad [2.14]$$

where G is the growth rate, $t_{0.5}$ is the time for X=0.5, and D is the mean grain size of specimens, they suggested that equation [2.12] becomes:

(i) for a grain boundary nucleation reaction, n=1,

$$X=1-\exp(-2SGt) \qquad [2.15]$$

(ii) for a grain edge nucleation reaction, n=2,

$$X=1-\exp(-\pi LG^2t^2) \qquad [2.16]$$

where S is the boundary area per unit volume and L is the edge length per unit volume.

Experimental results of Tsubakino et al. (1981) in terms of $\log\log\{1/(1-X)\}$ vs. $\log t$ plots, as shown in Figure 2.21, indicate that the values of G satisfy the criterion in equation [2.14], suggesting that equations [2.15] and

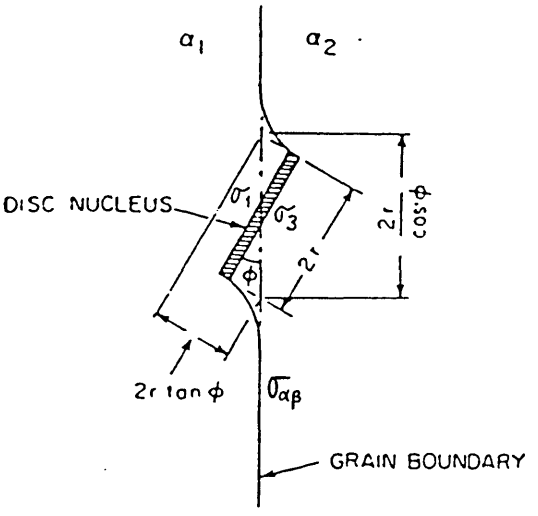


Figure 2.19- The "pucker" mechanism of nucleation at a grain boundary (Aaranson and Aaron, 1972).

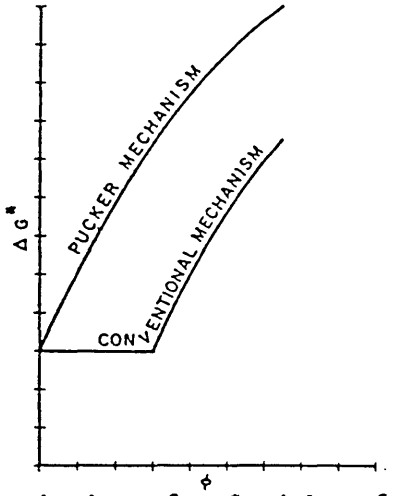


Figure 2.20- Scematic of the variation of ΔG^* with ø for the conven-tional and for the pucker mechanism when $\sigma_1 > \sigma_{\alpha\alpha}/2$, as shown in Figure 2.19 (Aaranson and Aaron, 1972).

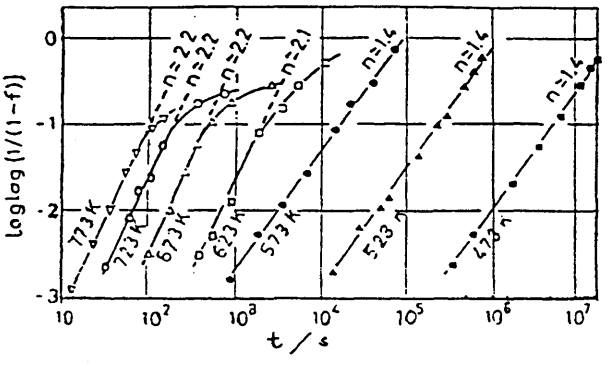


Figure 2.21- Plots of loglog[1/(1-X)] vs. ageing time (t) at various ageing temperatures (after Tsubakino et al., 1981).

[2.16] are applicable to the kinetics of discontinuous precipitation. Thus, they proposed that, at T_A<350°C, the values of n (n=1.4) are closer to 1 than 2, and hence nucleation on grain boundaries, in addition to nucleation on grain edges, becomes possible since the large elastic strains (caused by the formation of G.P. zones and fine γ' precipitates in the matrix prior to discontinuous precipi--tation) contribute to the driving force for the cell nucleation on grain boundaries. On ageing at T_A>350°C, their results indicate that the values of n are close to 2, and hence discontinuous precipitates are considered to nucleate on grain boundary edges.

It should be noted that there is a deviation from straight lines, at T_A>350°C, as shown in Figure 2.21. This deviation is attributed to the growth rate of cells, G, not remaining constant with time; during the later stages of ageing G starts to decrease and the interlamellar spacing increases due to the pinning effect of γ' precipitates on cellular growth. Borchers and Schulz (1976) support this view. However, such phenomena were not observed at $T_A \leq T2$, suggesting that the matrix γ' precipitates (formed after G.P. zones but prior to discontinuous precipitation) are so fine that they have little effect on the growth rate.

Table 2.2

n values for discontinuous precipitation in Cu-Be alloys at various ageing temperatures

n values	Temperature (°C)							
	200	250	300	350	400	450	500	550
Cu 1.5wt% Be (*)	-	-	0.42	-	1.26	-	1.67	1.62
Cu 2.1wt% Be (§)	1.4	1.4	1.4	2.1	2.2	2.2	2.2	-

(*) Borchers and Schulz (1976)

(§) Tsubakino et al. (1981)

Similarly, Tsubakino and Nozato (1978) described the change of G and the interlamellar spacing, l, with t at different ageing temperatures, T_A, by considering the relationships, $G \alpha M \Delta F$ (Cahn, 1959) and $l \alpha 1/\Delta F$ (Zener, 1946) where M is the mobility of the advancing interfaces, ΔF is the chemical free energy change for the reaction. They proposed that at $T_A \leq T_2$ the same phenomenon as that described by Tsubakino et al. (1981) is observed, whereas at $T_A > T_2$ G decreases and l increases because the precipitation of γ' reduces the degree of supersaturation, and hence causes a reduction in ΔF. Also, the pinning effect of the γ' precipitates significantly reduces M. Thus, it was concluded that the higher the ageing temperature, the greater the reduction in ΔF and M, and hence the greater the influence of continuous precipitation on cellular growth (Tsubakino et al., 1981)

2.7 Effect of Prior Deformation on Ageing Kinetics

When a supersaturated alloy is deformed, a large number of heterogeneous nucleation sites, e.g. excess vacancies, dislocations, stacking faults, and twins, are introduced into the structure. The dislocations introduced by prior strain are well known as effective sites for the nucleation of precipitates. They accommodate the lattice misfit between a precipitate and the surrounding matrix for a partially coherent precipitate if the Burgers vector of dislocations is parallel to the misfit vector of the precipitate (Kelly and Nicholson, 1963). Therefore, although there is no clear evidence that dislocations can act as sites for the preferential nucleation of G.P. zones, a high density of dislocations may provide competing sites for the nucleation of other semicoherent intermediate phases (Nutting, 1971). Thus, the amount of prior strain is an important determining factor for the mode of precipitation during subsequent ageing.

The effect of cold work on the kinetics of the precipitation of different metastable phases is well illustrated by the Al-Cu system. On prior cold working and

ageing of Al-Cu alloys, an accelerated nucleation of θ' phase (Tavassoli, 1974) and almost complete suppression of the θ" phase (Nutting, 1971) have been observed. This was attributed to the dislocations providing favourable sites for θ' precipitation, and hence the formation of more intermediate precipitates at the expense of G.P. zones.

The situation in Cu-Be alloys is complicated by discontinuous precipitation. Consequently, Bonfield and Edwards (1974) have proposed that three distinct processes must be considered in order to fully explain the effect of prior cold work on ageing kinetics of Cu-Be alloys; namely, continuous precipitation, discontinuous precipitation, and recovery and recrystallisation. In the following sections, these processes will be discussed in terms of the amount of prior cold work and the conditions of subsequent ageing.

2.7.1 Effect of cold work on continuous precipitation

Cold working after quenching can noticeably affect the continuous precipitation in age-hardening alloys. Depending on the degree of supersaturation of the solid solution, the ageing temperature, and the amount of prior deformation, different types of microstructural features have been observed on ageing the prior cold worked Cu-Be alloys. It has been proposed (Bonfield and Edwards, 1974; Djuric et al., 1980; Jovanovic et al., 1986) that prior deformation retards the G.P. zone formation at lower tempe--ratures ($T \leq 300°C$) due to the fact that dislocations act as sinks for quenched-in vacancies, which are necessary for the growth of G.P. zones, thus reducing their concentra--tion. On the other hand, prior deformation may introduce a vacancy concentration of about 10^{-6} as a result of dislocation interactions (Nutting, 1971), but the reduction in the quenched-in vacancy concentration by glissile and sessile dislocations is thought to predominate.

At higher temperatures ($T > 300°C$), however, it has been found (Armitage, 1963; Bonfield and Edwards, 1974; Nutting, 1971; Bonfield, 1967) that the G.P. zone formation is hardly retarded in cold worked material since the

recovery of dislocations reduces the decrease in vacancy concentration.

It has been proposed that in Al-Cu and Ni based alloys (Nutting, 1971) dislocations can act as preferred sites for the nucleation of intermediate phases since the elastic distortion, caused by intermediate precipitates in the surrounding matrix, can be accommodated by the stress fields of dislocations. Thus, consistent with this model, the results obtained by some workers from prior cold worked Cu-Be alloys show that on ageing at high temperatures (T>300°C) prior deformation accelerates the formation of the γ' phase in the matrix (Nutting, 1971; Yamamoto, 1973; Bonfield and Edwards, 1974).

In contrast, the work of Djuric et al. (1980) and Jovanovic et al (1986) on the high temperature ageing of Cu-Be alloys appears to indicate that prior cold work does not significantly affect the ageing kinetics. There does not seem to be the same degree of confusion about the effect of prior cold work on γ' precipitation at low temperatures. At low temperatures, the limited amount of information available suggests that continuous precipita-tion is retarded.

2.7.2 Effect of cold work on discontinuous precipitation

In Section 2.5.5, it was explained that the precipi-tates in the matrix can reduce the rate of discontinuous reaction when they are large enough to pin the advancing interface. The introduction of lattice defects into super-saturated solid solutions may also effectively suppress discontinuous precipitation (Hornbogen, 1972); this is because heterogeneous nucleation at defects can enhance continuous precipitation at the discontinuous reaction front and decrease the growth rate of cellular reaction through the pinning effect of the continuous precipitates.

The results obtained from the cold worked (50%) Cu 1.81 wt% Be 0.28 wt% Co alloys, aged at 175, 315, and 425 °C, (Bonfield and Edwards, 1974) have shown that discon-ti-nuous precipitates do not form, but that recrystallisation

occurs at faster rates at 425°C than at lower temperatures producing new grains of the α-matrix and the γ equilibrium precipitate. However, Nutting (1971) reported that since Cu-Be alloys have relatively low stacking fault energies, deformation twins, which are preferential sites for discontinuous precipitation, are introduced when the material is highly strained (100%). Thus, on ageing at high temperatures, deformation twins act as additional nuclea--tion sites and accelerate the discontinuous mode of preci--pitation (Armitage, 1963).

Kreye (1971) investigated the effect of prior cold work (0-90 %) on the ageing kinetics of Cu 2 wt% Be alloys in more detail. He observed various precipitation modes depending on the amount of prior cold work and ageing temperature and explained these phenomena in terms of the change in the driving force for discontinuous reaction, which is given by

$$P = P_C + P_N + P_P \qquad [2.17]$$

where P_C, P_N, and P_P refer to the contributions from the chemical free energy, density of dislocations, and pinning effect by particles, respectively. The change of P_C, P_N, P_P, and the density of discontinuous reaction sites, N_D (in front of the interface) with prior strain is shown in Figure 2.22. In this respect, the main propositions of Kreye (1971) may be summarised as follows:

(i) At 285°C: When the G.P. zone to γ' phase transform--ation occurs the discontinuous precipitation starts only from the grain boundaries. Prior strains resulting in less than 30% reduction in area (RA) do not influence the discontinuous reaction. However, higher amounts of prior strain (i.e., up to 50% RA) result in the formation of deformation bands with high dislocation densities, and hence in an increase in P_N. On subsequent ageing, dislocations in these regions rearrange to form new grain boundaries which act as additional sites for discontinuous precipitation, i.e. high degrees of prior strain increase N_D, and thus the reaction rate and the volume fraction of discontinuous precipitates (Figure 2.23-a). Up to 50% RA,

P_C gradually decreases due to the reduction in Be concen--tration by continuous precipitation of the γ' phase. The γ' precipitates are too small to be efficient in suppressing the discontinuous reaction, and they can dissolve at the advancing interface of the discontinuous reaction. Therefore, P_P remains constant up to 50 % RA. For prior strains greater than 50%, enhanced diffusion along the subgrain boundaries together with the lowered activation energy for nucleation of the γ phase at subgrain boundaries results in the $\gamma' \longrightarrow \gamma$ transformation occurring in the matrix before the discontinuous precipitation is completed (P_P starts to reduce). These precipitates slow down the discontinuous reaction by pinning the advancing interface (Figure 2.22).

(ii) At 470°C, the decomposition kinetics differ from that discussed above in that prior strains up to 20% RA reduce the rate of discontinuous precipitation. This is because the nucleation of the γ' phase at dislocations (without prior G.P. zones formation) is facilitated by the dislocations accommodating the elastic distortions produced by the γ' precipitates in the matrix. These γ' precipitates grow in size, becoming a few times larger than those in undeformed alloys, and suppress the growth of boundary precipitates. Prior strains in the range 20 to 50 % RA accelerate the discontinuous precipitation (Figure 2.22-b) since the increase in dislocation density, P_N, results in a higher density of new grain boundaries formed by the rearrangement of dislocations.

In contrast, for prior strains greater than 50 % RA, the rate of discontinuous reaction and the volume fraction covered by the discontinuous reaction decrease progress--ively with prior strain; this is due to the competition between the discontinuous precipitation and the combined continuous precipitation and recrystallisation. Both the reduction in solute content due to the precipitation of the equilibrium γ phase in the matrix (which contributes to P_C) and the substantial pinning effect of those precipitates (which contributes to P_P) reduce the overall driving force,

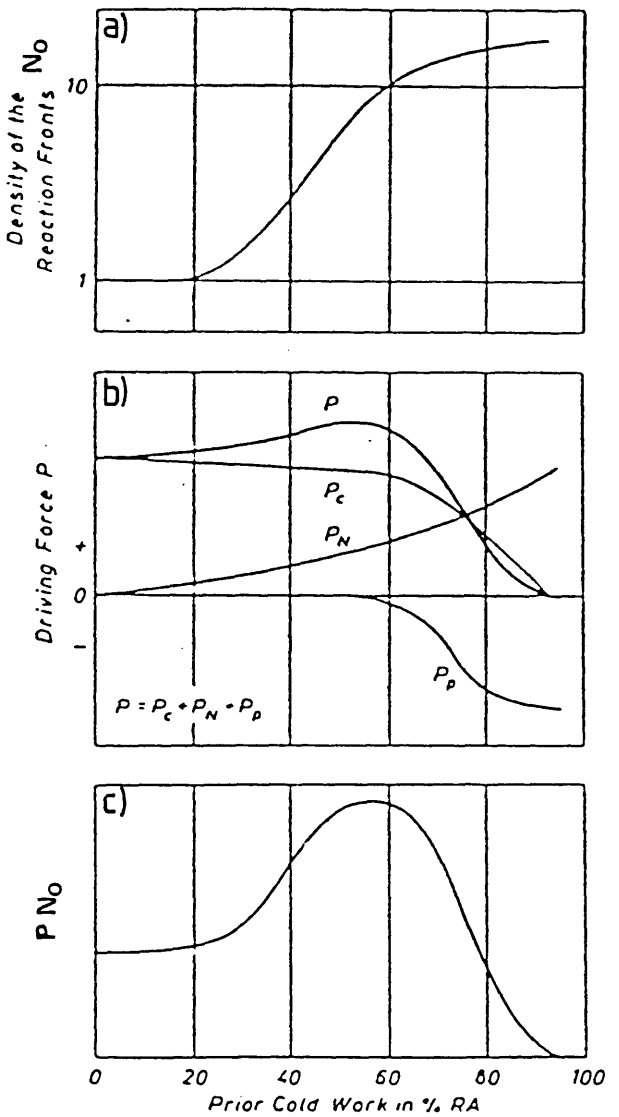


Figure 2.22- (a) Change in density of the discontinuous reaction sites (N_0) vs. amount of prior cold work, as obtained from the optical micrographs.

(b) Schematic plot of driving force P at reaction sites vs. amount of prior cold work; P_P, P_N, P_P, represent the contributions from the chemical free energy, dislocation content, and the pinning by γ' particles, respectively.

(c) Product PN_0 as a measure for the increase in volume fraction after a given ageing time and temperature, vs. amount of prior cold work (after Kreye, 1971).

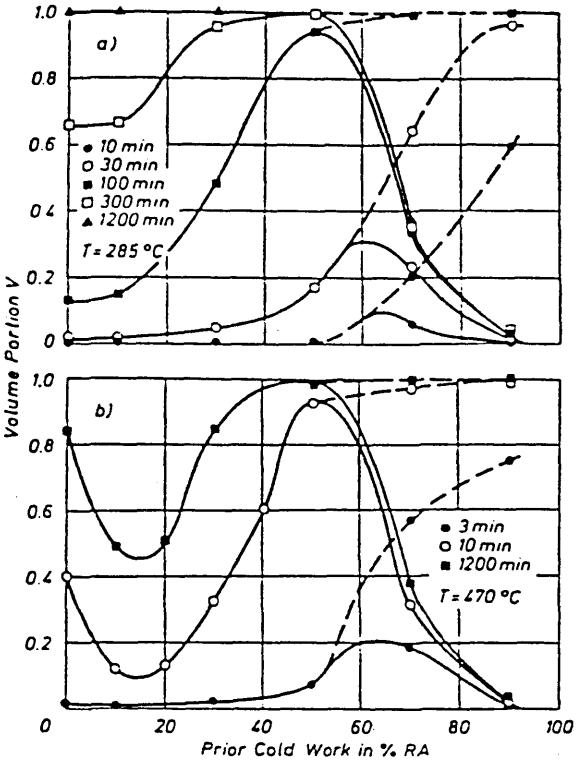
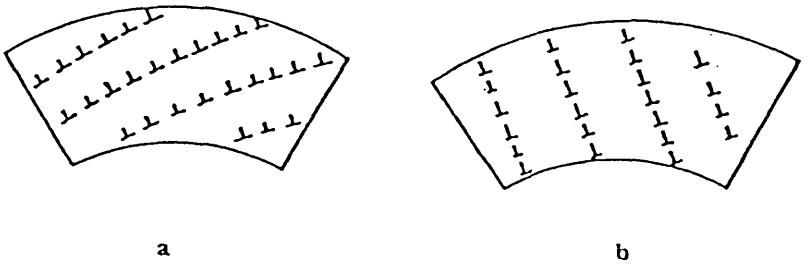


Figure 2.23- Volume fraction covered by the discontinuous precipitates after different ageing times, vs. amount of cold work. Ageing temperature(Kreye, 1971):
(a) 285°C
(b) 470°C.



a b

Figure 2.24- Dislocation arrangements (a) after deformation (b) after polygonization (Stüve, 1970).

P (Figure 2.22-b). When the prior strain is increased to 90 % RA, this process predominates, and hence no discontinuous precipitates form (Figure 2.23-b).

2.8 Recovery and Recrystallisation

Since Cu-Be alloys have a low stacking fault energy, the microstructure of the deformed state exhibits an irregular distribution of dislocations rather than well-developed cell structures or sub-grains, (Bonfield and Edwards, 1974), fine deformation twins, and slip bands (Chernyakova et al., 1980; Armitage, 1963).

The recovery and recrystallisation of Cu-Be alloys induces three major processes (Tofpenets et al., 1979):

(i) re-orientation of dislocations which will result in the development of a cell structure,

(ii) polygonization producing low angle grain boundaries and,

(iii) nucleation of recrystallised grains in the regions of large strain gradients.

The driving force for these processes is the stored energy introduced by prior strain. Because the deformed material is in a thermodynamically unstable state, subsequent ageing lower its free energy by the annihilation of defects and the rearrangement of dislocations (Haessner, 1970). During ageing of the cold work alloy, dislocations may rearrange to produce either a piled-up dislocation structure on slip planes or sub-grain boundaries by polygonization, as shown in Figure 2.24-a and b (Stüve, 1970). On further ageing, small defect-free nuclei are formed by dislocation climb and rearrangement (Cahn, 1983). Most of these nuclei form at or near grain boundaries (Cahn, 1983), and are separated by the newly formed large angle boundaries. This process is called "primary recrystallisation".

The basic principles of primary recrystallisation suggest that a minimum (critical) deformation (Cahn, 1983), or a dislocation density greater than 10^{10} cm^{-2} (Haessner, 1970), is required to initiate recrystallisation. Electron microscopy analyses have shown (Tofpenets et al., 1979) that, in a 50% cold worked Cu 1.9 wt% Be alloy, the density of dislocations reaches about 1.5 x 10^{10} cm^{-2}, suggesting that the material is capable of primary recrystallisation. However, information obtained from Cu-Be alloys, deformed to considerably less than 50 %, indicates (Jovanovic et al., 1986; Djuric et al., 1980) that recrystallisation accompanying the discontinuous precipitation can occur after long ageing at temperatures as low as 350°C.

Experimental information concerning primary recrys--tallisation suggests that, in general, increasing the ageing time decreases the ageing temperature and the amount of prior strain required for recrystallisation (Cahn,1983). In cold worked Cu-Be solid solutions, however, the recrystallisation process is complicated by the concomitant precipitation.

The data obtained from the prior cold worked (50%) Cu 1.9 wt% Be alloys has shown (Tofpenets et al.1978) that, on ageing at 300°C, the formation of semicoherent γ' phase initially hinders the movement of dislocations. Later, the dislocation redistribution in the matrix, achieved by cross-slip of dislocations and translation of dislocations on slip planes, results in a cell structure. On further ageing, dislocation climb causes the growth of newly formed sub-grains within large-angle boundaries; this process simul--taneously involves the precipitation of the equilibrium γ phase in recrystallised grains. Bonfield and Edwards (1974) observed the same results on ageing a 50% prior cold worked Cu 1.81 wt% Be 0.28 wt% Co alloy. They also noted that the γ' precipitation in the matrix and the nucleation of recrystallised grains are two competing reactions when the material is aged at 425°C.

2.9 Effect of Ternary Additions on Precipitation

It is well-known that ternary additions can change the precipitation characteristics by affecting the nucleation process and/or suppressing grain boundary movement. Also, the segregation of ternary elements to grain boundaries and in front of the cellular structure may suppress the nucleation and growth of discontinuous precipitates on grain boundaries.

As discussed in Section 2.5.1, in Cu-based alloys, the atomic size ratio, $\Delta r=(r_B-r_A)/r_A$, of the solute r_B and the solvent r_A atoms should be greater than 0.11 for discontinuous precipitation (Böhm, 1961). Also, grain boundary cellular precipitation may occur when the volume change during precipitation, Δv, is between 0.3 and 0.9 % (Williams and Butler, 1981). Therefore, if the ternary elements possess a Δr value less than 0.11, and lower the volume change Δv for the precipitation in the matrix, continuous precipitation is favoured and discontinuous reaction at grain boundaries will be suppressed (Williams and Butler, 1981).

Minor alloying additions may affect discontinuous precipitation in other ways. Additional elements, which strongly segregate to grain boundaries, retard the discontinuous precipitation by lowering the grain boundary energy and its mobility via a solute drag effect (Williams and Butler, 1981). However, increasing the ageing temperature increases the growth rate of discontinuous precipitates or the rate of boundary migration; furthermore, the segregant atoms may not be able to follow the reaction front or the boundary, and hence become incapable of retarding the discontinuous precipitation (Hornbogen, 1972).

In the preceding sections, the ageing characteristics and other microstructural features of Cu-Be binary and Cu-Be-Co ternary alloys have been discussed in terms of continuous and discontinuous precipitation. It has also been noted that, with prolonged ageing, the discontinuous precipitation at grain boundaries and the development of cellular structures growing into the matrix can replace the

continuous precipitates, and thereby, reduce the strength and hardness. Therefore, in order to achieve a suppression effect on cellular growth, ternary additions of Co, Ni, Fe, Mn, Si, Ti, Mg, In, Cd, Sn, P, Ce, and Sb have been inves--tigated in the literature (Miki et al., 1983; Murakami et al., 1968; Mishima et al., 1969; Williams 1978; Thomas and Wilke-Dörfurt, 1959; Tsubakino et al., 1980; Baumann and Williams, 1980). It has been reported that some of these elements interfere with the precipitation reactions and grain boundary migration in a different manner to the others (Miki et al., 1983; Mishima et al., 1969); this will be discussed in detail in the following sections.

2.9.1 Effects of ternary elements on continuous precipitation

As mentioned in previous sections, the first stage of hardening in Cu-Be alloys occurs by the formation of G.P. zones, followed by the formation of other metastable phases, when the material is aged at low temperatures (T<350 °C). However, age hardening at higher temperatures starts with the γ' precipitation both in the matrix and at grain boundaries. An additional element either accelerates or suppresses the continuous precipitation, and hence results in opposite effects on the discontinuous precipita--tion (Murakami et al., 1968; Miki et al., 1983).

Several authors (Miki et al., 1983; Murakami et al., 1968; Mishima et al., 1969; Thomas and Wilke-Dörfurt, 1959; Kunze and Wincierz, 1965) have investigated the effect of various ternary alloying elements on the kinetics of the decomposition reactions in Cu-Be alloys. Most experi--ments led to the following results for the formation of G.P. zones and the γ' phase; namely:

(i) G.P. zones: The formation of G.P. zones was promoted by the addition of 0.3wt% In, 0.07wt%Mg, or 0.3wt%Zn, but strongly retarded by the addition of 0.2-0.3wt%Co, 0.3wt% Mn, 0.1-0.5wt%Ti, or 0.3wt%Cr. The addition of 0.07-0.3 wt% Fe, 0.02-0.3wt%Al, or 0.1-0.3Si produces very little

retardation of the G.P. zone formation; among these elements, Fe is found to be more effective than the others.

(ii) γ' phase: The precipitation of the γ' phase in the matrix is facilitated by the addition of 0.3wt%In, 0.3wt% Ni, 0.3wt%Fe, or 0.07wt%Mg, but is retarded by the addition of 0.2-0.3wt%Co, 0.3wt%Mn, 0.1-0.5wt%Ti, 0.02-0.1wt%P or 0.3wt%Cr.

Only limited information is available in the literature regarding the effect of these additional elements on the kinetics of precipitation. Nevertheless, it has been proposed that a 0.2-0.3wt% Co addition suppresses the formation of G.P. zones because the Co atoms have high binding energies with vacancies, and hence trap the vacancies, reducing the effective vacancy concentration for the formation of G.P. zones (Murakami et al., 1968). It was presumed (Murakami et al., 1968; Miki et al. 1983) that since the addition of Co reduces the overall grain size, thereby increasing the density of grain boundaries, which act as sinks for vacancies during ageing, its addition effectively increases the annihilation of excess vacancies. Another possibility is that Co leads to an increase in the activation energy for vacancy migration, and hence reduces the transfer of solute by vacancies, to the clusters (Kunze and Wincierz,1965). Therefore, a significant decrease in the rate of G.P. zone formation would be expected. The role of Mg and Zn atoms in accelerating G.P. zone formation was attributed to the fact that these atoms are larger than Cu atoms; hence they attract several Be atoms around them and thereby form simple clusters instantly, which perhaps play an effective role in the formation of G.P. zones (Murakami et al., 1968).

Miki et al. (1983) followed the effect of additional elements on γ' precipitation by the increase in the lattice parameter of the matrix as shown in Figure 2.25. They proposed that an increase in lattice parameter indicates a decrease in the Be concentration of the matrix due to the precipitation of the γ' phase (see Section 2.2) They

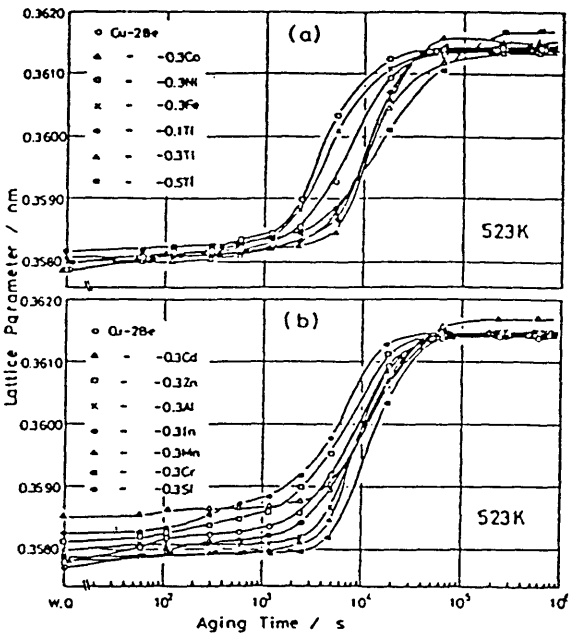


Figure 2.25- Lattice parameter of Cu 2wt%Be and Cu 2wt%Be-X alloys aged at 350°C (after Miki et al., 1983).

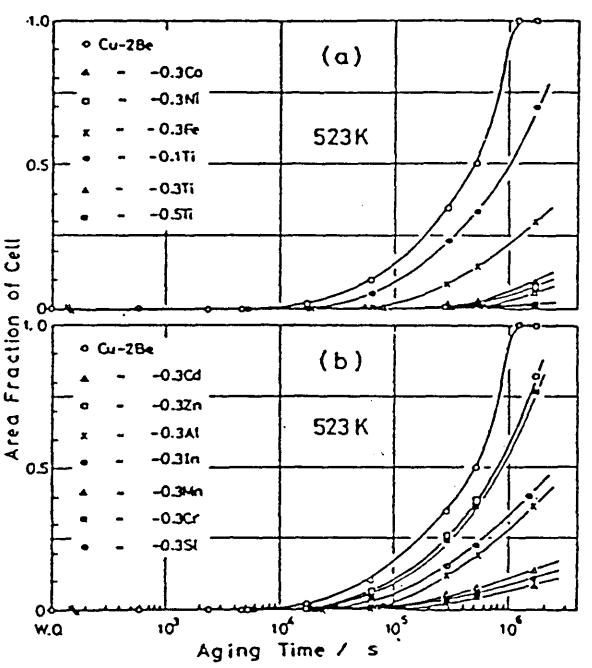


Figure 2.26- Area fraction of cellular structure in Cu 2wt%Be and Cu 2wt%Be-X alloys aged at 350°C (after Miki et al.,1983).

consequently concluded that the ternary addition of Co, Mn, Ti, or Cr, which slows down the increase in the lattice parameter of the matrix, suppresses the continuous precipi--tation of the γ' phase. Whereas, additions of Ni, Fe, or In operate in the opposite manner and thus accelerate γ' precipitation in the matrix. Thomas and Wilke-Dörfurt (1959) also found that the addition of Co or Ni strongly retards the γ' precipitation and that Fe does likewise if the material is solution treated at T>800°C.

It was noted (Murakami et al., 1968) that the presence of Mg and Fe atoms in the matrix facilitates the formation of the semicoherent γ' phase by reducing the coherency strain. On the other hand, the introduction of P to Cu-Be alloys reduces the mobility of vacancies in the solid solution and hence it is difficult for large precipitates of the γ' phase to form in the matrix (Rakhshtadt and Tkhagapsoyev, 1975). However. it is not clear from the literature whether any of the above ternary additions affects the formation of the equilibrium γ phase.

2.9.2 Effects of ternary elements on discontinuous precipitation

The literature data on the influence of ternary additions on discontinuous precipitation in Cu-Be alloys (Miki et al., 1983; Butler and Williams, 1980; Amano and Koyama, 1971) suggest that additional ternary elements can be classified into three groups by reference to their ability to suppress discontinuous precipitation; namely:

(i) Co, Ce, Ni, Mg, Mn, In, Cd, and Ti are very effective.

(ii) Fe, Si, and Al are moderately effective.

(ii) Zn and Cr have little effect.

The results for various ternary alloys aged at 250 °C (Miki et al., 1983) are shown in Figure 2.26, which clearly

demonstrates the relative effectiveness of the additions on discontinuous precipitation. It may be concluded from these results that the suppressing effect of additional elements on discontinuous precipitation is not always due to their acceleration of the γ' precipitation which creates a reverse driving force on the migrating boundaries of cellular structure, i.e. In, Ni, Mg, and Fe facilitate γ' precipitation in the matrix, whereas Mn, Ti, and Co retard it. The alternative explanation is that the presence of Mn, Ti, and Co in the matrix reduces the mobility of advancing boundaries of the cellular structure and/or their marked segregation at grain boundaries suppresses the discontinu--ous reaction by a solute-drag effect (Miki et al., 1983; Hornbogen, 1972; Bonfield and Edwards, 1974).

Investigations on the effect of Co addition on discontinuous precipitation have led to the following results:

(i) Co atoms tie up ledges and steps at grain boundaries and reduce the boundary mobility (Bonfield, and Edwards, 1974), while

(ii) Co-rich cuboidal particles of Be and Co, formed during solution treatment, limit the migration of grain boundaries and the growth of discontinuous precipitates by a pinning effect (Baumann and Williams, 1980). However, there is no clear evidence of other ternary elements, forming such particles with Be.

The suppression mechanisms of some additions are strongly dependent on ageing temperature. It has been reported (Bonfield and Edwards, 1974) that the addition of 0.28 wt% Co in Cu 1.8 wt% Be alloys retards discontinuous precipitation on ageing at $T<380°C$, but has no effect at higher temperatures. It is suggested that, at low tempera--tures, Co atoms diffuse with the boundary and hence are effective in altering the boundary step density, whereas at higher temperatures the boundary migration rate is faster than the diffusion rate of Co atoms, and thus the Co

segregation is reduced. The mechanical pinning by cuboidal particles also becomes a less effective suppression mechan-ism at high ageing temperatures (Baumann and Williams, 1980). Nevertheless, Ce addition was found to be very effective in reducing the growth kinetics of discontinuous precipitates even at temperatures above 400°C since Ce readily segregates to the boundaries during both the solution treatment and the subsequent ageing (Baumann and Williams, 1980).

CHAPTER 3

EXPERIMENTAL PROCEDURE AND TECHNIQUES

3.1 Materials

Mill-hardened Cu-Be-Co alloys, solution treated and then cold worked, are designated as W (solution treated), W1/4H, W1/2H, and WH (H denoting the existence of cold work). The alloys, studied in this work, were received from the manufacturer (Telcon Metals Ltd.) in both solution treated and solution treated and then cold rolled conditi--ons. The sequence of producing the strip alloys at the manufacturer was that the alloys, which had been rolled to strip form, were first solution treated (annealed at 800°C) to form the homogeneous α phase, water-quenched to room temperature to obtain a supersaturated solid solution, and then cold rolled in a continuous process to achieve various degrees of prior deformation (up to 40% reduction in thickness). The nominal compositions of the alloys and the relative degrees of prior deformation are given in Table 3.1. These alloys, which were all classified as "Cu-Be 250 strip" materials in commercial use, had very similar chemical compositions.

3.2 Heat Treatments

The specimens for the various tests, which were carried out in this work, were heat treated in a horizontal tube furnace. The ageing temperatures and times, chosen for the specimens for each technique, are listed in Table 3.2. At each temperature, the samples were kept in the furnace for a chosen time required for a specific test, and cooled naturally in air. It should be noted that the heat treat--ment times, which are quoted in this work, are the times in the furnace, and are not the times at the stated temperatures, which would be shorter. Thus, the laboratory heat treatment is almost identical to the continuous heat treatment used to produce the mill hardened material in

industry. In order to determine temperature-time relation--ships for annealing in the furnace at different tempera--tures, a thermocouple was attached to dummy specimens, and according to the recorded temperature-time plots, it was found that the specimens reach within ±5°C of the stated temperatures after a few minutes, e.g. 3 and 4 minutes for ageing at 350 and 500 °C, respectively. After heat treat--ments, specimens had the thin surface oxide layer which removed by grinding with fine silicon carbide paper.

For bendability and tensile tests and electrical resistivity measurements, which will be described in detail in the following sections, large samples (50 mm in length) were required. The heat treatment of these samples were successfully carried out in the same furnace since, over 25 mm distance in the longitudinal directions from the centre of the furnace, the temperature gradient was ≤ ±1.5°C at all temperatures. Also, the hardness values, measured across a 50 mm long dummy specimen, remained within the normal experimental scatter. Therefore, it was concluded that this temperature gradient does not affect hardening noticeably because

(i) the age hardening is not sensitive to such small changes in temperature, and

(ii) the high thermal conductivity of the material can partly balance the temperature gradient through the long axis of samples.

3.3 Mechanical Tests

3.3.1 Hardness measurements

Specimens (5mm x 5mm) were cut from the heat treated strip samples, some of which had been previously tested on the cantilever-type bend rig, and then finely diamond polished (1/4 micron). The polished specimens were too thin for macrohardness tests, and hence Vickers microhardness (VMH) tests were carried out on a Leitz Miniload 2 micro-

Table 3.1

Nominal composition and amount of prior cold work of mill-hardened alloys, studied in this work.

Alloys	Code	Cold work (%)	Thick--ness (mm)	Composition (weight %)				
				Be	Co	Ni	Fe	Sn
W	UD	0	0.41	1.88	0.25	0.01	0.01	0.08
W1/6H(*)	D5	5	0.37	1.91	0.24	"	"	"
W1/4H	D10	10	0.37	1.88	0.25	"	"	"
W1/3H(*)	D18	18	0.32	1.91	0.24	"	"	"
W1/2H	D21	21	0.21	1.85	"	"	0.03	-
W1/2H	D24	24	0.31	1.88	0.25	"	0.01	"
W2/3H(*)	D32	32	0.28	"	"	"	"	"
WH	D37	37	0.22	1.85	0.28	0.02	0.04	-
WH	D41	41	0.24	1.88	0.25	0.01	0.01	"

(*) indicates the special designations in this work to specify the grades of prior cold work, which are not included in the standard commercial classifications.

Table 3.2

Ageing treatments of Cu-Be-Co samples for the tests techniques and analysis used in the present work

Method	Cold work(%)	Temperature (°C) and ageing time (minutes)
Cantilever type bend tests and hardness measurements		
W	0	
W1/6H	5	At 350, 380, 400, and 420 °C for times in the range 0 to 100 minutes with intervals of 5 minutes
W1/4H	10	
W1/3H	18	
W1/2H	24	
W2/3H	32	
WH	41	At 350, 380, 400, and 420 °C for times in the range 0 to 100 minutes with intervals of 2.5 minutes.
Tensile and 90° bend tests		
W	0	At 460 °C for 30 and 35 minutes.
W1/4H	10	At 350 °C for 2 minutes, at 380 °C for 6 and 13 minutes, at 400 and 420 °C for 4, 6, and 15 minutes, at 440 °C for 4, 6, and 13 minutes, and at 460 °C for 2.5 and 4 minutes.
W1/2H	21	At 350 °C for 5 and 7 minutes, at 380 °C for 2, 3, and 5 minutes,
WH	37	At 400 °C for 2, 3, and 4 minutes, at 420 °C for 4 and 7 minutes, and at 440 °C for 2, 3, and 4 minutes.

CONTD.....

Table 3.2 Continued.

Method	Cold work(%)	Temperature (°C) and ageing time (minutes)
X-ray diffractometry		
W	0	At 350 and 380 °C for times in the range 0 to 40 minutes with
W1/4H	10	intervals of 2.5 or 5 minutes.
W1/2H	24	At 400 °C for times in the range 0 to 30 minutes with intervals
W2/3H	32	of 2.5 minutes.
WH	41	
X-ray texture analysis		
W	0	Unaged
W1/4H	10	
W1/2H	21	At 400 °C for 18 and 60 minutes.
W2/3H	32	
WH	41	At 400 °C for 18, 60, and 240 minutes.
		at 500 °C for 60 and 240 minutes.
Electrical resistivity measurements		
W	0	
W1/4H	10	At 300 and 380 °C for times in the range 0 to 20 minutes.
W1/2H	24	Solution treated samples (W) were also heat treated
W2/3H	32	for 30 minutes at these temperatures.
WH	41	

hardness tester. An indentation load of 4.903 N was used. At least six indentations were measured for each specimen from which the mean and the standard deviation were calculated. The majority of measurements indicated a scatter of ±2-6 (VMH).

3.3.2 Tensile tests

Strip tensile tests specimens were punched from as-received alloys in the longitudinal direction (i.e. tensile axis parallel to rolling direction), and machined to obtain the test piece geometry shown in Figure 3.1. Tensile tests were carried out on a JJ T20K testing machine operating at a cross-head speed of 1.0 mm/min (strain rate of 7.5×10^{-4} s^{-1}). An MTS Model TTEX-12 extensometer with a gauge length of 15.8 mm was used for the continuous record of load vs. elongation on a plotter. The 0.2% off-set yield stress, maximum tensile strength, and the amount of elastic and plastic deformations were calculated from the plots.

3.3.3 Conventional 90° bend tests

90° bend testing is one of the well-accepted test methods (ASTM B194-81) to specify the formability of sheet materials. This technique is based on forming a strip material by a punch (with an edge radius (R) varying from sharp through to 6 mm) in a V-shaped block and determining the minimum ratio of edge radius and thickness (t) of specimen (R/t) for the material which can be formed without crack formation at the bend apex.

In the present work, a 90° bend rig, which consists of a series of punches with the edge radius of 0 (sharp), 0.25, 0.50, 0.75, 1.0, 1.25, 1.75, 2.0, 2.25, and 2.5 mm, and a V-shaped block press, was made. The punches and the V-block were fixed on a drilling machine (Figure 3.2). The specimens of 40 mm length and 15 mm width were cut from the strip alloys in the longitudinal direction and heat treated as for the tensile test specimens.

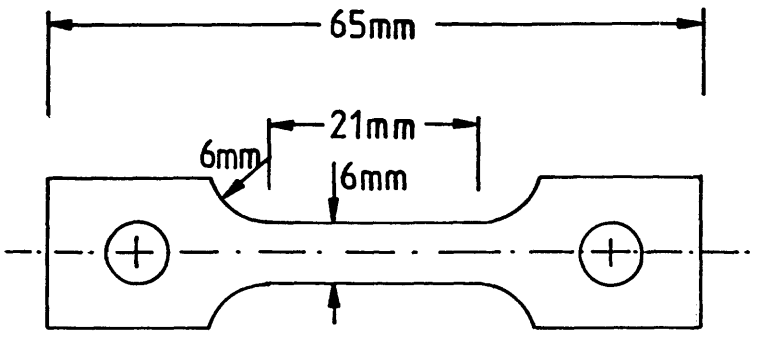


Figure 3.1- The geometry of tensile test specimens.

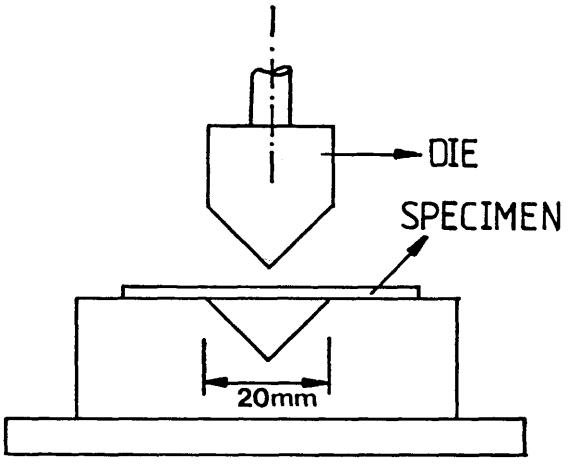


Figure 3.2- 90° Bending fixture.

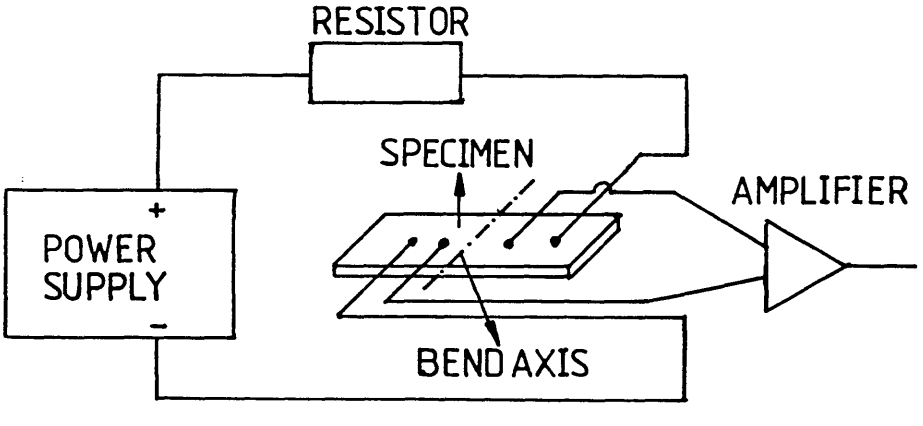


Figure 3.3- AC potential drop system.

Bend tests were carried out manually to determine minimum bend radius at which fracture did not occur at the bend apex. The bend apex of each specimen was viewed on a binocular stereo microscope, and the criterion for acceptance was that there should be no evidence of surface cracking at the bend apex of a tested sample.

Also, some preliminary experiments were carried out on the same rig to assess the feasibility of using the AC potential drop (ACPD) technique to detect the crack forma--tion during bend tests. It has recently been proved that a potential drop system, which consists of a constant AC current source and a signal processing unit to amplify the small signal developed across the specimen, is sensitive to the initiation of any surface cracking since the AC current at high frequency is restricted to the surface of the specimen (Okumora et al., 1981; Unvala, 1986). A Matelect CGM-5 crack growth monitor was employed for this study. A current frequency of 100 kHz was chosen so that even very small cracks could be detected as the penetration depth of current for Cu reduces to 0.1 mm at 100 kHz. A schematical illustration of the equipment is shown in Figure 3.3. For these experiments, the 90° bending rig was used in conjunction with an Instron testing machine so that the displacement of the punch could be monitored. The bending load and the potential drop were recorded as a function of displacement.

3.3.4 Cantilever-type bend tests

The conventional 90° bend test analysis employs the R/t ratio as an indication of the formability of strip materials. For the samples of the same thickness, the punch radius, R, becomes the only determinative parameter for formability, and hence a large number of punches are required. Furthermore, it is often difficult to detect cracking by optical microscopy and the assessment tends to be rather subjective.

Clearly, there is a need for a strip formability test which has the following characteristics:

(i) Results are obtained in digital or chart form such that subjective decisions do not have to be made.

(ii) Capable of detecting small changes in formability.

(iii) Economical with test material.

(iv) Specimen preparation simple.

(v) Aparatus robust and relatively maintenance free.

(vi) Tests quick to perform and reproducible.

With these characteristics in mind, a new cantilever-type bend rig, which would operate on an Instron testing machine, was designed to follow the change in the formability of strip alloys with age hardening.

The cantilever type test procedure covered in ASTM Standard D 747-70 involves the measurement of applied bending moment and corresponding deflection angle of rectangular strips. The method also covers determining the modulus of elasticity, an off-set bending yield stress and the secant modulus to estimate the contact force when design stresses exceed the elastic limit (Brenneman et al., 1979). In these tests, the aim is to determine the contact pressure of flat springs, and only small bending deflec--tions is required.

The present research is concerned with investigating the effect of various thermo-mechanical treatments on the formability of Cu-Be-Co strip alloys. Therefore, large bend deflections to failure of samples ought to be applied to determine the optimum conditions of several thermo-mecha--nical treatments. For this reason, the design of the cantilever type bend rig and its method of testing was basically different from those specified in ASTM standards.

As shown in Figure 3.4, the cantilever-type bend test aparatus consists of the parts, namely;

(i) A sharp stationary die (V-shaped) with an angle of 45° fixed on the main support of the rig (marked 7 on Figure 3.4-b). The edge of the die is adjusted to the centre of the bending rotation. The die is also an integral component of the stage where the bend specimens are clamped for tests (parts 8 and 9).

(ii) A rotating round block supported by ball bearings (part 2). The rotation centre is in alignment with the edge of the sharp die where the specimen is bent.

(iii) A bending pin (part 6) is incorporated into the adjustable bending pin unit which is fixed to the rotating round block. The pin rotates around the centre of bending, and therefore transfers the continuous force for bending to the free part of the specimen.

(iv) The adjustable part unit (part 3), which is fixed to the rotating round block was designed to position the pin at the required distance from the centre of bending rotation. This distance was always kept as twice the thickness of specimens so as to avoid friction between the surfaces of the specimen and the pin.

(v) A flat-link chain (part 5) which connects the rotating round block to the load cell of the Instron machine; one end is connected to the load cell and the other end is wound on to the round block in a pulley grove.

(vi) Base plate (part 10) which is clamped to the base of the Instron testing machine.

The use of ball bearings for the rotation of the round block minimises the friction during the bending of the strip samples, and hence the results should be more accurate than those from the 90° bend test which involves a

Figure 3.4

(a) Cantilever-type bend rig

(b) Main structure of the rig, which consists of the following parts:

(1) main support
(2) rotating round block
(3) adjustable pin unit
(4) specimen (bent to ≈40°)
(5) flat-link chain
(6) bending pin
(7) sharp die
(8)&(9) specimen clamping parts
(10) base plate

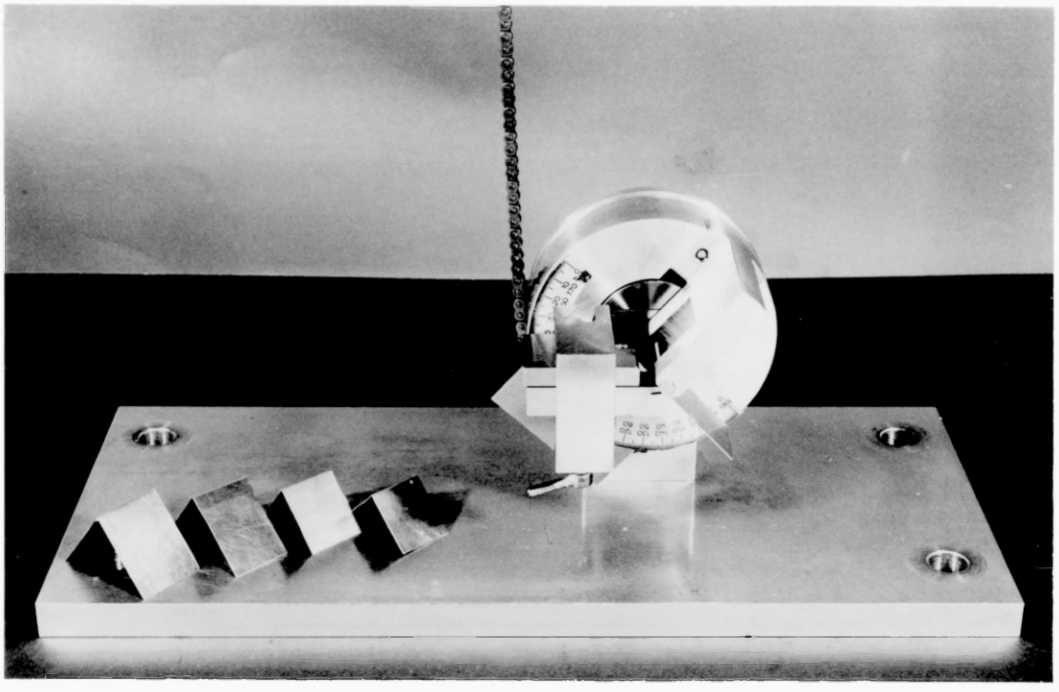


Figure 3.4 (a)

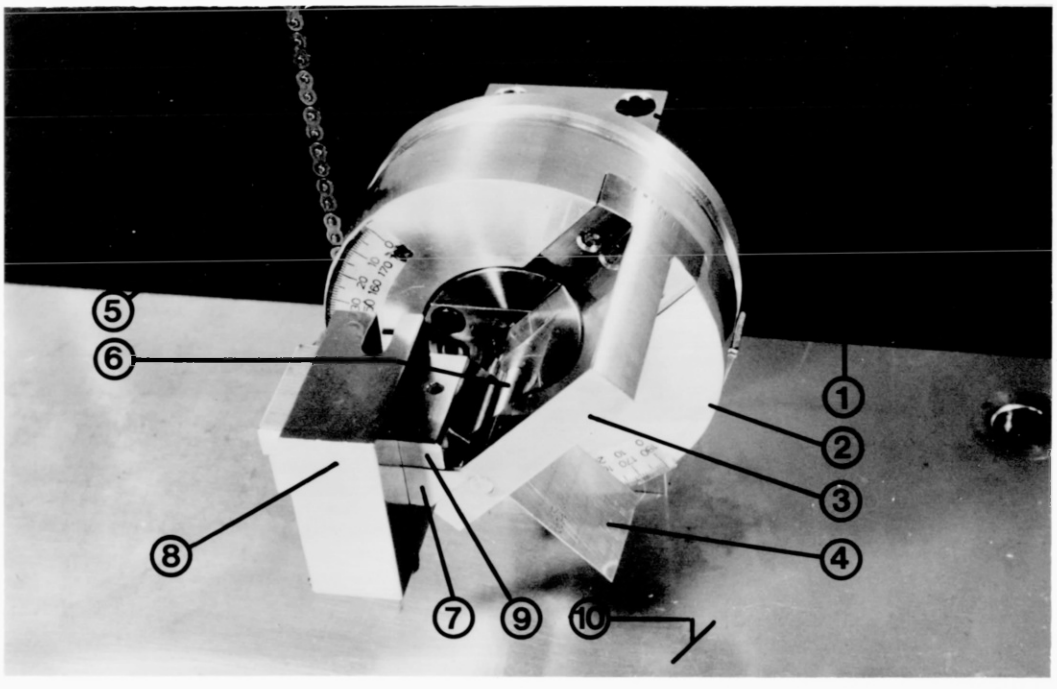


Figure 3.4 (b)

great amount of friction as the bend samples take the shape of the V-block.

3.3.4.1 Preparation of specimens for cantilever-type bend test

Specimens of 50 mm x 18 mm were cut from the strip alloys, and heat treated in the horizontal tube furnace, described previously. The heat treatment conditions for the specimens of various degree of cold work are given in Table 3.2. For bend tests, the surface smoothness is important since the existence of small scratches or rolling marks on the surface can reduce the crack resistance of material. Therefore, after the heat treatments, in order to insure that all tests were carried out on specimens in the same surface condition, a standard grinding procedure was followed. Both the large surfaces and the edges of the specimens were ground with a 1200 grid silicon carbide paper in the direction perpendicular to the bending edge so that scratches introduced by grinding would be in the same direction and parallel to the tensile stress produced by the bending on the outer surface of the specimen.

3.3.4.2 Test method for cantilever-type bend test

The procedure of the tests in this work was to clamp the specimen on one side in a position that the middle of the specimen was situated at the edge of the sharp die. The cross-head speed was 50 mm/minutes, which gave a rotation rate of the rotating block unit of 12° per minute. As the cross-head moved, the free end of the specimen was bent by the rotating bending pin continuously to an angle (between 0 and 135°), at which a crack forms at the bend apex. A lubricant (hyprez spray) was used to avoid friction between the loading pin and the surface of the specimen. Bending load and corresponding deflection angle were simultaneously recorded on the plotter of the Instron machine. The bending surface of each specimen was continuously viewed during the test by a binocular stereo light microscope.

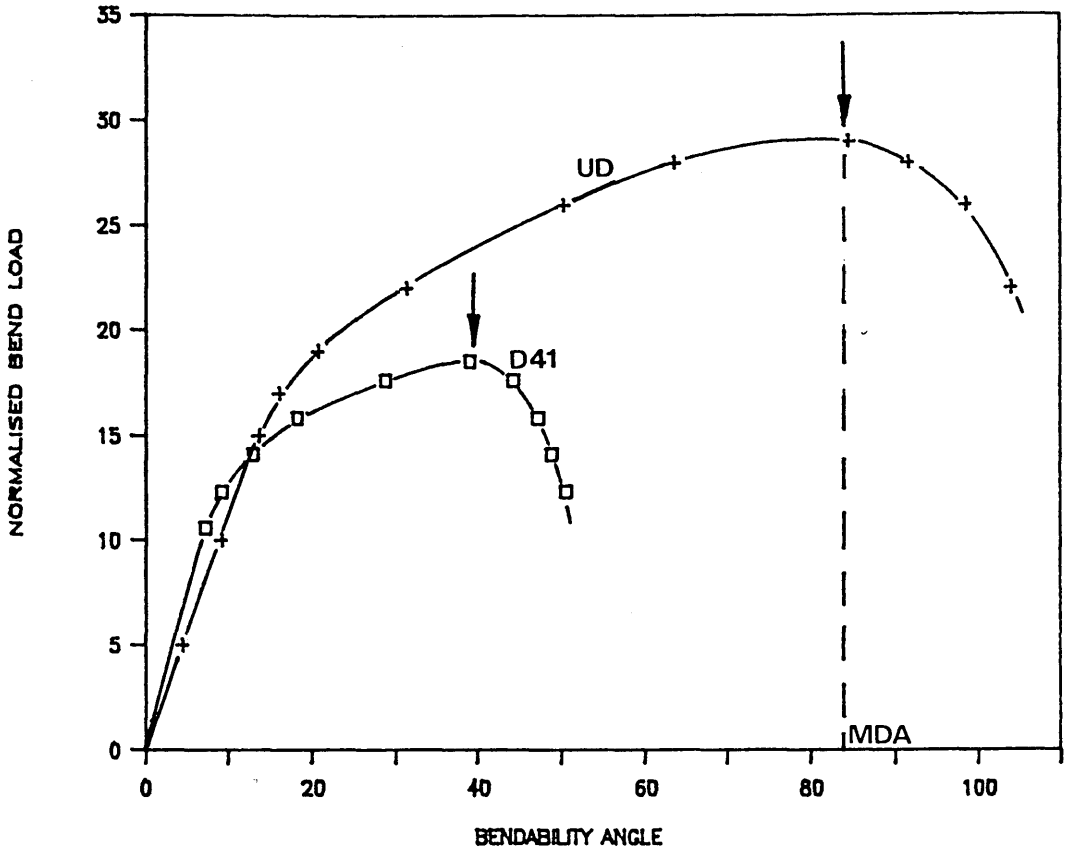


Figure 3.5- The plots of normalised cantilever-type bending load vs. deflection angle for alloys UD and D41, aged at 400°C for 25 minutes. Arrows indicate the maximum deflection angle (MDA) at which small cracks are initiated at bend apex of the samples during bending.

The nature of bending load vs. deflection plots and the observation with the stereo microscope confirmed that a number of small cracks forms at the bend apex when the bending load starts to drop from the maximum, as shown in Figure 3.5. On the basis of these observations, for each test, the maximum deflection angle (MDA), in other words, maximum bendability angle, at which the specimen cracks, was determined from the experimental plots. Repeat tests indicated that the reproducibility was good, e.g. the experimental scatter in the maximum deflection angle was typically only ±2°. Nevertheless, the bend tests for each thermo-mechanical treatments were repeated three times on identical specimens and mean values of MDA and the corresponding standard deviation were calculated.

3.3.5 Fractography

A Jeol T200 scanning elecron microscope (SEM) was used to examine the fracture surfaces of some of tensile test and bend test specimens. In order to follow the change in the nature of crack development during the cantilever type bend tests of specimens, as a function of thermo-mechanical treatment, some samples were bent to angles at which light striations, heavy striations, or small cracks were observed at the outer fibre of the bend specimens, and the surfaces were subsequently examined on the SEM.

3.4 Thermal Analysis

3.4.1 Background

Thermal analysis, i.e. differential thermal analysis (DTA) and differential scanning calorimetry (DSC), have been widely used as a technique to follow chemical or physical changes during the isothermal or non-isothermal heat treatment of a material. The basic principle of DTA is to compare the temperature of a sample with that of a thermally inert reference material, whereas in DSC the rate of energy absorbtion by the sample is recorded relative to

that of the reference material. In both cases, readings are taken as a function of time either as the sample and the reference material are heated or cooled at a uniform rate, or as they are kept at a constant temperature (Wendlandt, 1986; Pope and Judd, 1985). Depending on the type of reaction in the sample, exothermic or endothermic peaks are obtained, and their shape, size, and position with reference to temperature and time may be used for both qualitative and quantitative explanation of the events which took place in the sample.

There have been numerous studies using DTA and DSC techniques to follow phase transformations involving nucleation and growth during isothermal or non-isothermal treatments (Ozawa, 1971; Borchardt and Daniels, 1957; Chen, 1978; Piloyan et al., 1966; Henderson, 1979; Sestak, 1979). Many theories concerning the theoretical interpretation of DTA or DSC peaks have been developed using the formal theory of transformation kinetics, developed by Johnson and Mehl (1939) and Avrami (1941) (equation [2.12]). The most common of these theories are summarised in Appendix I. The equations are mainly concerned with determining the rate constant, K, the time exponent or Avrami constant, n, and the activation energies for nucleation, crystal growth, and diffusion.

3.4.2 Differential thermal analysis (DTA)

The DTA experiments were carried out on strip samples (3mmx3mm in diameter), which weighed about 0.5 g, using a computer controlled Stanton Redcroft STA 780 simul--taneous thermal analyser. A schematic illustration of the thermal analyser is shown in Figure 3.6. In DTA experiments reliability of results can be improved by using a reference which is as similar as possible in thermal characteristics to the samples under investigation. For this reason, the Cu-Be-Co strip materials, which were of the same size and weight as those of the DTA samples, were used as reference after a heat treatment to obtain the overaged condition. Care was taken to ensure that the decomposition reaction in

the Cu-Be-Co reference sample was entirely completed so that it was stable during the DTA runs. Therefore, the isothermal and non-isothermal DTA tests on the heat treated reference samples were repeated three times, using alumina powder as reference. The results indicated that the overaged Cu-Be-Co reference samples behave as a thermally inert material at temperatures up to 620°C, which is the temperature for eutectoid transformation, and hence it was safe to use these samples as reference for the DTA runs at temperatures up to 600°C.

The sample and the reference were carefully placed on the sample holder so that a good thermal contact was made between the surfaces of both sample and reference and the sample holder. Crucibles were not used in order to improve the thermal contact and thus the DTA signals, as the metastable phase transformations in Cu-Be alloys involve very little heat in comparison to a bulk phase transformation.

Non-isothermal DTA experiments were carried out on the samples, prepared from the undeformed UD and deformed D5, D10, D24, D32, and D41 alloys (see Table 1.1). The procedure of the tests was that both sample and reference were heated from the room temperature (20 °C) to 600 °C, in the DTA furnace using a controlled nitrogen atmosphere, at heating rates of 5, 10, 15, 20, 25, 30, 35, 40, 45, and 50 °C/minute . The DTA traces were produced from the data collected by the computer, and then recorded on a plotter. In addition, a modified procedure, called as "isothermal DTA" was used. This method more closely represents the decomposition of metastable solid solution during commer--cial heat treatments of Cu-Be-Co alloys to produce mill-hardened products. The procedure consisted of placing the specimen in the DTA furnace at a fixed temperature and monitoring the difference in temperature of the specimen and the reference as a function of time. This type of experiment was carried out on undeformed and deformed samples at 300, 325, 350, 375, 400, 425, 450, 475, and 500 °C, and the isothermal DTA data were recorded and plotted, as described for the conventional DTA analysis.

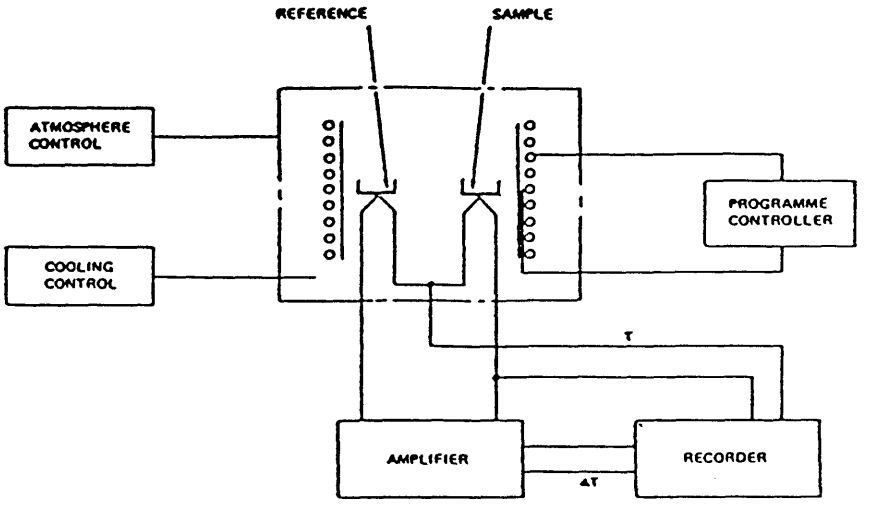


Figure 3.6- Schematic of a DTA system.

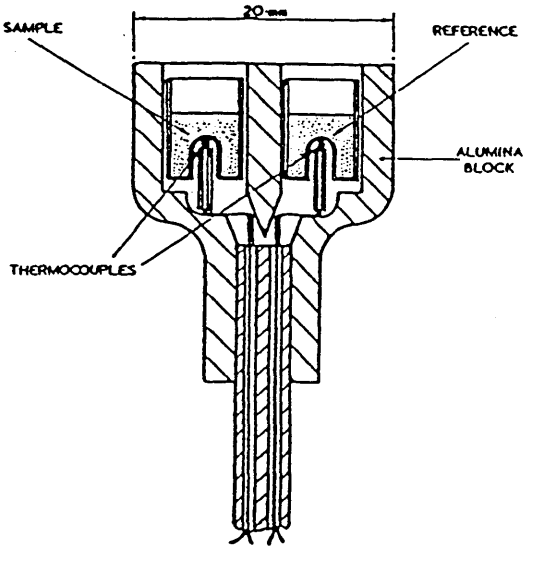


Figure 3.7- Schematic of the sample holder of a DSC system.

3.4.3 Differential scanning calorimetry (DSC)

Non-isothermal DSC analysis on undeformed samples (UD) samples was carried out using a computer controlled Stanton Redcroft DSC 1500 thermal analyser. The sample size and geometry and the reference material were the same as those used for the DTA analysis. The DSC analysis consisted of heating sample and reference, which were placed on the DSC sample holder (Figure 3.7), from room temperature to 600 °C, and recording the change in the rate of energy absorbtion by the sample, relative to that of the reference, as a function of temperature or time, by using a data processing computer program. The applied heating rates were 5, 10, 20, 30, and 40 °C/minutes.

3.5 Microstructural Analysis

Microstructural analysis was carried out on selected samples, which had received different thermo-mechanical treatments (see Table 3.2), in either a Philips or a Jeol 120 CX Temscan transmission electron microscope (TEM) with a double tilt stage. The discs for thin foil preparation were spark machined from strip materials; some from the heat treated samples for hardness measurements and others from the tested bend specimens and from DTA samples. The discs were ground to 0.2 mm thickness if necessary, and then electropolished in a Struers polishing unit with a solution of 20% nitric acid in methanol at -40°C. Following the preparation of the thin foils, they were immediately examined in the TEM. Thin foils were kept in vacuum in case of the necessity for further examination.

3.6 X-ray Diffractometry

The decomposition processes in solution treated or solution treated and cold worked strip alloys were investi-gated by the change in lattice parameter of the α-matrix. Round samples of 20 mm in diameter were spark machined from strip alloys, and then heat treated (see Table 3.2). In

order to remove the thin oxide film, formed during heat treatments, and the highly deformed surface layer due to rolling, samples were ground with a fine grinding paper and electropolished in a solution of 20% nitric acid in methanol at -40°C with a current of 0.5 A.

X-ray diffractometry was carried out on a computer controlled Philips PW 1710 difractometer with $Cu_{K\alpha}$ radiation using a Ni filter. The effects of anisotropy were minimised by rotating the samples. The diffraction lines including the (111), (200), (220), (311), (331), and (420) fundamental peaks were monitored using a scan programme at a scan speed of 0.008 2θ/s. In all cases, the mean values for the lattice parameter of the matrix were calculated from the relevant peaks, and most of the data remained within the scatter of ±0.0003 nm.

3.7 X-ray Texture Determination

The changes in the recrystallisation and cold rolling textures with the degree of deformation and preci--pitation in the strip alloys were determined using $Co_{K\alpha}$ radiation on a Philips X-ray texture goniometer, which operates in the reflection mode.

Square samples of 25mm x 25mm in diameter were cut from the strip alloys. After the heat treatments (see Table 3.2), the oxide film on the surface of samples was removed by grinding and fine polishing (1/4 μm). Using the texture camera, interfaced to a BBC Model B microcomputer, the partial (111) and (200) pole figures were obtained. The samples were rotated at 360°/8 minutes, and a lateral angular rotation of 5°/8 minutes. The intensity of the reflecting radiation was recorded as a stereographic projection on the microcomputer using a texture analysis program, and the contour maps (pole figures) were recorded on a plotter. In this method, the pole figures include the features up to 80° rotation from the centre to the side of pole figures. The remaining 10°, which is all that remains for a complete pole figure, is omitted because of the strong absorption at large angles (θ>80°).

3.8 Electrical Resistivity

Electrical resistivity measurements, which employ the four point test method, were used to follow the initial decomposition reaction in Cu-Be-Co strip alloys. The method requires a specimen of uniform cross-sectional area A and a specimen geometry which would make it possible to follow the decomposition reaction in a material by a resistivity change R due to a voltage drop V along a distance L when a current I is applied. This implies long specimens of small, but constant, cross section. The resistivity, ρ, is then calculated according to the equation (Rossiter, 1985):

$$\rho = RA/L \qquad [3.1]$$

where $R = R_s(V/I)$ where R_s is the resistivity of a standard resistor, used as the resistivity measure of a specimen.

The specimens of nominal dimensions 0.25 to 0.40 mm x 2 mm x 50 mm were cut from undeformed (UD) and deformed D10, D18, D24, D32, and D41 strip alloys, in the longitu--dinal direction (long axis of specimen was parallel to the rolling direction). Care was taken to ensure that specimens had a uniform cross-sectional area. Specimens were then heat treated under the conditions described in section 3.2 and Table 3.2 with slight modification in that the specimens were quenched from the ageing temperature to avoid any further decomposition reaction. After removing the thin film of oxide layer formed during heat treatments by grinding, thin Ni wires were spot welded at four points (separated about 15 mm from each other) on each specimen for electrical contact. The specimen geometry and the placement of the contacts were chosen so as to minimise the errors in using equation [3.1] which are discussed in detail by Persiano (1986).

The electrical resistivity measurements of the specimens were carried out on a resistivity rig with the circuit design as shown in Figure 3.8. All the measurements were taken at 20 ±0.5 °C. The inversion in the current flow is applied in order to eliminate the effect of possible

thermal e.m.f at contacts, and the electrical resistance readings were then averaged. The electrical resistivity of specimens were calculated according to equation [3.1].

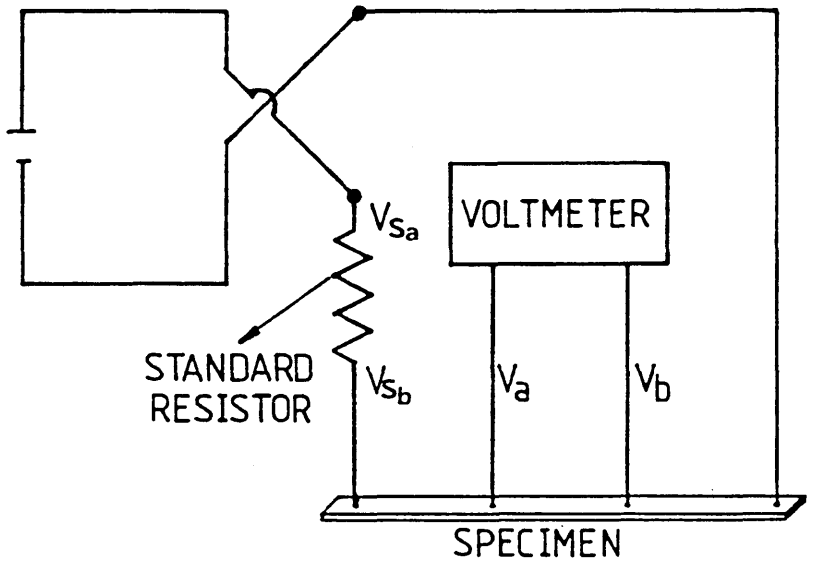


Figure 3.8- The main circuit for resistivity measurements, showing the details of the electrical connec--tions of a sample.

CHAPTER 4

EXPERIMENTAL RESULTS

4.1 The Hardening of Copper-Beryllium-Cobalt Alloys

The mill-hardened Cu-Be alloys rely on precipitation hardening to develop their strength potential. As a preli--minary to more detailed mechanical property measurements, the ageing response of the alloys was characterised by hardness measurements. The hardness data for alloys, UD, D5, D10, D18, D24, D32, and D41, obtained on ageing at 350, 380, 400, and 420°C, are summarised in Appendix B. Also, the results selected to exemplify the characteristic changes in the hardening response of Cu-Be-Co alloys with prior cold work, ageing time, and temperature are presented in Figures 4.1, 4.2, 4.3, and 4.4. In Chapter 5, the complete hardness data will be analysed further with reference to the TEM and the bendability test results by plotting hardness vs. ageing temperature and time in three-dimensions. In the following sections, the effect of various thermo-mechanical treatments on hardening behaviour of Cu-Be-Co alloys will be presented with reference to the hardness data.

4.1.1 Hardening in the solution treated alloy

On ageing at 350°C, hardness values increased sharply to a maximum (335 VMH) after an incubation period (about 15 minutes), as shown in Figure 4.1. This was followed by a gradual decrease in hardness on further ageing. A small increase in hardness prior to the large increase was also noticed. Ageing at 380°C resulted in an increase in hardness to a maximum (275 VMH after 35 min.) without going through an incubation period, and the rate of increase in hardness was somewhat lower than that at 350 °C. Attainment of the maximum was followed by a decrease in hardness to ≈245 VMH after 60 min., and further ageing did not significantly reduce hardness; the hardness curve

remains almost parallel to the time axis for times as long as 100 minutes (Figure 4.1). During ageing at 400 and 420°C, the hardening response of solution treated alloys was very similar; hardness starts increasing soon after heat treatment commences, which occurs earlier at 420°C than at 400°C. After attaining the maximum hardness (240 VMH at 400°C and 230 VMH at 420°C), hardness does not drop noticeably.

It must be noted that the increase in temperature results in an earlier onset of the hardness increase and a shifting of the maximum to shorter times, but a fall in the maximum hardness increment.

4.1.2 Hardening after prior cold work

The hardness data, obtained from prior cold worked alloys in unaged condition, suggests that the work hardening introduced by prior cold work in the range 5 to 41% RA results in a linear increase in hardness, e.g. 41% prior cold work increases the hardness by 145 in units of VMH, as shown in Figure 4.5-a.

On ageing at 350°C, the hardness increased immedi--ately on beginning the heat treatment, and after the hardness value had reached a maximum, there was a gradual decrease in hardness (Figures 4.2, 4.3, and 4.4); a similar hardness decrease on over-ageing was also observed when ageing solution treated alloys at 350°C. The amount of decrease in hardness of 41% prior cold worked alloys was more pronounced than the decrement in the solution treated and less cold worked alloys; futhermore the over-ageing process in the heavily deformed alloy took place in two steps, which commenced at ageing times of 20 minutes and 60 minutes, as indicated by the arrows in Figure 4.4.

On ageing at 380, 400, and 420°C, the hardness vs. time plots, some of which are given in Figures 4.2, 4.3, and 4.4, revealed the same characteristics as the 41% prior cold worked alloy, aged at 350°C, namely:

(i) a first hardening phenomenon which corresponds to the initial increase in hardness to a maximum,

(ii) a secondary hardening phenomenon that results in a plateau after a drop in hardness from the peak, and

(iii) a decrease in hardness following the plateau.

These features, which are separated by broken lines on the hardness curves in Figure 4.2, 4.3, and 4.4, become much clearer when prior cold work exceeds 10% RA. The ageing temperature or the amount of prior cold work does not change the characteristic shape of hardness curves, all of which reveal the above features; however, the higher the temperature, and/or the greater the amount of prior cold work, the lower the overall hardening and the shorter the time for hardness to reach a maximum.

The effect of prior cold work on the overall hardening, or the maximum hardness increment, is worthy of further discussion. Although introducing prior cold work accelerated the age hardening of Cu-Be-Co alloys, the prior cold work, exceeding 10% RA, reduced the overall hardening of the alloys. Defining the overall hardening, ΔH, as the difference in hardness values before ageing and at the hardness maximum, the value of ΔH was not affected by prior cold work $\leq$ 10% RA on ageing at 350 °C, but greater degrees of prior cold work reduced ΔH considerably, e.g. 40% reduc-tion in ΔH occurred after 41% prior cold work, as shown in Figure 4.5-b. In contrast, on ageing at 400 and 420 °C, the value of ΔH was initially increased by prior cold work less than 10% RA, but, a further increase in prior cold work reduced ΔH (Figure 4.5-b); the lower the ageing tempera-ture, the greater the decrease in ΔH.

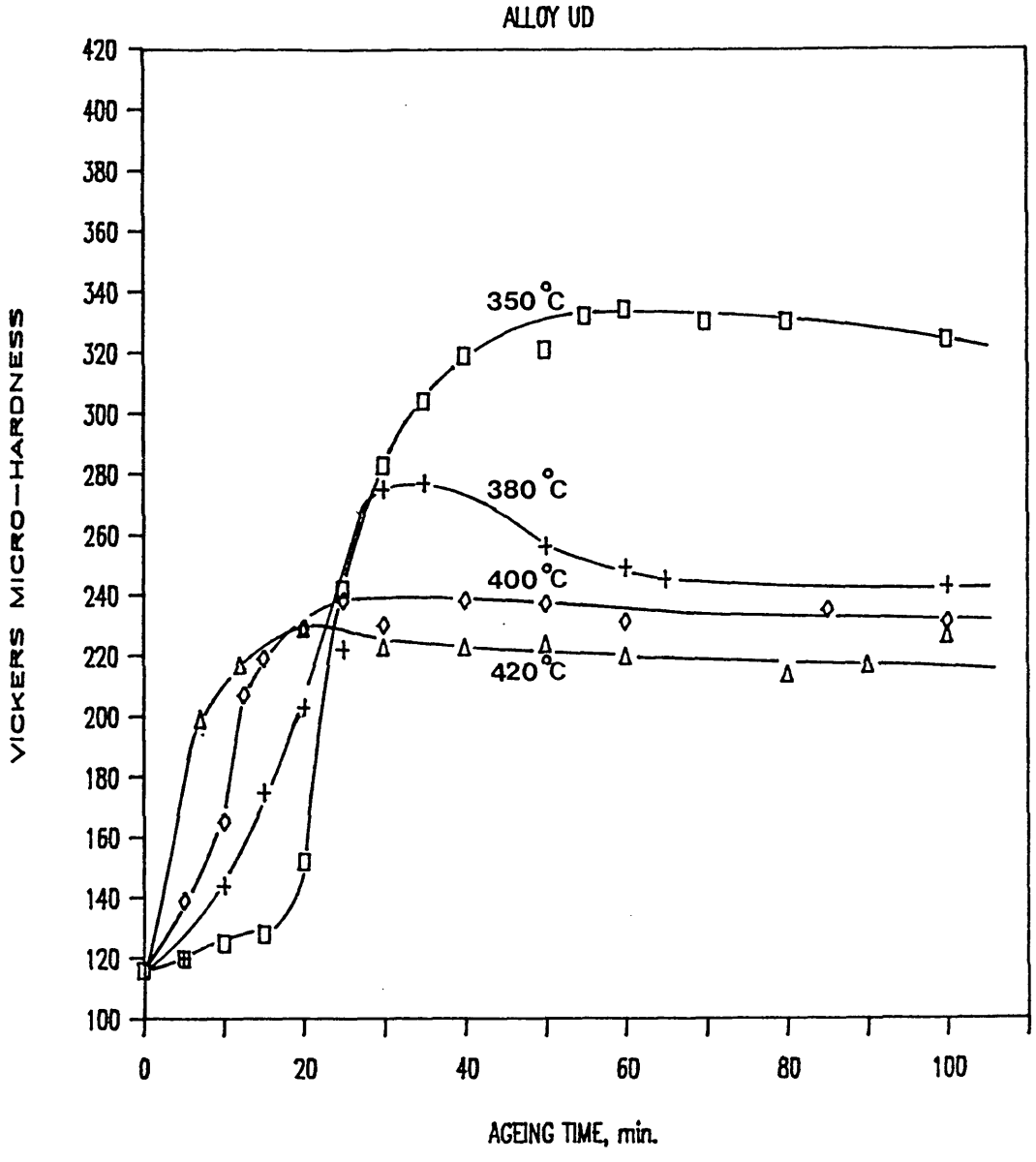


Figure 4.1- Hardness curves of the solution treated alloy on ageing at (□) 350°C, (+) 380°C, (◇) 400°C, and (Δ) 420°C.

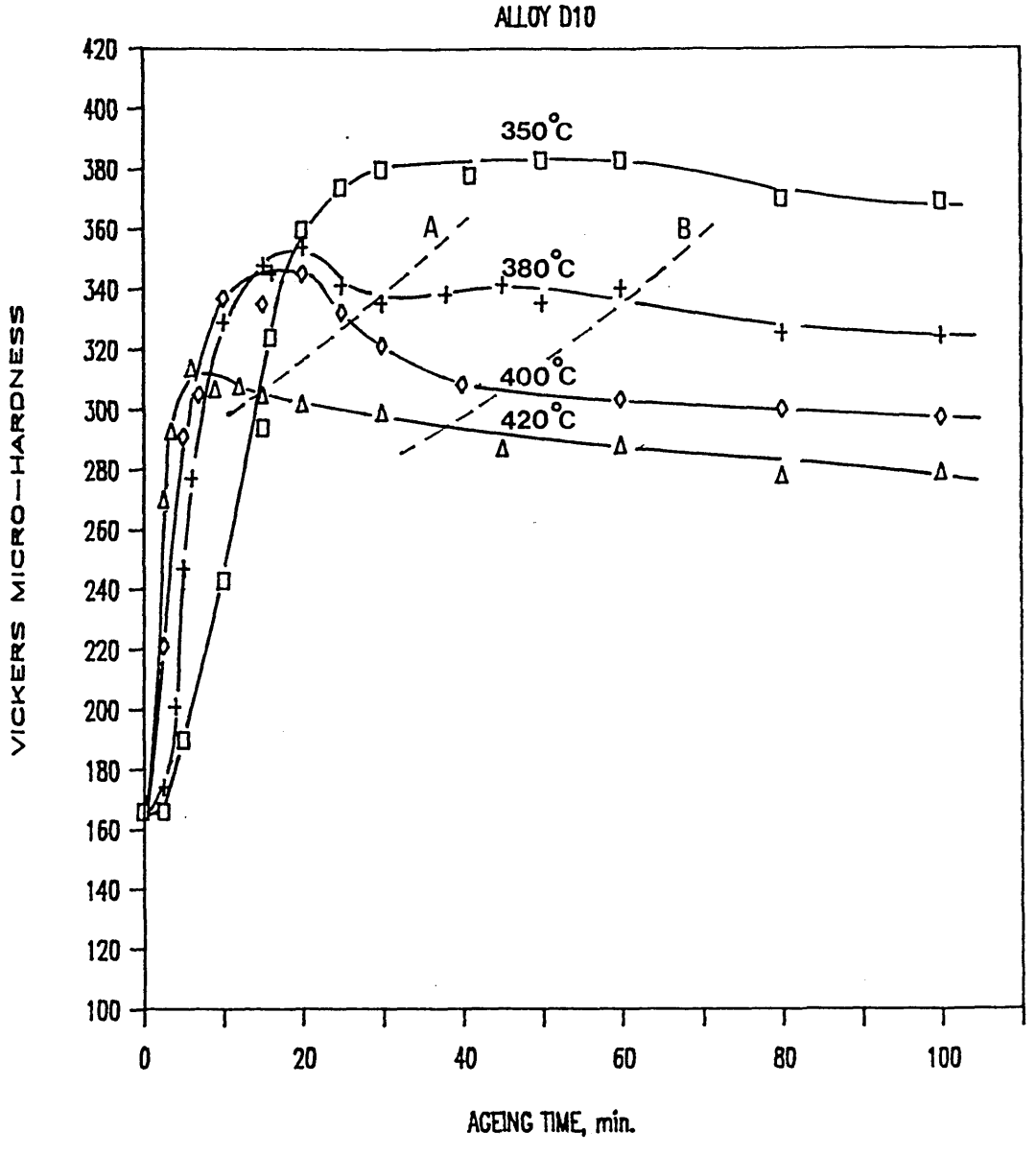


Figure 4.2- Hardness curves of the 10% prior cold worked alloy on ageing at (□) 350°C, (+) 380°C, (◇) 400°C, and (Δ) 420°C. The broken lines A and B indicate the onset and finish of the secondary hardening phenomenon, respectively.

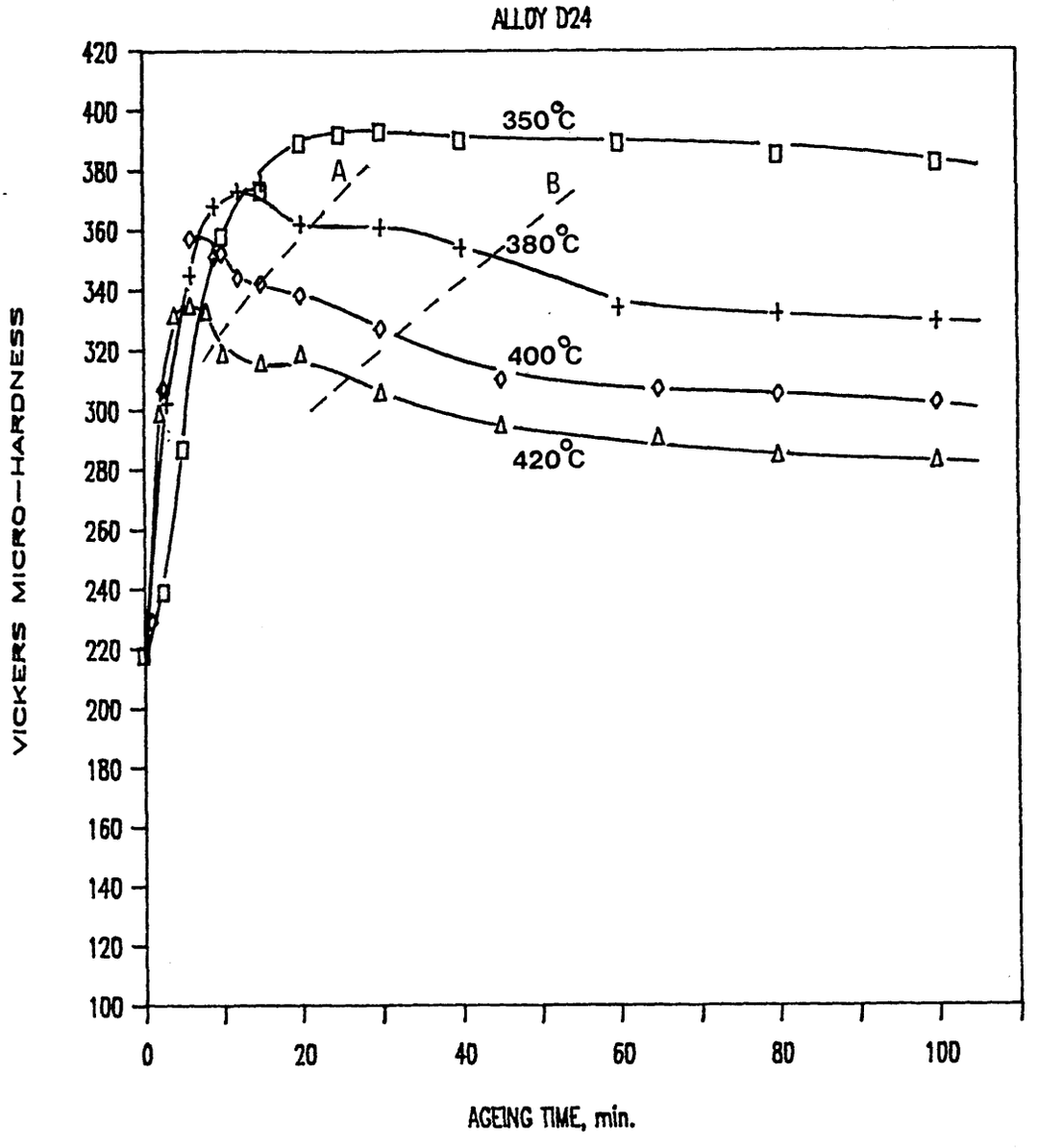


Figure 4.3- Hardness curves of the 24% prior cold worked alloy on ageing at (□) 350°C, (+) 380°C, (◇) 400°C, and (Δ) 420°C. The broken lines A and B indicate the onset and finish of the secondary hardening phenomenon, respectively.

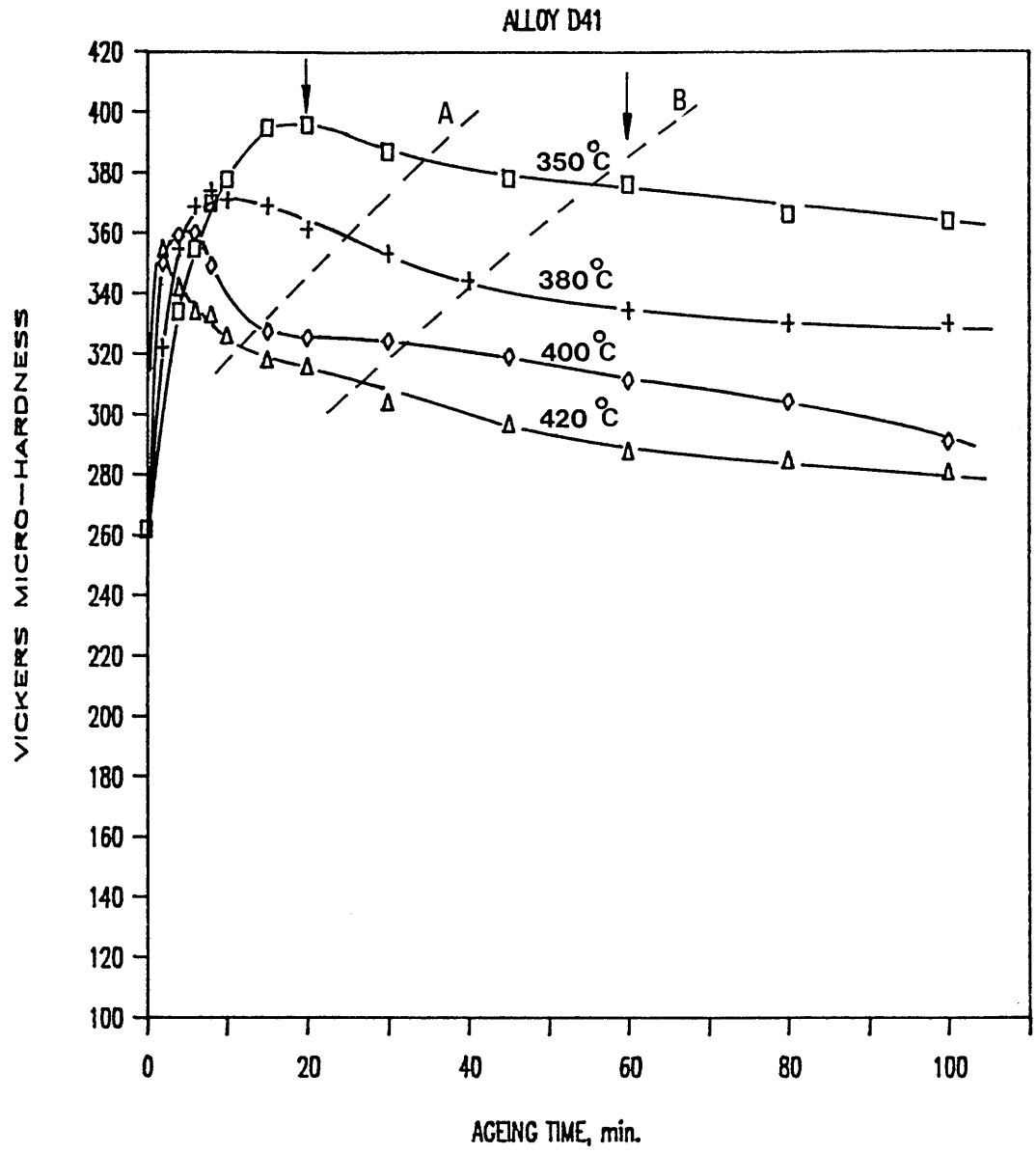


Figure 4.4- Hardness curves of the 41% prior cold worked alloy on ageing at (□) 350°C, (+) 380°C, (◇) 400°C, and (Δ) 420°C. The broken lines A and B indicate the onset and finish of the secondary hardening, respectively.

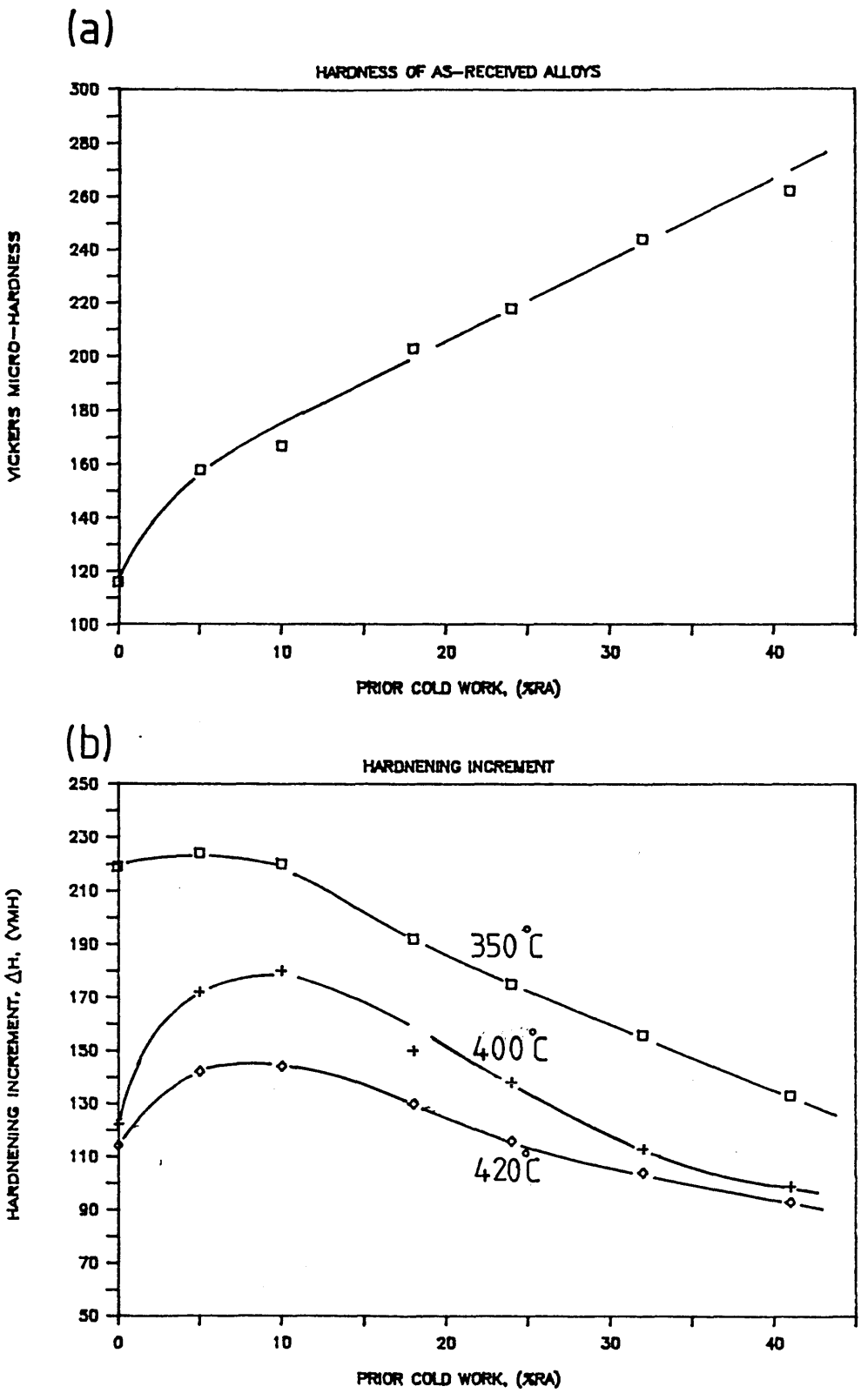


Figure 4.5-
(a) Hardening by prior cold work in as-received alloys.
(b) Effect of prior cold work on hardening increment, ΔH, attained on ageing at 350, 400, and 420°C.

4.2 TEM Analysis of Decomposition Reactions

4.2.1 Structure of as-received alloys

Examination of the structure of the solution treated alloy, UD, revealed the presence of a large number of annealing twins and insoluble cuboidal particles in the matrix and near grain boundaries. Vacancy loops and helical dislocations were not observed, but, for certain foil orientations, the supersaturated solid solution showed a mottled structure, as illustrated in the bright field (BF) micrograph in Figure 4.6-a. In this figure, the selected area diffraction pattern (SADP) shows double diffraction spots (DDS) (satellite spots) around the diffracted spots.

The structure of the prior cold worked alloys (up to 41%RA) contained a uniform distribution of dislocations and distorted annealing twins. In some areas of the matrix, cuboidal particles were also present. A typical micro--structure of the 24% prior cold worked alloy is shown in Figure 4.6-b. The density of dislocations increased with prior cold work, and hence the annealing twins could not be resolved in the structure. Even after 41% prior cold work, no cell structure was observed.

4.2.2 Precipitation in the solution treated alloy

(1) Ageing at 350°C

The first observable feature in the decomposition reaction of the supersaturated solid solution was the formation of plate-like precipitates at grain boundaries after 8 minutes of ageing (Figure 4.7-a). The corresponding SADP indicated that these precipitates were the γ'_D phase with a body-centred cubic structure, having a = 0.27 nm, with the crystallographic orientation relationship:

$$(113)_\alpha \;//\; (103)_{\gamma'D} \;;\; [110]_\alpha \;//\; [001]_{\gamma'D}$$

According to literature (Bonfield and Edwards, 1974), this phase forms on $\{113\}_\alpha$ habit planes. Grain edges presented a more developed structure, i.e. large plate-like γ'_D preci-

-pitates in cellular structure, and further ageing resulted in the cellular growth, which developed the "double seam" morphology (Figure 4.7-b).

The discontinuous γ'_D precipitation (see Figure 4.7-a) was followed by the nucleation of G.P. zones on $(100)_\alpha$ planes. The G.P. zones were identified after 15 minutes of ageing by the appearance of striations along the traces of $(110)_\alpha$ planes, which were resolved at the bend extinction contours, as shown in the BF image of Figure 4.8-a, and the <110> short relrods (SR) as cross-hatching patterns at each reflected spot in the corresponding SADP. The occurrence of these features has been repeatedly reported in the literature (Tanner, 1968; Tanaka et al., 1963; Phillips and Tanner, 1973; Bonfield and Edwards, 1974), and the development of the striations has been attributed to the coherency stress fields of the G.P. zones that result in elastic deformation of the matrix along (110)<110>. At this stage of ageing, G.P. zones are not large enough to contribute to the image by diffraction themselves.

On further ageing, i.e. ageing for 20 minutes, the G.P. zones grew in size and resulted in the development of continuous streaks on <100> directions in the SADP, which are well recognised as typical for well-developed G.P. zones and correspond to the regularly oriented markings in the BF micrograph as shown in Figure 4.8-b. Also, some faint intensity maxima (IM) at the <100> streaks at about 2/3 of {200} reciprocal lattice points were present in the SADP of Figure 4.8-b (see arrows). It is evident from the <100> streaks in the SADP of Figure 4.8-b that, at this stage, G.P. zones are still present, but the presence of the intensity maxima at these streaks shows that there is a break down in the coherency of G.P. zones in the regions where the zones grew to a critical size for the subsequent nucleation of the semicoherent γ' precipitates.

Indeed, after ageing for 30 minutes, the diffuse arrowhead-type intensity maxima (ATIM) developed at the <100> streaks in the SADP (Figure 4.9-a). The corresponding dark field (DF) micrographs, obtained from the ATIM,

(Figure 4.9-b) consisted of various plate-like precipita--tes, which differed from each other by their orientation and size, namely (i) very small precipitates oriented in <110> directions and (ii) larger precipitates oriented between the <110> and <112> directions, as indicated by the arrows in Figure 4.9-b.

It seems that, at this stage, G.P. zones on $\{100\}_\alpha$ planes, producing striations along <110> directions in the BF micrographs, nucleated the semicoherent γ' phase by a gradual change in their orientation to <112> directions; as the γ' precipitates grow in size, their orientation is inclined to the $\{112\}_\alpha$ planes, where the misfit can be better accommodated. This process can be followed more clearly by comparing the SADP in Figures 4.8-b (20 min. ageing) and 4.9-a (30 min. ageing), in that the intensity maxima (Figure 4.8-b) develop into the ATIM (Figure 4.9-a). During this process, the arrowheads gradually fan out until the streaks at each arrowhead are inclined to the <112> directions. This orientation of the arrowheads in fact refers to $(112)_\alpha$ planes where the γ' precipitates form since the streaks develop when s=0 and the plate-like precipitates are perpendicular to the incident beam and hence the habit plane of the precipitates would be the planes perpendicular to the direction of the streaks. Thus, the structure in Figure 4.8-b consists of the mixture of G.P. zones and very small γ' precipitates while that in Figure 4.9-b contains only fine γ' precipitates since the <100> streaks in the corresponding SADP have almost disappeared.

(2) Ageing at 400°C

Ageing kinetics are noticeably accelerated in comparison to those at 350°C, and the G.P. zones did not form at this temperature; the SADP did not show any evidence for the presence of the <100> streaks. The predominant mode of the decomposition reaction up to 20 minutes was the formation of the γ'_D precipitates hetero--geneously from the solid solution at grain boundaries and

the subsequent cellular growth of these precipitates into the matrix (Figure 4.10-a). This was followed by the formation of the γ' precipitates directly in the matrix, where the cellular growth had not taken place. At this stage the SADP of the matrix regions (Figure 4.11-b) indicated only the well-developed split-spot reflections (SSR), which were produced by the formation of the plate-like γ' precipitates (Figure 4.11-a). The orientation rela-tionship of the γ' and the γ'_D formed at this temperature was the same as that previously given for the discontinuous γ'_D precipitates at 350°C.

After 30 minutes ageing, a more advanced stage of cellular precipitation than that which occurred at 350°C, was observed at the grain boundaries. The reaction products in the cellular regions were large plate-like γ'_D precipi-tates and small nodular γ_D precipitates (white particles) in a reoriented α-matrix, as shown in Figure 4.10-b.

The main features of the SADP's, together with the abbreviations used, and the associated precipitation phenomena are summarised below:

(i) short relrods (SR): G.P. zones,

(ii) continuous streaks (CS): G.P. zones,

(iii) intensity maxima (IM) on continuous streaks: the nucleation of the γ' precipitates,

(iv) arrowhead-type intensity maxima (ATIM): the growth of the γ' nuclei, and

(v) split-spot reflections (SSR): well-developed γ'pre-cipitates.

Using these abbreviations, the precipitation sequence in solution treated (UD) and prior cold worked (D10, D24, D32, and D41) alloys at 350 and 400°C is summarised in Table 4.1. The precipitation sequence in prior cold worked alloys will be presented in detail, employing the same abbrevi-ations, in the following section.

Figure 4.6

(a) Mottled structure in the matrix of the solution treated alloy before ageing.

(b) The dislocation network in the 24% prior cold worked alloy before ageing; an annealing twin is also visible in the structure.

Figure 4.7

(a) The γ' precipitates at an original grain boundary, in the solution treated alloy, aged at 350°C for 8 minutes and the SADP from a (110) surface, revealing additional reflections from one of the γ' precipitates.

(b) Cellular structure. containing the γ'_D precipita--tes in grain boundary regions of the solution treated alloy, aged at 350°C for 20 minutes.

Figure 4.8

(a) Striations, caused by the nucleation of G.P. zones on (100) of the matrix, in the solution treated alloy, aged at 350°C for 15 minutes, and the SADP shows the <110> short relrods as cross-hatching patterns at each reflections.

(b) B.F. image of the G.P. zones transforming to the γ' precipitates, which is evident from the presence of IM in the corresponding SADP (see arrows), obtained from the solution treated alloy after ageing at 350°C for 20 minutes.

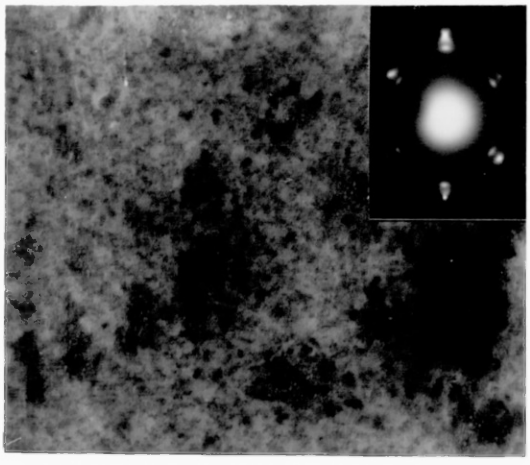
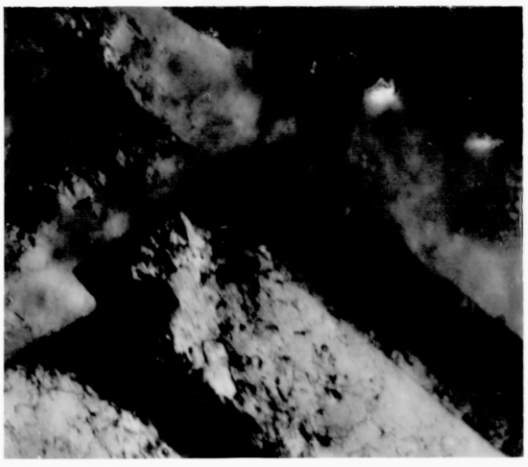


Figure 4.6 (a)

0.23 μm



(b)

0.23 μm

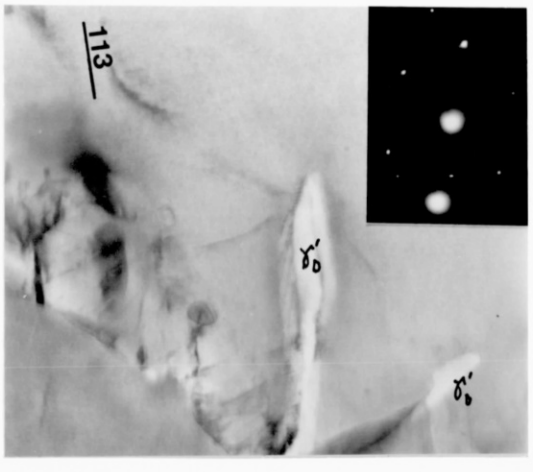
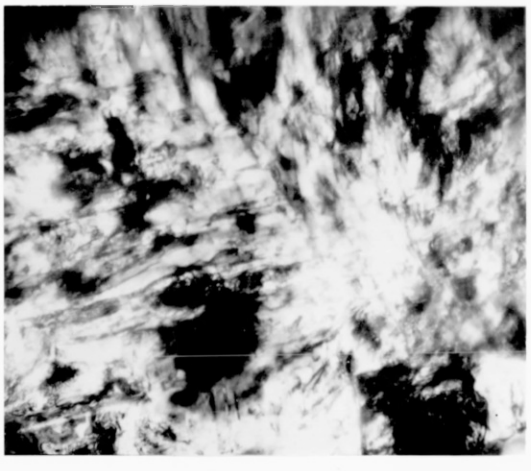


Figure 4.7 (a)

0.23 μm



(b)

0.7 μm

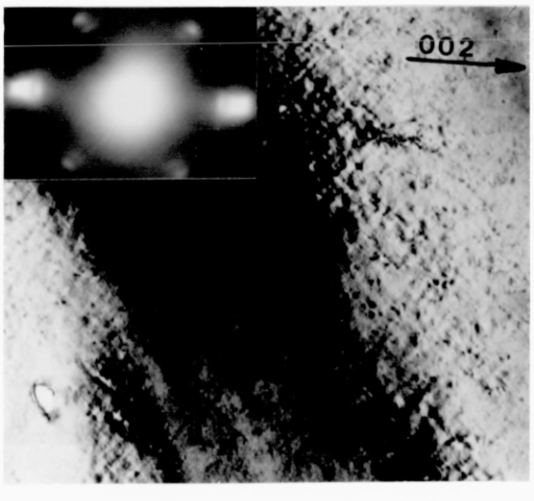
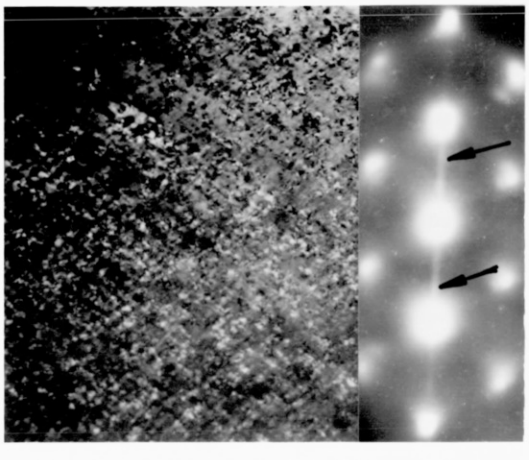


Figure 4.8 (a)

0.23 μm



(b)

0.2 μm

Figure 4.9

(a) B.F. micrograph of the matrix of the solution treated alloy, showing small γ' precipitates, after ageing at 400°C for 30 min.

(b) DF micrograph of (a), obtained from the ATIM in the corresponding SADP, which indicates γ' precipitation.

Figure 4.10

(a) Cellular precipitation, engulfing the interior of the grain, in the solution treated alloy after ageing at 400°C for 10 minutes.

(b) The plate-like γ'_D and the nodular γ_D precipitates (bright points), formed in a cellular reaction in a grain boundary region after ageing the solution treated alloy at 400°C for 30 minutes.

Figure 4.11

(a) The γ'_D precipitates in region A and the γ' precipitates in the matrix (region B) in the solution treated alloy after ageing at 400°C for 30 minutes.

(b) The SADP from region B in B.F. image in (a), revealing additional spots from the γ' precipitates; the beam direction is very close to [110].

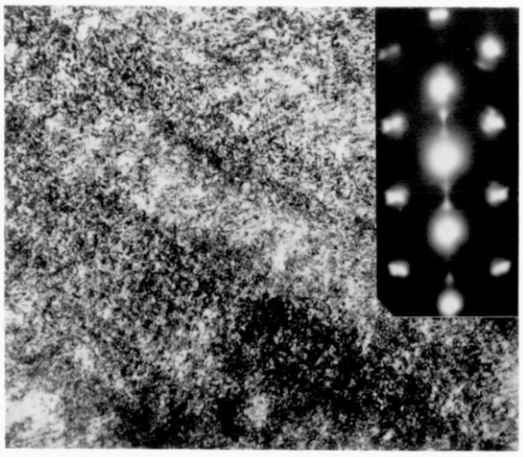
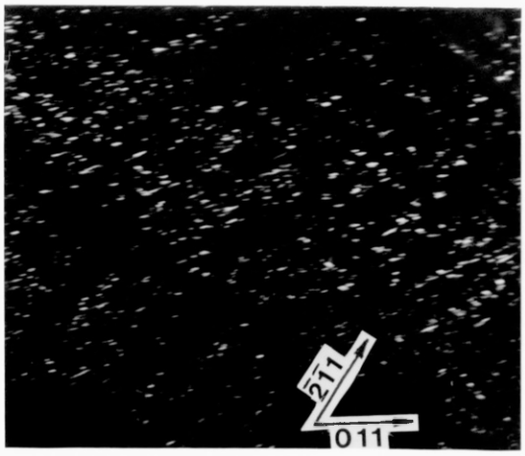


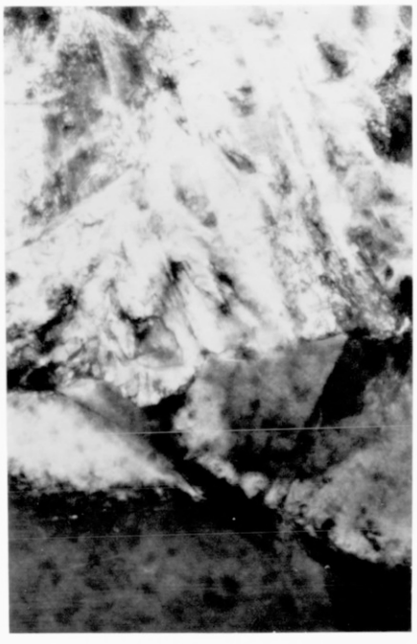
Figure 4.9 (a) 0.2 μm



(b) 0.2 μm



Figure 4.10 (a) 0.5 μm



(b) 0.2 μm

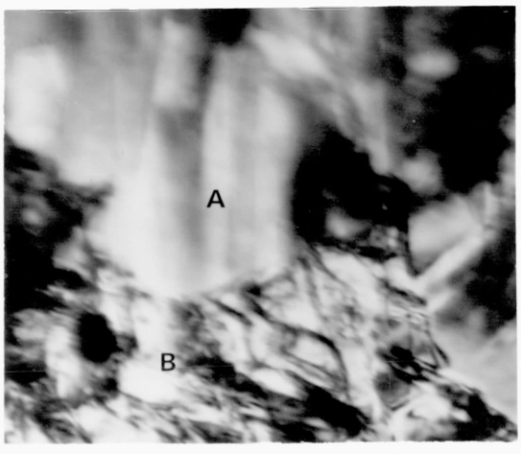
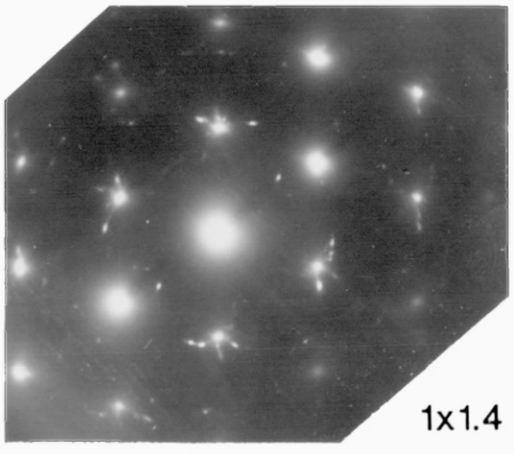


Figure 4.11 (a) 0.2 μm



(b)

4.2.3 Precipitation in prior cold worked alloys

(1) Ageing at 350°C

At the initial stages of ageing it was not possible to resolve G.P. zones due to the presence of the dislocation network. With the advance of recovery on further ageing, some areas of the matrix of low dislocation density revealed the <100> continuous streaks and the intensity maxima at these streaks at 2/3 of $\{200\}_\alpha$ recipro-cal lattice points, which correspond to G.P. zones and the nucleation of the γ' precipitates respectively. This stage of ageing in 10% prior cold worked alloys was achieved after 10 minutes of ageing (Figure 4.12-a), which can be compared with 20 minutes for solution treated alloys (see Figure 4.8). For degrees of prior cold work greater than 10% RA, the SADP of the matrix in the specimens aged for times as short as 5 minutes revealed only the ATIM, which represents a more developed stage of γ' precipitation, as shown for 24% prior cold worked alloy in Figure 4.13-a. It must be noted that the development of the ATIM for 10% deformed alloys occurred only after 20 minutes ageing, as shown in Figure 4.12-b. However, prior cold work greater than 24% RA did not noticeably accelerate γ' precipitation in the matrix, as the micrographs and the SADP of 24, 32 and 41% cold worked specimens indicated similar features after identical heat treatments. Further ageing resulted in the growth of the γ' precipitates in the matrix as the corresponding SADP indicated the gradual development of the SSR. This process in the 24% prior cold worked alloy is presented in Figure 4.13-a, b, and c, in sequence.

The SADP of the matrix, obtained from the 24% prior cold worked specimen, aged for 30 minutes (Figure 4.13-c), indicated additional reflections, some of which were in characteristic shapes, e.g. elongated {110} and curved {100} reflections. These reflections were produced by the γ' precipitates, having a body-centred tetragonal struc-ture. The measurements, taken from the elongated and the curved reflections indicated a variety of unit cell dimen-

-sions for the γ' phase, which were a=b=0.27 to 0.28 nm and c=0.258 to 0.262 nm. The crystallographic orientation relationship of this structure was close to:

$$(112)_\alpha \;//\; (120)_{\gamma'} \;;\; [110]_\alpha \;//\; [001]_{\gamma'}$$

The formation of the γ'_D precipitates at grain boundaries, accompanying the deformation recovery, preceded the matrix precipitation, i.e. G.P. zone formation, in 10% prior cold worked alloys. As shown in Figure 4.14-a and b, after 5 minutes ageing of 10 and 24% prior cold worked alloys, a series of plate-like γ'_D precipitates formed at grain boundaries in a pucker-type process, which was previously suggested by Baumann et al. (1981). However, for prior cold work greater than 10% RA, 5 minutes ageing resulted in the formation of the γ' in the matrix (note the ATIM in the SADP in Figure 4.12-b) and the γ'_D at grain boundaries at the same time (note the plate-like precipita--tes in puckered condition in Figure 4.14-b). During the pucker-type process, the formation of the γ'_D precipitates involved grain boundary movements in addition to the reduction of the Be content in the surrounding regions, which resulted in the development of dislocation-free reoriented regions of the α-matrix, as indicated with arrows in Figure 4.14-b. On further ageing, the discontinu--ous reaction was mainly the growth of the reoriented α-matrix into the deformed matrix and the formation of the nodular γ_D precipitates inside these regions at the expense of the γ'_D precipitates, as shown in Figure 4.14-c.

The grain boundary precipitation in 10 and 41% prior cold worked alloys, aged for 10 minutes, is compared in Figure 4.15-a and b, respectively. Typical features of the grain boundary regions in 10% prior cold worked alloys (Figure 4.15-a) were large plate-like γ'_D precipitates in the dislocation-free reoriented α-matrix; the grain boundary regions that had undergone the discontinuous reaction were much less in volume than these observed in solution treated alloys. When the prior cold work was increased above 24% RA, small recrystallised grains at the grain boundaries and the presence of the nuclei of the nodular γ_D precipitates in these grains were observed.

However, γ'_D precipitation did not occur even after 10 minutes ageing. These features, developed in the 41% cold worked alloy on ageing at 350°C for 10 minutes, are shown in Figure 4.15-b.

The micrographs in Figure 4.15-a and b represent boundary regions, where a reasonable amount of precipita--tion has occurred, not the grain edges. It must be noted that some boundaries had almost no precipitation while most of the grain edges had a considerable amount of discontinu--ous precipitates in cellular form; a typical micrograph revealing the characteristic features at a grain edge in the 24% prior cold worked alloy, aged for 5 minutes is shown in Figure 4.15-c.

(2) Ageing at 400°C

Recovery proceeded at a faster rate than at 350°C, with accelerated γ' precipitation in the matrix taking place directly from the supersaturated solid solution without the formation of G.P. zones. Selected micrographs and the corresponding SADP's for 10 and 24% prior cold worked alloy, revealing the γ' precipitates in the matrix, are shown in in Figures 4.16 and 4.17, respectively. From the analysis of the SADP's, which have SSR, the γ' precipi--tates in prior cold worked alloys were found to exhibit the same crystallography and structure as those formed in the solution treated alloys at 400°C.

The grain boundary reaction in the 10, 24, and 32% prior cold worked alloys started with the development of strain-free reoriented regions at grain boundaries. This was induced by the grain boundary movements, i.e. bowing of the boundary into the deformed α-matrix, where the continuous γ' precipitation had already taken place, as shown in Figure 4.18-a. At this stage of ageing, a limited amount of γ'_D precipitation has been found to occur at moving grain boundaries in the 10 and 24% deformed alloys, whereas, at higher deformations, γ'_D precipitation at grain boundaries does not seem to occur whilst the continuous γ' precipitation predominates.

On further ageing, the growth of strain-free regions resulted in the nucleation of recrystallised grains at grain boundaries (Figure 4.18-b), containing the nuclei of the equilibrium γ_D phase. These regions were confined to a narrow band at grain boundaries, as exemplified in Figure 4.18-b for the 32% prior cold worked alloy, whereas, the grain edges and corners revealed a more advanced stage of the discontinuous reaction. As shown in Figure 4.18-c, on ageing the 41% cold worked alloy even after 4 minutes, the development of the strain-free regions occurs extensively, and these regions contain the equilibrium γ_D phase and the nuclei of recrystallised grains.

(3) Ageing at 500°C

In the present work, only the 41% prior cold worked alloy, aged for 18 minutes, was investigated. Additional TEM investigations on the 24 and 32% prior cold worked alloys, which were isothermally tested in the DTA furnace at 500°C, were also carried out, and the related results will be separately presented in section 4.5.

The TEM analysis on 41% cold worked alloys, aged for 18 minutes, indicated that the decomposition reaction proceeded at a faster rate than that at lower temperatures with the precipitation of the γ' phase in the matrix, accompanying enhanced recovery and recrystallisation. The nature of the continuous precipitation is represented in Figure 4.19. The γ' precipitates, formed at this tempera-ture, were identical in structure and crystallography with those at 400°C, but were larger in size. It was noticed that, at this temperature, the migrating grain boundaries occur in highly deformed regions; this leads to the simultaneous annihilation of dislocations and the nuclea-tion of recrystallised grains in dislocation free regions. As shown in Figure 4.20, well-developed recrystallised grains, containing annealing twins, and the nodular γ_D precipitates inside these grains were present in the original grain boundary regions (large recrystallised grains) and in highly deformed regions of the matrix (small

Figure 4.12

(a) The matrix of the 10% prior cold worked alloy; the SADP indicates both CS and IM, which correspond to the G.P. zones transforming to the γ' phase, after ageing at 350°C for 10 minutes; [110] beam direction.

(b) D.F. micrograph of the 10% prior cold worked alloy, aged at 350°C for 20 minutes, obtained from the ATIM in the corresponding SADP, revealing small γ' precipitates

Figure 4.13

D.F. micrographs, revealing small γ' precipitates, nucleated by the G.P. zones in the matrix of the 24% prior cold worked alloy after ageing at 350°C for
(a) 5 min.,
(b) 10 min., and
(c) 30 min.
Note the ATIM in the SADP of (a) and (b) and the ATIM transformed to the SSR in that of (c); the SADP's are from (110) planes of samples.

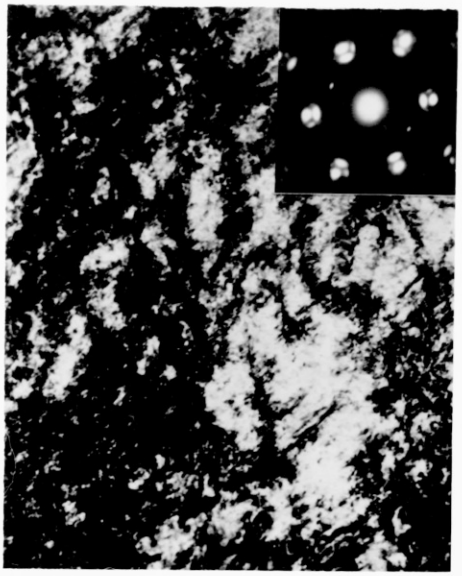
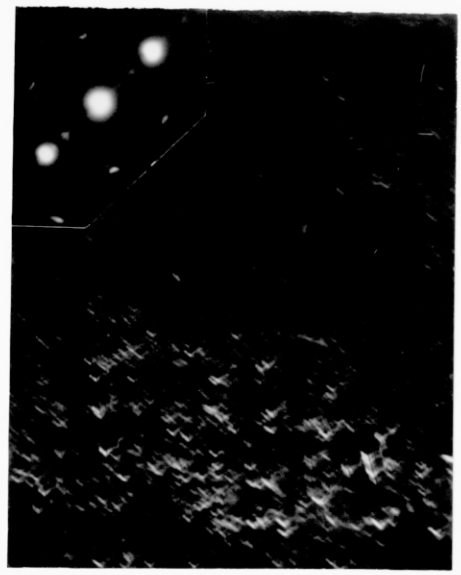


Figure 4.12 (a)

0.14 μm



(b)

0.14 μm

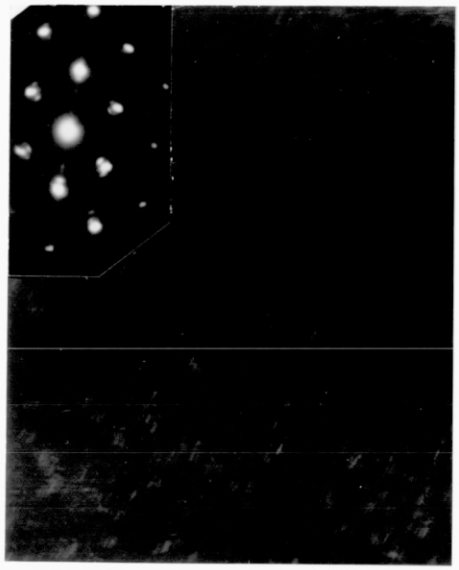
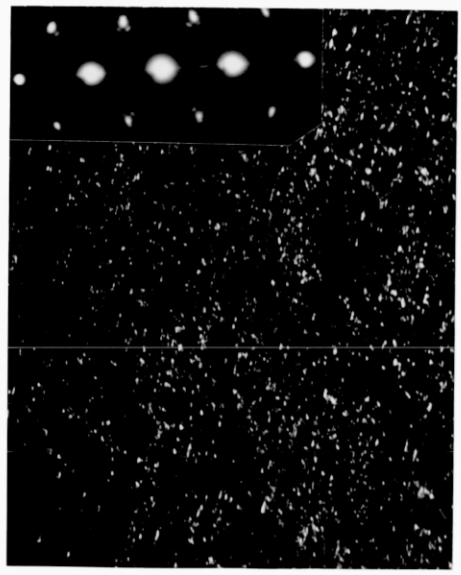


Figure 4.13 (a)

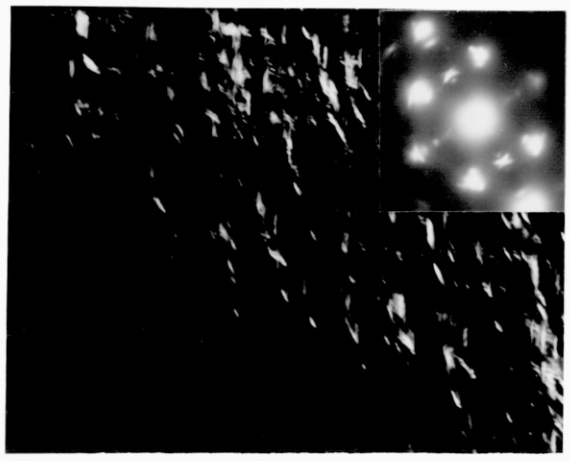
0.14 μm



(b)

0.14 μm

(c)



0.14 μm

Figure 4.14

(a) The plate-like γ'_D precipitates at a grain boundary in the 10% cold worked alloy after ageing at 350°C for 5 min.

(b) shows the same type of precipitates and also the strain free regions at the grain boundary (see arrows) in the 24% prior cold worked alloy, aged at 350°C for 15 min.

(c) shows the nodular γ_D precipitates (black grains) at a grain boundary in the 24% prior cold worked alloy, aged at 350°C for 30 minutes.

Figure 4.15

(a) The γ'_D precipitates at a grain boundary in the 10% prior cold worked alloy after ageing at 350°C for 10 min.

(b) Recrystallised grains at a grain boundary, containing the nuclei of the nodular γ_D precipitates in the 41% prior cold worked alloy, aged at 350°C for 10 min.

(c) Cellular structure, containing the γ'_D precipitates in a grain edge region in the 24% prior cold worked alloy, aged at 350°C for 5 min.

Figure 4.16

D.F. micrographs, revealing the γ' precipitates in the matrix after ageing the 10% prior cold worked alloy at 400°C for (a) 10 min. and (b) 20 min. The corresponding SADP's are from the (110) planes, showing SSR.



Figure 4.14 (a) 0.4 μm

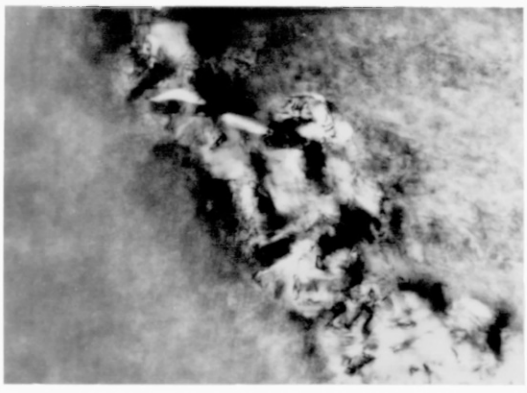


Figure 4.15 (a) 0.4 μm

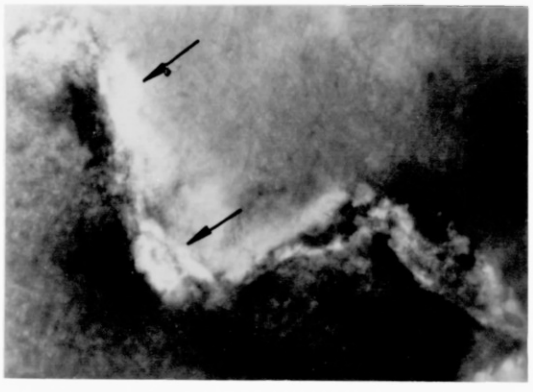


Figure 4.14 (b) 0.4 μm

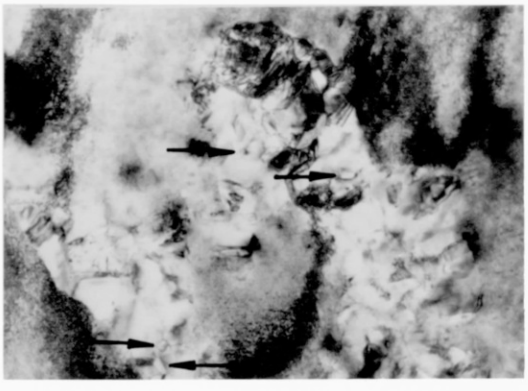


Figure 4.15 (b) 0.4 μm

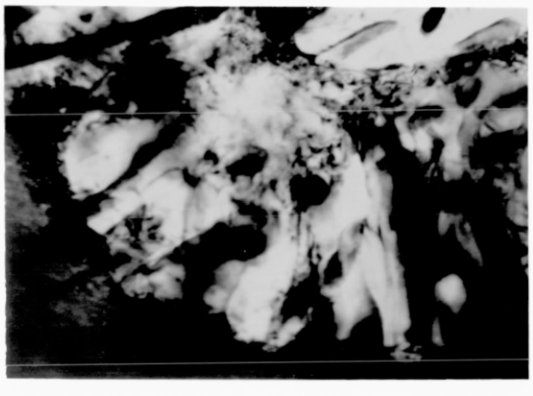


Figure 4.14 (c) 0.4 μm

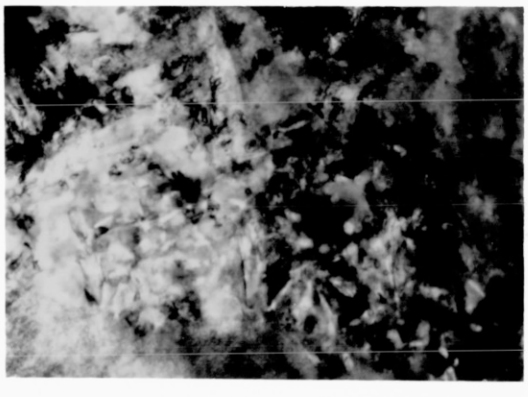


Figure 4.15 (c) 0.4 μm

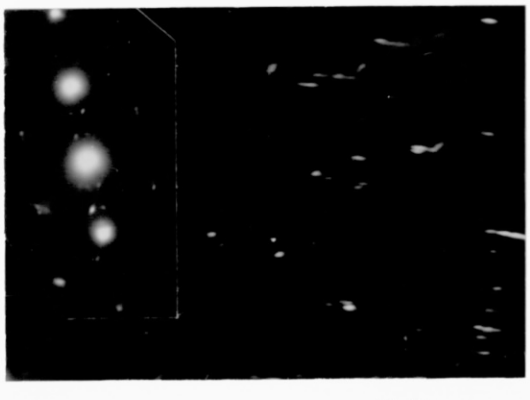
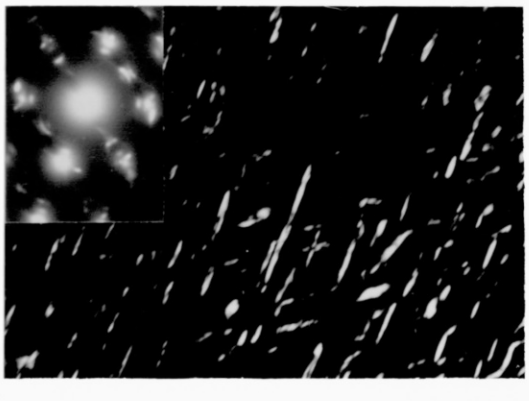


Figure 4.16 (a) 0.2 μm



(b) 0.2 μm

Figure 4.17

(a) B.F. micrograph , showing the γ' precipitates in the matrix of the 32% prior cold worked alloy, aged at 400°C for 10 min.

(b) D.F. micrograph, obtained from one of the SSR in the corresponding SADP, revealing the γ' precipitates in the matrix of the 32 % prior cold worked alloy after ageing at 400°C for 20 min.

Figure 4.18

(a) Strain-free regions at a grain boundary in the 10% prior cold worked alloy, aged at 400°C for 7 min.

(b) The nuclei of the recrystallised grains at a grain boundary in the 32% prior cold worked alloy, aged at 400°C for 10 min.

(c) B.F. micrograph, showing an initial stage of recrystallisation in a grain edge region, inducing γ_D precipitation, in the 41% prior cold worked alloy after ageing at 400°C for 4 min.

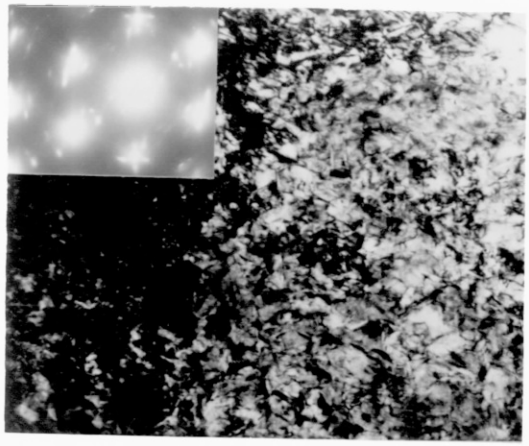
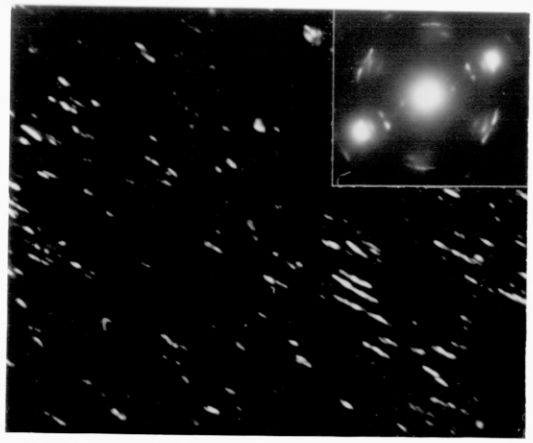


Figure 4.17 (a) 0.2 μm



(b) 0.2 μm



Figure 4.18 (a 0.2 μm



(b) 0.4 μm

(c)



0.4 μm

Figure 4.19

The γ' precipitates in the matrix, formed after ageing the 41% prior cold worked alloy at 500°C for 18 min.; the corresponding SADP from the (110) plane reveals the SSR; the [110] beam direction.

Figure 4.20

Recrystallised grains, containing the nodular γ_D precipitates in grain boundary regions and in the matrix in the 41% prior cold worked alloy, aged at 500°C for 18 min.

Figure 4.21

Another example of the structure in Figure 4.20. Arrows indicate the γ' precipitates, dissolving at the advancing boundaries of recrystallised grains.

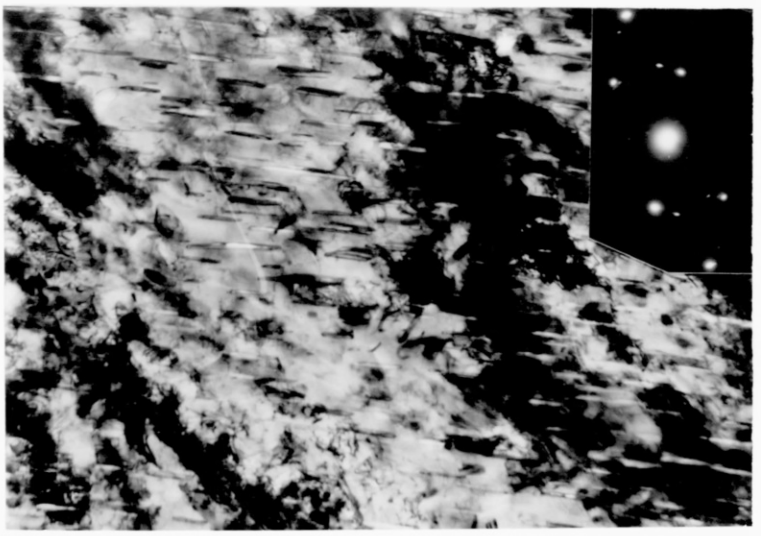


Figure 4.19

0.35 μm

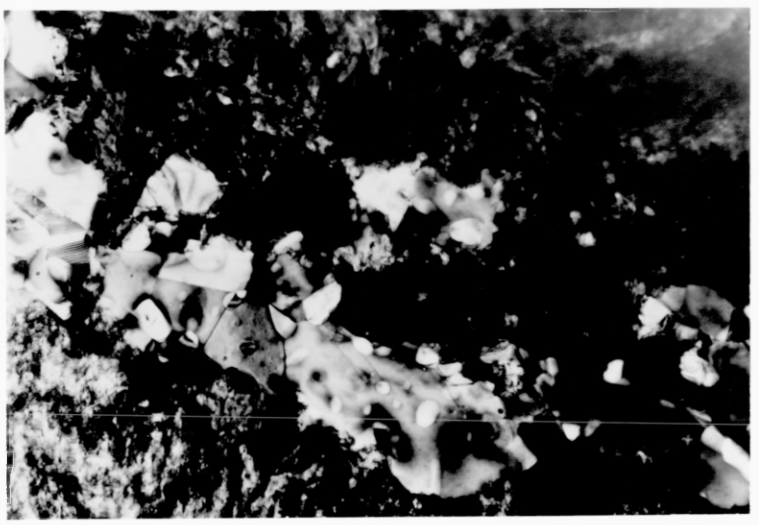


Figure 4.20

1 μm

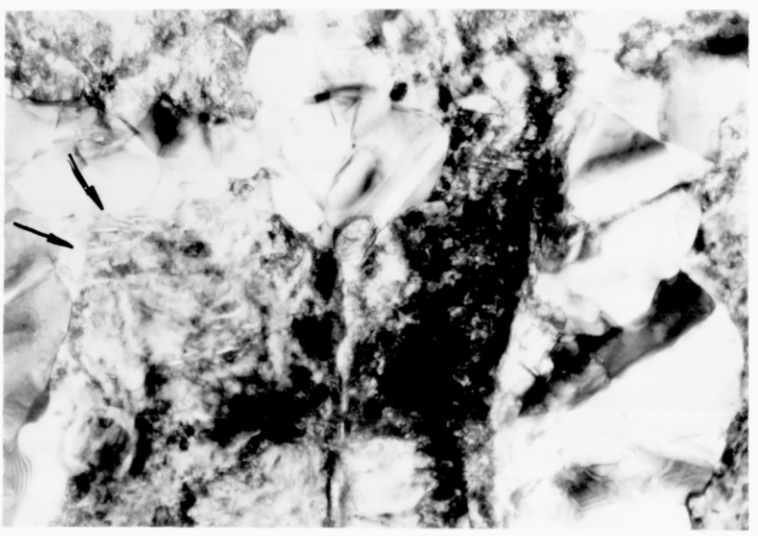


Figure 4.21

0.6 μm

Table 4.1

Precipitation products in alloys UD, D10, D24, D32, and D41, at different temperatures and times. The types of features, observed in the corresponding SADP of the matrix, are indicated in brackets with abbreviations, which are described in section 4.3.2.

Alloy	Prior cold work (%RA)	Ageing temp. (°C)	Ageing time, t, (minutes)				
			2<t<5	5≤t≤10	t≤15	t≤20	t≤30
UD	0	350		γ'_D (SSR)	γ'_D, G.P. (SR)	γ'_D, G.P. (CS), γ' (IM)	γ'_D, G.P. (CS) γ' (ATIM)
		400		γ'_D	γ'_D		γ'_D, γ' (SSR)
D10	10	350		γ'_D, G.P. (CS)	γ'_D, G.P. (CS), γ' (IM)	γ'_D, G.P. (CS) γ' (ATIM)	
		400		γ'_D, γ' (SSR)	γ'_D, γ' (SSR)	γ_D, γ' (SSR)	
D24	24	350	G.P.(CS), γ'D	γ'_D, G.P. (CS) γ' (ATIM)	γ'_D, G.P.(CS) γ' (ATIM)		γ_D, γ' (SSR)
		400		γ'_D, γ' (SSR)		γ_D, γ' (SSR)	
D32	32	350		γ_D, G.P (CS), γ' (ATIM)	γ_D, γ' (SSR)		
		400	γ_D, γ'	γ_D, γ' (SSR)			
D41	41	350		γ_D, G.P. (CS) γ' (ATIM)	γ_D, γ' (SSR)		
		400	γ_D, γ'(SSR)	γ_D, γ' (SSR)			
		500	γ_D + recrystallisation, γ' (SSR)				

grains), after 18 minutes of ageing. It must be noted that the growth of recrystallised grains is restricted by the presence of considerably larger γ' precipitates in the matrix. Therefore, it seems that the growth reaction is restricted by the γ' precipitates in the matrix dissolving at the advancing boundaries of the recrystallised grains, and the growth of the nodular γ_D precipitates occurring at the expense of the γ' precipitates, as indicated by the arrows in Figure 4.21.

4.3 X-ray Diffraction Data Analysis

4.3.1 Evolution of X-ray diffraction peaks during ageing

The X-ray diffraction line profiles, obtained from the unaged alloys, UD, D32, and D41, are compared in Figure 4.22-a, b, and c. Increasing prior cold work introduced a broadening effect on all diffraction peaks, some of which are shown in Figure 4.22. In particular, the (200) profile was broadened enormously and the height of this peak for the 41% cold worked alloy was only 1/10 of that for the solution treated alloy. The (220) and the other large angle diffraction profiles of the solution treated alloy are resolved into the $Cu_{K\alpha 1}$ and $Cu_{K\alpha 2}$ profiles (Figure 4.22-a), but, in the cold worked condition (10 to 41% RA), the $Cu_{K\alpha 2}$ profiles could not be resolved due to the large amount of broadening (Figure 4.22-b and c). According to the peak position of these lines, a lattice parameter of 0.3575 ±0.0002 nm was calculated for as-received alloys, irrespective of prior cold work.

During ageing the solution treated alloy at 350°C, the diffraction lines undergo an asymmetrical broadening with the formation of a shoulder on the small angle scattering side, which later develops into a second peak. This phenomenon is shown for the (111) diffraction line in Figure 4.23-a to e. In the present work, the sharp profiles of the initial (unaged) reflection and the second peak, represented schematically by discontinuous lines, are designated as I_0 and I_1, respectively. On ageing at higher

temperatures, i.e. 380 and 400°C, shoulders form in a shorter time, which is followed by the development of the second peak, I_1, as shown in Figure 4.23-a and b. On further ageing, the height of I_1 peaks increases while that of I_0 peaks of the initial reflection reduces.

It must be noted that, during the evolution of the diffraction lines as described above, both I_0 and I_1 profiles shift towards lower angles. The shifting of I_1 profiles is a continuous process, which starts with the formation of a shoulder, and then the intensity maximum of the I_1 peak gradually approaches the 2θ angle, which corresponds to the lattice parameter of copper (0.361 nm), e.g. the calculated lattice parameters from the I_1 peak positions on ageing at 350°C are 0.3586 nm after 10 minutes 0.3600 nm after 20 minutes, and 0.3603 nm after 40 minutes. But, the I_0 profiles also start shifting towards lower angles after a certain ageing period, e.g. 30 minutes at 350°C, 26 minutes at 380 °C, and 12 minutes at 400°C. When the ageing reaches a certain stage, e.g. 20 minutes at 400°C (see Figure 4.23-e) and longer times at lower ageing temperatures, the I_0 and I_1 profiles completely overlap, suggesting that the lattice parameter, corresponding to the intensity maxima of the I_0 peak is close to 0.3603 nm, i.e. the lattice parameter corresponding to the final position of the I_1 peak. The detailed data on the change in lattice parameter of the matrix, determined from I_0 and I_1 peaks, with ageing time will be presented in the following section.

During the ageing of prior cold worked alloys, the evolution of diffraction lines went through a similar sequence as described above for solution treated alloys. However, because of the line broadening associated with the prior cold work, the development of the characteristic features on diffraction line profiles were masked to an extent that I_1 peaks could not be resolved clearly. As can be seen on the (111) lines for 32% cold worked alloys at 350°C in Figure 4.24-a to d, the development of the I_1 profile can only be followed by the formation of the shoulder, which commences after 2.5 minutes of ageing. The

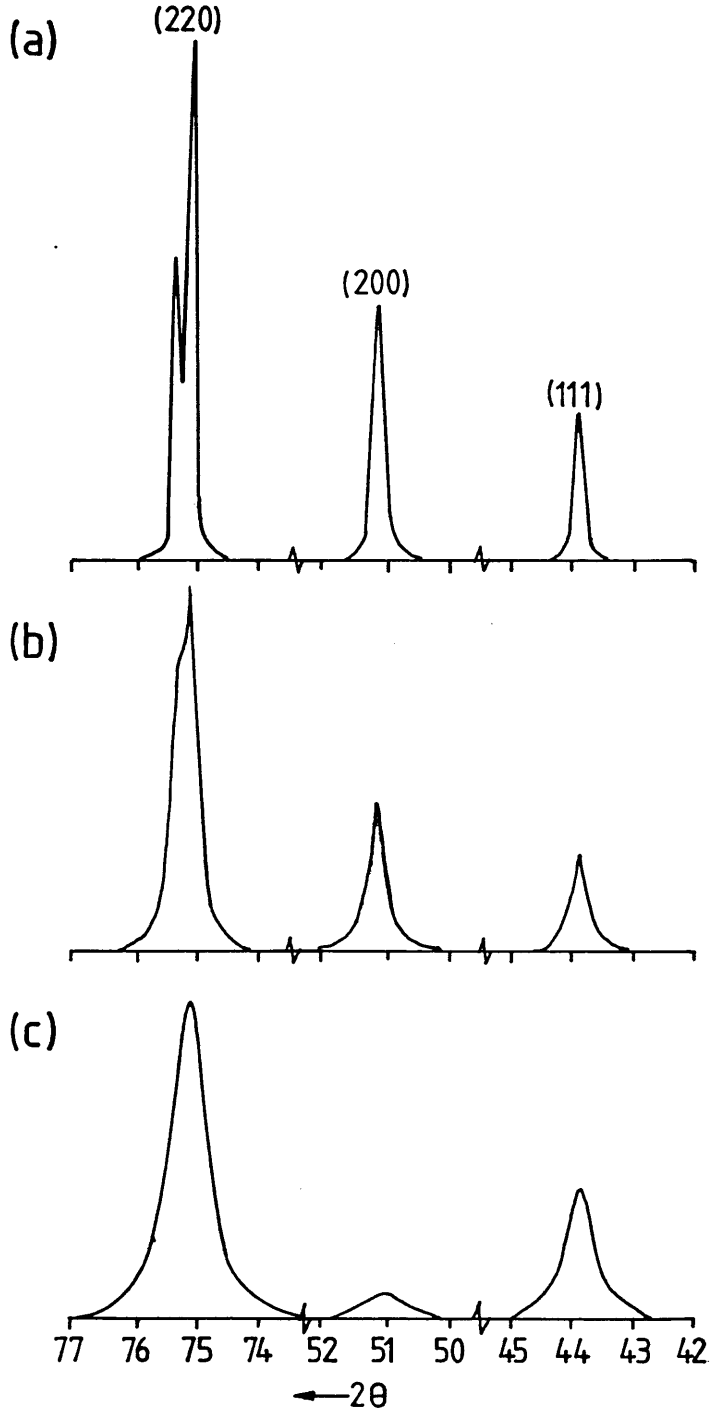


Figure 4.22- Variation in the profiles of (220), (200), and (111) diffraction lines of the α-matrix with increasing degree of prior cold work in the range 0 to 41% RA. (a) alloy UD, (b) alloy D32, and (c) alloy D41.

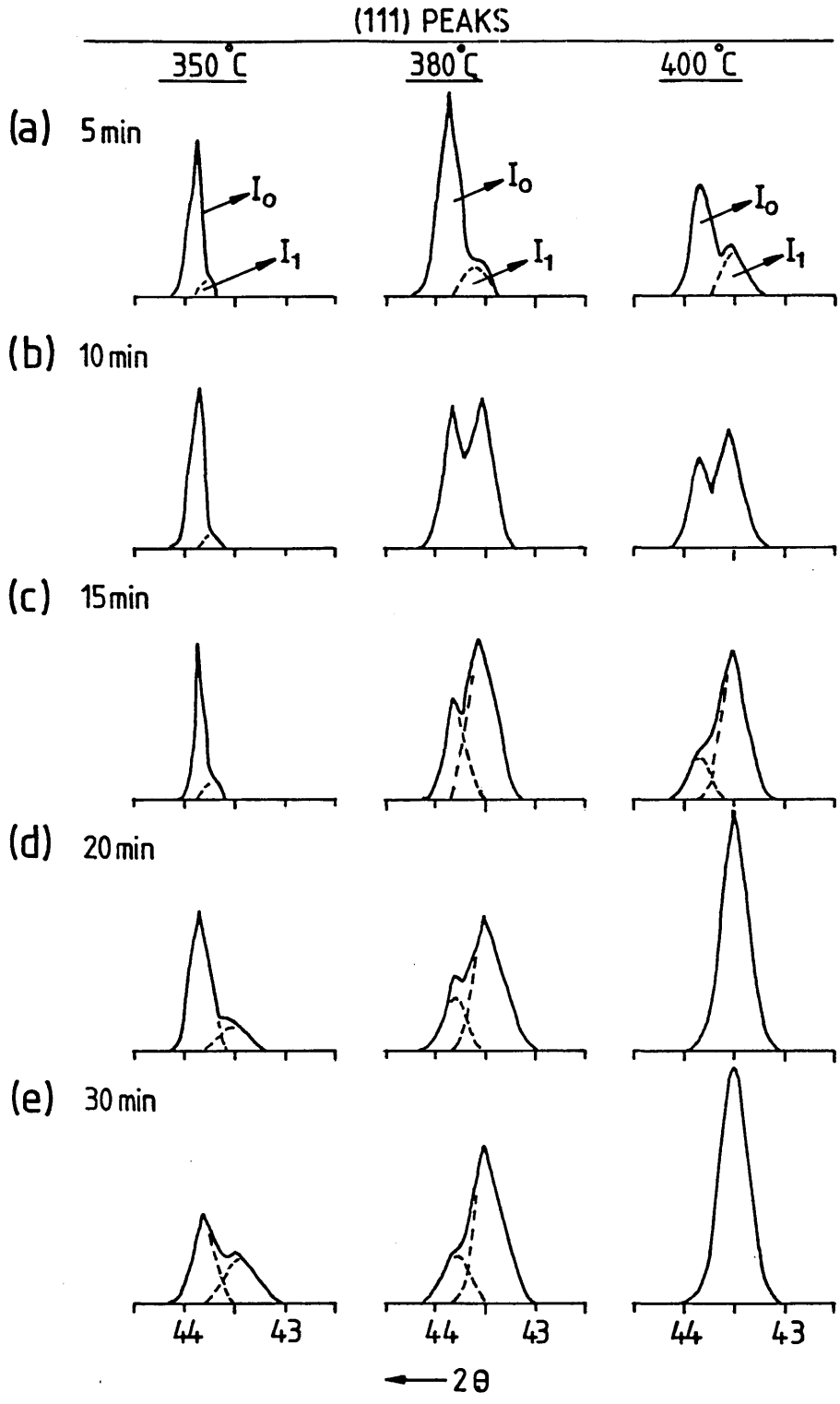


Figure 4.23- The development of I_1 profiles on (111) diffraction lines of the solution treated alloy, during ageing at 350, 380, and 400°C for times (a) 5 min. (b) 10 min. (c) 15 min. (d) 20 min. and (e) 30 min.

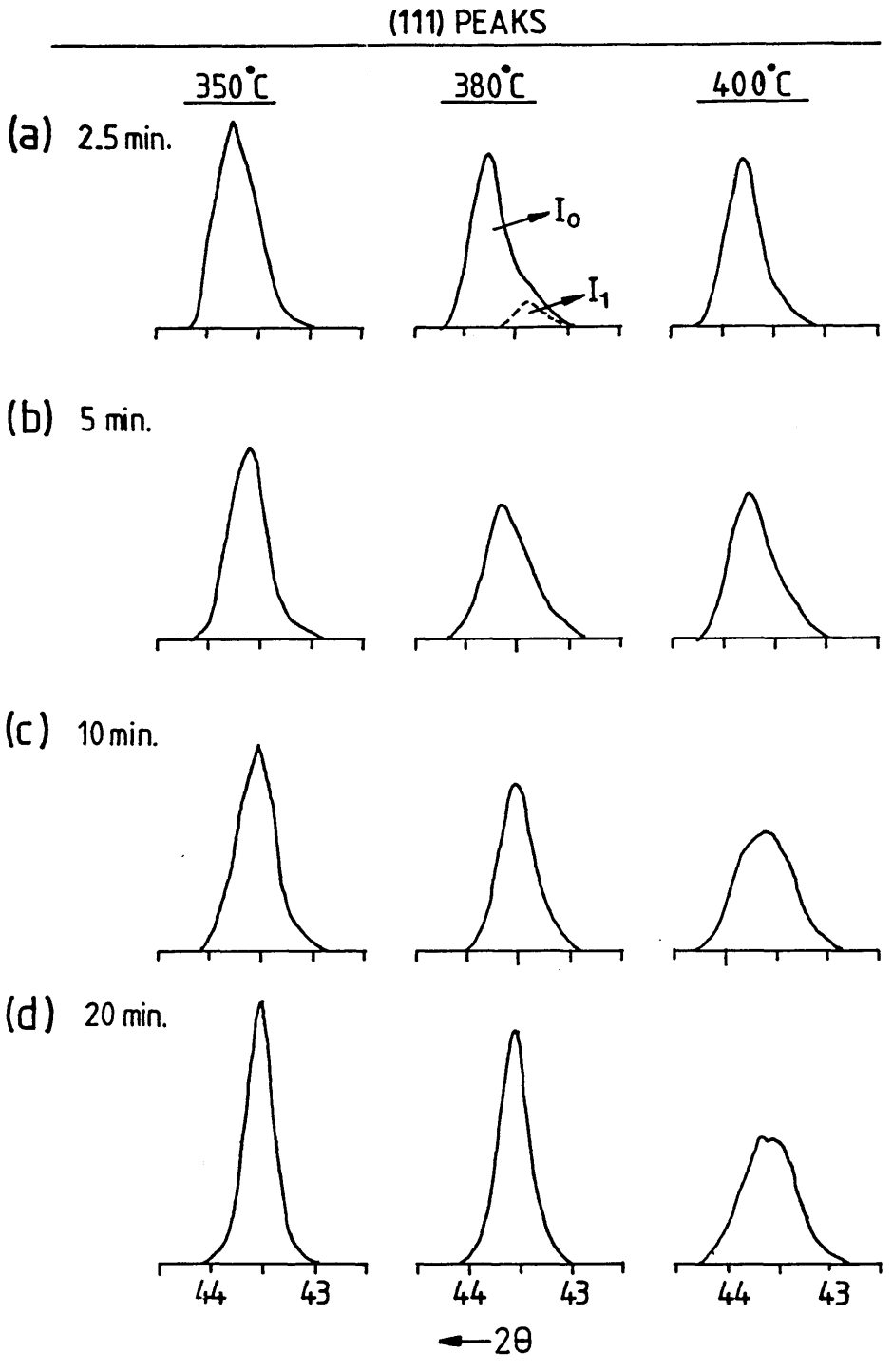


Figure 4.24- The evolution of the (111) diffraction lines of the 32% prior cold worked alloy during ageing at 350, 380, and 400°C for times (a) 2.5 min. (b) 5 min. (c) 10 min. and (d) 20 min.

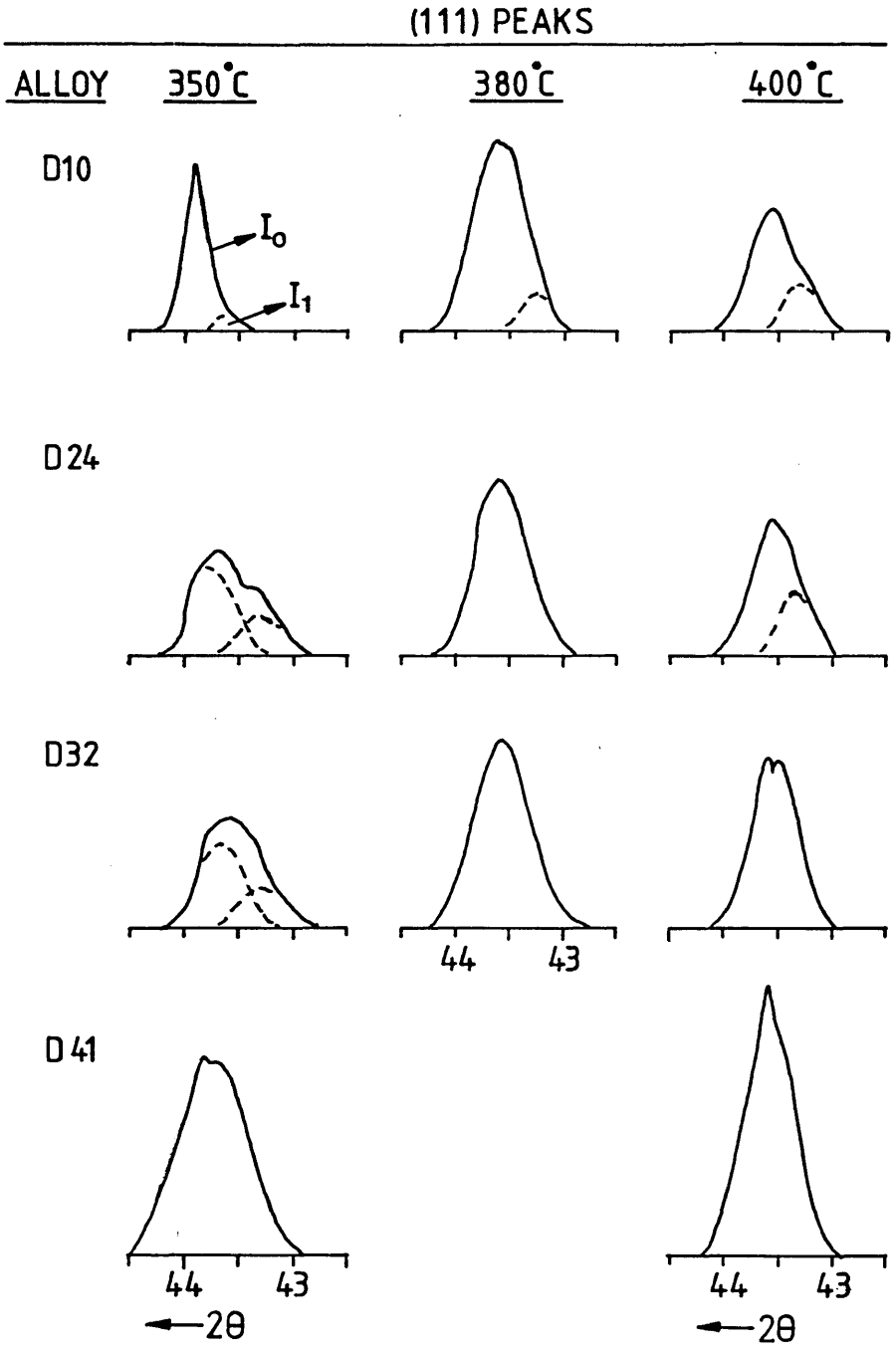


Figure 4.25- The (111) diffraction lines, obtained after ageing alloys (a) D10, (b) D24, (c) D32, and (d) D41 at 350, 380, and 400°C.

height of the shoulder increases with ageing temperature and time, causing an increase in broadening, but it is not possible to determine the peak position of the I_1 profiles. At later stages of ageing, e.g. 20 minutes at 350°C and 10 minutes at 380 and 400°C, the I_0 peak starts to move towards lower angles. This results in the sharpening of the diffraction lines and an increase in the height of the peaks, as the I_0 and I_1 profiles gradually come into a completely overlapping position.

The effects of the prior cold work and the ageing temperature on the development of the I_0 and I_1 profiles are demonstrated by a series of (111) profiles obtained after 10 minutes ageing of the alloys, D10, D24, D32, and D41 in Figure 4.25-a, b, c, and d, respectively. As can be seen, increasing prior cold work and ageing temperature resulted in an acceleration in the development of I_1 profiles and the shifting of I_0 and I_1 peaks towards lower angles.

4.3.2 Change in lattice parameter of the α-matrix

As described in the previous section, the movement of both I_0 and I_1 profiles on the diffraction pattern to lower angles corresponds to an increase in the lattice parameter of two types of matrix regions, and in the present work these are designated as a_0 of the α_0-matrix and a_1 of the α_1-matrix, respectively.

The change in a_0 values of the α_0-matrix during ageing of alloys UD, D10, D24, D32, and D41 at 350, 380, and 400°C is presented in Figure 4.26-a, b, and c, respec--tively. The a_0 values for each specimen start to increase after a certain time of ageing and then on continuing the ageing the rate of increase reduces gradually. It must be noted that, on ageing at 350 and 380°C, there is a slight increase in a_0 preceding the large increase, but the amount of increase is very small, as marked in Figure 4.26-a & b.

A comparison of the lattice parameter plots in Figure 4.26-a, b, and c clearly indicates that raising the ageing temperature from 350 to 400°C increases the maximum

rate of change in a_0 for all alloys, and shifts the onset of this process (marked with arrows on the plots) towards shorter ageing times. Prior cold work up to 41% RA is also effective in shifting the onset of the increase in a_0 towards shorter ageing times at 380 and 400°C (see the a rrows in Figure 4.26-b, and c). However, on ageing at 350 °C, although a degree of prior cold work of less than 24% RA is effective in the same manner as described for the higher ageing temperatures (Figure 4.26-a), for greater amounts of cold work, there is little change in the time of onset of the increase in a_0 or of the rate of change of the increase.

The change in the a_1 values of the α_1-matrix was followed by the development of the I_1 profiles on the I_0 diffraction lines of the initial reflections when it was possible to determine the intensity maxima of the I_1 profiles. The results for solution treated alloys, given in Figure 4.27, indicate that an increase in temperature reduces the time for the onset of the increase in a_1, and slightly increases the maximum rate of change in a_1 values. Also the maximum rate of change of a_1 for the α_1-matrix was found to be higher than that of a_0 of the α_0-matrix. Unfortunately, for the prior cold worked alloys, it was not possible to detect the I_1 intensity maxima for all ageing conditions because of the enormous broadening of the diffraction profiles due to prior cold work, and hence a complete set of experimental data on the lattice parameter change of the α_1-matrix in prior cold worked alloys could not be produced. Nevertheless, additional information concerning the change in the peak position of both I_0 and I_1 profiles for prior cold worked alloys, was obtained from the half-breadth measurements of the broadened diffraction profiles, and the results will be presented in the following section.

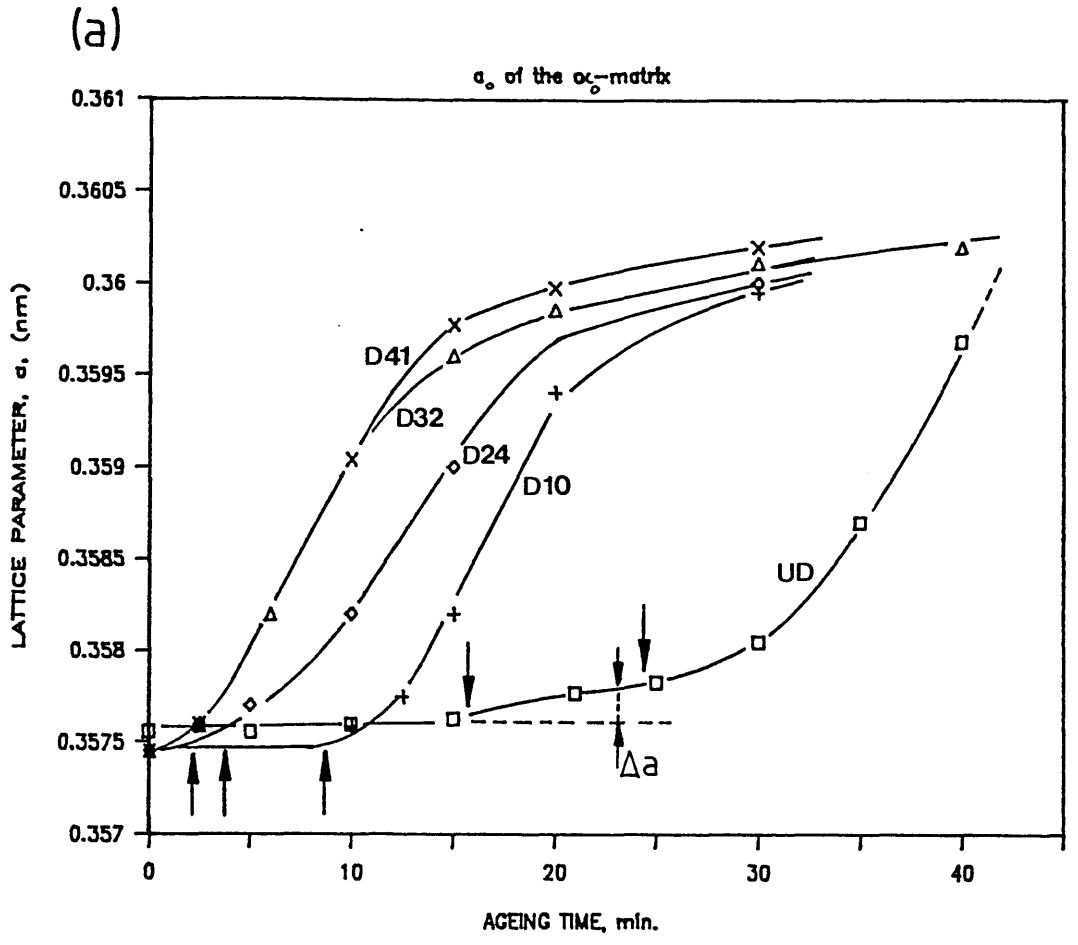
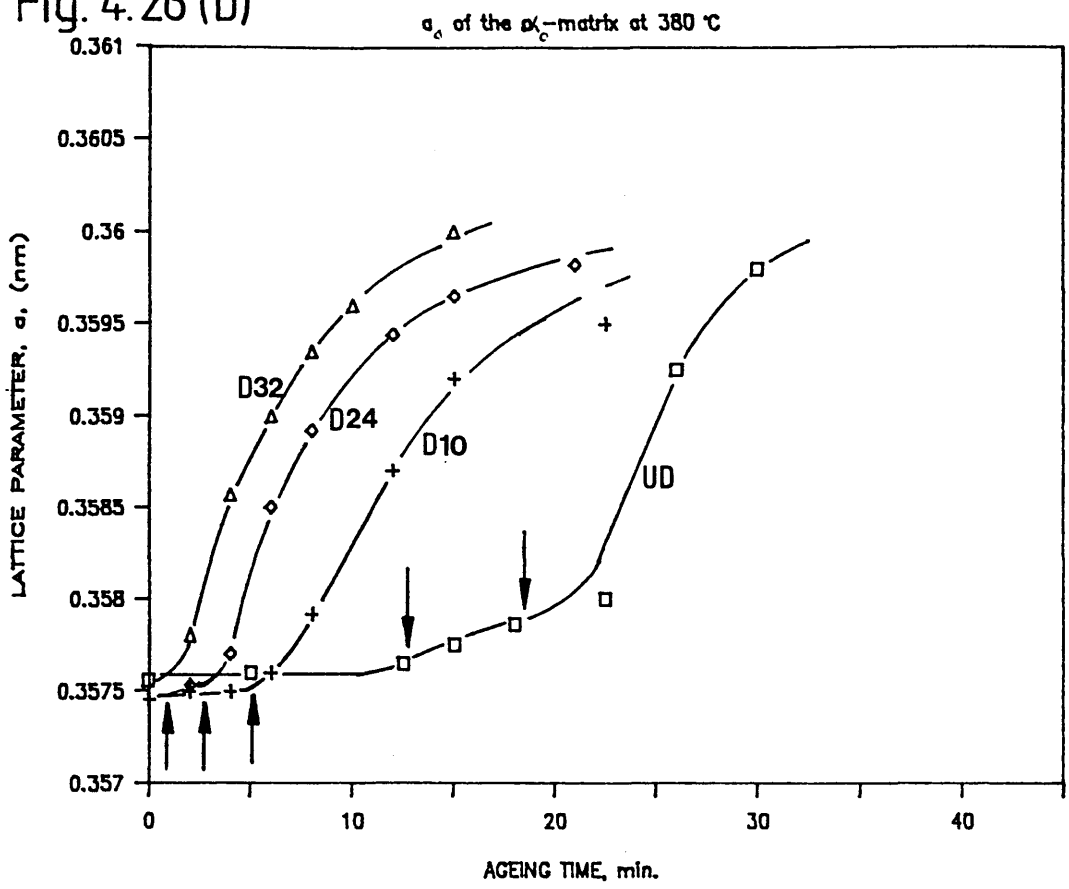
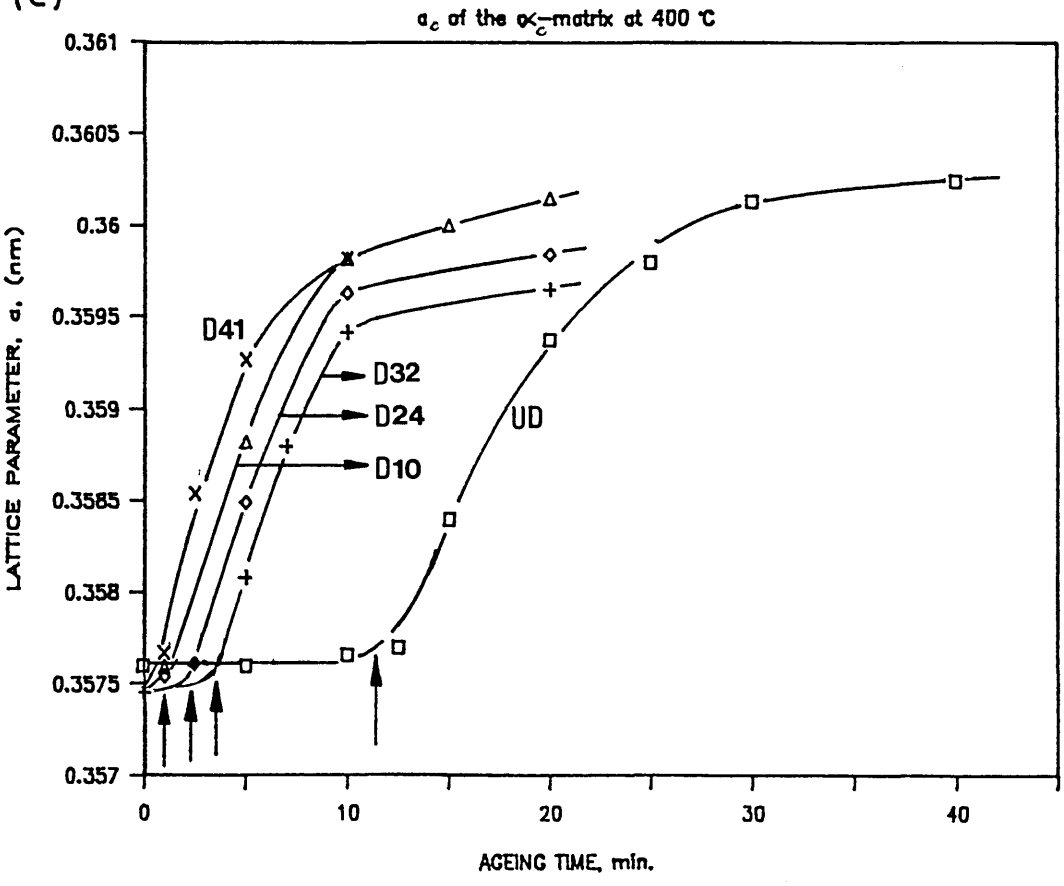


Figure 4.26- Change in the lattice parameter of the α_0-matrix during ageing alloys UD, D10, D24, D32, and D41, at:
(a) 350°C
(b) 380°C
(c) 400°C

Fig. 4.26 (b)


a_c of the α'_c-matrix at 380 °C
LATTICE PARAMETER, a, (nm)
0.361
0.3605
0.36
0.3595
0.359
0.3585
0.358
0.3575
0.357
0
10
20
30
40
AGEING TIME, min.
D32
D24
D10
UD

(c)


a_c of the α'_c-matrix at 400 °C
LATTICE PARAMETER, a, (nm)
0.361
0.3605
0.36
0.3595
0.359
0.3585
0.358
0.3575
0.357
0
10
20
30
40
AGEING TIME, min.
D41
D32
D24
D10
UD

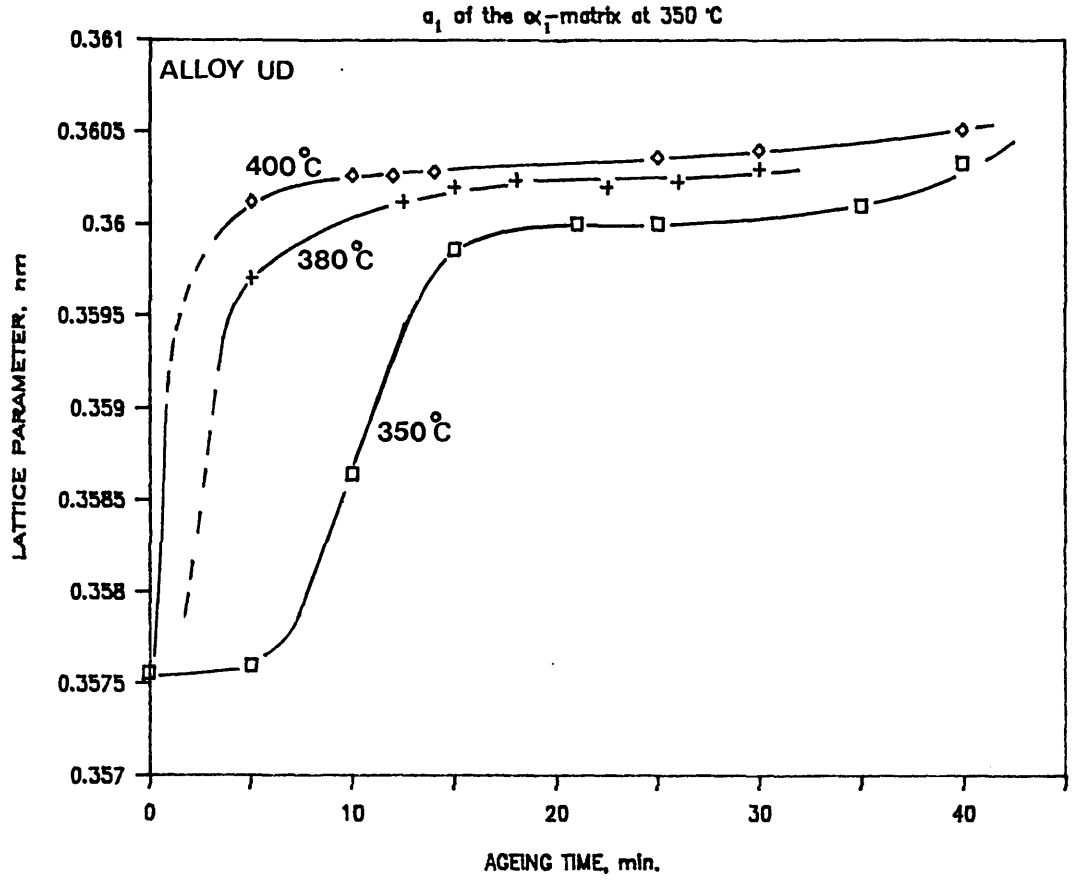


Figure 4.27- Change in the lattice parameter of the α_1-matrix on ageing alloy UD at 350, 380, and 400°C.

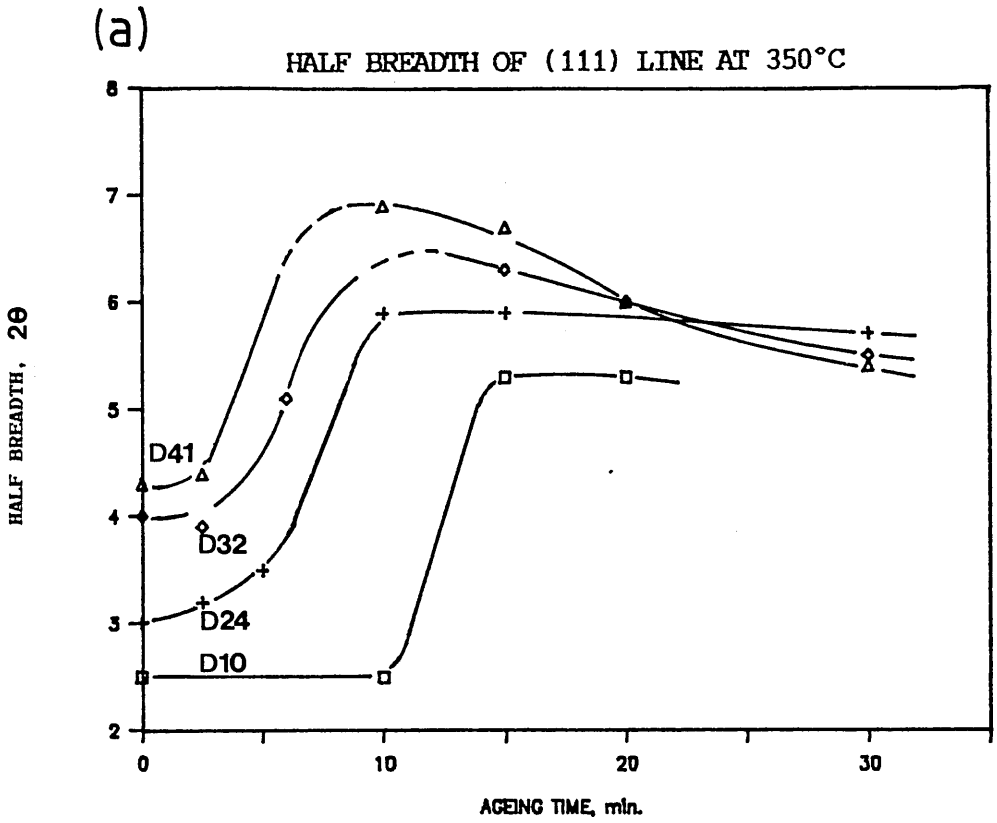
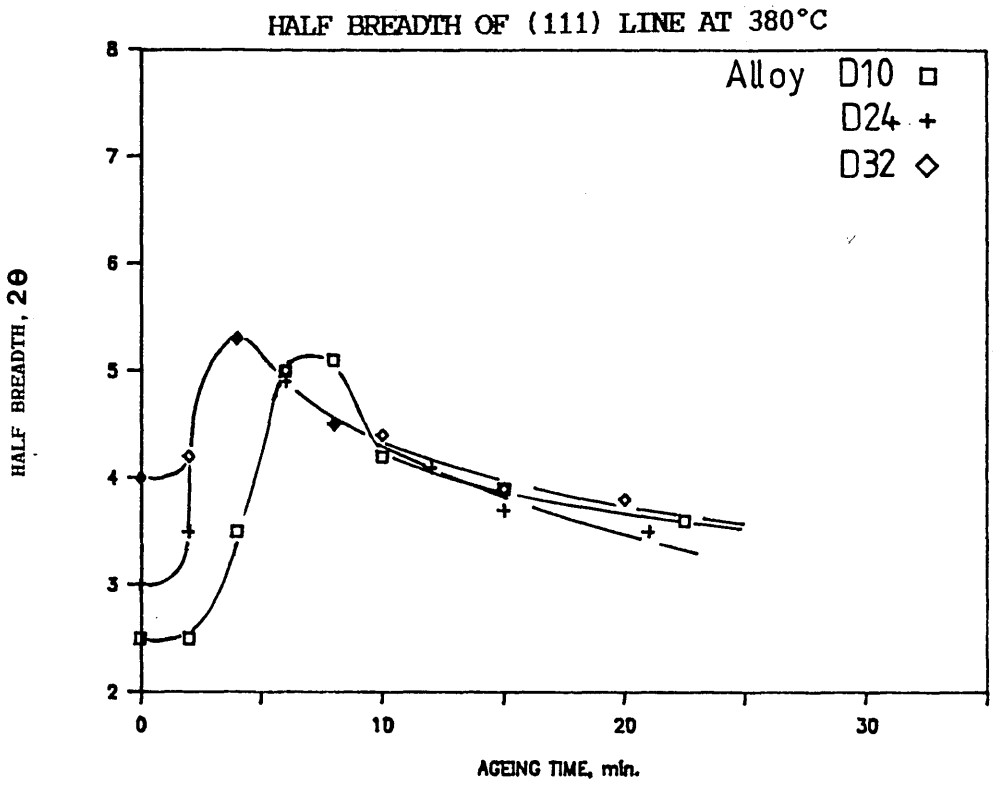
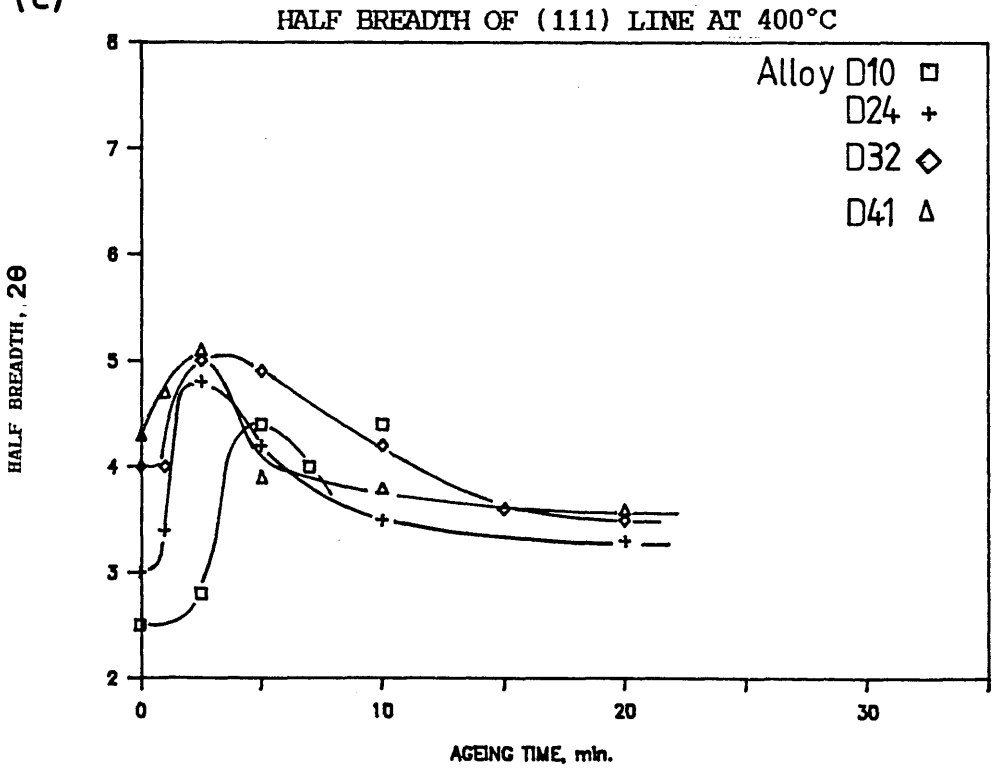


Figure 4.28- Change in the half-breadth of the (111) peaks during ageing alloys D10, D24, D32, and D41, at temperatures:
(a) 350°C
(b) 380°C
(c) 400°C

Fig. 4.28 (b)


HALF BREADTH OF (111) LINE AT 380°C
Alloy D10 □
D24 +
D32 ◇
HALF BREADTH, 2θ
AGEING TIME, min.
0
10
20
30
2
3
4
5
6
7
8

(c)


HALF BREADTH OF (111) LINE AT 400°C
Alloy D10 □
D24 +
D32 ◇
D41 Δ
HALF BREADTH, 2θ
AGEING TIME, min.
0
10
20
30
2
3
4
5
6
7
8

4.3.3 Half-breadth measurements for cold worked alloys

The change in the half-breadth of the (111) lines during ageing of the prior cold worked alloys at 350, 380, and 400°C is presented in Figure 4.28-a, b, and c respec--tively. On each plot, the onset of the increase and the decrease in half breadth is indicated with arrows.

As shown in Figure 4.24, the broadened diffraction lines of prior cold worked alloys consist of overlapping I_0 and I_1 profiles. The shifting of I_1 profiles towards lower angles precedes that of I_0 profiles; the first causes the broadening of the peaks and the latter the sharpening of them. Therefore, an increase in the half breadth of the peaks refers to the increase in the lattice parameter of the α_1-matrix, and a decrease in the half breadth corresponds to an increase in the lattice parameter of the α_0-matrix. In this respect, it is evident from the data (Figure 4.28) that the greater the amount of prior cold work and the higher the ageing temperature, the shorter the the time for the onset of the increase in half breadth, which corresponds to onset of the increase in a_1. Indeed, the half breadth plots for 32 and 41% prior cold worked alloys, aged at 400°C in Figure 4.28-c suggest that the increase in the lattice parameter of the α_1-matrix at 400°C starts in the first minute of ageing, which can be compared with 3 minutes at 350°C.

4.4 Non-Isothermal Differential Thermal Analysis

Typical exothermic DTA peaks, recorded during the the DTA tests of solution treated samples, at different heating rates, α, are shown in Figure 4.29. Each DTA run was immediately repeated with the same specimen; the repeat runs showed no evidence of any peaks, associated with any further reaction, and therefore they were used as base lines, which are plotted as broken lines (-·-) in Figure 4.29. The peaks at low heating rates, e.g. $\alpha<10$°C/min., were much lower and flatter than those at high heating rates. The shape of the low heating rate peaks was

attributed to the presence of two types of overlapping heat liberation, which are schematically shown as peak A and peak B in Figure 4.29. Over the heating rate range of 3 to 15°C/min. inclusive, the peak B became larger in size whereas the peak A remained approximately the same. At the higher heating rates, the peak B completely dominated the DTA plots. There was some evidence of a peak at lower temperatures, which will be shown later to be due to a different precipitate process to that responsible for peak A and is therefore designated as peak C.

In order to assess the reliability of the non-isothermal DTA data, presented above, DSC runs at heating rates (α), 5, 10, 15, 20, and 30°C/min. were carried out under identical conditions with these of the previous DTA runs. The DSC results were in complete agreement with those from the DTA runs in every detail, namely the position and the shape of peaks A, B, and C at different heating rates.

The TEM analysis of the DTA samples (solution treated), which were tested at α=20°C/min. and removed from the DTA furnace at the temperatures marked by the arrows, TEM I and TEM II, on the plot of Figure 4.29, provided evidence for the precipitation reactions associated with the DTA peak. The micrographs of the matrix and the grain boundary regions in Figure 4.30 indicate that the heat liberated at the lower temperature, i.e. peak C, was due to the formation of the plate-like γ'_D precipitates at grain boundaries (Figure 4.30-a); at this stage no precipitation had occurred in the matrix (see the SADP in Figure 4.30-b). The heat liberation at peak B was produced by a large amount of cellular growth into the α-matrix; this took place by the repeated nucleation and growth of the γ'_D precipitates at the migrating interface into the matrix, as indicated by arrows in Figure 4.30-c. In Section 4.2.2, it has been clarified that at temperatures below 400°C the γ' phase precipitated in the matrix before any cellular reaction. Thus, lowering the heating rate below 15°C/min. allowed the formation of the γ' precipitates in the matrix at the lower temperatures and this resulted in peak A.

The heating rate dependence of the onset of peak C (T_0) and the maximum of peak B (T_P) was determined by plotting the values of of T_0 and T_P values against heating rate, α, as given in Figure 4.31. It is evident from the fitted curves on data points of peak C (+) and peak B (□) in Figure 4.31 that the heating rate dependancy of peak B is greater than that of peak C.

Typical DTA curves for 5% prior cold worked alloys are given in Figure 4.32. A comparison of Figures 4.29 and 4.32 demonstrates that 5% prior cold work did not significantly change the shape or size of the DTA peaks. However, for greater degrees of prior cold work, the DTA plots differ from those from UD and D5 alloys. The TEM investigation (section 4.2.3) has shown that prior cold work inhibits the discontinuous γ'_D precipitation and enhances the γ' precipitation in the matrix. Thus, on the DTA plots for heavily deformed alloys (Figures 4.33 and 4.34), peak A, which is associated with the γ' phase, grows at the expense of peaks B and C. This interpretation was confirmed by an electron microscopy investigation of 32% prior cold worked DTA samples, which will be briefly summarised.

In order to assess the possible occurrence of any additional precipitation, responsible for the growth of peak A, a TEM investigation was carried out on 32% prior cold worked DTA samples, which were heated in the DTA furnace at α=20°C/min. to the temperatures, marked by the arrows, TEM I and TEM II on the DTA curve in Figure 4.34, and removed from the furnace immediately. The DF micrograph in Figure 4.35-a shows that, at the peak position TEM I, nuclei of the γ' precipitates had already formed in the matrix while the grain boundaries indicated only the development of dislocation-free regions as a result of grain boundary movements (Figure 4.35-b). The presence of the ATIM in Figure 4.35-a suggests that the γ' precipitates are nucleated by G.P. zones since the ATIM cannot form without the development of CS and IM (for detail, see section 4.2.2). At the peak position TEM II, the SADP (Figure 4.36-a) exhibited the SSR that is indicative of the

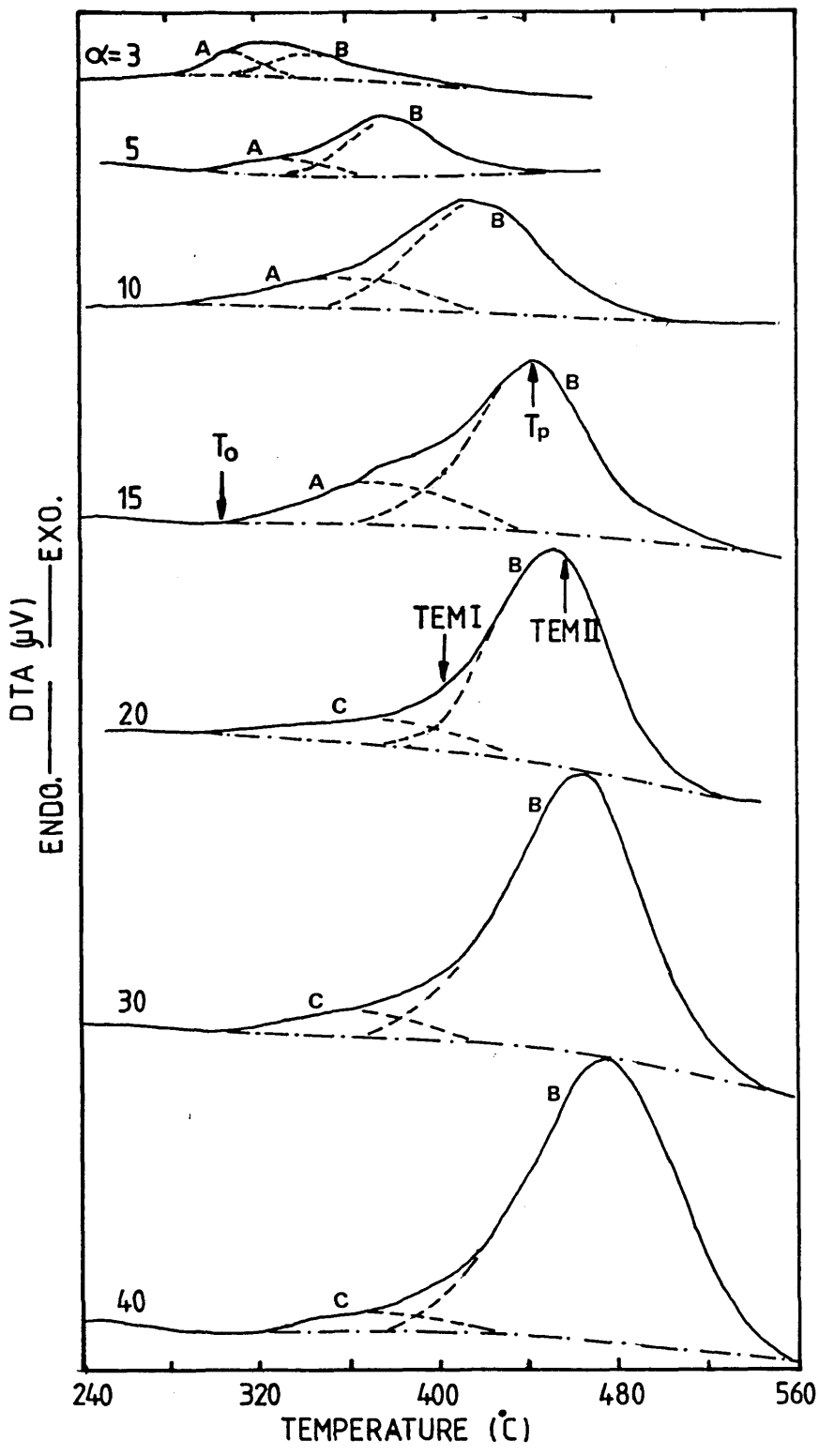


Figure 4.29- The non-isothermal DTA peaks of the solution treated alloy. α indicates the heating rate in the range 3 to 40°C/min.

Figure 4.30

(a) γ'_D precipitation at grain boundaries in the non-isothermal DTA specimen of the solution treated alloy, heated up to the position TEM I on the DTA curve, obtained at α=20°C/min. (see Figure 4.29).

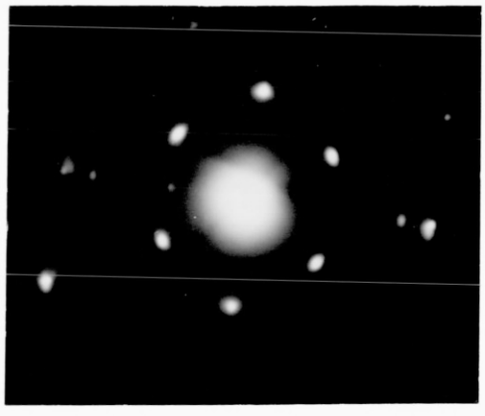
(b) The SADP from the matrix of (a), showing the absence of precipitates.

(c) Cellular growth, inducing the repeated nucleation and growth of the γ'_D precipitates in a grain (see arrows for the direction of the growth) in the non-isothermal DTA specimen of the solution treated alloy, heated up to the position TEM II of the DTA run at α=20°C/min. (see Figure 4.29).



0.2 μm

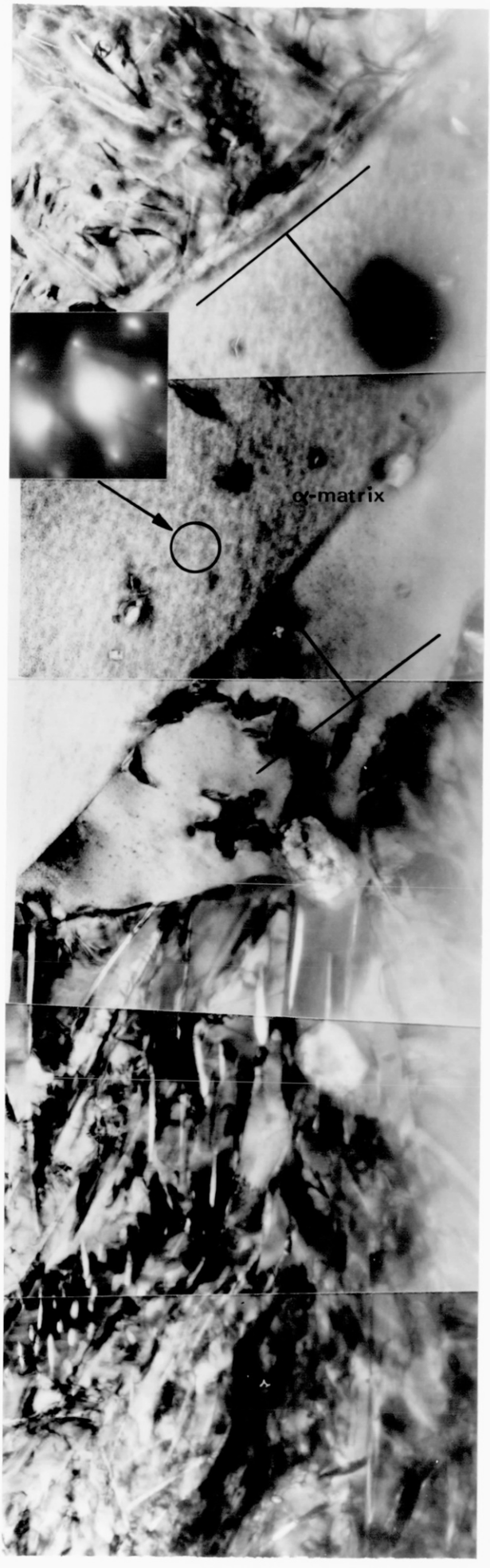
Figure 4.30 (a)



1x1.4

(b)

(c)



0.4 μm

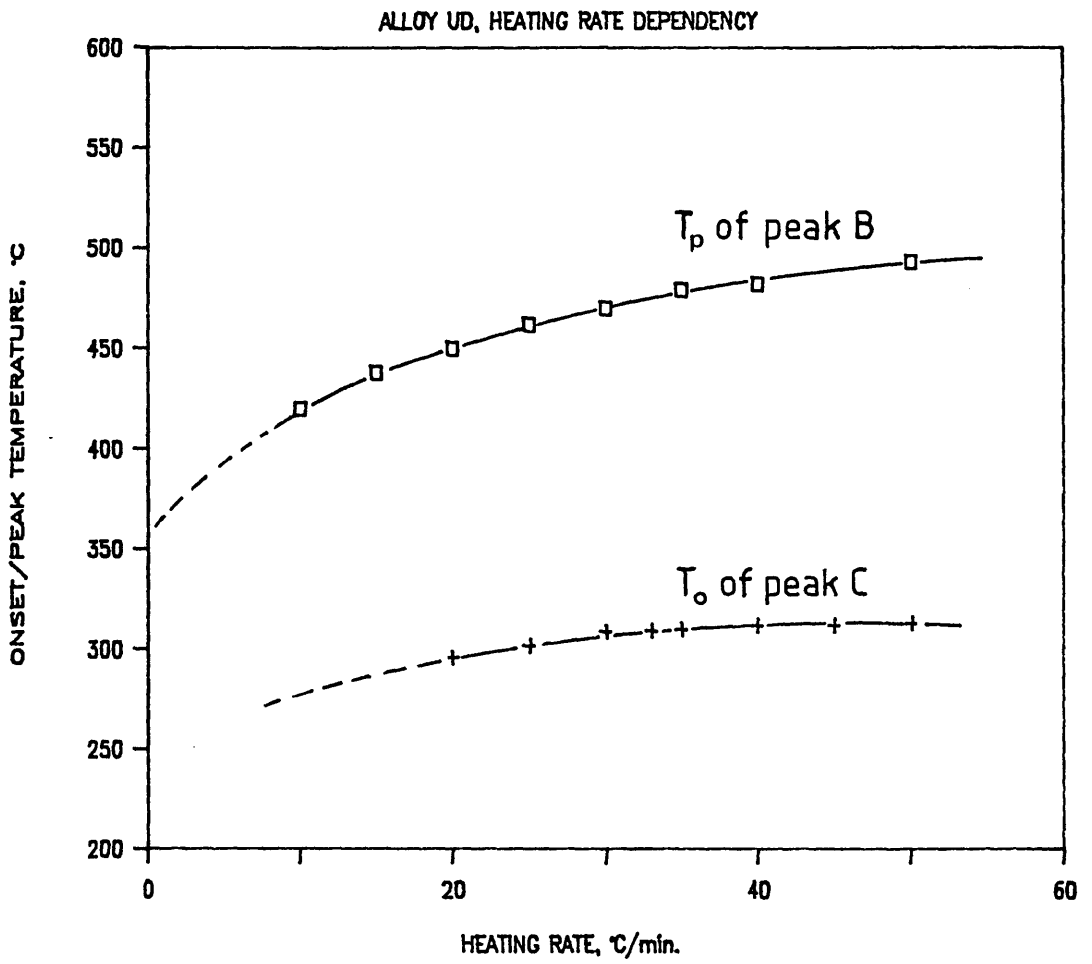


Figure 4.31- The change in T_P of peak B and T_0 of peak C with heating rate, α, on the non-isothermal DTA runs of alloy UD.

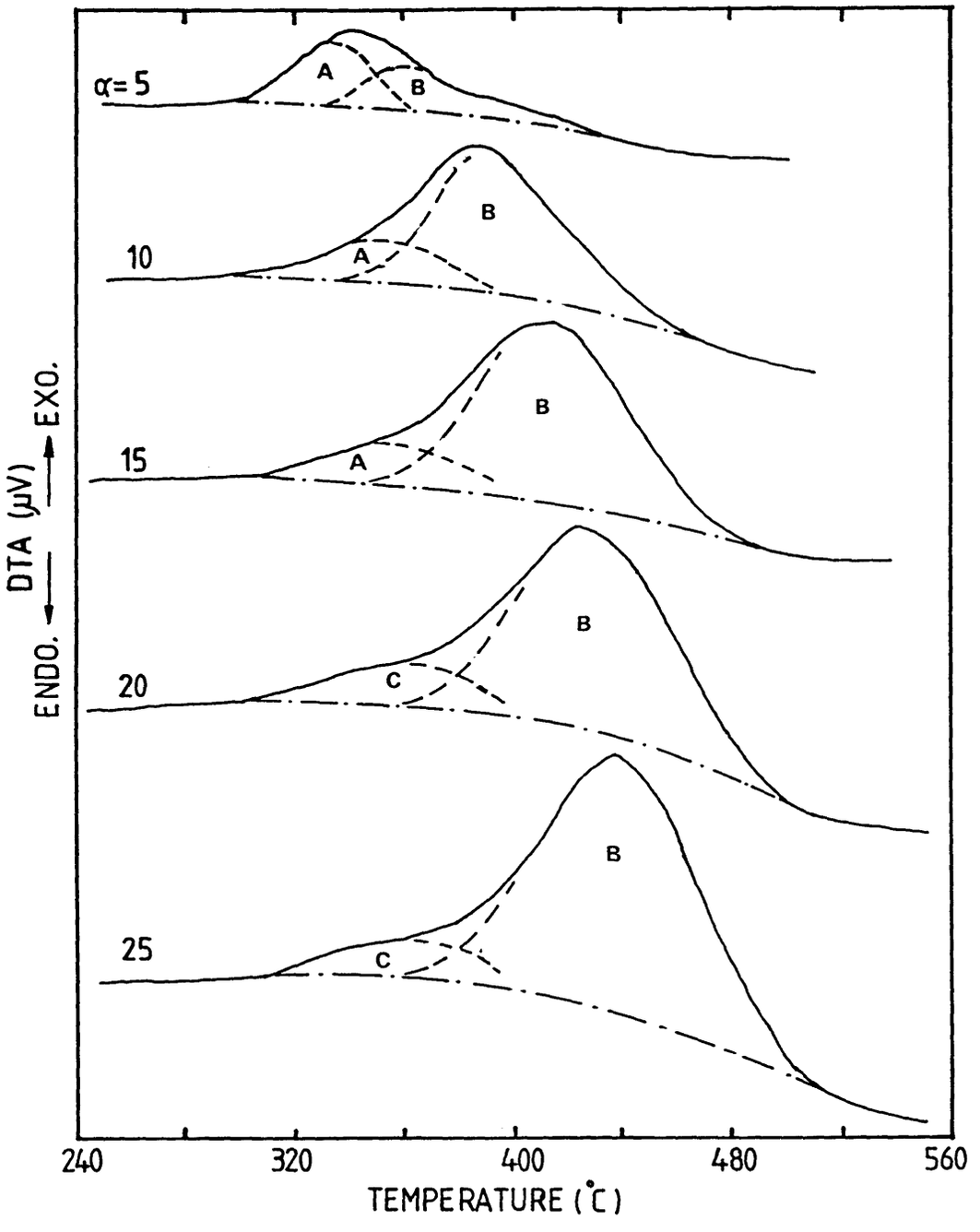


Figure 4.32- The non-isothermal DTA peaks of the 5% prior cold worked alloy. α indicates the heating rate in the range 5 to 25°C/min.

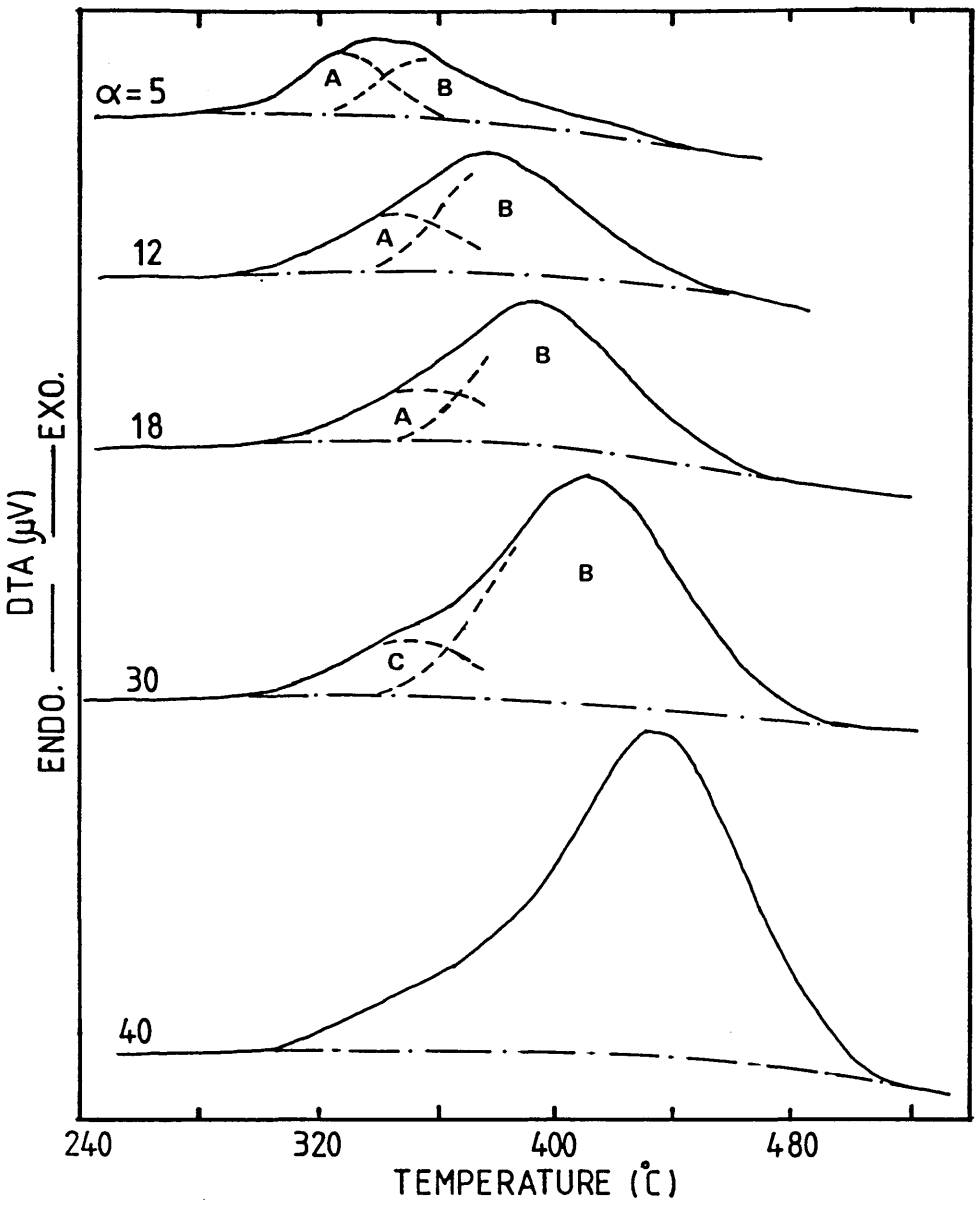


Figure 4.33- The non-isothermal DTA peaks of the 10% prior cold worked alloy. α indicates the heating rate in the range 5 to 40°C/min.

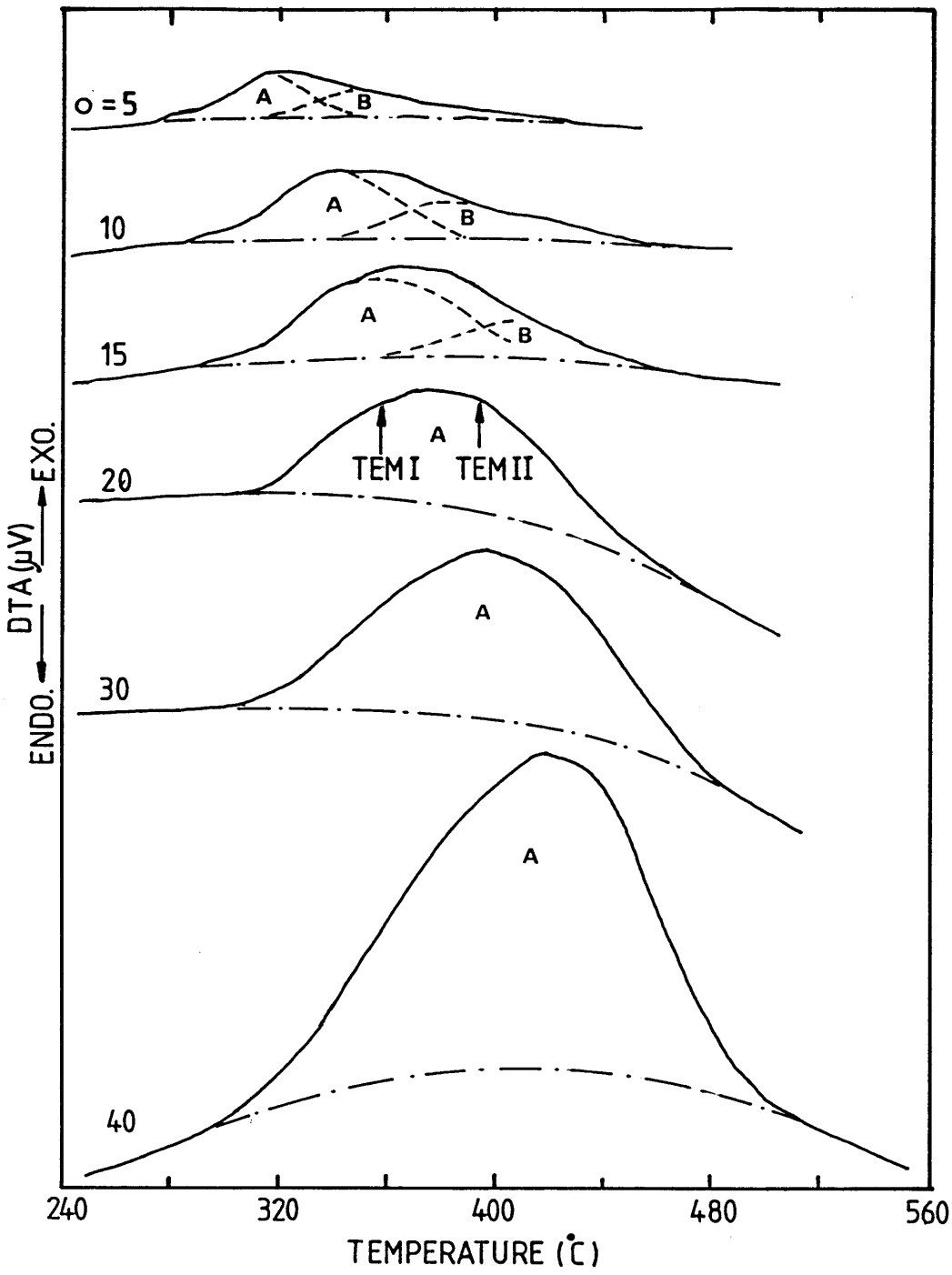


Figure 4.34- The non-isothermal DTA peaks of the 32% prior cold worked alloy. α indicates the heating rate in the range 5 to 40°C/min.

Figure 4.35

(a) The nuclei of the γ' precipitates in the matrix visible in the D.F. micrograph , obtained from the ATIM in the corresponding SADP from the (110) planes, in the non- isothermal DTA specimen of the 32% prior cold worked alloy, heated at α=20°C/min. up to the peak position I, as shown in Figure 4.34.

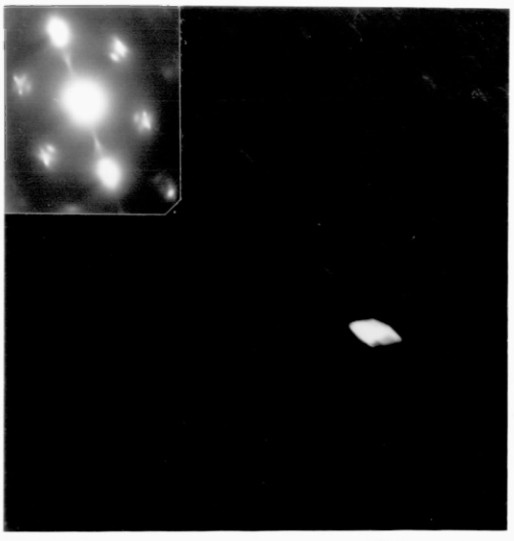
(b) The strain-free regions at a grain boundary in the specimen of (a).

Figure 4.36

(a) The dark field micrograph, obtained from the SSR in the corresponding SADP, which reveals the γ' precipitates in the matrix in the non-isothermal DTA specimen of the 32% prior cold worked alloy, heated at α=20°C/min. up to the peak position II as shown in Figure 4.34.

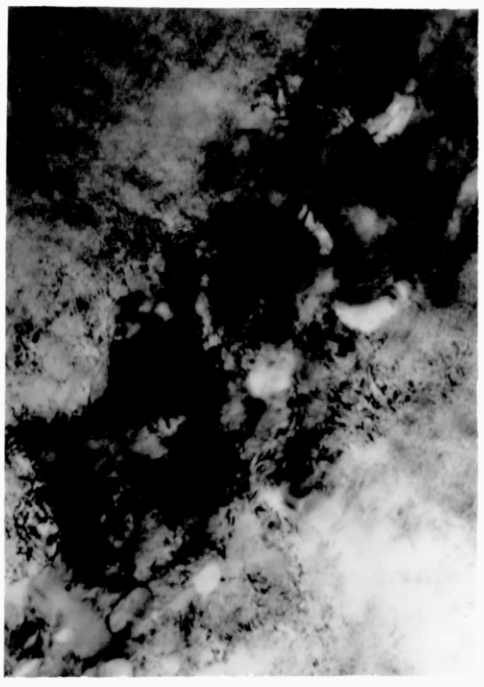
(b) The strain-free regions, containing the γ'_D precipitates, at a grain boundary in the specimen of (a).

Figure 4.35 (a)



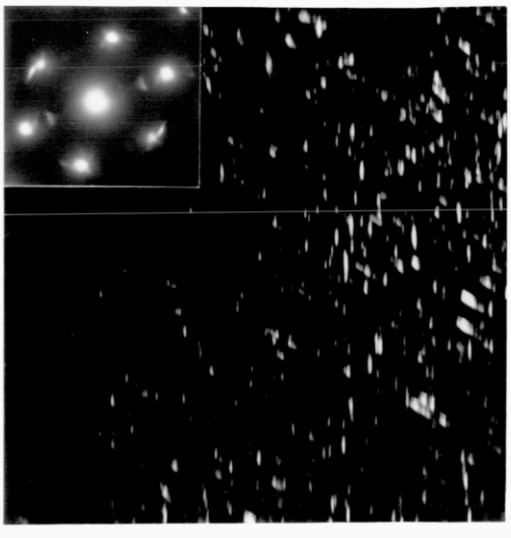
0.2 μm

(b)



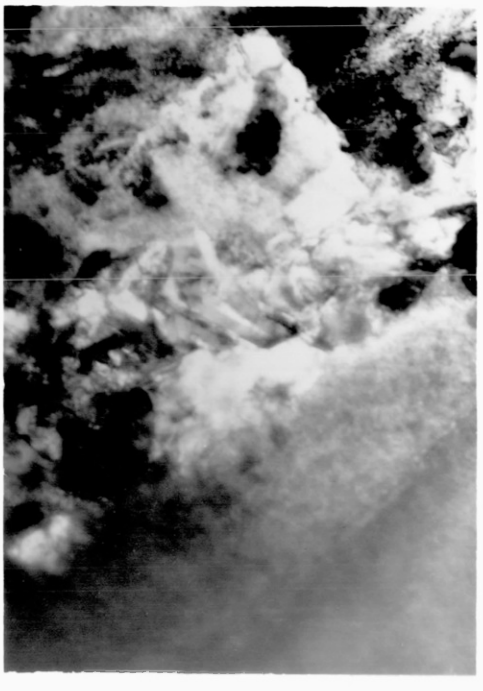
0.2 μm

Figure 4.36 (a)



0.2 μm

(b)



0.7 μm

growth of the γ' precipitates, and the grain boundary regions revealed the γ'_D precipitates in cellular form (Figure 4.36-b). In this respect, the DTA peaks of 10 and 32% prior cold worked samples represent the overlapped heat liberation, produced by the formation of the γ' (peak A) and the γ'_D precipitates (peak B).

4.5 Isothermal Differential Thermal Analysis

The DTA (μV) vs. time plots, obtained from the preliminary DTA runs on pure Cu, using pure Cu as reference, at temperatures in the range 300 to 500°C show that the insertion of the sample into the DTA furnace at a constant temperature distorts the shape of the plots as the sample temperature rapidly increases to the preset temperature. This distortion manifested itself as either a maximum or a minimum in the DTA vs. time plots; however, when the temperature of the sample stabilised at the preset temperature, the curve became both smooth and parallel to the time axis.

The nature of the DTA curve prior to stabilisation varied both with size and geometry of the specimen and/or reference. Furthermore, over the temperature range of investigation, 300 to 500°C, the time to stabilisation decreased with increasing temperature, but was always less than 250 s and sometimes as low as 100 s. Typical plots of the DTA vs. time and the temperature vs. time plots, obtained from the isothermal DTA of a pure Cu sample at 400°C, are given in Figure 4.37; as can be seen, the DTA vs. time plot is distorted during the inital stages of the run, but smooths out after stabilization of the sample at the preset temperature.

The initial disturbance in the DTA signals was also observed during the runs on the Cu-Be samples, using heat treated Cu-Be as reference (the preparation of the refer--ence was described in section 2.5.2). As shown in Figure 4.38-a, at low temperatures, e.g. $T<400°C$ for solution treated samples and $T<325°C$ for 32% prior cold worked samples, the isothermal DTA runs revealed exothermic peaks

in the regions where the temperature is stabilised. However, when the DTA tests were carried out at higher temperatures, the DTA peaks were shifted towards shorter ageing times with increasing temperature (Figure 4.38-b), and their position was in the non-isothermal region where the steep decrease in the DTA signals occurred because of the increase in the temperature of the sample to T_{Iso}.

The repeat runs of each DTA test gave no peaks, indicating no further precipitation, and the curves always coincided with those parts of the first DTA run, where there was no heat liberation. Therefore, the DTA curves of the repeat runs were used as base lines (these are plotted with broken lines in Figure 4.38) in order to determine the times for onset, t_0, and the maximum heat liberation, t_P; the latter was determined by measuring the maximum ΔT_M, as shown with arrows in Figure 4.38-b and c. This method was particularly successful for the runs at high temperatures, where the DTA peaks were distorted at short times due to the disturbance of DTA signals.

The DTA vs. time plots of the samples UD, D10, D24, D32, and D41, recorded at 350, 400, 450, and 500°C, are shown in Figure 4.39-a, b, c, and d, respectively; the onset and the maximum heat liberation points are indicated with arrows, t_0, and t_P on each peak. Both t_0 and t_P are shifted towards shorter ageing times with increasing prior cold work and temperature. It was found that the times required for the sample temperature to reach any T_{Iso} in the ordinary tube furnace, which was used for the heat treatments of TEM samples, and the DTA furnace did not significantly differ. Therefore, the TEM results, presented in section 4.2, are applicable to the decomposition reactions, which are responsible for the heat liberation during the isothermal DTA runs. Thus, the isothermal DTA peaks of Cu-Be-Co samples in Figure 4.39 were analysed with reference to the TEM results, summarised in Table 4.1.

The data in Table 4.1 suggest that the broad peak, which had steps on both the high and low temperature side, of solution treated samples from runs at T≤350°C was produced by γ'_D, G.P. zones, and γ' precipitation, namely:

(i) The formation of the γ'_D precipitates at the origi--nal grain boundaries in a pucker-type process prior to any matrix precipitation. This process corresponds to the onset (first step), as indicated by t_0 in Figure 4.39-a.

(ii) G.P. zone formation, which corresponds to the second step as indicated by $t_{G.P.}$ in Figure 4.39.

(iii) The transformation of G.P. zones to the γ' precipi--tates, which is associated with the third step on the low temperature side of the peak, indicated by $t_{\gamma'}$. Also, t_P corresponds to the maximum rate of heat liberation, which is produced by the growth of the γ' precipitates in the matrix.

It was established for the non-isothermal DTA peaks of solution treated samples (see section 4.4) that the nucleation and the growth of the γ'_D precipitates at grain boundaries and the cellular reaction, inducing nucleation and growth of the γ'_D precipitates at the advancing interface, produced two types of heat liberation, which were characterised as peak C and peak B, respectively. It is assumed that in the absence of the matrix precipitation, this would be the same in isothermal DTA plots since γ'_D precipitation follows the same sequence under isothermal conditions. Thus, the development of these features is schematically plotted on the isothermal peak of solution treated samples in Figure 4.39-a (note that the maximum of peak B is situated at the step on the high temperature side of the isothermal peak).

When T_{iso} for solution treated samples exceeded 350 °C, no steps were present on either temperature side of the DTA peak (Figure 4.39-b, c, and d). The TEM results suggest that G.P. zones do not form above a temperature in between 350 and 400°C, and the products of the decomposition reaction at 400°C are the γ'_D and the γ' precipitates, which produces the overlapping heat liberation, as shown schematically in Figure 4.39-b. At higher temperatures (T>400 °C), the DTA peaks are much sharper due to the heat

liberation, produced by γ'_D and γ' precipitation being coincident (Figure 4.39-c and d).

For prior cold worked alloys, the coincidence of the heat liberation on DTA runs, produced by γ'_D and γ' preci--pitation, also occurred at temperatures as low as 300°C because the prior cold work shifts the γ' and γ'_D sub-peaks to shorter ageing times at different rates; the movement of the γ' peak to shorter times is more marked than that of the γ'_D peak due to the accelerated γ' precipitation and hence retarded γ'_D precipitation by prior cold work. Furthermore, the DTA peaks at 350°C did not reveal any characteristic change in the heat liberation, such as steps on both side of the peak, corresponding to G.P. zone formation and their transformation to the γ' phase, since the time elapsed during these reactions was shortened very much with increasing prior cold work.

According to the TEM analysis of 41% cold worked specimens, the γ'_D precipitates cannot form at 500°C and recrystallisation at grain boundaries, involving the nucleation of the nodular-type γ_D precipitates, is the predominant process of discontinuous reaction (see Figure 4.21). Further information on the process associated with the DTA peak was obtained from 24 and 32% prior cold worked DTA samples, which were aged isothermaly in the DTA furnace at 500°C for 300 seconds (5 minutes), that is aged to the completion of heat liberation. The DF micrographs in Figures 4.40-a and b show two sets of the plate-like γ' precipitates in the matrix of 24 and 32% cold worked alloys, respectively. These precipitates are visible lying in the directions $[1\bar{1}1]$ and $[1\bar{1}\bar{1}]$. The micrographs of the grain boundary regions in 24% prior cold worked specimens (Figure 4.41-a) reveal the cellular growth of the γ'_D precipitates; small nodular γ_D precipitates are also present in the cells as shown in Figure 4.41-b. In contrast, the grain boundary regions of 32% cold worked specimens had only recrystallised grains, containing the nodular γ_D precipitates (Figure 4.41-c). Therefore, for prior cold work up to 32% RA, the heat liberation on DTA runs at 500°C is produced by the formation of the γ'_D, γ_D,

Fig. 4.37

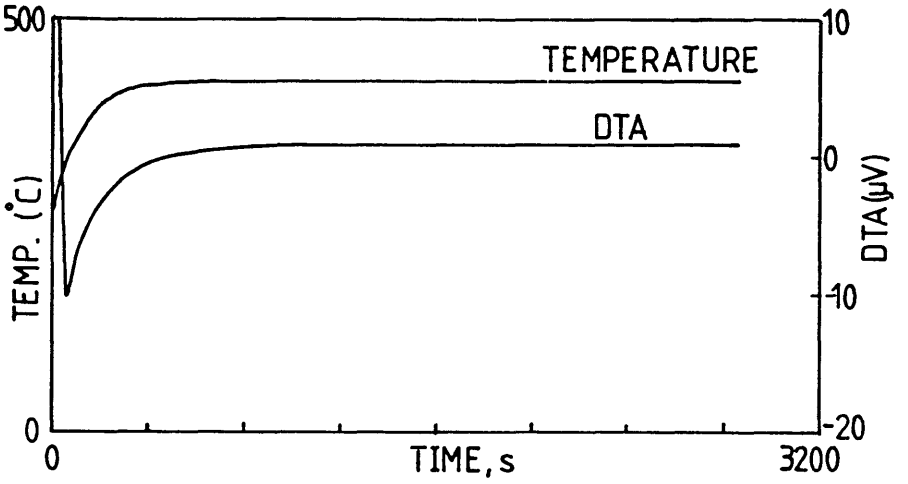


Fig. 4.38 (a)

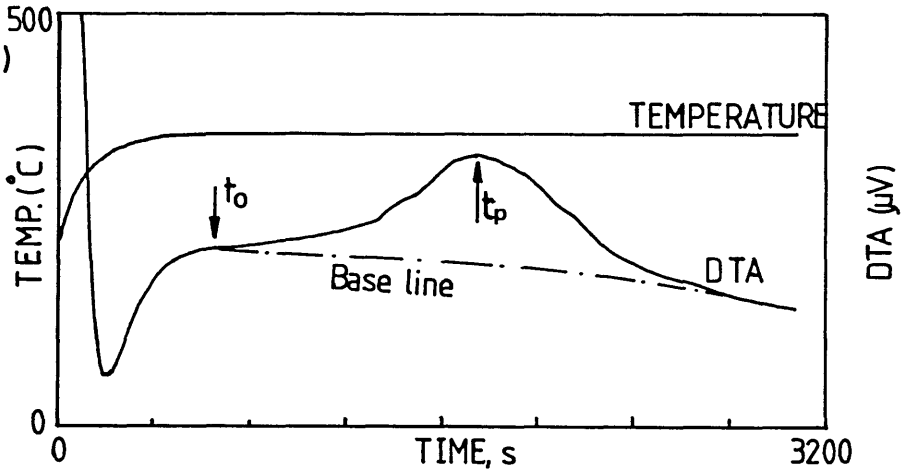


Fig. 4.38 (b)

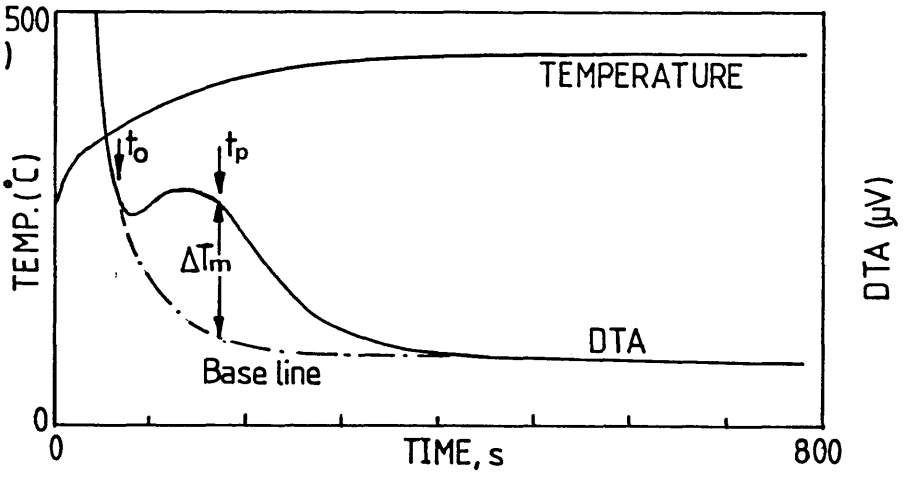


Figure 4.37- The isothermal DTA curve, obtained from a DTA run of pure Cu sample at 400°C.

Figure 4.38- (a) The isothermal DTA curve of a solution treated sample (full curve) and the repeat run (broken line) at 350°C.

(b) The isothermal DTA curve of a 32% prior cold worked sample (full curve) and the repeat run (broken line) at 450°C.

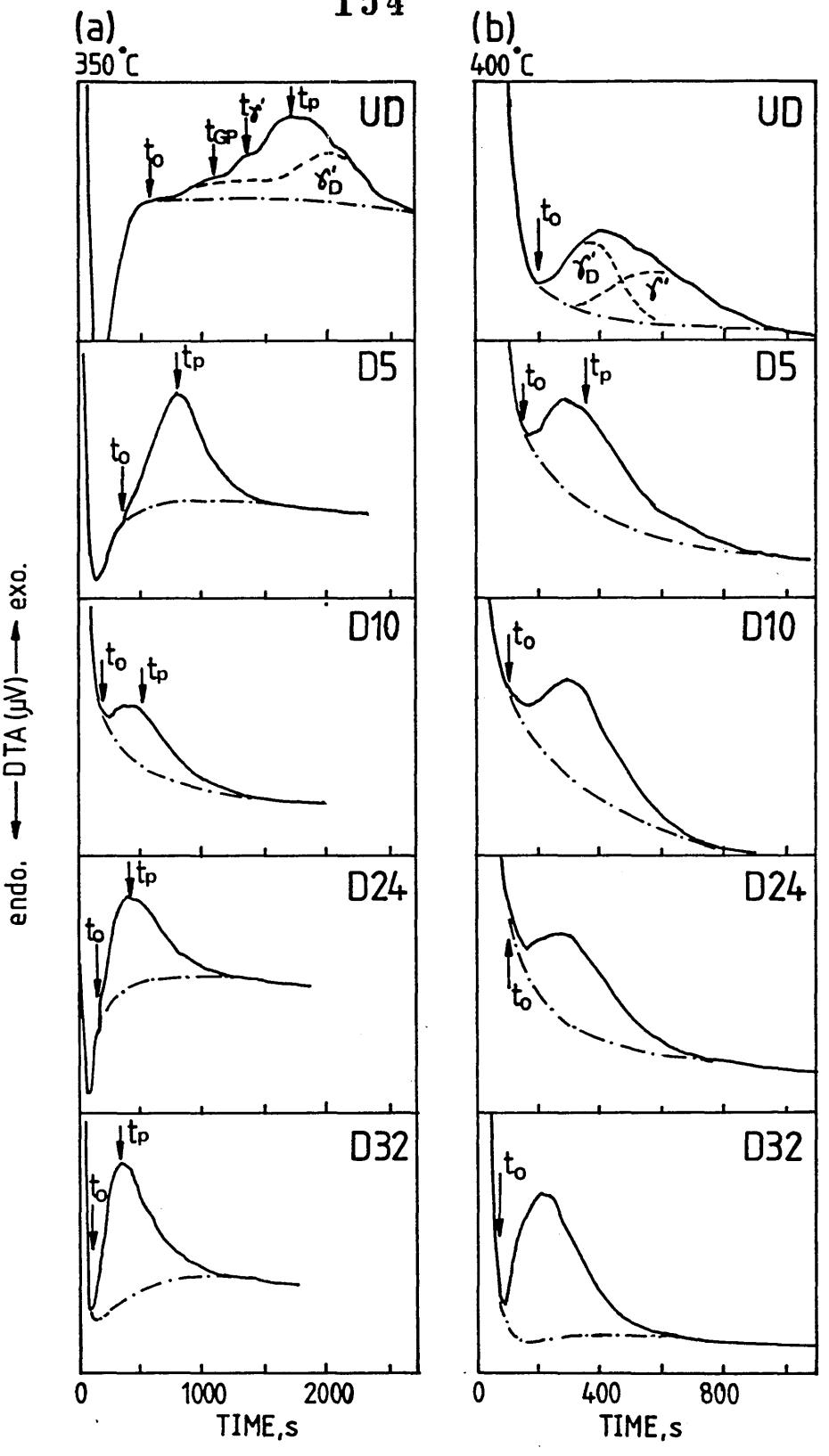


Figure 4.39- Isothermal DTA curves of alloys UD, D5, D10, D24, and D32 as indicated for each curve, at (a) 350°C, (b) 400°C, (c) 450°C, and (d) 500°C.

Fig4.39(c) (d)

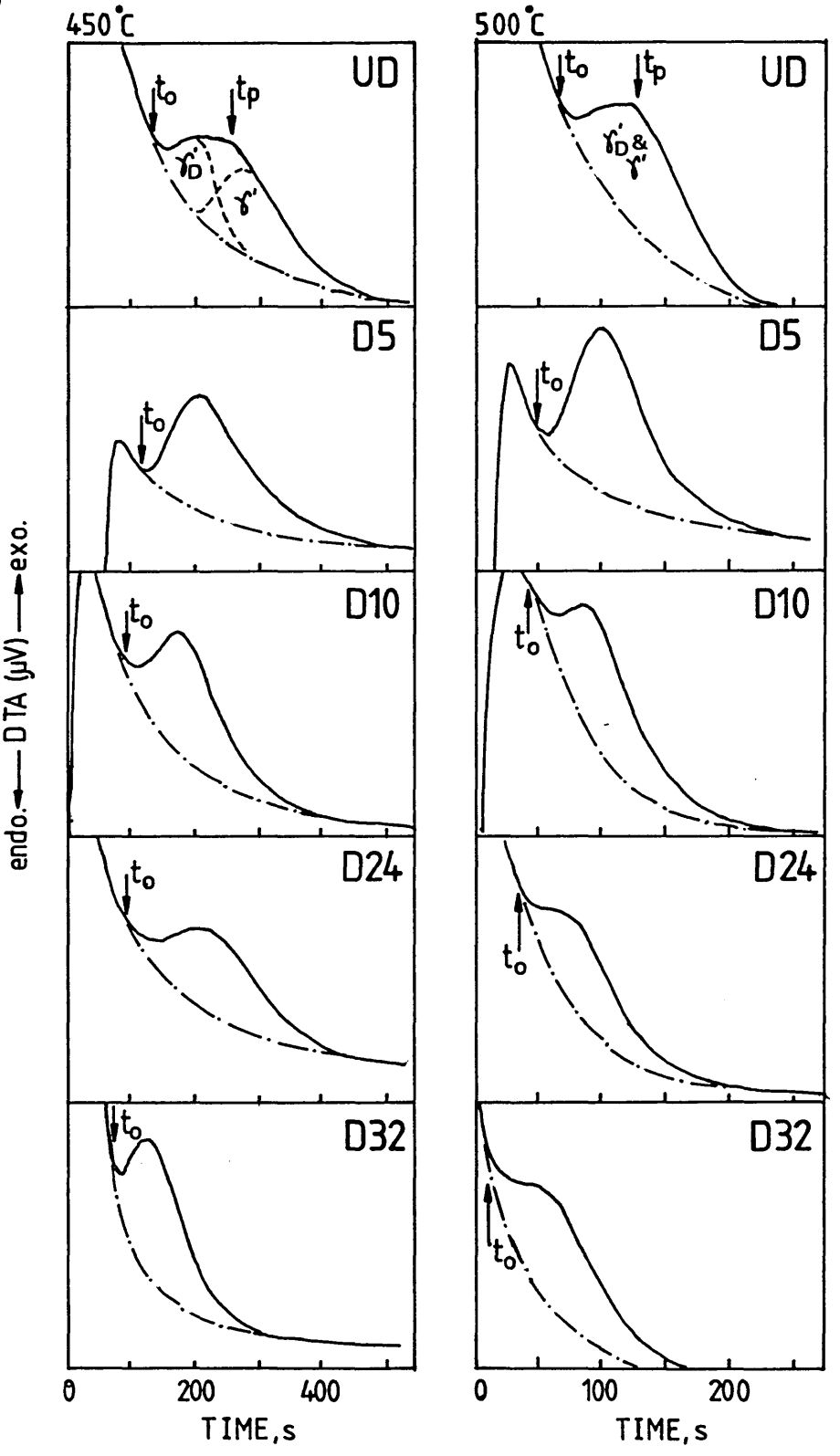

450°C
500°C
UD
D5
D10
D24
D32
t_o
t_p
γ'_D
γ'
γ'_D & γ'
endo. ← DTA (μV) → exo.
0
200
400
100
TIME, s

Figure 4.40

D.F. micrographs, obtained from the SSR in the corre--sponding SADP, revealing the γ' precipitates in the matrix of (a) the 24% cold worked alloy and (b) the 32% cold worked alloy, aged isothermally in the DTA furnace at 500°C for 5 min.

Figure 4.41

(a) The strain-free reoriented regions, containing the γ'_D precipitates at a grain boundary in the specimen of Figure 4.40-a.

(b) Another example of the structure in (a), containing the γ'_D and the nuclei of the equilibrium γ_D precipitates (see arrows).

(c) Recrystallised grains at a grain boundary in the specimen of Figure 4.40-b.

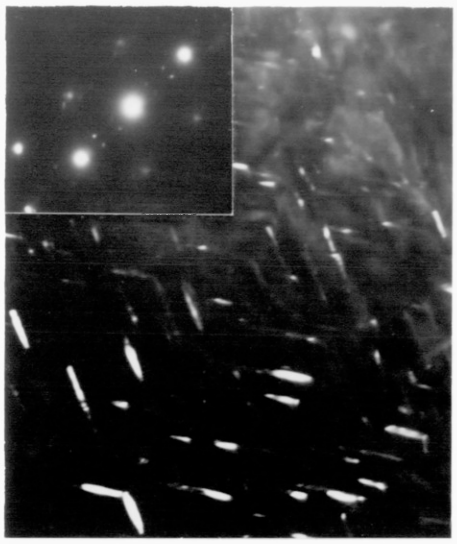
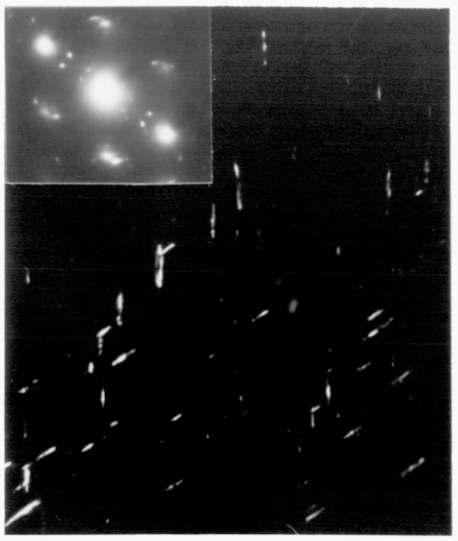


Figure 4.40 (a) 0.2 μm



(b) 0.2 μm

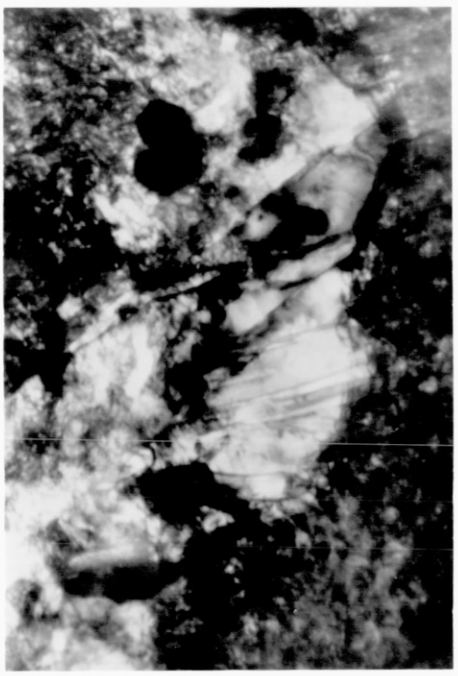
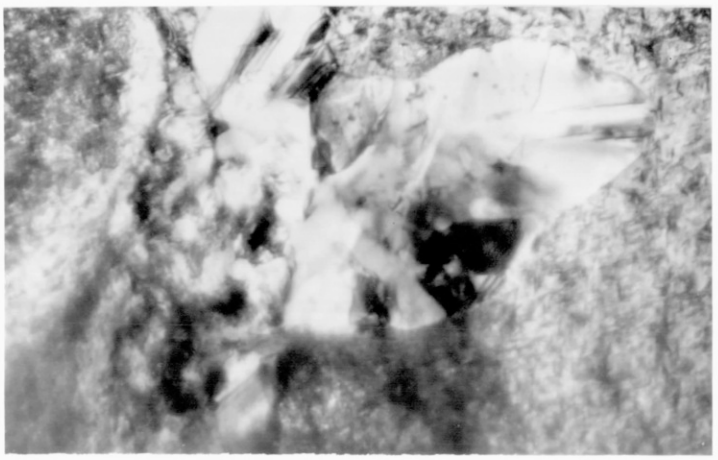


Figure 4.41 (a) 0.2 μm



(b) 0.2 μm

(c)



0.2 μm

and γ' precipitates, and for 32% and 41% prior cold work, by γ' precipitation in the matrix and the recrystallisation inducing nodular γ_D precipitation. These reactions occur at the same time and hence produce single isothermal peaks, as can be seen in Figure 4.39-d.

It must be noted that recovery and recrystallisation must also produce heat liberation during a DTA run. The data obtained from deformed pure Cu (Gordon, 1955, as cited by Reed-Hill, 1979) shows that the amount of heat flow, produced by recovery and recrystallisation during an isothermal run can only be detected with the aid of extremely sensitive equipment, i.e. a micro-calorimeter capable of measuring a heat flow as low as 3.5×10^{-6} J/s. This amount of energy release is beyond the sensitivity of conventional DTA and DSC equipment. Therefore, the DTA peaks of prior cold worked alloys, studied in this work, only represent the precipitation reactions, which induce considerably high heat liberation detectable by the DTA equipment.

Also, considering that the volume of the grain boundary reaction products in prior cold worked alloys is very small in comparison to that of the matrix precipita--tes, the isothermal peaks for cold worked alloys represent the heat liberation produced mostly by γ' precipitation in the matrix.

4.6 Analysis of 90° Bend Test Data

As a measure of the bendability of strip alloys, the minimum bend ratio, R/t was determined for various thermo-mechanical treatments of Cu-Be-Co strip alloys. The average results for each treatment were analysed with reference to the 0.2 off-set yield stress values of the specimens, which had received the same thermo-mechanical treatments as those of the bend test samples. Figure 4.42 shows the plot of yield stress vs. minimum bend ratio, R/t, for alloys UD, D10, D21 and D37. On this plot, the data points of the same sign correspond to a given condition prior to ageing, i.e. UD, D10, D21, etc., which has received different heat

treatments. It can be seen that different heat treatments lead to a wide range of yield stress values for a given R/t ratio, e.g. for alloy D10 the yield stress varies from 530 to 930 MN/m^2 for R/t equal to 1. Practical experience indicates that formability is strongly dependant on heat treatment, hence these results indicate that R/t is not a sensitive measure of formability or bendability. Nevertheless, the marked change in formability of alloys due to prior cold work in the range 0 to 37% RA was large enough to be detected by the technique, as shown by the higher R/t values for the more heavily deformed conditions. Note that the increase in R/t with prior cold work is accompanied by an increase in yield stress of alloys, as can be seen by the curve fitted to the experimental data points in Figure 4.42.

4.7 Use of AC Potential Drop Method on 90° Bend Tests

A number of selected specimens, i.e. some were known to crack and the others to bend without cracking, were tested using the AC potential drop equipment, in order to assess the performance and the applicability of ACPD system in monitoring the formation of cracks during 90° bend tests of strip alloys. Typical results as regards the change in the bending load and the AC potential drop (ACPD) signals with the displacement of the punch during bending are shown in Figure 4.43. This plot is from one of the preliminary tests carried out in order to assess whether the ACPD technique could be employed for crack detection during bending. Curve B in Figure 4.43 shows the change in ACPD for a sample which cracked and curve A for a sample which did not crack during 90° bending; curves C and D give the change in applied bending load for curves A and B, respectively. Curves A and B initially show a drop in ACPD, and then a sharp increase in ACPD occurs on curve B, as indicated with an arrow in Figure 4.43. The increase in ACPD is probably due to the crack formation at the bend apex since the current travels a longer route after crack formation and consequently there is an increase in the

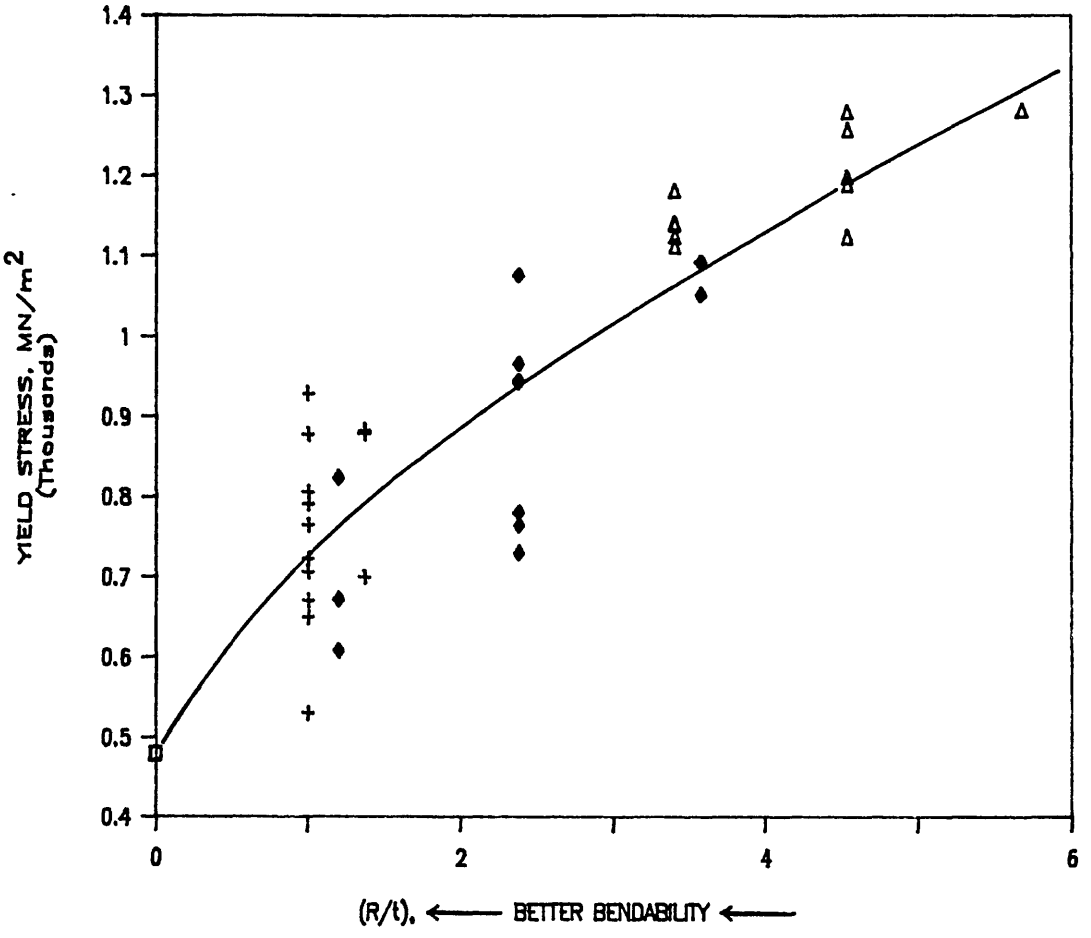


Figure 4.42- Yield stress vs. bendability ratio, R/t, plot for (□) alloy UD, (+) alloy D10, (◆) alloy D21, and (Δ) alloy D37.

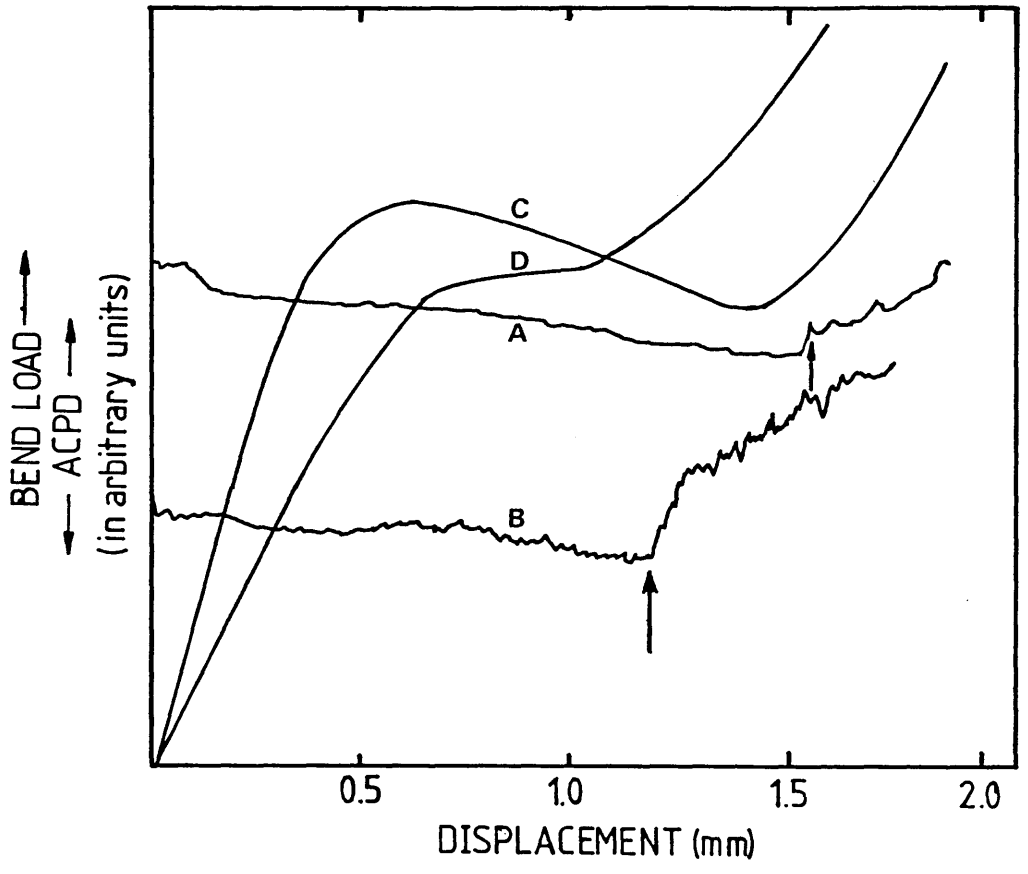


Figure 4.43- The bend load vs. displacement plots on a 90° bend test for uncracked (curve C) and cracked (curve D) samples. Curves A and B are the ACPD traces for curves C and D, respectively.

potential drop output. A small increase in ACPD also occurs on curve A at large displacements (see the arrow in Figure 4.43) although the test sample did not crack during bending to 90°.

Although these tests demonstrated that the technique was capable of detecting cracking in Cu-Be strip alloys during bending, a major experimental difficulty was encountered. It was difficult to judge whether a sharp increase in ACPD corresponded to crack formation because during bending to 90° the electrical connection leads move as they are attached to the surface of specimen, and even a slight movement of the connection leads can cause large disturbances in the ACPD signals. Therefore, the AC potential drop method is applicable for the detection of crack formation during bending strip materials only when the interference caused by the leads movements is completely avoided.

4.8 Cantilever-Type Bend Test Results

4.8.1 Remarks on "maximum bendability angle, θ_M"

The cantilever-type bend test apparatus, designed in the present work, gave a satisfactorily sensitive measure of the maximum bendability angle, θ_M, for Cu-Be-Co strip alloys, which had received various thermo-mechanical treatments. However, the test samples were of different thicknesses since the commercial production of the mill-hardened Cu-Be-Co involves various amounts of cold rolling after the solution treatment and hence the final thickness of the strip alloys differed, depending on the amount of cold rolling, i.e. the thickness of the as-received alloys, tested in this work, was in the range 0.24 to 0.41 mm.

During the cantilever-type bend testing it was observed that, when testing the strip samples of identical thermo-mechanical treatments but of different thicknesses, a thicker sample yielded lower θ values than those obtained from thinner samples. This was because the radius of curva-ture, R, at the outer fibre of the bent sample increases

with thickness, and hence two samples of the same thermo-mechanical treatment, deformed to the same θ, the thicker sample receives a larger amount of deformation than the thinner one. Therefore, the cantilever-type bend test results of the strip alloys with different thicknesses could not be compared. In order to overcome this difficulty, a thickness correction factor had to be introduced. An analytical approach to eliminate the thickness effect on the experi--mental θ_M values was made, and it was concluded that the θ_M values, obtained from the samples with different thicknesses, could be compared when θ_M values of thinner samples are multiplied by a correction factor N_{COR}, given by

$$N_{COR} = (t_1/t_{max}) \qquad [4.1]$$

where t_1 is the thickness of a strip sample, t_{max} is the thickness of a sample to which the data is being normalised and would correspond to the thickness of the thickest sample under investigation.

The analytical approach to obtain the correction factor, N_{COR}, and the detailed discussion on the relevant experimental results will be given in section 5.4.1. In the following section, the corrected maximum bendability angles will be used to present the the change in the bendability of Cu-Be-Co alloys with thermo-mechanical treatments.

4.8.2 Corrected bendability data for Cu-Be-Co alloys

The plots of corrected bendability angle, θ, vs. ageing time for alloys UD, D15, D10, D18, D24, D32, and D41 are given in Figure 4.44-a to g. The θ values, measured before ageing, show that the increase in the amount of prior cold work reduces the bendability of alloys, i.e. the θ value for alloy UD (145°) was reduced to 60° after 41% prior cold work.

During ageing solution treated alloy at 350°C, first a gradual and then a sharp drop in θ value (after 20 minutes ageing) occurred (Figure 4.44-a). Further ageing for times as long as 100 min. did not noticeably change the

bendability of the alloy. Ageing solution treated alloys at 380°C resulted in first a decrease in θ to a minimum (35 minutes), and then an increase in θ to a maximum (60 minutes) (Figure 4.44-a). On further ageing, θ started to decrease again. At 400°C, the change in bendability was the same as that observed at 380°C, except prolonged ageing did not reduce the bendability of the alloy and the increase in θ was continuous up to 100 minutes ageing. At 420°C, a sharp drop in θ to a plateau occurred and the value of θ did not noticeably change with further ageing times as long as 100 minutes. The role of the increase in temperature was to shorten the time to the initial drop in θ and to increase the bendability achieved after the initial drop; bendability curves are shifted towards higher θ values as can be seen in Figure 4.44-a.

The change in bendability as a function of ageing time of prior cold worked alloys at 350°C was similar to that observed on ageing solution treated alloy at 350 °C, but the greater the amount of prior cold work, the smaller the amount of drop, $\Delta\theta$, and the lower the bendability achieved after ageing (Figure 4.44-b to g). The reduction in bendability in the aged condition due to prior cold work may be exemplified by the θ values for alloys UD, D10, D32, and D41, aged at 350°C for 100 minutes; these are 42°, 34°, 29°, and 25°, respectively, which can be compared with θ=49° for the solution treated (UD) alloy given the same ageing treatment. Also, the time to initial drop to a plateau was shortened by increasing prior cold work. It must be noted that when prior cold work exceeded 18% RA, ageing resulted in an immediate sharp drop in θ value to a plateau followed by a negligibly small increase in θ values (3-4° after 100 minutes).

The change in bendability of prior cold worked alloys during ageing at 380°C and above was similar to that observed on ageing solution treated at 400°C. The bendability of cold worked alloys dropped to a minimum, and then started to increase; the increase in θ was mostly continuous on ageing all alloys at 380°C and the 5% prior cold worked alloy at all temperatures, whereas, for prior

cold work greater than 5% RA, during ageing at 400 and 420 °C the greatest amount of recovery in bendability occurred up to 25 minutes, and further ageing (maximum 100 minutes) had little effect in increasing bendability.

In general, the greater the prior cold work, the earlier the initial drop in bendability and the lower the bendability achieved after ageing for a chosen time. Also, the amount of drop in θ values ($\Delta\theta$) was reduced and the ageing time for the onset of the increase in bendability is shortened with the increase in both prior cold work and ageing temperature as shown by arrows in Figure 4.44-a to g. The reduction in $\Delta\theta$ with prior cold work does not necessarily mean an increase in bendability obtained after ageing. In fact, prior cold work results in a significant reduction in bendability before ageing, which is not compensated by the decrease in $\Delta\theta$ on ageing.

Although prior cold worked alloys recovered a considerable amount of bendability during ageing above 350 °C, full recovery of bendability could not be achieved even after 100 minutes of ageing. Furthermore, even after these long heat treatments the larger amounts of prior cold work resulted in lower θ values, i.e. the θ values for alloys UD, D10, D32, and D41, aged at 400°C for 100 minutes were 90°, 61°, 53°, and 46°, respectively.

The trend of the data plotted in Figure 4.44-a to g suggests that there is a close relationship between the change in hardness and that in bendability of alloys during ageing. In other words, an increase in hardness corresponds to a decrease in bendability under identical ageing conditions of the same alloy, or vice versa. This can be followed by comparing the hardness vs. time (Figures 4.1, 4.2, 4.3, and 4.4) and bendability vs. time plots (Figure 4.44-a to g) of a chosen alloy, i.e. both plots for identical thermo-mechanical treatments show symmetry when they are superimposed.

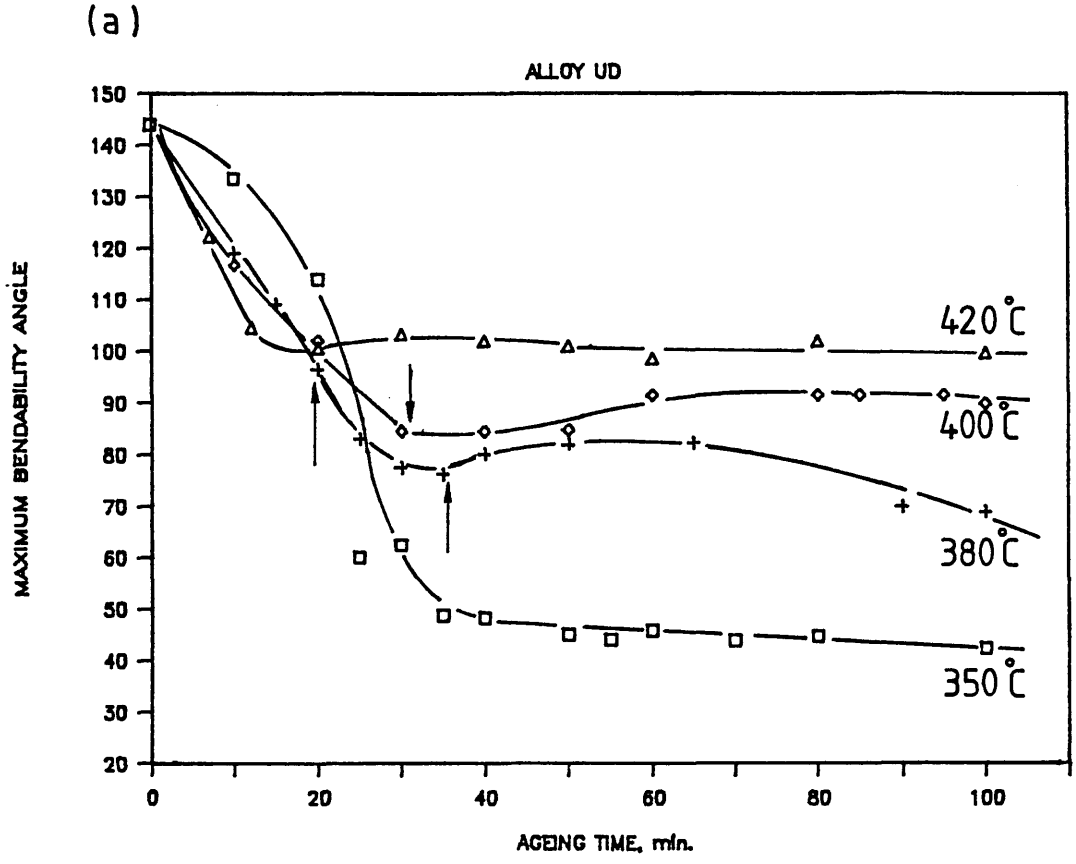
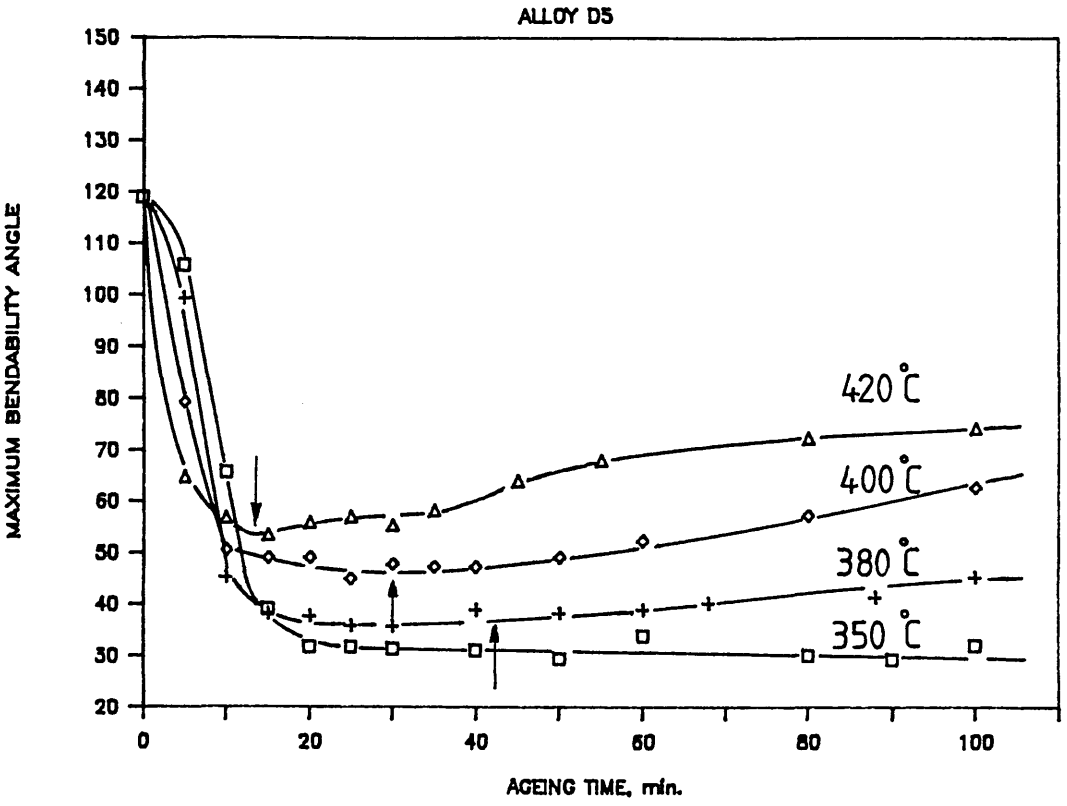


Figure 4.44- Change in the maximum bendability angle of following alloys during ageing at 350, 380, 400, and 420°C:

(a) alloy UD
(b) alloy D5
(c) alloy D10
(d) alloy D18
(e) alloy D24
(f) alloy D32
(g) alloy D41

Fig. 4.44 (b)


ALLOY D5
MAXIMUM BENDABILITY ANGLE
AGEING TIME, min.
420°C
400°C
380°C
350°C

(c)

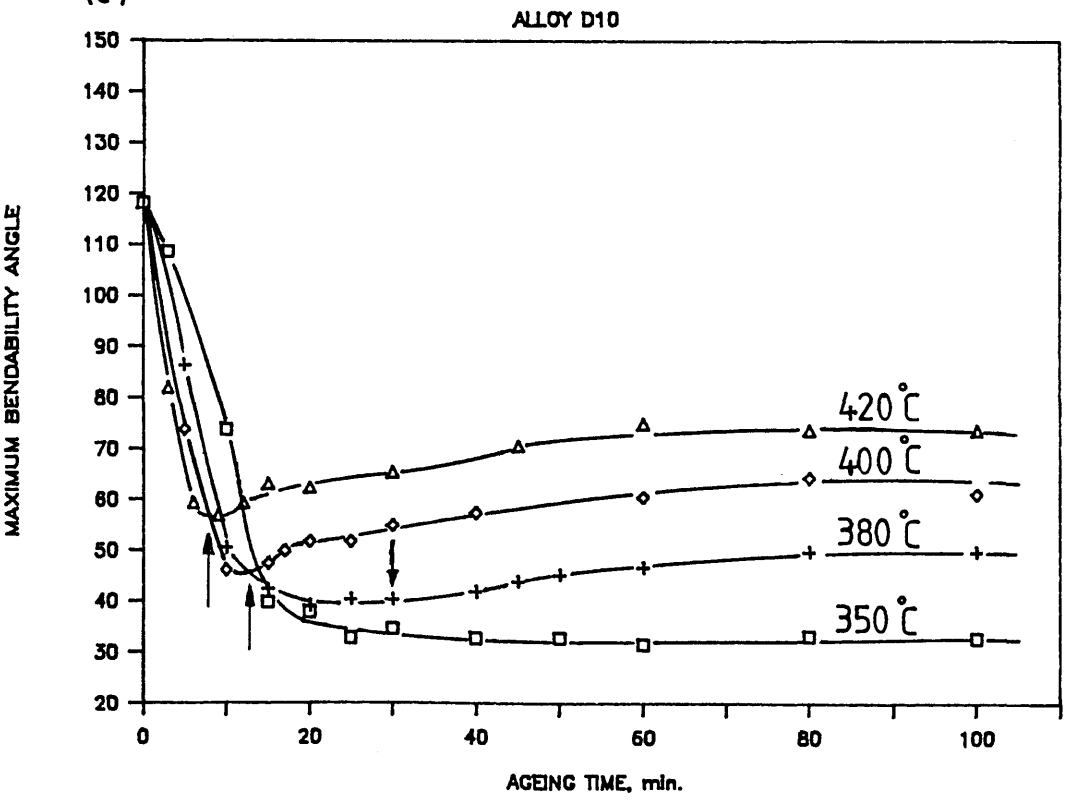
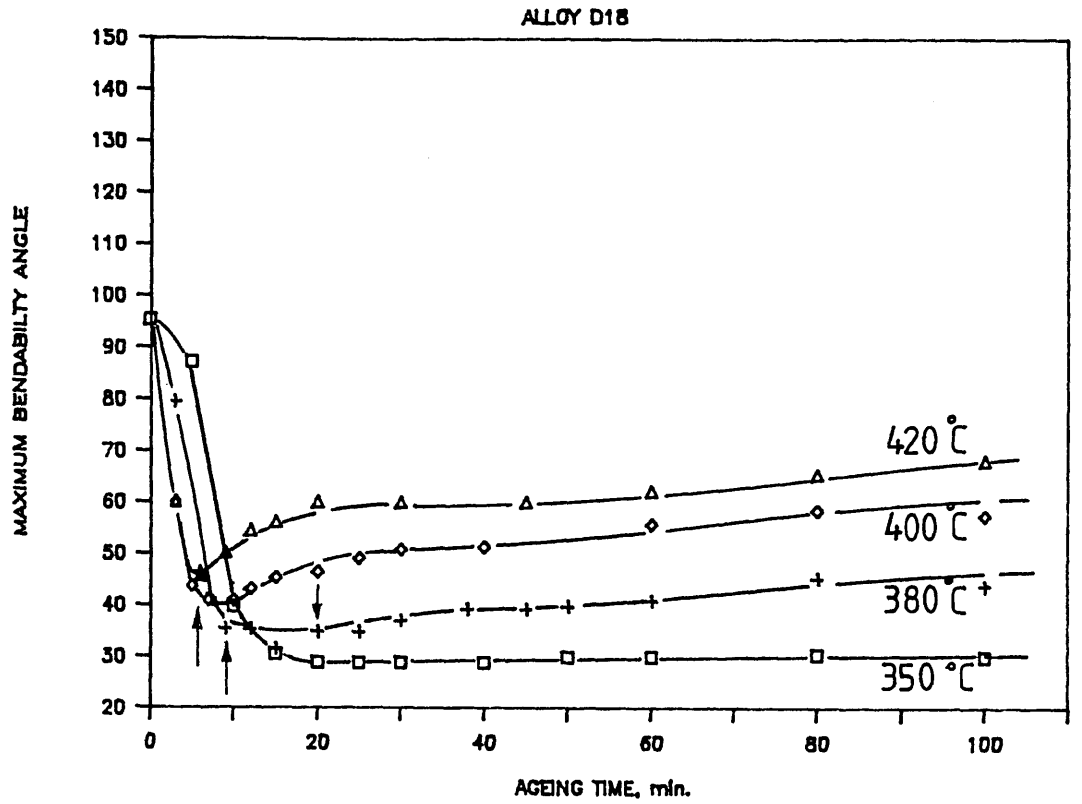

ALLOY D10
MAXIMUM BENDABILITY ANGLE
AGEING TIME, min.
420°C
400°C
380°C
350°C

Fig.4.44 (d)


ALLOY D16
MAXIMUM BENDABILITY ANGLE
AGEING TIME, min.
420°C
400°C
380°C
350°C

(e)

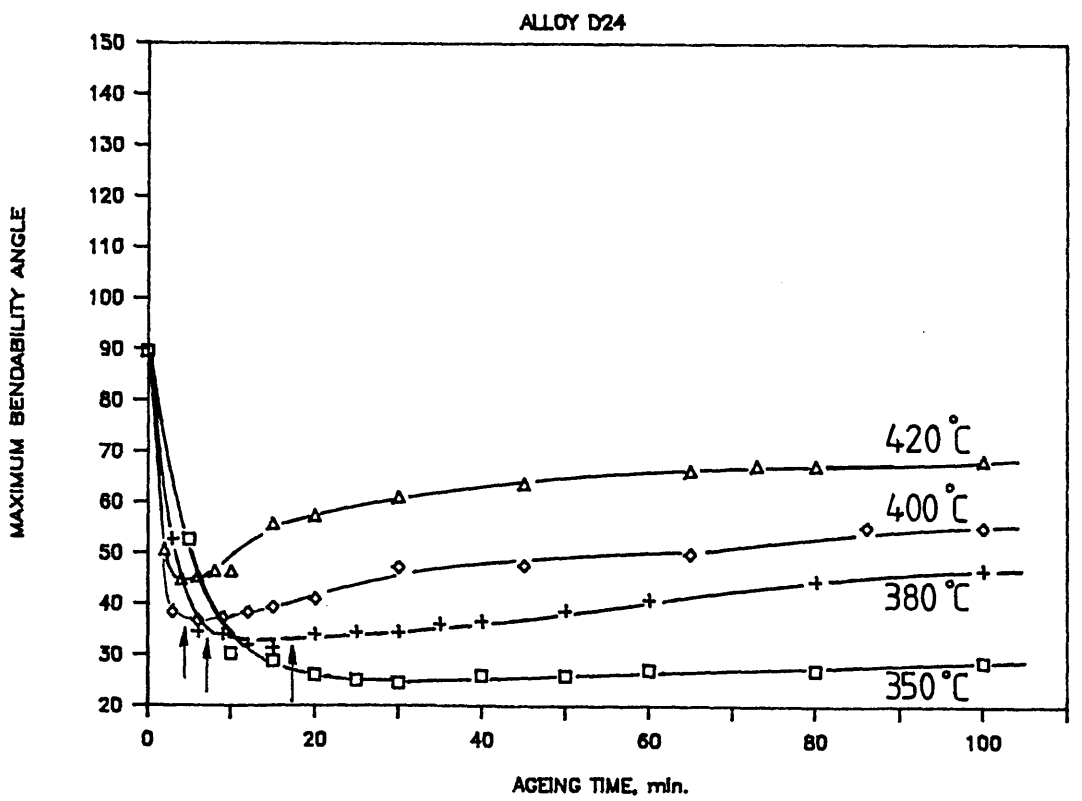
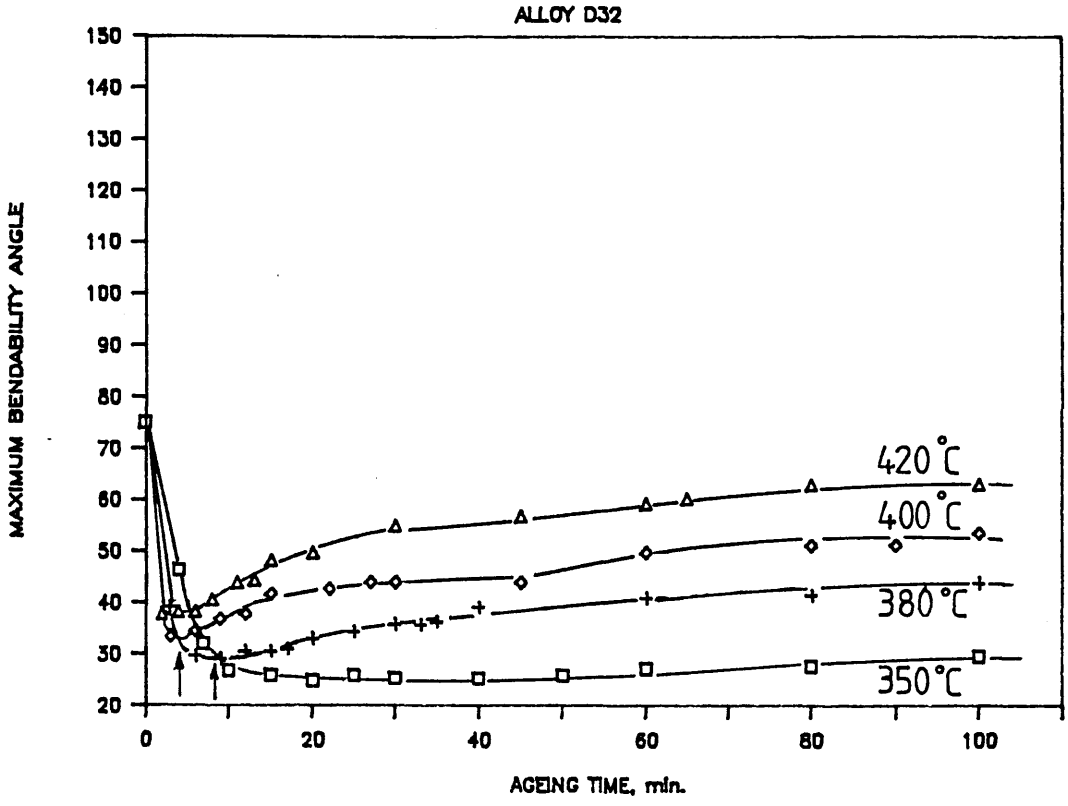
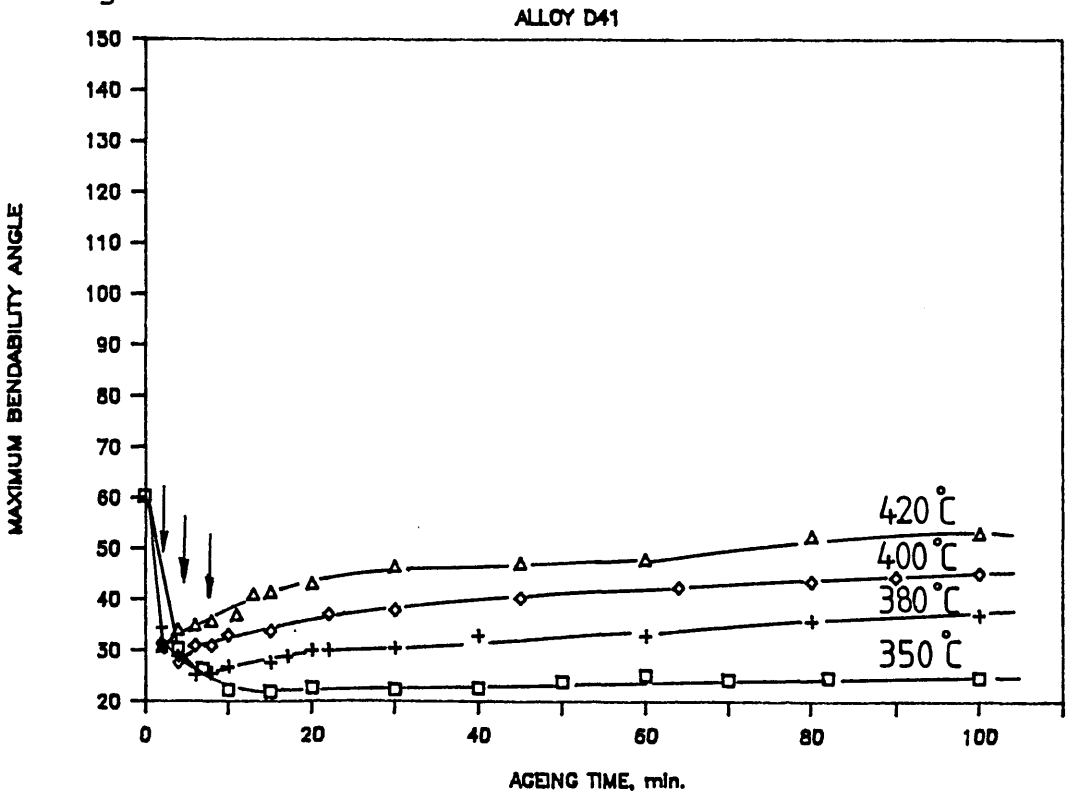

ALLOY D24
MAXIMUM BENDABILITY ANGLE
AGEING TIME, min.
420°C
400°C
380°C
350°C

Fig. 4.44 (f)


ALLOY D32
MAXIMUM BENDABILITY ANGLE
AGEING TIME, min.
420°C
400°C
380°C
350°C

(g)


ALLOY D41
MAXIMUM BENDABILITY ANGLE
AGEING TIME, min.
420°C
400°C
380°C
350°C

4.8.3 Fractography of tested samples

Normalised bend load vs. bendability plots for selected alloys, namely alloy UD aged at 350 and 400°C for 60 minutes and alloy D24 aged at 350 and 400°C for 25 min. are given in Figure 4.45-a, and b, respectively. Normalised bend load data plotted in these figures are in arbitrary units since these data were derived from experimental bending curves by normalising the recorded bend load with cross-sectional area, which was different for each sample.

In order to follow the development of cracks at bend apex during bending, some samples were bent to angles at which:

(i) local strain-inhomogenities in the form of light striations develop,

(ii) light striations become deeper and longer, and

(iii) genuine cracks are formed by "bunching up" of heavy striations in regions where the stress concentration is largest.

These three steps are indicated by SEM I, SEM II, and SEM III, respectively, on the normalised bend load vs. bend angle plots in Figure 4.45-a and b. The corresponding SEM micrographs, shown in Figures 4.46, 4.47, 4.48, and 4.49 reveal two types of deformation processes during bending, which depends on ageing temperature, namely:

(a) On ageing at 350°C, light striations form at the bend apex as shown in Figures 4.46-a and 4.47-a; this corresponds to SEM I on the bend plots in Figure 4.45-a and b. This is followed by catastrophic failure or sudden rupture without the light striations having grown in size as shown in Figures 4.46-b and 47-b; this corresponds to SEM III on the same plots. This type of failure was the same for all alloys, aged at 350°C for times that resulted in peak and/or over hardening but very low bendability (see

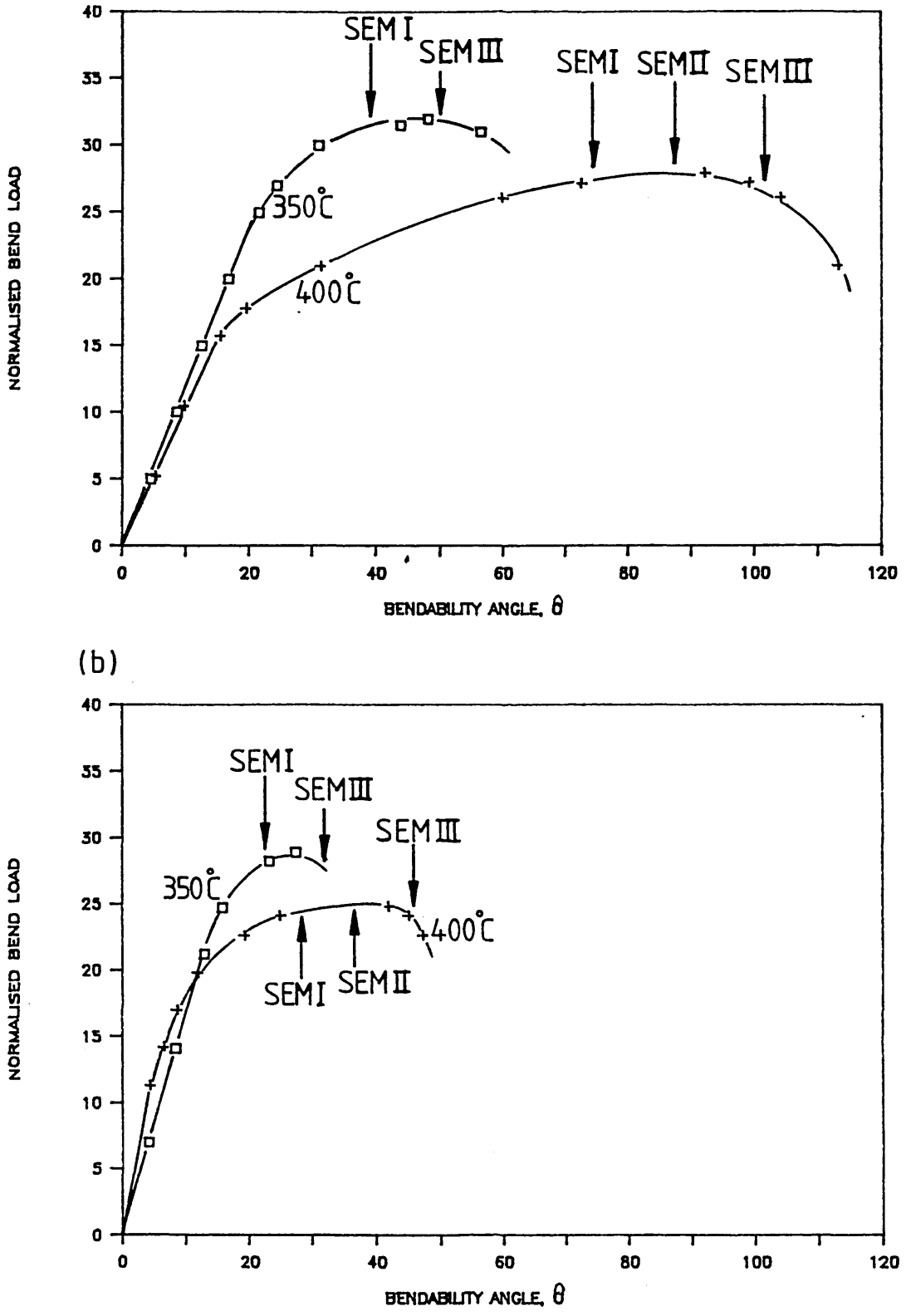
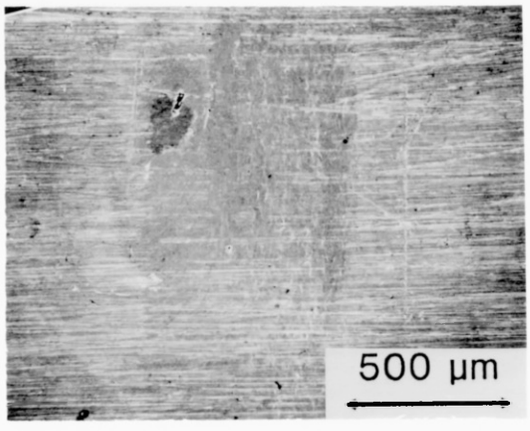


Figure 4.45- Normalised bend load vs. bendability angle plots of (a) alloy UD aged at 350 and 400°C for 60 min., and (b) alloy D24 aged at 350 and 400°C for 25 min. Arrows indicate the angles at which the SEM samples were bent; the SEM photographs corresponding to these points are shown in Figures 4.46 to 4.49.

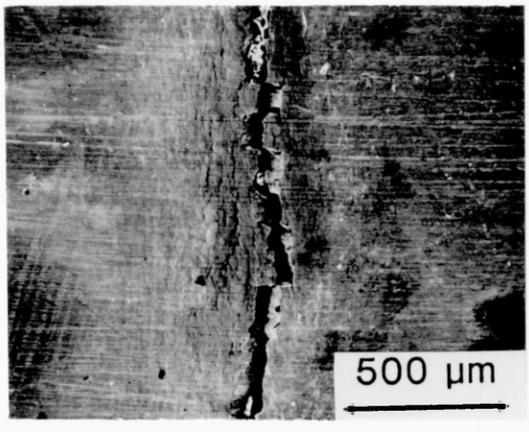
the corresponding curves in Figures 4.1, 4.2, 4.3, 4.4, and 4.44), and hence demonstrated the high resistance of Cu-Be-Co alloys to forming when aged at 350°C.

(b) On ageing above 350°C, the three steps described above were observed in the bend samples. These three steps, which result in the characteristic features at the bend apex of samples, can be followed in Figures 4.48-a, b, & c and 4.49-a, b, & c, for alloys UD and D24, respectively; the corresponding points on bend curves (Figure 4.45-a and b) for photographs a, b, and c in both figures are indicated with SEM I, II, and III, respectively. In this case, the striations deepened with increasing θ and the cracks developed gradually leading to a slower failure process. This type of failure was in operation for all alloys aged at 380°C and above, with the exception that prior cold worked alloys, aged at 380°C for times less than 30 minutes, behaved like those aged at 350°C.

SEM investigations on the nature of striations indicated that the striations were actually localised wavy slip bands. This type of features are shown in Figure 4.50-a; long continuous marks are the grinding marks perpen--dicular to the bending axis, introduced during specimen preparation, and the localised wavy marks are crossing them parallel to the bending axis. Also, localised discontinuous cracks had developed in regions of intense slip bands as can be seen in Figure 4.50. Further bending to large angles, which introduces larger amount of plastic deforma--tion at the outer fibre of the sample, resulted in joining of the localised cracks (Figures 4.46-b and 4.47-b). The localised cracks join together to produce a continuous crack across the with of the specimen at the outer fibre, where tensile stresses occurred. The crack was at an angle to the specimen surface (known as a slant fracture), however, the angle could not be accurately measured since the outer surface has a curvature due to bending. Sometimes two discontinuous cracks with opposite angles coalesced to give the feature illustrated in Figure 4.50-b.

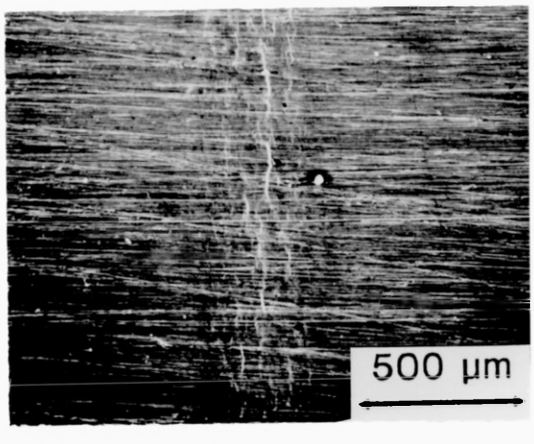


(a)

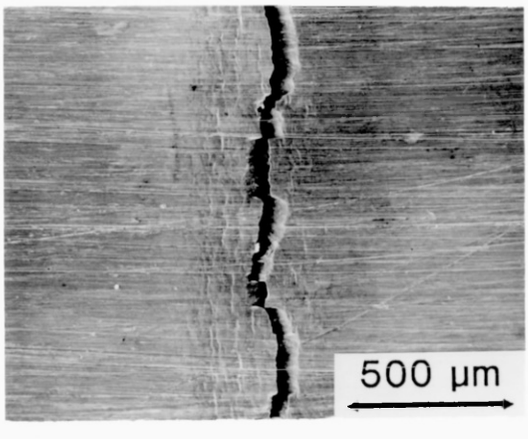


(b)

Figure 4.46: Crack formation at the bend apex of the sample from alloy UD, aged at 350°C for 60 min. (See the corresponding points, indicated with (a) SEM I and (b) SEM III on the bend curve in Figure 4.45-a).



(a)



(b)

Figure 4.47: Crack formation at the bend apex of the sample from alloy D24, aged at 400°C for 25 min. (See the corresponding points, indicated with (a) SEM I and (b) SEM III on the bend curve in Figure 4.45-b).

Figure 4.48

Development of cracks at the bend apex of the sample from allou UD, aged at 400°C for 60 min., after bending to angles that correspond to (a) SEM I, (b) SEM II, and (c) SEM III on the bend curve in Figure 4.45-a.

Figure 4.49

Development of cracks at the bend apex of the sample from alloy D24, aged at 400°C for 25 min., after bending to angles that correspond to (a) SEM I, (b) SEM II, and (c) SEM III on the bend curve in Figure 4.45-b.

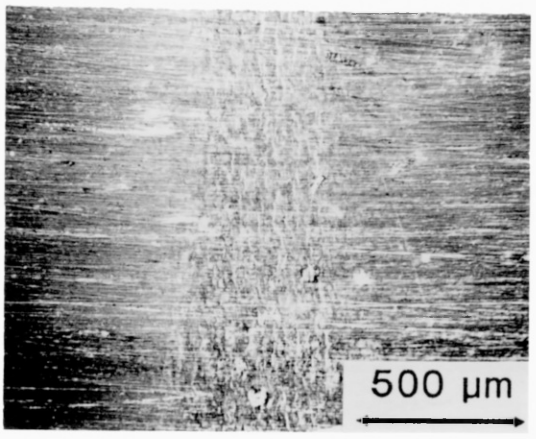


Figure 4.48 (a)

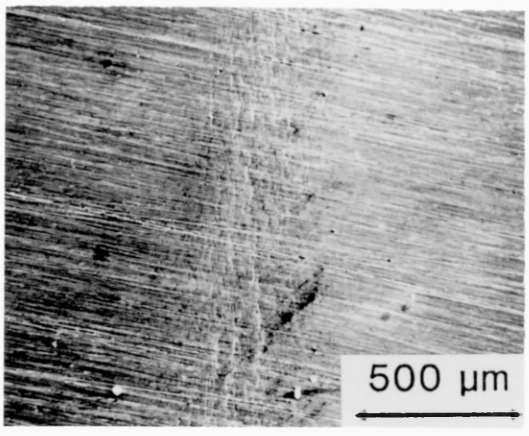
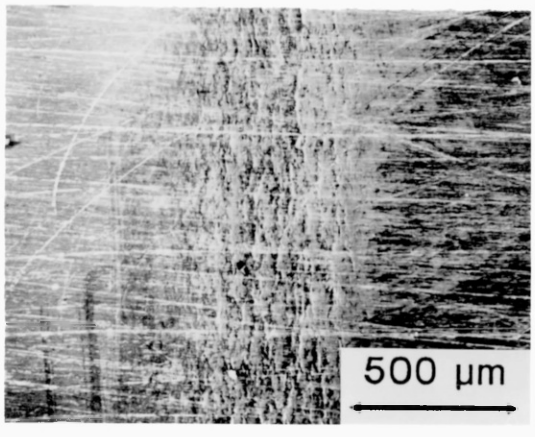
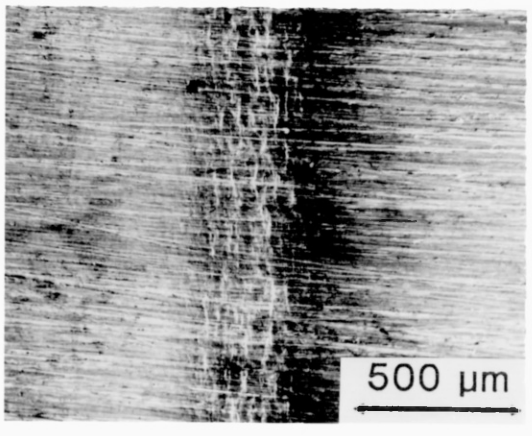


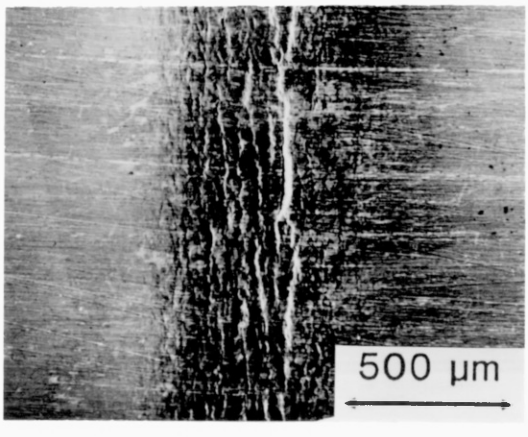
Figure 4.49 (a)



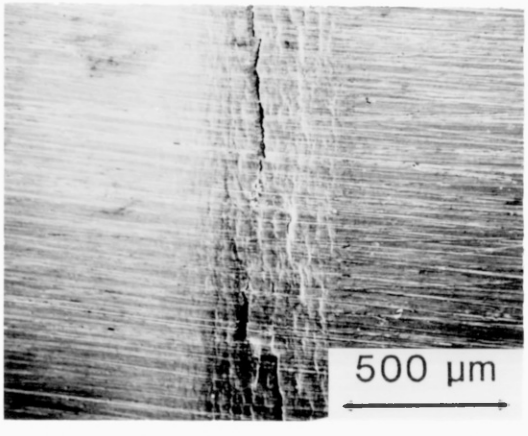
(b)



(b)



(c)



(c)

Figure 4.50

(a) Localised wavy slip bands and cracks formed at these slip bands on the bend apex of the sample from alloy UD aged at 400°C for 25 min. Both slip bands and cracks are perpendicular to the bending direction.

(b) Slant fracture surfaces after the sample of (a) was bent to larger angles for failure.

Figure 4.51

(a) Fracture surface of a sample from alloy D24, aged at 400°C for 25 min., containing three different regions, namely (i) the sheared region at the top, (ii) the middle part, deformed in mode I, and (iii) the bottom part, deformed under compression.

(b) Shear dimples from the mode II region in (a).

(c) Equiaxed dimples from the mode I region in (a).



Figure 4.50 (a)

30 μm



(b)

30 μm

Figure 4.51 (a)



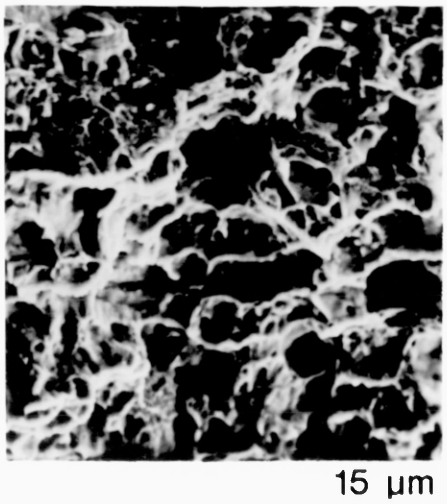
30 μm

(b)



15 μm

(c)



15 μm

SEM micrographs taken from one of the fracture surfaces of the sample from alloy D24, aged at 400 °C for 25 minutes, given in Figure 4.51, show three regions across the thickness, namely:

(A) shear fracture region (deformed in mode II) where the slant fracture occurs initially; the surface contains shear dimples, oriented in shear directions, which are reverse on opposite surfaces, as shown in Figure 4.51-b.

(B) the region where equiaxed dimples are present (beneath the shear fracture region) as shown in Figure 4.51-c; tensile stresses give rise to the "opening mode" denoted as mode I.

(C) the region where the cross section is compressed during bending; this part (the bottom region in Figure 4.51-a) was not fractured and was separated by hand after the test for microscopy.

It was noticed that the shear fracture region for samples aged at 350°C covers almost all of the fracture surface on the tension side. This suggests that the sudden rupture, which is the characteristic failure of alloys aged at 350 °C, occurs in shear mode. The border separating the compressed region and the equiaxed dimple region is the neutral plane where zero deformation occurs; during elastic deformation the neutral axis is situated in the middle of the sample, but during plastic deformation it shifts towards the inner surface.

4.9 Texture Determination for Cu-Be-Co Alloys

The texture, as a documentation of crystal-orienta--tion distributions in a material, is characterised with ideal orientations, consisting of the crystal planes parallel to rolling plane (hkl) and the crystal directions parallel to rolling direction <uvw>. Two dimensional pole figures, which describe the orientation distributions with

contour lines, are usually employed to determine several orientation components often existing simultaneously. Often, more than one pole figure is desirable to characterise the texture of a given material. In this respect, the textures for Cu-Be-Co strip alloys (solution treated and solution treated plus cold rolled) were determined, using (111) and (200) pole figures. The specific (hkl)<uvw) orientations were determined on the experimental pole figures according to the method described by Hansen et al. (1978). The results for recrystallisation texture after solution treatments, rolling texture after prior cold work in the range 10 to 41% RA, and the annealing texture of prior cold worked alloys will be presented in the following sections.

4.9.1 Recrystallisation texture

In section 4.2, it has been shown that the micro--structure of solution treated alloy consists of recrys--tallised grains, containing annealing twins. The X-ray pole figures (111) and (200) of solution treated alloy, shown in Figure 4.52-a, also indicated recrystallisation texture. The texture, shown in both pole figures (Figure 4.52-a), was identified with the indices (X) (210)<001> and (□) (225)<73$\bar{4}$> plus (O) (522)<$\bar{4}$55> and, in addition, some retained rolling texture (●) (146)<21$\bar{1}$> was present. The (225)<73$\bar{4}$> texture is renowned as brass type recrystallisa--tion texture, but the other orientations are intermediate to copper and brass type recrystallisation texture, and their occurrence depends on the deformation history prior to solution treatment.

4.9.2 Rolling texture

The (111) and (200) pole figures for alloys, prior cold rolled to 10, 21, 32, and 41% reduction in thickness, are given in Figure 4.52-b, c, d, and e, respectively. The pole figures show a continuous transformation in texture from copper type to brass type with the increase in amount

of cold rolling. The transformation from copper to brass type texture is much clearer on (200) pole figures, and the change in the orientations corresponding to the texture intensity maxima are as follows:

(i) After 10% prior cold work, there was a break away from recrystallisation texture; the (210)<001> orientation (x) was replaced by (110)<001> (◆) and some other odd texture intensities (Figure 4.52-b). Also, a spread of orientations, which were determined to be from (522)<$\bar{4}$55> (O) to (146)<21$\bar{1}$> (●) and intermediate orientations such as (123)<63$\bar{4}$> (*) and (326)<63$\bar{4}$> (⧫), were used to describe the texture at this deformation level. The (146)<21$\bar{1}$> orientation is very close to (123)<41$\bar{2}$>, which is renowned as the copper type rolling texture.

(ii) After 21% prior cold work, there was no trace of either (210)<001> or (110)<001> orientations, but the extent of the spread orientations, observed in 10% prior cold rolled alloy, reached (110)<$\bar{1}$12> (■), which is the extreme in the texture spread for brass type (Figure 4.52-c).

(iii) After 32% prior cold work, the spread of orienta--tions from (522)<$\bar{4}$55> to (110)<$\bar{1}$12> was the same as that observed for 21% prior cold worked alloy, but the texture intensity at (110)<$\bar{1}$12> became more pronounced while those of intermediate orientations were reduced (Figure 4.52-d).

(iv) After 41% prior cold work, the spread of texture texture maxima corresponding to the intermediate orienta--tions diminished entirely and the (110)<$\bar{1}$12> orientation, which is the brass type ideal texture, became the predominant texture.

It must be noted that the development of the brass type texture by a gradual transition via various inter--mediate orientations, with the increase in the amount of prior cold work, could not be distinguished on (111) pole

figures (Figure 4.52-b to d). This is because many of the intermediate orientations, e.g. (123)<63$\bar{4}$>, (146)<21$\bar{1}$>, are in the same region of the (111) pole figures as the (110)<$\bar{1}$12>. Nevertheless, the texture maxima on the (111) pole figure became more intense with the increase in prior cold work as it induced a gradual transition to brass type texture.

4.9.3 Annealing texture of prior cold worked alloys

The annealing texture of prior cold worked alloys was investigated after ageing at 400°C for 18 and 60 minutes; also, for the 41% prior cold worked alloy, the ageing treatments were extended to 4 hours at 400 and 500°C in order to determine the effect of recrystallisation on rolling texture. Selected (111) and (200) pole figures, obtained after ageing prior cold worked alloys at 400 and 500°C for maximum ageing times, are shown in Figure 4.53.

Ageing prior cold worked alloys at 400°C for 1 hour did not cause in any change in the texture and the related orientations, described for each alloy in above section (see Figures 4.52-b to d and 4.53-a to c). However, the (200) pole figures for 41% prior cold worked alloy, aged for 4 hours at 400 and 500°C (Figure 4.53-d and e), revealed a second texture intensity maximum, represented by (110)<$\bar{1}$12> orientation (■).

Although the (111) pole figures did not reveal much information, concerning the texture orientation distribu--tions, they generally indicated a characteristic change in the intensity of the texture maxima during annealing. Ageing 21, 32 and 41% prior cold worked alloys at 400°C for 18 minutes resulted in an increase in the intensity of the texture maxima on (111) pole figures, and with prolonged ageing for 1 hour the intensity reduced almost to original intensity levels, as shown in Figure 4.54. However, the increase in the texture intensity of the 10% cold worked alloy was less than those of heavily deformed alloys, and continuous for ageing times up to 1 hour. On further ageing the 41% prior cold worked alloy at 400°C for 4 hours, the

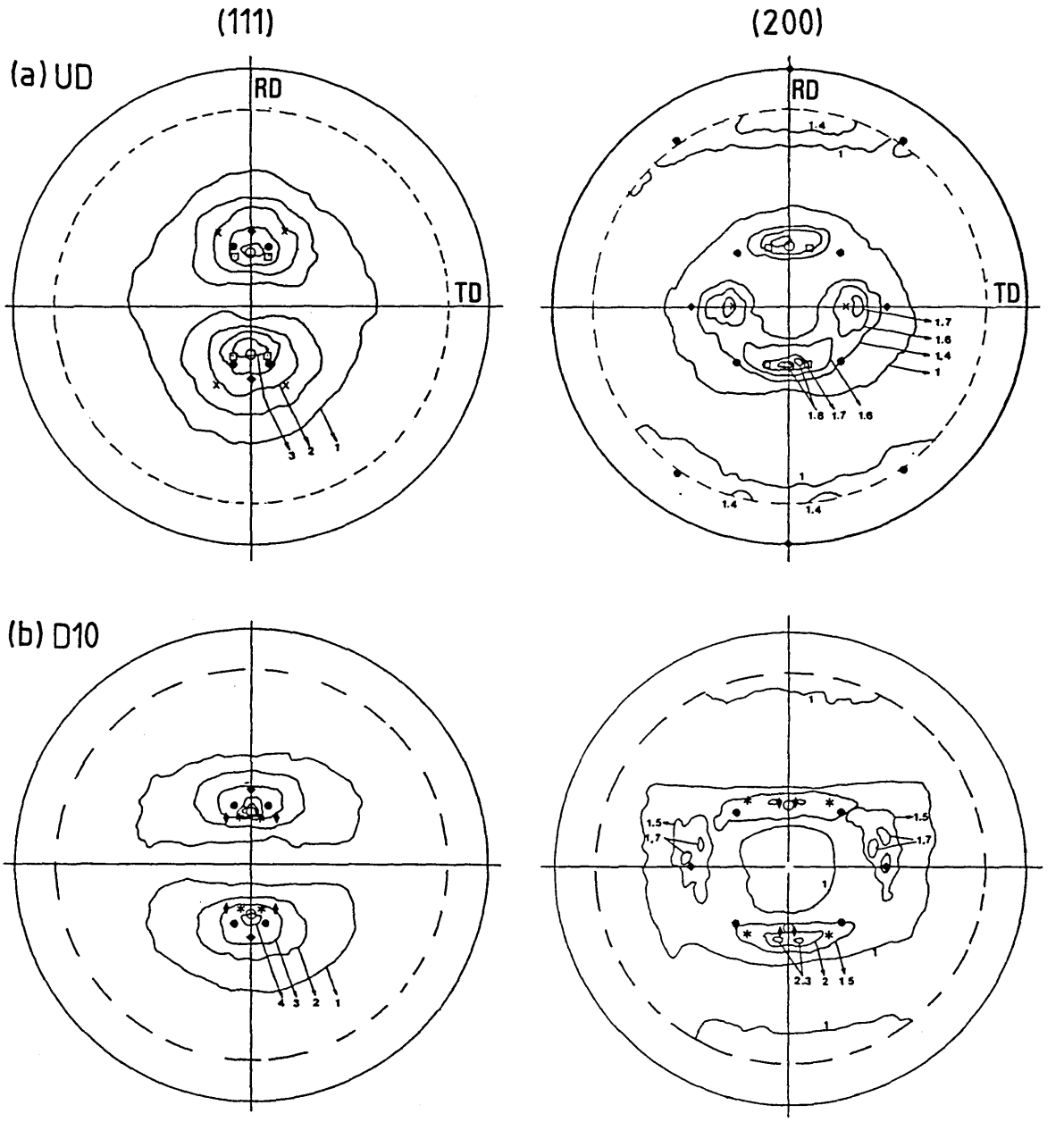
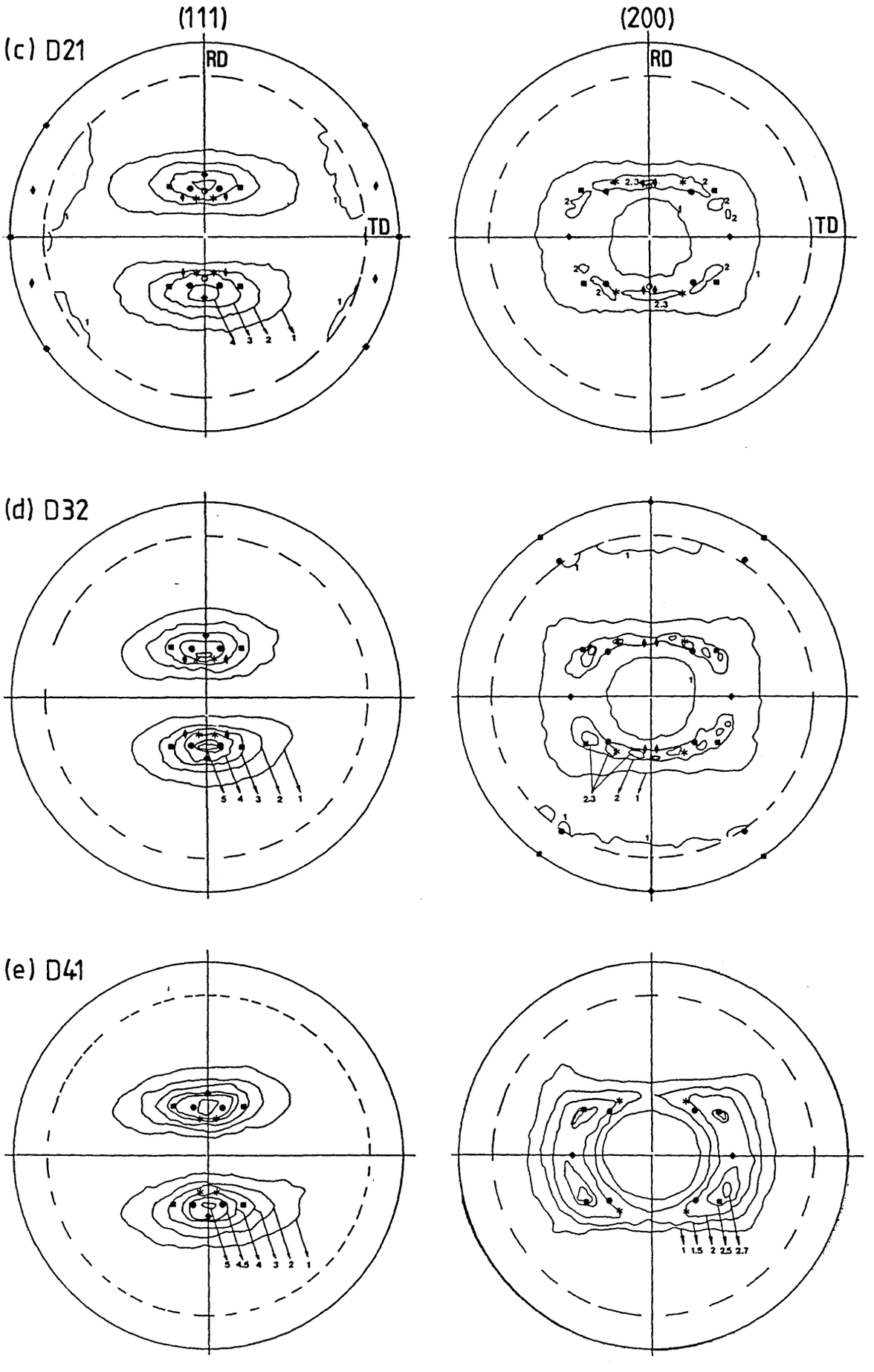


Figure 4.52- (111) and (200) pole figures of alloys (a) UD, (b) D10, (c) D21, (d) D32, and (e) D41 before ageing. Orientations indicated with different signs are:

(●) (146)<21$\bar{1}$>
(■) (110)<$\bar{1}$12>
(✳) (123)<63$\bar{4}$>
(◆) (110)<001>
(⧫) (326)<63$\bar{4}$>
(○) (522)<$\bar{4}$55>
(□) (225)<73$\bar{4}$>
(X) (210)<001>


(111)
(200)
(c) D21
RD
TD
RD
TD
(d) D32
(e) D41

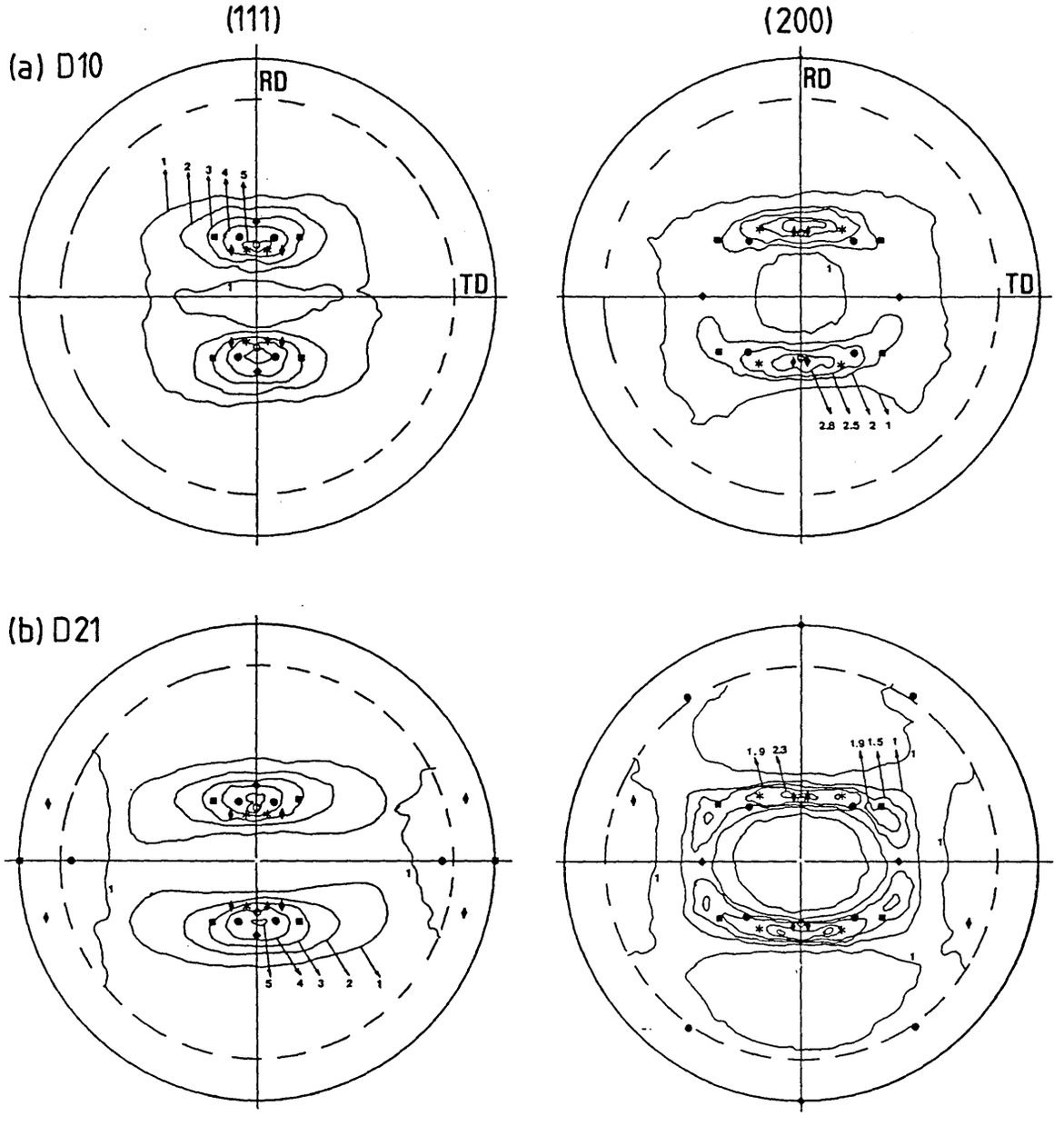
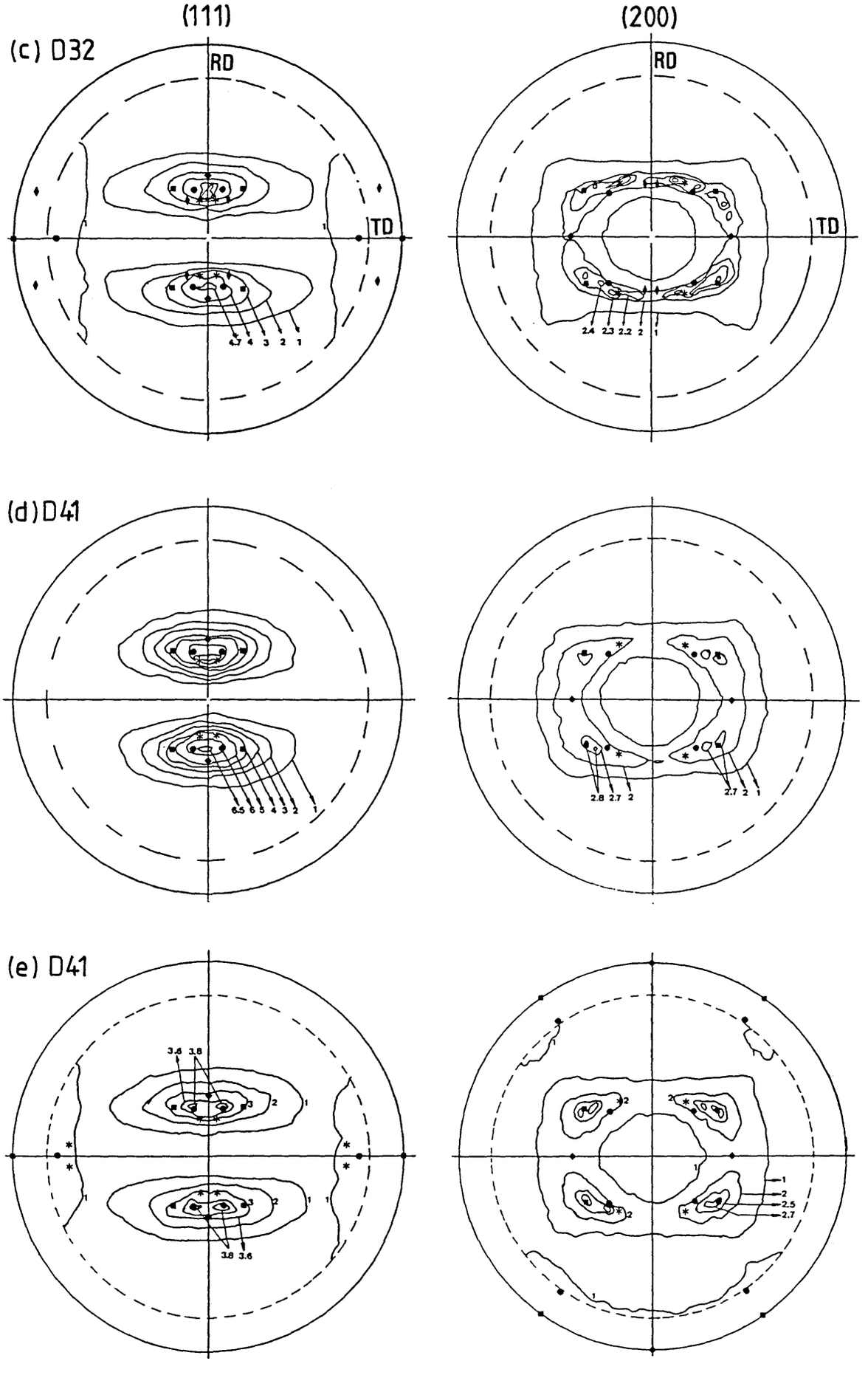


Figure 4.53- (111) and (200) pole figures of alloys (a) D10, (b) D21, and (c) D32, aged at 400°C for 1 hour, (d) D41, aged at 400°C for 4 hours, and (e) D41 aged at 500°C for 4 hours. Orientations indicated with different signs are:

(●) (146)<21$\bar{1}$> (⧫) (326)<63$\bar{4}$>

(■) (110)<$\bar{1}$12> (○) (522)<$\bar{4}$55>

(✳) (123)<63$\bar{4}$> (◆) (110)<001>


(111)
(200)
(c) D32
RD
TD
RD
TD
4.7 4 3 2 1
2.4 2.3 2.2 2 1
(d) D41
6.5 6 5 4 3 2 1
2.8 2.7 2
2.7 2 1
(e) D41
3.6 3.8
3.8 3.6
1
2
2.5
2.7

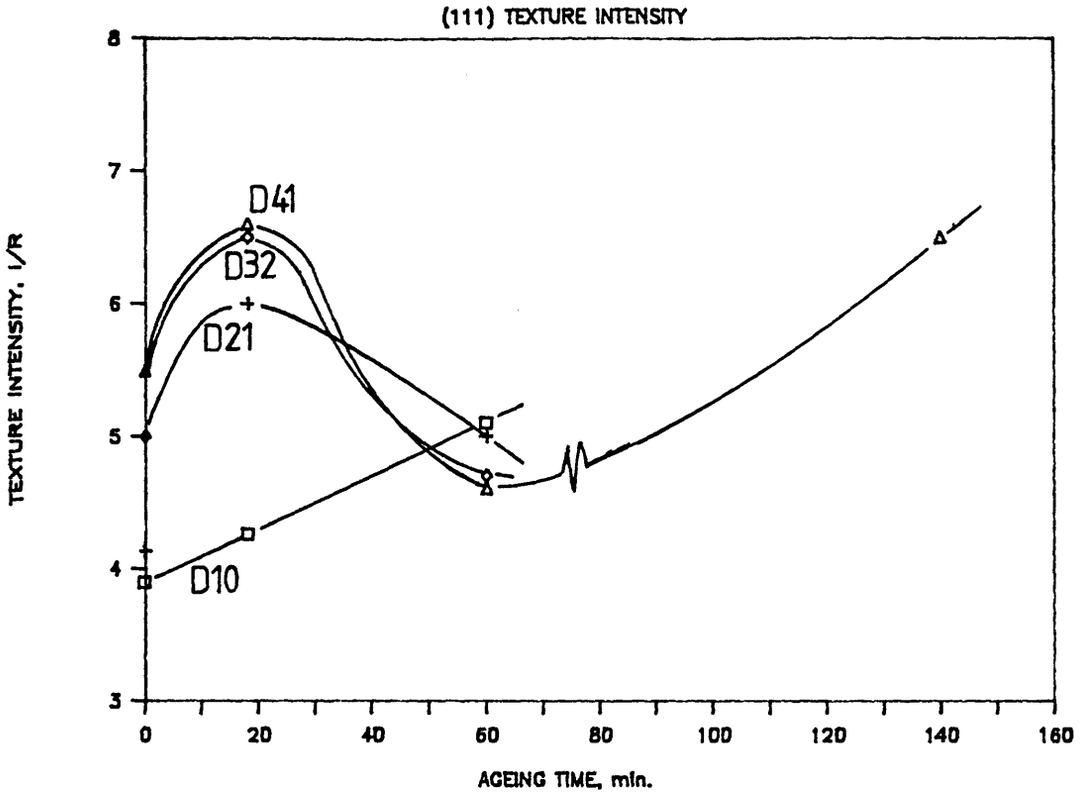


Figure 4.54- Change in the intensity of the texture maxima on (111) pole figures of alloys D10, D24, D32, and D41, during ageing at 400°C.

intensity of texture maxima increased again (Figure 4.54).

4.10 Electrical Resistivity Measurements

The change in electrical resistivity of alloys UD, D10, D24, D32, and D41 during ageing at 300 and 380 °C are compared on the plots of the fractional resistivity change, $\Delta\rho=(\rho_1-\rho_0)/\rho_0$, as a function of ageing time, given in Figure 4.55-a and b. During ageing at 300°C, the resisti--vity curve of the solution treated alloy (UD) showed an initial increase in resistivity to a maximum (10 minutes), followed by a continuous decrease. In contrast, the fractional resistivity change, $\Delta\rho$, of prior cold worked alloys reduced sharply to a plateau, and after about 10 minutes ageing started to fall again (Figure 4.55-a). The reduction in $\Delta\rho$ and the rate of decrease both increased with increasing amount of prior cold work.

On ageing at 380°C, the resistivity of the solution treated alloy and all prior cold worked alloys reduced continuously over the complete time range (Figure 4.55-b). Also, the increasing prior cold work accelerated the decrease in $\Delta\rho$ of the alloys during ageing. In general, the rate of reduction in resistivity was high up to a certain ageing time, and then it started to decrease; the ageing time corresponding to this change is indicated with an arrow for each alloy in Figure 4.55-b. It appears that the ageing time for the start of the decrease in the rate of resistivity reduction becomes shorter with increaseing amount of prior cold work.

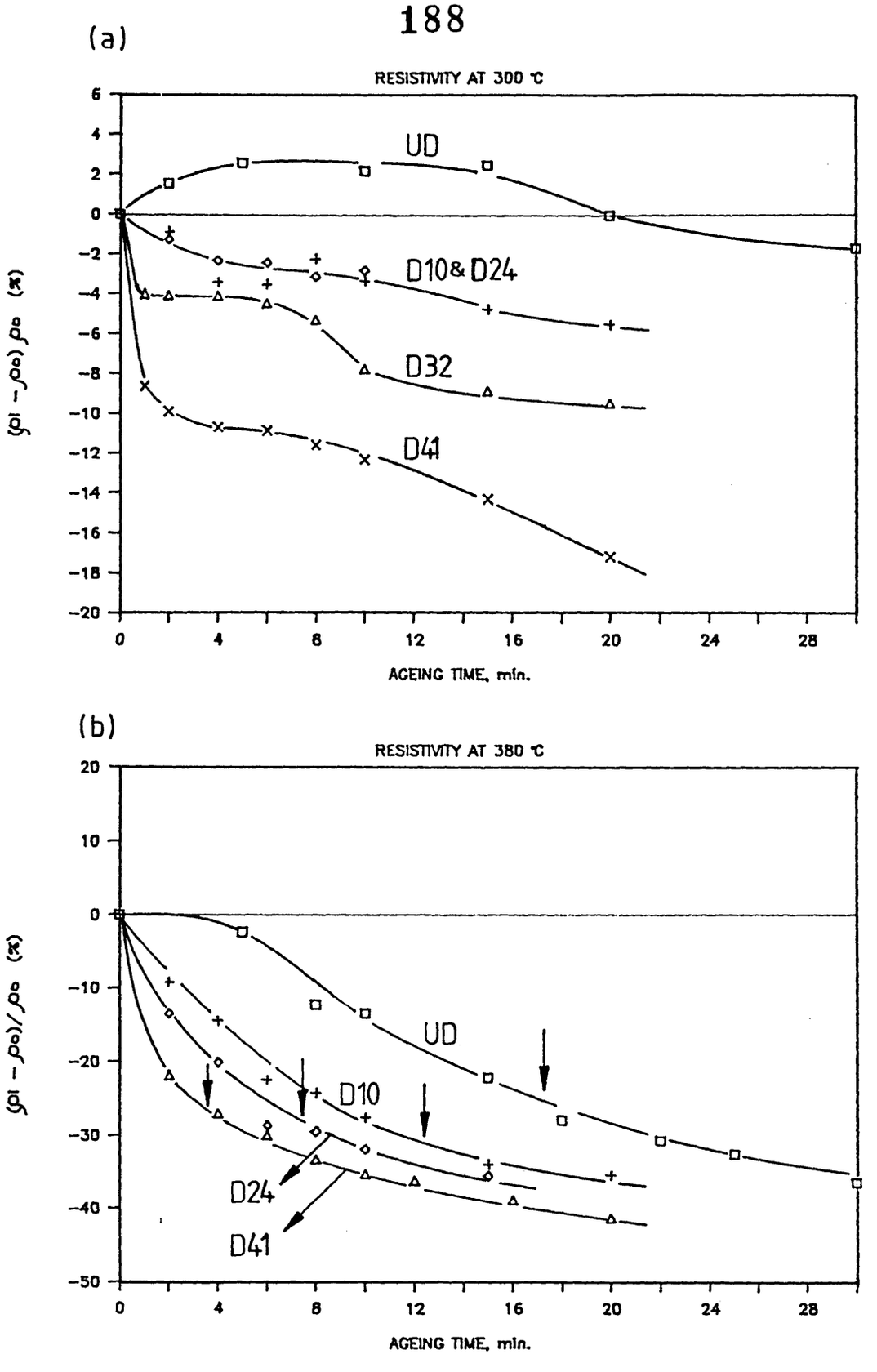


Figure 4.55- Change in the fractional resistivity change, $\Delta\rho$, of alloys UD, D10, D24, D32, and D41, during ageing at (a) 300°C and (b) 380°C.

CHAPTER 5

DISCUSSION

The decomposition reactions in solution treated Cu-Be alloys have been widely studied in the literature. Various models concerning the precipitation sequence, mechanism, and morphology, etc., have been proposed. However, there has been limited investigation on the effect of prior cold rolling on the precipitation mechanisms; the available information always covers only a certain range of prior cold work, which in most cases involved large strains (50% RA and above), and therefore are not directly applicable to the commercial production of the alloy. This is because large deformations are not usually introduced to the alloy in the industry since the strip material becomes too brittle for the following forming processes.

In addition, the effect of thermo-mechanical treat--ments on mechanical properties, among which formability is the most important parameter for sheet metal shaping appli--cations, has not been thoroughly investigated. Most of the previous work is limited to the spring back properties of contact materials, and some on formability analysis has been conducted on a qualitative basis for the industrial quality control purposes. In these cases, the related microstructural details have been obtained from only optical metallography.

The aim of the following discussion is therefore to have a better insight into the interrelation between the mechanical properties after various heat treatment regimes and the corresponding microstructural details; this information is essential for the development of a continu--ous strip process for the production of mill-hardened Cu-Be alloys capable of being formed. Also, some micro--structural details, which are not clear in the literature, will be discussed and compared with the results of the previous investigations.

5.1 Precipitation Hardening in the Solution Treated Alloy

5.1.1 The microstructure after isothermal treatments

Most of the interpretations in the literature, concerning the occurrence and the precipitation mechanisms of G.P. zones, the γ' and the γ phases, are in fair agreement. In contrast, the occurrence of the γ'' phase prior to the γ' has been a matter of considerable debate, details of which are given in Section 2.4.3.

The TEM investigations of the present work have shown that the occurrence of G.P. zones and the γ' and/or the γ'_D phase is temperature dependant. In summary, G.P. zones nucleate the γ' in the matrix at a temperature below 400°C, and the γ' precipitates are finely dispersed in the matrix. However, at higher temperatures the γ' phase forms directly in the matrix without G.P. zones being formed, and the γ' precipitates possess a larger particle size and spacing than these nucleated by G.P. zones. At 350°C, the growth of the γ'_D precipitates that form a cellular structure is limited to the original grain boundaries. At higher temperatures the cellular growth is more extensive and predominates until a considerable amount of the γ' precipitate forms in the matrix and pins the cellular interface so hindering growth.

From the experimentally determined solvus curves for metastable phases in binary Cu-Be alloys (Laughlin and Tanner, 1981; Shiromizu et al., 1971), the solvus tempera--ture for the G.P. zones, corresponding to the Be content of the present alloy, 1.9wt%Be, is estimated to be about 410°C (see Figure 2.1-b). However, the TEM investigations in the present work have shown the absence of the G.P. zones at 400°C. In previous investigations, the solvus curve for the G.P. zones has been determined for Cu-Be binary alloys. However, small amounts of Co addition are known to retard G.P. zone formation (Bonfield and Edwards, 1974) by either increasing the density of grain boundaries due to the reduction in grain size and hence increasing the

loss of vacancies at grain boundaries, or trapping of vacancies by Co atoms, which consequently reduces the rate of G.P. zone formation significantly (Murakami et al., 1968). In either event, Co atoms cause a reduction in the amount of quenched in vacancies which are necessary for the transport of Be atoms to the nuclei of G.P. zones, denoted as the clusters.

One would expect that, at a critical ageing tempera--ture, the vacancy annihilation rate exceeds the rate of G.P. zone nucleation, and hence the available vacancy concentration becomes much less than that required for the transport of Be atoms to the nuclei of the G.P. zones. Thus, above the critical temperature the G.P. zones cannot be nucleated in the matrix. Similarly, the presence of Co atoms in the structure is believed to reduce the vacancy concentration by either of the mechanisms, described above, and hence becomes responsible for lowering the solvus temperature.

Furthermore, clusters, which are usually reported as Be-vacancy complexes (Be atoms with usually more than one vacancy), may be formed during quenching and grow during the early stages of ageing (Wilkes, 1968; Wilkes and Barrand, 1968; Lawley et al., 1967). The electrical resistivity results have shown that on ageing at 300°C the fractional resistivity change, $\Delta\rho$, reaches a maximum value and then drops below zero. It has been established that a resistance maximum corresponds to a critical cluster size at which a maximum scattering for the conducting electrons occurs because the cluster size (≈1-2 nm) becomes compar--able with the estimate of the electronic mean free path length (≈2 nm) and hence the boundaries of the clusters result in a maximum scattering of electrons (Rossiter amd Wells, 1971). Further growth of the clusters induces the nucleation of the G.P. zones and results in the transition from increasing to decreasing resistivity; this process occurs gradually as observed in Al-Zn and Al-Ag alloys (Rossiter and Wells, 1971; Rossiter, 1985). This phenomenon was found to occur in the solution treated alloy; as can be seen in Figure 4.55-a, it is clear that the critical

cluster size is achieved after ≈10-15 minutes of ageing at 300°C. The drop in $\Delta\rho$ on further ageing therefore corresponds to the growth of the clusters and finally the nucleation of G.P. zones.

At 380°C, the change in $\Delta\rho$ does not yield a maximum, but the resistivity curve initially shows a plateau before $\Delta\rho$ begins to decrease (see Figure 4.55-b). This suggests that due to a greater thermal activation at this temperature the G.P. zones form before the clusters reach a critical size to give a maximum scattering of conducting electrons and the associated resistance maximum. The nucleation of the G.P. zones results in the decrease in the resistance that was observed after the plateau region of the resistivity curve. This is in general agreement with the previous resistivity studies of Cu-Be alloys by Thomas and Wilke-Dörfurt (1959) and Sachslehner et al. (1984); they reported that the upper temperature limit at which a resistivity maximum can occur is about 325°C.

It is now possible to conclude that the solvus temperature for G.P. zones in the present solution treated Cu 1.9%Be 0.25%Co alloy alloy can be described more speci--fically as a temperature between 380 and 400°C. It must be noted that in the previous investigations, the effect of discontinuous γ'_D precipitation on the resistivity change has not been considered. The present results show that the formation of individual γ'_D precipitates at grain bound--aries does not noticeably affect the resistance, whereas the development of cellular precipitation seems to contrib--ute an additional factor to reduction in $\Delta\rho$ that occurs after the plateau on the resistivity curve.

Concerning discontinuous precipitation in the sol--ution treated alloy, the present results suggests that the the cellular reaction involves the nucleation of several plate-like γ'_D precipitates heterogeneously from the super--saturated solid solution and the growth of the precipita--tes as the interface of the cells migrates, sweeping through the matrix. The continuous γ' precipitation in the α_0-matrix during the cellular growth introduces a pinning effect as well as reducing the Be content in the matrix,

and hence the cellular reaction seems to be hindered. This is in agreement with previously obtained results from Cu-Be binary alloys (Tsubakino and Nozato, 1978; Tsubakino et al., 1981; Nakagawa, 1968).

Also, it is well known that Co segregates at grain boundaries and forms the finely dispersed Co-Be or Cu-Be-Co particles in the matrix and/or at grain boundaries, as well as remaining in the solid solution as Co-vacancy pairs (Baumann and Williams, 1980; Williams, 1980). The presence of Co in the matrix and at grain boundaries in any form reduces the boundary mobility below 380°C in a manner analogous to the effect of third elements on recrystall--isation, as suggested by Bonfield and Edwards (1974). According to the "pucker" type mechanisms for discontinuous precipitation, confirmed in the present work (see Figure 4.7-a), the grain boundary migration rate determines the rate of discontinuous reaction. Thus, the presence of Co in the structure is bound to reduce the rate of discontinuous precipitation, and therefore the formation of the meta--stable phases in the matrix is favoured; such effects, induced by Co addition, should be taken into account when comparing the present results with those obtained previously from binary alloys.

As far as the occurrence of the δ'' phase is concerned, the evolution of the features in the TEM dark field micrographs and the corresponding SADP's on ageing at both 350 and 400°C does not provide evidence for the presence of a phase intermediate between G.P. zones and γ'. However, it has been shown that the G.P. zones, which formed on $\{100\}_\alpha$ habit planes, nucleate the γ' precipitates. The γ' nucleation is basically the growth of the G.P. zones over a critical size, which induces changing of the habit plane from {100} to {112}, as shown previously in Figure 4.9. In agreement with the TEM results, the interpretation of various types of heat liberation during the isothermal DTA runs has shown the occurrence of the G.P. zones and the γ' in the matrix and the γ'_D at grain boundaries. But, no particular heat liberation for γ'' precipitation has been found, which is consistent with the TEM observations.

An alternative mechanism for γ' nucleation in the matrix, proposed by Sachslehner et al. (1984), is that the G.P. zones should dissolve to facilitate the growth of the γ' precipitates that are nucleated in between the zones. It is generally found in non-isothermal DTA and DSC experi--ments that the dissolution of any phase results in an endothermic peak, e.g. the dissolution of the G.P. zones and the metastable η' in an Al-Cu-Mg alloy (Lloyd and Chaturvedi, 1982; Howard et al., 1985) and that of the G.P. zones in Al-Cu alloys (Thompson, 1969). Indeed, the differential calorimetry studies on Cu-Be binary alloys (Gavrilenko et al., 1968 & 1969) have indicated a slight endothermic heat liberation at about 300°C, but it is not clear whether this corresponds to G.P. zone dissolution. In the present work, both isothermal and non-isothermal DTA traces have shown no indication of an endothermic peak for the dissolution of the G.P. zones, suggesting that the G.P. zones nucleate the γ' precipitates. Alternatively, the heat associated with the exothermic formation of γ' may outweigh that due to the endothermic dissolution of G.P. zones and hence the latter process was not detected.

In summary, the most probable precipitation sequence at 350°C is that the G.P. zones, formed on the $\{100\}_\alpha$ habit planes, nucleate the γ' precipitates. The transformation of G.P. zones to the γ' phase is a continuous ordering process that involves a gradual change in the orientation of the "over-grown" G.P. zones until the habit plane is aligned to $\{112\}_\alpha$. This is partly similar to the mechanism proposed by Baburaj et al. (1979), but differs in the sense that the ordering process is not the evolution of the equilibrium γ phase, initiated by G.P. zone formation. Various propositions, cited in the literature (Rioja and Laoughlin, 1980; Yamamoto et al., 1971; Geisler et al., 1952; Shimizu et al., 1971), as to the presence of the γ'' phase intermediate to the γ' were not substantiated. At higher temperatures, i.e. T>380°C, the G.P. zones cannot form and the γ' precipitates are nucleated directly from the solid solution with the same structure and the crystallography as those of the γ'_D precipitates.

5.1.2 Change in the features of diffraction lines during ageing

During the ageing process of the solution treated alloy, the diffraction lines undergo an asymmetrical line broadening (see Figure 4.23). In summary, the broadening involves the following processes:

(i) the formation of a shoulder on the small angle scat--tering side of the I_0 peak, which later leads to the development of a second peak, I_1,

(ii) a reduction in the height of the I_0 peak, and

(iii) the shift of both the I_0 and I_1 peaks towards short angles.

The present TEM and X-ray diffraction investigations on ageing the solution treated alloy at 350°C show that the reduction in the height of the I_0 peak starts with the formation of G.P. zones and becomes more marked during the nucleation and the growth of the γ' precipitates. As suggested by Gitgarts and Tolstoy (1979), the elastic anisotropic displacements due to continuous precipitation in the α_0-matrix may also be partly responsible for the decrease in the height of the I_0 peak.

The reduction in the height of the I_0 peak could also be attributed to the cellular reaction at grain boundaries that involves the formation of large plate-like γ'_D precipitates. The TEM observations indicate that the development of large γ'_D precipitates results in a considerable Be denudation in the cells and therefore the α-matrix is reoriented in these regions. The reoriented matrix, denoted as the α_1-matrix, gives reflections on the diffraction lines that initially produce a shoulder at the small angle scattering side of the I_0 peak (normal reflect--ions). On further ageing, the shoulder develops into the I_1 peak. As the cellular reaction advances, the volume of the reoriented matrix (the α_1-matrix) increases and hence

the intensity of the I_1-peak also increases. Thus, peak I_1 can be used to monitor discontinuous precipitation, whereas, the I_0 peak represents the α_0-matrix where continuous precipitation takes place. The reduction in the volume of the α_0-matrix therefore results in a decrease in the intensity of the I_0 peak, in addition to that contributed by the elastic anisotropic displacements due to continuous precipitation in the α_0-matrix.

It may now be possible to relate the I_0 and I_1 peaks to the microstructural changes in the α_0- and α_1-matrices, respectively. In this respect, the onset of the shift of both I_0-and I_1 peaks towards lower angles, in other words the onset of the increase in the lattice parameter of the α_0- and α_1-matrices, corresponds to (i) continuous precipi--tation and (ii) discontinuous precipitation, respectively. In fact, Miki et al. (1983) and Nakagawa (1968) have used the change in the lattice parameter of the α-matrix to follow γ' precipitation in the matrix; the α-matrix in their work corresponds to the α_0-matrix here. They did not however consider continuous and discontinuous precipitation separately.

The present results show that at 350°C the G.P. zone formation results in a very small increase in the lattice parameter, a_0, of the α_0-matrix ($\Delta a_0 \approx 0.0005$ nm, as can be seen in Figure 4.26), whereas the onset of the large increase in a_0 corresponds to the nucleation of the γ' precipitates in the matrix. At 380°C, the presence of the initial small increase in a_0 suggests that the G.P. zones can still form at this temperature, but nucleate the γ' precipitates earlier than at 350°C; this is evident from the shift in the onset of the large increase in a_0 towards shorter times with the increase in temperature. In contrast, at 400°C the initial increase in a_0 is not observed, indicating that the G.P. zones cannot form at this temperature. Therefore, the γ' precipitates form directly from the supersaturated solid solution and the time for the onset of the γ' nucleation is shortened due to thermal activation. With reference to the TEM and the electrical resistivity results, discussed in the above section,

it may be concluded that the solvus curve of G.P. zones for the present alloy composition is at a temperature between 380 and 400°C.

It is clear from Figures 4.26 and 4.27 that, the increase in a_1 occurs earlier than that of a_0, i.e. γ'_D precipitation at grain boundaries precedes γ' precipitation in the matrix. Also, there is an acceleration in the kinetics of γ'_D precipitation with increasing temperature, as can be followed by the shift in the onset of the increase in a_1 towards shorter ageing times with tempera-ture in Figure 4.27.

5.1.3 Hardening response during ageing

The hardening response of the solution treated alloys has been found to change with ageing temperature. Comparison of the hardness curves of the alloy in Figure 4.1 with the results from TEM, X-ray diffraction, and isothermal DTA investigations demonstrates that on ageing at 350°C, the hardening in the alloy is achieved by the following reactions:

(i) γ'_D precipitation at the original grain boundaries that results in the slight increase in hardness prior to the sharp increase, and

(ii) G.P. zone formation and γ' precipitation via the G.P. zones, which correspond to the sharp increases in hardness to a maximum value.

The BF micrograph in Figure 4.7-a shows that the formation of the individual γ'_D precipitates in "puckered" condition at grain boundaries precedes G.P. zone formation. However, it seems that the γ'_D precipitation of this type does not noticeably contribute to the hardness increase since the volume of these precipitates is very low at the initial stages of ageing. During the increase in hardness to a maximum, G.P. zones nucleate the γ' precipitates in the matrix, and the completion of this process corresponds

to the beginning of the plateau on the hardness curve (see Figure 4.1), at which the peak hardness is achieved. The initiation of hardening takes longer at 350°C than at higher temperatures since the solute diffusion is slower and the the incubation period for G.P. zone formation is prolonged. However, a larger maximum hardness increment was achieved at this temperature than at higher temperatures. This is mainly attributed to the γ' precipitates being finely dispersed in the matrix.

During the cellular growth at 350°C, accompanying the continuous γ' precipitation in the matrix, the plate-like γ'_D precipitates in the cells grow to large dimensions, i.e. 10-15 times larger in plate length than that of the γ' precipitates in the matrix, and hence the γ'_D precipitates do not contribute to the hardening to the same extent as the γ' precipitates. In the presence of the finely dispersed γ' precipitates, the role of cellular precipitation is to reduce the attainable hardness by γ' precipitation in the matrix in proportion to the extent of the reaction. However, cellular precipitation does not extensively occur at this temperature; the X-ray diffraction lines show that the intensity of the I_1 peak, which is used as a measure of cellular precipitation, is much lower than that at higher temperatures as can be seen in Figure 4.23. This suggests that the contribution of the large γ'_D precipitates towards reducing the hardness is much less than that at higher temperatures.

In the preceding sections, it has been shown that G.P. zones can form even at 380°C when they subsequently nucleate the γ' phase in a short time; this occurs after ≈17 minutes of ageing at 380°C according to the lattice parameter measurements of the α_0-matrix (see Figure 4.26). However, at 380°C, a considerable intensification of the I_1 peak, which is associated with the discontinuous precipita-tion, occurs in a period as short as 5 minutes and becomes more pronounced with prolonged ageing than that at 350°C, as illustrated in Figure 4.23. This suggests that the cellular precipitation precedes G.P. zone formation and therefore corresponds to the initial slow increase in

hardness. On further ageing, the G.P. zones form and subsequently nucleate the γ' precipitates. This results in overshooting of the hardness to a maximum (see Figure 4.1), but the maximum hardness is much lower that that at 350°C. This is followed by a drop in hardness to a plateau that is attributed to extensive cellular precipitation, involving repeated nucleation and growth of large γ'_D precipitates in the α_1-matrix. This process also accompanies the coarsening of the γ' precipitates in the α_0-matrix.

As described previously, on ageing at higher temperatures (T>380°C), the γ' precipitates are nucleated directly from the supersaturated solute solution and have a larger particle size and spacing than those nucleated by the G.P. zones below 380°C. Also, it has been shown that the formation of the large plate-like γ'_D precipitates in a cellular reaction is the predominant mode until the advancing interface of the cells are stopped by the γ' precipitates in the matrix. Therefore, the cellular precipitation and the coarser distribution of the γ' precipitates at higher temperatures must have a considerable contribution to reducing the overall hardening. Considering that cellular growth occurs more readily at 400°C and above, engulfing the grain interior, one would expect a large reduction in hardness as the γ'_D precipitates grow in size, and therefore the overall hardening becomes less in comparison to that achieved at lower temperatures.

It must be noted that, on ageing at 400 amd 420°C, cellular precipitation is responsible for the onset of hardening, and the peak hardness is achieved by both cellular precipitation and the formation of the γ' precipitates directly in the α_0-matrix. After peak hardness has been attained there was a plateau region on the hardness curves, and the hardness did not drop noticeably for ageing times as long as 100 minutes. This is attributed to the growth of γ' precipitates in the matrix, reducing the kinetics of cellular precipitation. The γ' precipitates grow in size in a shorter time than that at lower temperatures and most probably introduce a pinning effect at the advancing interface of the cellular reaction. Thus, the

hardness of the alloy is maintained at a high level for up to 100 minutes of ageing due to consecutive precipitation at grain boundaries and in the matrix.

5.1.4. Current TTT diagrams proposed for Cu-Be alloys

The precipitation mechanisms in Cu-Be alloys are complicated by the overlapping matastable phase transfrom--ations. Although a considerable amount of work has been carried out by previous investigators to present the decomposition process by constructing temperature-time-transformation (TTT) diagrams, those TTT diagrams are mostly based on a single technique, such as lattice parameter measurements (Nakagawa, 1965) and hardness measurements (Tsubakino and Nozato, 1978; Tsubakino et al., 1981; Entwisle and Wynn, 1961), in some cases the hardness data are complemented with electrical conductivity and tensile strength measurements (Toda, 1970) or the TEM investigations (Jovanovic et al., 1986). The data obtained by employing some of these methods, e.g. hardness tests, do not successfully reflect details of overlapping microstruc--tural changes during ageing the alloy, i.e. γ'_D and γ_D precipitation at grain boundaries and the formation of G.P. zones, the γ', and the γ phases in the matrix. In addition, in previous investigations the alloy compositions differed considerably from current commercial alloys and in most cases the studied ageing temperatures did not fully cover the anticipated temperature range for industrial production.

Nevertheless, the trend of the data from the previously obtained results generally indicates the existence of an upper and a lower "C" curve for both continuous and discontinuous precipitation. An additional "C" curve at intermediate temperatures compared to the upper and the lower "C" curves has also been proposed for continuous precipitation, as shown in Figure 2.18-a and b (Tsubakino and Nozato, 1978). The temperatures, separating these "C" curves seem to increase with Be content and reduce with the ternary Co addition.

5.1.5 The present TTT diagrams for the solution treated alloy

By means of the usual experimental methods of X-ray diffraction, hardness, TEM, etc. it is difficult and time consuming to analyse the overall precipitation kinetics, and to determine the factors affecting the occurrence of various types of precipitates. Therefore, a method that would sensitively monitor the microstructural changes during ageing is required; it was for this reason that the isothermal DTA and DSC techniques were assessed in the present investigation. The isothermal DTA and DSC tech--niques have been widely used to study the crystallisation kinetics in various types of glasses and ceramics on the basis of the formal theory of transformation kinetics, which was summarised in Appendix A. Recently, the use of the isothermal DTA or DSC techniques to estimate the TTT diagrams for the devitrification in glasses has been shown to be feasible (Uhlmann, 1983; Esnault-Grosdemouge et al., 1985; Zarzycki, 1982). The advent of good DTA and DSC equipments in late 1950s made it possible to follow the kinetics of precipitation in alloys relatively easily and quickly and in a manner that is often more sensitive than the usual experimental methods. However, the use of DTA and DSC techniques in precipitation studies has been limited to the non-isothermal investigations, and the data have been used mostly to construct phase diagrams. To the authors' knowledge, isothermal DTA and DSC techniques has not been previously used to determine TTT diagrams for precipitation in alloys.

In the present work, the isothermal DTA peaks of Cu-Be-Co alloys, obtained from the runs at temperatures in the range 300 to 500°C (Figure 4.39), have provided detailed information about the kinetics of decomposition reactions. The onset and the completion of the nucleation of G.P. zones, the γ' and the γ'_D, were determined from the isothermal DTA peaks; the plots of the data demonstrated the presence of the separate "C" curves for each reaction, as shown in Figure 5.1. Complementary data were also

obtained from other techniques, and the criteria used to produce the data were as follows:

(i) the characteristic features in the TEM micrographs and the corresponding SADPs, obtained from samples from the isothermal DTA runs and from isothermal heat treatments,

(ii) ageing time, required for the onset of the increase in the lattice parameter of both the α_0- and the α_1-matrices,

(iii) ageing time, required for the onset of the increase and the following decrease in half-breadth of the I_0 peaks; these were used for only prior cold worked alloys, and

(iv) ageing time, required for the onset of the hardening and that for maximum hardness.

The data, deduced via these criteria, are indicated by different signs on the temperature-time-transformation diagrams, as shown in Figure 5.1, and demonstrate a good agreement with the isothermal DTA results. The implication of each "C" curve and the corresponding details are given in Table 5.1. For convenience, the reaction kinetics for the various "C" curves, proposed in the present work for the solution treated alloy, will be discussed separately with reference to the occurrence of continuous and discontinuous precipitation.

Before discussing the details of the TTT diagrams, it must be noted that according to the features, identified by the TEM investigations, it is clear that the onset of different types of heat liberation during the isothermal DTA runs represent only nucleation and early stages of growth of various phases in the sequence of precipitation, but not the main growth process. This is evident from the experimental results, namely:

(a) The TEM micrographs of both deformed and undeformed samples reveal the continuation of growth of the γ' and the

γ'_D precipitates after the heat liberation during the isothermal DTA runs is completed.

(b) The increase in the lattice parameter, a_0, of the α_0-matrix occurs continuously but with a reduced rate after the completion of the heat liberation during the DTA runs at a temperature. For example, at 400°C, only 70% of the increase in a_0 occurs after 30 minutes of ageing, which corresponds to the completion of the DTA peak.

Considering that the increase in a_0 is proportional to the amount of reduction in Be content in the α_0-matrix, most of Be atoms (≈70%) are removed from the solid solution in the early stages of ageing, which also involves the growth of certain amount of γ'. The growth of γ' then becomes a slow process since the Be content in the surrounding regions is reduced considerably during nucleation and Be atoms have longer diffusion path to travel. The slow nature of the process suggests that the growth reaction produces very little heat in a given time period and this is most probably beyond the sensitivity of the DTA equipment. This may be analogous to the heat liberation during recrystall--isation that can only be detected with the aid of a micro-calorimeter, as described in Section 4.5. However, there is a possibility that when the growth of precipitates proceeds at faster rates the heat involved may contribute to the overall heat liberation though it is not possible to resolve this on the DTA peaks. Nevertheless, having determined the onset of each reaction, the isothermal DTA curves serve their purpose well and enable the modes of precipitation at different temperatures to be established and a TTT diagram to be produced easily.

5.1.6 TTT curves for continuous precipitation

The description of each "C" curve, illustrated in Figure 5.1, and the details of the corresponding data are given in Table 5.1. In summary, the "C" curves, marked by B, C, and F, corresponds to the onset of (i) G.P. zone

formation, (ii) γ' formation via G.P. zones, and (iii) γ' formation directly from the supersaturated solid solution in the absence of the G.P. zones, respectively.

In Sections 5.1.1 and 5.1.2, the presence of a solvus temperature for the G.P. zones between 380 and 400°C has been shown to be plausible for the solution treated alloy. As can be seen in Figure 5.1, both "C" curves for the G.P. zones (curve B) and the γ' phase, nucleated directly from the solute solution above the solvus of the G.P. zones (curve F), cross at T_2, suggesting a solvus temperature for the G.P. zones, which is closely estimated to be ≈385°C. This value has not been determined rigorously by previous investigators and the values, given in the literature for alloys with similar Be contents to that of the present alloy, were not more than a temperature range, i.e. 350 to 400°C (Jovanovic et al., 1986, 325 ±10°C (Tsubakino and Nozato, 1978). However, their methods were not able to detect the onset of γ'_D precipitation at the original grain boundaries (curve A in Figure 5.1) which will be discussed in the following section.

In previous investigations, it is assumed that below a temperature or a temperature range, which is equivalent to T_2 here, the decomposition reaction is initiated by G.P. zone formation in the matrix, and hence the reaction is mostly represented by a single "C" curve. Whereas, it is evident from the microstructural details, discussed in above sections, that G.P. zone nucleation occurs after the pucker-type γ'_D precipitation at grain boundaries. With prolonged ageing, the γ' precipitates are nucleated by G.P. zones. Considering that the sequence of nucleation reactions follow the path of increasing magnitude of the critical activation free energy, ΔG^*, for the formation of a critical nucleus, the kinetic approach of Rioja and Laughlin (1980) seems to be applicable for explaining the successive nucleation process, described in the present work, and hence further details are referred to the corresponding discussion in Section 2.6.1.

The features observed on the TEM micrographs and the corresponding SADPs, are indicated by the arrow-marked abbreviations on the TTT diagram, details of which are given in sub-section 4.2.1-(2). Although the TEM data are limited to certain ageing treatments, they show a complete agreement with the data from the other techniques employed. For example, on ageing at 350°C, the sequence of precipita--tion, namely the discontinuous γ'_D precipitation, followed by the continuous reaction, identified as the α_0-matrix $\longrightarrow$ G.P. zones$\longrightarrow$ γ', is well defined by the TEM results. Thus, curves A, B and C in Figure 5.1 describe the mechanisms of various types of precipitation in a more precise manner than these proposed in the literature. It must be noted that any change in the heating condition to a temperature may result in shifting of these "C" curves; the direction of the shift will depend on the heating rate.

On ageing above T_2, two subsequent reaction, namely the consecutive precipitation of the γ'_D at grain bound--aries and γ' in the matrix occur as can be followed by curves G and F, respectively, in Figure 5.1. Experimental data for γ' precipitation (curve F) at higher temperatures are not available, and therefore the extent of the curve F above 420°C (broken part of the curve) illustrates schematically the acceleration in γ' precipitation due to thermal activation. On this assumption, it is concluded that although discontinuous precipitation inducing cellular growth dominates at the initial stages of ageing, with prolonged ageing the γ' precipitates in the matrix grow in size and seems to interfere with the cellular growth; this will be discussed in detail in the following section.

5.1.7 TTT curves for discontinuous precipitation

From the above sections, it is known that the decomposi--tion of the supersaturated solid solution starts with the discontinuous nucleation of the γ'_D precipitates at grain boundaries. As can be followed by "C" curves in Figure 5.1, there seems to be a change in the kinetics of γ'_D precipi--tation with temperature, which is evident from the

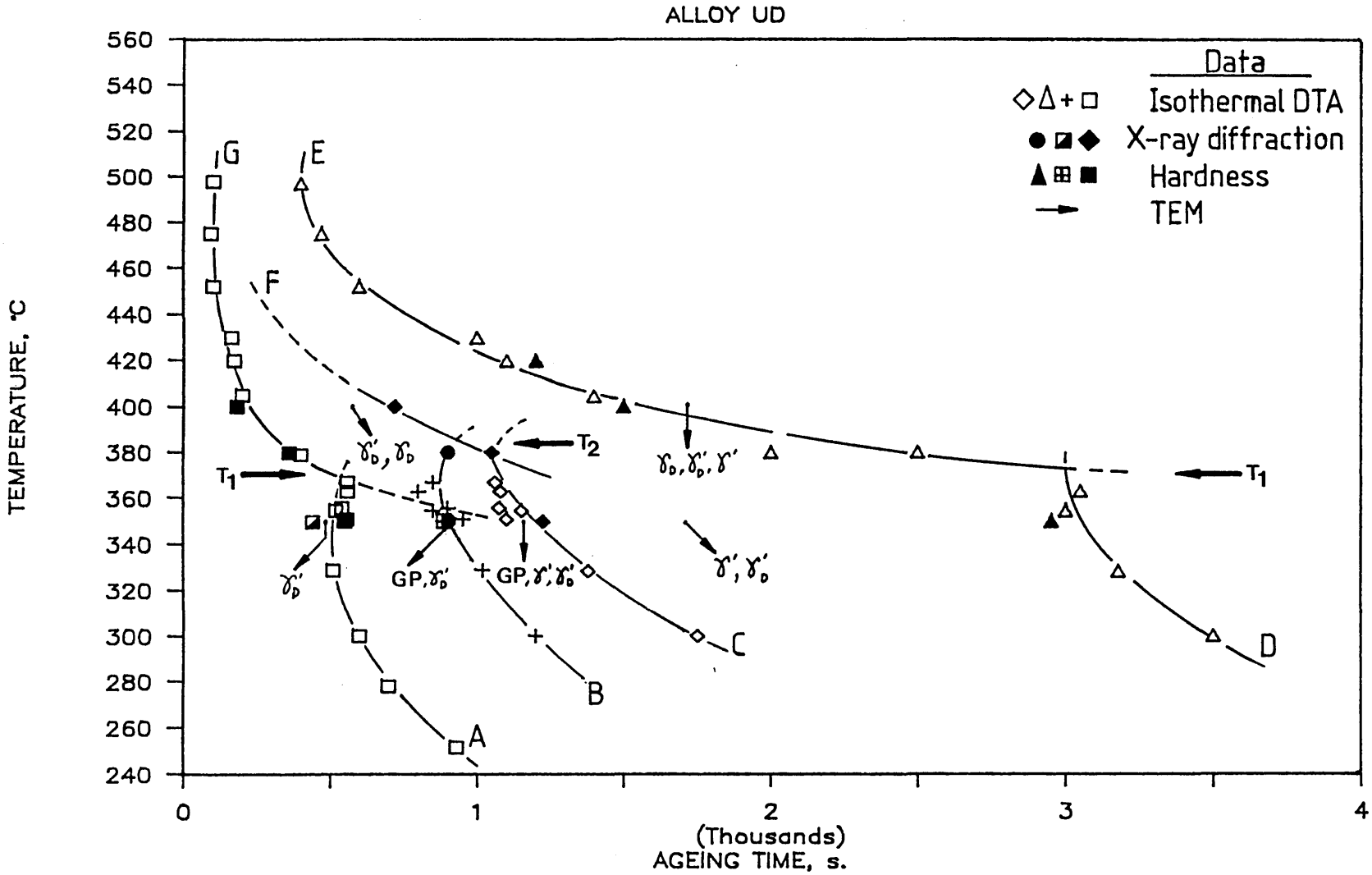


Figure 5.1- TTT diagrams for the solution treated alloy (see Table 5.1 for details of symbols).

Table 5.1

Description of "C" curves for the solution treated alloy, given in Figure 5.1

Curve	Temperature limit (°C)	Experimental evidence	Implication
A	$T \leq T_1 = 370$	(TEM) = γ'_D precipitation in puckered position at original G.B. (X-ray) = (◪) Onset of the increase in a_1 of the α_1-matrix (DTA) = (□) Onset of the isothermal DTA peaks (Hardness) = (■) Onset of the small increase in hardness prior to the sharp increase.	Discontinuous γ'_D precipi-tation at original G.B.
B	$T \leq T_1 = 385$	(TEM) = The presence of the G.P. zones that corresponds to SR in the SADP's. (X-ray) = (●) The initial little increase in a_0 (DTA) = (+) Onset of the first step on isothermal DTA peaks (Hardness) = (■) Onset of the sharp increase in hardness	G.P. zone formation in the matrix
C	$T \leq T_2 = 385$	(TEM) = Development of IM on the (100) continuous streaks in the SADP's (X-ray) = (◆) Onset of the large increase in a_0 (DTA) = (◇) Onset of the second step on isothermal DTA peaks	γ'nucleation in the matrix by the G.P. zones
D& E	$T < T_1 = 370$ $T > T_1 = 370$	(DTA) = (Δ) Times for the completion of isothermal DTA peaks (Hardness) = (Δ) Time to attain peak hardness	Completion of any type of nucleation event
F	$T \geq T_2$	(X-ray) = (◆) onset of the increase in a_0	γ' nucleation directly in the α_0-matrix
G	$T > T_1$	(TEM) = Cellular reaction inducing γ'_D and γ_D precipitation (DTA) = (□) Onset of isothermal DTA peaks (Hardness) = (■) Onset of hardening	Cellular reaction, inducing γ'_D and γ_D precitation, engulfing the α_0-matrix

presence of an upper and a lower "C" curves for the same reaction, namely curves A and G, separated at $T_1 \approx 370°C$. In contrast, previously obtained results by Tsubakino and Nozato (1978) and Tsubakino et al. (1981), using the data from hardness measurements, suggest that, as exemplified in Figure 2.18, the onset of γ'_D precipitation at grain boundaries is represented by a single "C" curve designated t_1, and below a temperature, T_2, the precipitation in the matrix is represented by another "C" curve (t_2), which precedes the formation of the γ'_D precipitates at grain boundaries. It is clear that the use of the isothermal DTA technique in the present work offers a more sensitive detection of the γ'_D precipitation than the use of hardness data. In this respect, the reaction kinetics relevant to the presence of an upper and a lower "C" curves for γ'_D require further discussion. Therefore, the following section will concentrate on the kinetics of discontinuous precipitation in the solution treated alloy and its temperature dependence.

5.1.7.1 Kinetics of discontinuous precipitation in the solution treated alloy

In the above sections, two types of discontinuous precipitation have been described; these are (i) γ'_D precipitation at grain boundaries and (ii) cellular growth involving repeated nucleation and growth of γ'_D precipita--tes during concurrent cell-boundary migration. For convenience, the former will be referred to as "stage I" and the latter "stage II" type precipitation, and the kinetics of both reactions may be explained as follows:

(a) Stage I: The pucker type γ'_D precipitation on grain boundaries occurs in the initial stages of ageing. The initiation and the growth mechanisms for γ'_D precipitation, observed in the present work, are in agreement with the altered "pucker-type" model of Baumann et al. (1981), details of which has been discussed in detail in Sections 2.5.2 and 2.5.3. In order to avoid confusion as to the

temperature dependent nature of γ' nucleation, i.e. different nucleation mechanisms have been observed in Cu-Be alloys on ageing below and above $T_M/2$=500°C (see Section 2.5.2), it must be clarified that the studied ageing temperatures were below 500°C, and therefore the nucleation of a series of the plate-like γ'_D precipitates can occur on both sides of a grain boundary without the aid of the thermally activated grain boundary migration. The γ'_D precipitates are nucleated at an energetically favoured orientation with the matrix, i.e. $(113)_\alpha$ // $(130)_{\gamma'_D}$; $[110]_\alpha$ // $[001]_{\gamma'_D}$, and the growth of the precipitates induces the grain boundary movements, which brings the boundary into the favoured orientation (see Figures 2.11 and 4.14). Once the γ'_D precipitates form in series at a grain boundary, the grain boundary bows into the solute rich α-matrix between the precipitates, which will produce a cell boundary on further ageing.

(b) Stage II: The growth reaction on both sides of the boundary induces the formation of the double seam morphology, which is denoted as the cellular structure in the preceding sections. As the interface of the cells sweeps through the matrix, the Be content behind the interface reduces sharply, leaving the Be denuded (reoriented) α_1-matrix and the plate-like γ'_D precipitates; the lattice parameter of the α_1-matrix is much larger than that of the α_0-matrix due to γ'_D and/or γ_D precipitation that occurs before a considerable anount of matrix precipitation takes place. This process involves repeated nucleation and growth of several γ'_D precipitates behind the advancing interface of the cells into the α_0-matrix.

Both the stage I and II precipitations were followed more closely by the non-isothermal DTA runs at high heating rates (α>15°C/min.), at which continuous precipitation in the matrix cannot occur. The non-isothermal DTA peaks revealed two types of heat liberation, which are identified as peak C and peak B for stage I and II precipitation, respectively (see Figure 4.29). It has been shown that the

nucleation and growth of the individual γ'_D precipitates at grain boundaries (stage I) are less dependant on the heating rate than the nucleation and growth of the γ'_D during the cellular reaction (see Figure 4.31). Among various possibilities, the prior solute segregation at grain boundaries that may occur during the solution treatment is likely to be responsible for reducing the temperature dependency of γ'_D precipitation. On the other hand, the growth of the individual γ'_D precipitates (stage I) is believed to be controlled by volume diffusion until it results in a considerable reduction in Be content in the surrounding regions of the α_0-matrix since no cell boundary has yet developed. During this process, the boundary is brought into the alignment with the habit plane of the precipitates. This process indicates similarities with that observed in Pb-Sn solder alloys by Tu and Turnbull (1967). According to Tu and Turnbull, the movement of the grain boundary, until the completion of the alignment, is aided by the difference in the surface energies of the precipi--tate/matrix and the precipitate/boundary interfaces (for details, see Section 2.5.2). Alternatively, Meyrick (1974) proposed that during the growth of the γ'_D precipitates, the depletion of the solute population at the boundary increases the effective grain boundary energy, and the boundary bows into the adjacent matrix in order to reduce its energy. Either of the mechanisms ultimately indicates that the movement of the boundary results in the development of a cell of precipitates.

Once the cellular structure develops, the repeated nucleation and the growth of the γ'_D precipitates is controlled by the velocity of the interface of the cells. As can be seen in Figures 4.10 and 4.11, the cell boundary bows into the matrix between the plate-like γ'_D precipita--tes in the cell, having the centre of curvature in the cells. Since the orientation dependency of γ'_D formation is strictly defined, the repeated nucleation of the γ'_D would occur whenever the orientation of the boundary is in alignment with that of the γ' precipitates. The growth of these precipitates will then depend on the rate of boundary

diffusion to search for fresh solute. The growth rate of the cells, G, can therefore be closely described by Turnbull's expression based on the boundary diffusion mechanism (Turnbull, 1955):

$$G = [(C_0-C_E)/C_0]D_B\delta/S \qquad [5.1]$$

where, in the present case, C_0 and C_E are the Be concen--tration of the α_0- and the α_1-matrices respectively, S the interparticle spacing of the γ'_D precipitates, D_B the grain boundary diffusion coefficient of Be atoms in the α1-matrix (in the cells), δ the boundary thickness along which the solute atoms can diffuse rapidly. Recently, more complex equations have been suggested to replace equation [5.1], as reviewed by Hillert (1972), but principally all the theories were based on above expression.

The TEM investigations on the non-isothermally tested DTA samples have shown that above a critical heating rate (α>15°C/min.) the grain-interior precipitation cannot occur (see Figure 4.30) and the only reaction is γ'_D precipitation in a cellular reaction, which engulfs the interior of the grain. This suggests that the cellular reaction occurs at a faster rate than the continuous precipitation since the boundary diffusion has a lower activation energy than that of the volume diffusion. However, in isothermal conditions, as the ageing tempera--ture falls and the ageing time is prolonged, the matrix precipitation gradually becomes dominant.

5.1.7.2 Upper and lower "C" curves for discontinuous reaction

The presence of two "C" curves, marked by A and G in Figure 5.1, for discontinuous precipitation may be explained by the change in the kinetics of stage I and stage II reactions. In general, the pucker type boundary precipitation is seen as a precursor to the initiation of cellular reaction. Since the ageing temperatures are below $T_M/2\approx500$°C the boundary is effectively immobile before the

pucker type γ'_D precipitation commences. When γ'_D precipi--tation commences the movement of the boundary becomes vital for continuation of the process. It is expected that a single "C" curve should represent the initiation of γ'_D precipitation at grain boundaries, as shown with the broken line connecting curves A and G in Figure 5.1. However, the shape of curves A and G suggests that there is a delay in the kinetics of γ'_D precipitation at temperatures in the range 340 to 380°C.

It is well recognised that, in the presence of boundary inclusions or of matrix precipitates in front of the boundary, the kinetics of discontinuous precipitation are reduced considerably. When continuous precipitation in the matrix occurs readily before cellular precipitation, an additional contribution to the suppression of discontinuous γ'_D precipitation is introduced by the reduction in the solute content of the matrix. In addition, as can be seen in Figure 5.1, the "C" curve for G.P. zone formation (curve B) becomes closer at temperatures approaching 370°C, suggesting that the acceleration in G.P. zone formation has some effect on the growth of the γ'_D nuclei. From the previous sections, it is known that the clusters, formed during quenching, grow to a critical size prior to G.P. zone nucleation and hence a considerable drop in C_0 occurs at this stage. Also, the presence of a high binding energy between Be atoms and vacancies at the nuclei of the zones, $E = 0.32 \times 10^{-19}$ J according to Wilkes (1968), indicates that Be atoms are trapped at the growing clusters. During this process, the overall vacancy concentration is reduced considerably (Wilkes, 1968). Consequently, this means an increase in the energy required for the diffusion of Be atoms to the γ'_D precipitates. Therefore, it is tentatively suggested that once Be atoms are trapped at the clusters, the transfer of Be atoms from the clusters, which are about to nucleate the G.P. zones, to the nearest γ'_D nuclei at a grain boundary is limited by an energy barrier, introduced by theabove mechanisms.

In this respect, it is presumed that even though the γ'_D nuclei initially form at grain boundaries there is a delay in the growth of the γ'_D nuclei and hence in the kinetics of cellular precipitation. However, this mechanism seems to be operative only up to T_1=370°C, at which there is an acceleration in discontinuous precipitation as marked by T_1, in Figure 5.1. As summarised in Section 2.9.2, it has been shown that in a Cu 1.8wt% Be 0.28wt% Co alloy (this is very close to the composition of the present alloy) the segregation of Co atoms at boundaries (Bonfield and Edwards, 1974) and the presence of the Co rich cuboidal particles of Be and Co in the structure (Baumann and Williams, 1980) are effective in suppressing discontinuous precipitation at temperatures below 380°C. Certainly, at higher temperatures, grain boundaries can break away from these obstacles. The presence of cuboidal particles in the matrix has been confirmed in the present work, but the Co segregation has not been investigated. Nevertheless, according to data from repeated isothermal DTA runs, from the onset of hardening, and from the onset of the I_1 peak development on the X-ray diffraction lines, the critical temperature for a boundary to overcome the dragging forces, introduced by Co segregation and/or the cuboidal particles, is T_1=370°C, which corresponds to the crossing point of curves A and G in Figure 5.1.

Previously it has been proposed that the clusters, which are precursors to G.P. zones may reduce the availability of Be atoms for discontinuous precipitation. It should be noted that longer times are required for G.P. zone formation at temperatures in the range 370 to 385°C, which suggests that the clusters do not grow so easily or are decomposing. In either case, discontinuous precipita-tion might be expected to be enhanced.

It is therefore suggested that the formation of the γ'_D precipitates at grain boundaries and the following cellular growth can occur more readily when the ageing temperature exceeds 370°C due to the change in the overall reaction kinetics, which may be summarised as follows:

(i) a major increase in G above 370°C by the elimination of the dragging forces introduced by the Co addition, and

(ii) a reduction in the kinetics of cluster growth and G.P. zone nucleation above 370°C and the absence of G.P. zones above $T_2 \approx 385°C$, and therefore a diminishing suppression effect on reducing the growth rate of the γ'_D nuclei and a greater growth rate, G, of the cells.

Furthermore, above the solvus temperature of the G.P. zones, γ'_D precipitation occurs relatively earlier than γ' precipitation in the matrix (see curves G and F in Figure 5.1). Therefore, in the absence of the γ' precipi--tates, which are known to introduce a dragging force for cellular precipitation by reducing the availibility of solute atoms and/or pinning the advancing interface of the cells, γ'_D precipitation at grain boundaries (stage I) is immediately followed by the cellular precipitation (stage II), engulfing the interior of grains. As shown in Figure 4.10-b, the cellular reaction induces the formation of both the γ'_D and the equilibrium γ_D precipitates in the cells. In this respect, curve G of Figure 5.1 effectively represents the onsets of stage I and stage II of the cellular reaction. Whereas, the extent of curve G below 370°C (shown dotted to a single data point) clearly indicates a delay in stage II precipitation with respect to stage I as the temperature decreases due to the aforementioned dragging forces.

So far the onset of discontinuous precipitation has been discussed, but it is also of interest to consider the finish of this form of precipitation. It is evident from the TEM micrographs (Figure 4.30) of the non-isothermal DTA sample, tested at a heating rate, α=20°C/min., that the repeated nucleation and growth of the γ'_D precipitates occur at the advancing interface of the cells into the matrix where continuous γ' precipitation had not occurred since an incubation period is required for γ' nucleation. However, under isothermal heating conditions, the γ' precipitates can form in the matrix and grow to large

diameters. It may be concluded that when the γ' precipita--tes grow to a critical size, at which they can effectively pin the advancing interface of the cells, the cellular growth is arrested, and further γ'_D nucleation and growth cannot occur. This process occurs more readily above 370°C due to thermally activated growth of γ' in the matrix (curve F). At lower temperatures the γ' precipita--tes are nucleated by the G.P. zones, and they are finely distributed in the matrix, and hence needs longer ageing times to grow a critical size at which they can effectively reduce the growth rate of the cells. The delay in the growth of γ' and the suppression of discontinuous precipi--tation can be followed by curve D that is situated at long ageing times. On the other hand, curve E demonstrates the completion of the more rapid γ' precipitation in the G.P. zone free matrix and the arrest of the cellular reaction that occurs earlier as the temperature increases. Curves D and E therefore show the arrest of cellular growth (stage II) by γ' precipitation in the matrix and a considerable reduction in the growth of the γ' precipitates due to the decrease in the amount of available solute.

5.2 Precipitation Hardening in Prior Cold Worked Alloys

The microstructural features developed on ageing the prior cold worked alloys have been determined using the techniques as applied to the solution treated alloy. The results concerning the sequence of precipitation at different temperatures, the morphology, crystallography, and the structure have shown a good agreement with the observations on the solution treated alloy. However, the reaction kinetics and the predominant mode of precipitation at different temperatures have been found to change as a function of prior cold work. The following discussion will therefore mainly focus on the particular differences in the decomposition reactions in prior cold worked alloys from that in the solution treated alloy. It must be noted that the decomposition reaction in prior cold worked alloys is complicated by the interdependency of the processes, namely

continuous precipitation, discontinuous precipitation, recovery, and recrystallisation.

5.2.1 TTT diagrams for prior cold worked alloys

The TTT diagrams for alloys D5, D10, D24, and D32 & D41 are given in Figures 5.2 to 5.5, respectively; the data points for alloys D32 and D41 mostly overlap and therefore a single TTT diagram is given for both alloys (Figure 5.5). Three sets of "C" curves, separated by the temperatures T_1, T_2, and T_3 or T_4, can be distinguished in these diagrams and, as before, the data points from the various techniques are specified by different symbols These symbols, as well as the attribution of precipitation reactions to each of the "C" curves, are summarised in Tables 5.2 and 5.3.

In order to avoid confusion that may arise from the different types of reactions taking place simultaneously, the curves for the same type of reactions are designated by the same letters, namely A, B, C, etc. that were used to describe the TTT diagram for the solution treated alloy. In the following sections, the reactions, which are responsible for each "C" curve, will be explained and the kinetics of the processes will be discussed in detail.

5.2.1.1 "C" curves for alloys D5, D10, and D24

Unlike the extensive γ'_D precipitation at grain boundaries in the solution treated alloy, a substantial reduction in the amount of discontinuous γ'_D precipitation occurred in parallel with the increase in prior cold work. The TEM investigations have shown that, for prior cold work up to 32% RA, γ'_D precipitation is confined to the original grain boundaries. On further ageing they are transformed to the equilibriun γ_D precipitates; this process being accompanied by recrystallisation. The time for the onset of discontinuous precipitation is shortened by prior cold work. However, as can be seen from a comparison of curves A and G in Figures 5.1, 5.2, and 5.3, a large acceleration in γ'_D precipitation is introduced by prior cold work when

ageing below 380°C, but at higher temperatures the prior cold work does not affect the reaction kinetics so notice--ably. The similarity in the shape of both curves A and G and in the temperature, $T_1 \approx 370°C$, separating the curves, with those for the solution treated alloy indicates that the mechanisms of γ'_D precipitation in prior cold worked alloys on ageing below and above T_1 are identical to those described as stage I and stage II precipitation in the solution treated alloy. Therefore, the reader is referred to the discussion in Section 5.1.7.1 for details of γ'_D precipitation mechanisms in these two temperature ranges.

The data corresponding to the onset of hardening (■) for both alloys D5 and D10 fall on curves A and G. This suggests that regardless of ageing temperature the onset of hardening in these alloys is attributable to γ'_D precipita--tion (stage I) although the major increase in hardness is achieved by continuous γ' precipitation on further ageing. On ageing 24% prior cold worked alloy above T_1, curve F for the continuous γ' precipitation and curve G for γ'_D precipitation overlap and hence hardening is initiated by both types of reaction. As discussed in Section 5.1.7.1, above T_1 the stage I precipitation occurs in a very short time and the stage II precipitation commences almost immediately. Thus, curve G can be taken to prepresent stage II precipitation. This was supported by the data from the half breadth measurements which reveal the onset of stage II precipitation; note that these data points (x) in Figures 5.3 and 5.4 show agreement with those from the isothermal DTA curves and the hardness measurements. The half breadth data also indicate a continuing reduction in the kinetics of the stage II precipitation below $T_1 \approx 370°C$, as can be followed in Figure 5.3 by a large deviation on the lower part of curve G towards longer ageing times. However, there seems to be an acceleration in the stage II precipitation with the increase in prior cold work to 24% RA since the same part of curve G is situated at shorter ageing times (see Figure 5.4).

Concerning continuous precipitation in alloys D5, D10, and D24, prior cold work introduced a more pronounced acceleration in G.P. zone formation and/or γ' precipitation in the matrix than that observed in γ'_D precipitation. The TEM investigations revealed that the incubation period for G.P. zone formation is shortened by increasing prior cold work, and that the zones immediately begin to transform to the γ' precipitates; note the development of the SSR which initiates from the IM on <100> streaks in the SADPs (Figures 4.12 and 4.13). The onset of both G.P. zone formation and γ' nucleation are represented by a single "C" curve, curve B&C for alloys D10 and D24, since the time required for the nucleation of G.P. zones and the following γ' nucleation by G.P. zones is considerably shortened by prior cold work. For alloy D5, the available data for the "C" curves, corresponding to these reactions, are limited to the information obtained from the isothermal DTA peaks and the hardness curves and hence curves K and L in Figure 5.2 correspond to times for the highest heat liberation during decomposition reactions. Since the predominant mode of reaction in alloy D5 is the continuous precipitation, it is believed that the peak of the DTA curves is a measure of γ' precipitation in the matrix.

For ageing below T_2=385°C which is the solvus temperature of the G.P. zones, a comparison of curves B for alloys D10 and D24 and curve K for alloy D5 in Figures 5.1 to 5.4 clearly shows a pronounced acceleration by prior cold work in the kinetics of G.P. zone formation and the following γ' precipitation. Previous work on Cu-Be and Cu-Be-Co alloys with similar compositions to that of the investigated alloys, (Nutting, 1971; Bonfield and Edwards, 1974) suggests that above 300°C prior cold work in the range 10 to 50% RA accelerates G.P. zone formation and consequent-ly γ' precipitation in the matrix; this was attributed to the recovery of dislocations that reduces the decrease in vacancy concentration during ageing (see Section 2.7.1 for details). This mechanism seems to explain the acceleration in continuous precipitation by prior cold work in the investigated alloys.

Above T_2, the continuous γ' precipitation without G.P. zone formation is also accelerated by prior cold work. Note that curve F is shifted towards shorter ageing times with the increase in prior cold work from 0 to 24%, as can be seen in Figures 5.1 to 5.4. Also, the corresponding TEM results has shown that on ageing prior cold worked alloys above the solvus temperature of G.P. zones, the SSR in the SADPs develop earlier than that in the solution treated alloy. Since the G.P. zones cannot form at these higher temperatures and the growth of the γ' nuclei is limited by the presence of a large mismatch at the interface, the acceleration in γ' precipitation in the matrix cannot be fully explained by the reduction in the rate of vacancy annihilation due to recovery. On the other hand, it is well recognised that dislocations can accommodate the elastic distortions, caused by intermediate precipitates in the matrix (Nutting, 1971; Kelly and Nicholson, 1963). It is therefore believed that the acceleration in γ' precipita-tion is aided by the presence of dislocations that can accommodate the elastic distortion of the matrix, caused by the semicoherent γ' precipitation.

Although it has been proposed (Djuric et al., 1980; Jovanovic et el., 1986) that above 350°C prior strain has no effect on the kinetics of precipitation in Cu-Be alloys, the "C" curves (curve F for alloys D5, D10, and D24; see Table 5.2) in Figures 5.1 to 5.4 clearly demonstrate the presence of a considerable acceleration in the continuous γ' precipitation on ageing above 380°C. When the prior cold work is increased to 24% RA, the acceleration in γ'precipi-tation becomes so effective that curve F for continuous γ' precipitation and curve G for discontinuous γ'_D precipita-tion overlap completely; the overlapping precipitation is evident from the data points that are situated closely on curve G&F (thick curve) in Figure 5.4.

The increase in the kinetics of γ' precipitation in the matrix after 24% prior cold work consequently results in a decrease in that of γ'_D precipitation at grain boundaries. It is evident from the TEM investigations that γ'_D precipitation is limited to the grain edges and certain

grain boundaries whilst the development of dislocation-free reoriented regions at boundaries gradually becomes the predominant mode of discontinuous reaction. The development of the reoriented regions was also observed in less cold worked alloys, but the reaction became more pronounced with increasing cold work. This may be followed by the development of I_1 profiles on the X-ray diffraction lines. As shown in in Figure 4.25, on ageing at 400°C for 10 minutes, as the prior cold work increases, the I_1 profile on the (111) line, which correspond to the reflections from the strain-free reoriented regions, becomes more intense.

For less deformed alloys, the overlapping precipitation does not occur, but curve F crosses curve G at $T_3 \approx 450$°C (see Figure 5.2 and 5.3), suggesting that the continuous γ' precipitation precedes the discontinuous γ'_D precipitation at temperatures above T_3. However, when the the prior cold work is increased to 24% RA, ageing above 450°C results in a considerable increase in the kinetics of recrystallisation. Indeed, the TEM investigations on the 24% cold worked isothermal DTA samples, tested at 500°C for 5 min. revealed the γ' precipitates in the matrix and the recrystallised grains, which are nucleated at grain boundaries, containing the equilibrium γ_D precipitates (Figure 4.41). Also, some grain boundaries exhibited only the strain-free regions, containing the γ'_D precipitates; the recrystallised grains had not fully developed. Therefore, it may be concluded that further growth of the strain-free regions to form recrystallised grains may be a slow process, in which the γ' precipitates in front of the advancing interface dissolve and consequently the equilibrium γ_D phase is formed at the interface with the available solute atoms.

The times required for peak hardening correspond to the development of a structure containing (i) the finely dispersed γ' precipitates in the matrix, nucleated by G.P. zones below $T_2 \approx 385$°C and (ii) the larger γ' precipitates, formed directly from the supersaturated solute solution, above T_2. The data for alloys D5 and D10, corresponding to the peak hardness, demonstrate a good agreement with the

isothermal DTA data, revealing the completion of the heat liberation; see the corresponding data points (+,Δ) on curves D and E in Figures 5.2 and 5.3. Thus, curves D and E reveal the completion of γ' precipitation in the matrix. The isothermal DTA data for the 24% cold worked alloy also illustrate the presence of curves D and E, but the data points indicating the hardness maxima above T_2 are situated at shorter ageing times. The TEM results show that the development of the strain-free reoriented regions is accelerated by prior cold work, and that the extensive growth of these regions, which will induce recrystall--isation on further ageing, corresponds to the drop in hardness after the maxima. Considering that the strain-free reoriented regions are softer than the deformed α_0-matrix, the onset of the drop in hardness from the maxima indicates the growth of reoriented regions at grain boundaries. In the 5% prior cold worked alloy, the hardness does not drop noticeably, suggesting that the amount of deformation is not enough to induce this process at the investigated temperature range (350-420°C); the complete hardness data are given in Table B.1 in Appendix B. In contrast to alloy D5, for 10 and 24% prior cold worked alloys, a considerable drop in hardness followed the sharp hardness maxima, and the extent of the drop in hardness increased with prior cold work (see Figures 4.2 and 4.3). The TEM observations and the appearance of I_1 profiles on the diffraction lines also suggest that the initiation of recrystallisation corresponds to the onset of drop in hardness, which follows the hardness peak.

In this respect, as mentioned earlier, the data on the TTT diagrams, which correspond to the hardness maxima for alloys D5, D10 (see the corresponding data points on curves D and E in Figures 5.2 and 5.3), reveal that γ' precipitation is completed at the hardness maxima. Therefore, the recrystallisation occurs in these alloys only after the completion of γ' precipitation in the matrix, whereas, after 24% prior cold work, the data of the same type do not coincide with curve E on ageing above T_2 (see Figure 5.4). This suggests that growth of the strain-

free regions accompanies continuous precipitation in the matrix in this temperature range; the onset of the recrys--tallisation may be closely represented by curve H. With reference to curves H and F in Figure 5.4, it appears that above $T_4 \approx 470°C$ the grain boundary migration, inducing recrystallisation, occurs almost at the same time as γ' precipitation in the matrix, perhaps earlier than that, since curve H crosses curve F (thick curve) at T_4, and at higher temperatures curve F seems to deviate slightly towards longer ageing times. Below T_4 the charac--teristic shape of curve H shows that the recrystallisation is suppressed, or the incubation period for recystallisa--tion increases as the ageing temperature is reduced. It must be noted that the recrystallisation can still occur behind or below curve H, e.g. after 10 minutes ageing the 32% deformed material at 350°C (Figure 4.15-b), but recrystallised grains are limited to the original grain boundaries.

5.2.1.2 "C" curves for alloys D32 and D41

The occurrence of γ'_D precipitation at original grain boundaries in the early stages of ageing at 350°C and 400°C has been clarified by the TEM investigations for the alloys, cold worked up to 32%. Furthermore, it has been shown that with prolonged ageing γ'_D transforms to the equilibrium γ_D precipitates. The transformation of γ'_D to γ_D corresponds to the development of recrystallised grains as the grain boundaries move into the deformed α-matrix. In these alloys, the recrystallisation was found to initiate at grain boundaries possibly in the regions of high dislocation density, and longer ageing times were required to initiate the recrystallisation as the ageing temperature and prior cold work was reduced.

However, after 32 and 41% prior cold work, the predominant mode of discontinuous reaction was recrystall--isation, inducing the equilibrium γ_D precipitation. The TEM investigations are limited to the selected ageing treatment regimes and therefore do not provide clear

evidence as to whether the grain boundary migration inducing recrystallisation results in γ'_D precipitation in the initial stages of ageing, as observed in less deformed alloys. Nevertheless, considering that small recrystallised grains are present at grain boundaries even after a short ageing treatment at low temperatures, e.g. Figures 4.15-b and 4.18-b of alloy D32, a considerable reduction in the kinetics of γ'_D precipitation must have occurred due to the presence of the γ' precipitates in the matrix at a more advanced stage than these formed in less cold worked alloys. This was in fact supported by the experimental data that unanimously indicate the overlapping of curves A and B&C below $T_2 \approx 380°C$ and curves G and F above T_2 (Figure 5.5) for continuous and discontinuous reactions, respectively (see Table 5.3 for the implication drown from the data points).

As explained above for the 24% deformed alloy, the discontinuous reaction results in a large drop in hardness, and this becomes more pronounced after 32 and 41% prior cold work, suggesting that the recrystallisation occurs more readily in these alloys. Curve H for both alloys D32 and D41, plotted according to the data corresponding to the onset of the drop in hardness at different temperatures (Figure 5.5) indicates that the growth of recrystallised grains into the deformed α_0-matrix is accelerated by the increase in prior cold work and the incubation period for this process is shortened. Note that curve H is shifted towards shorter ageing times and lower ageing temperatures with the increase in prior cold work from 24% to 41% and T_4, which is ≈470 °C for alloy D24, is reduced to 450°C.

According to the trend of the data for curve H and the microstructural features, revealed by the TEM investigations, for alloys D24, D32 and D41, the following are proposed:

(i) Below or behind curve H continuous precipitation in the matrix predominates whilst the discontinuous reaction, inducing recrystallisation and the equilibrium γ_D precipi-tation, takes place at the original grain boundaries.

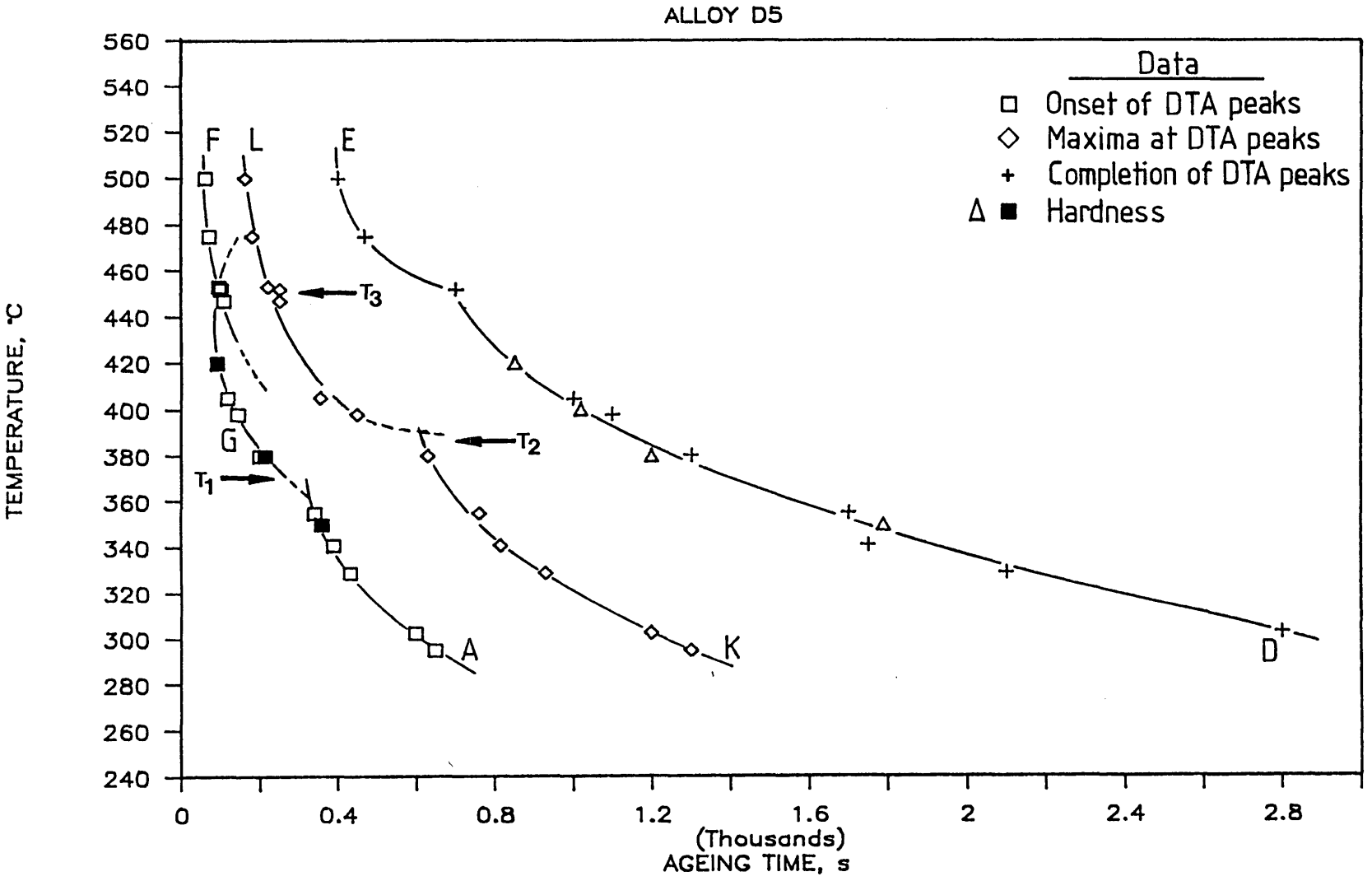


Figure 5.2- TTT diagrams for the 5% prior cold worked alloy (see Table 5.2 for details of symbols).

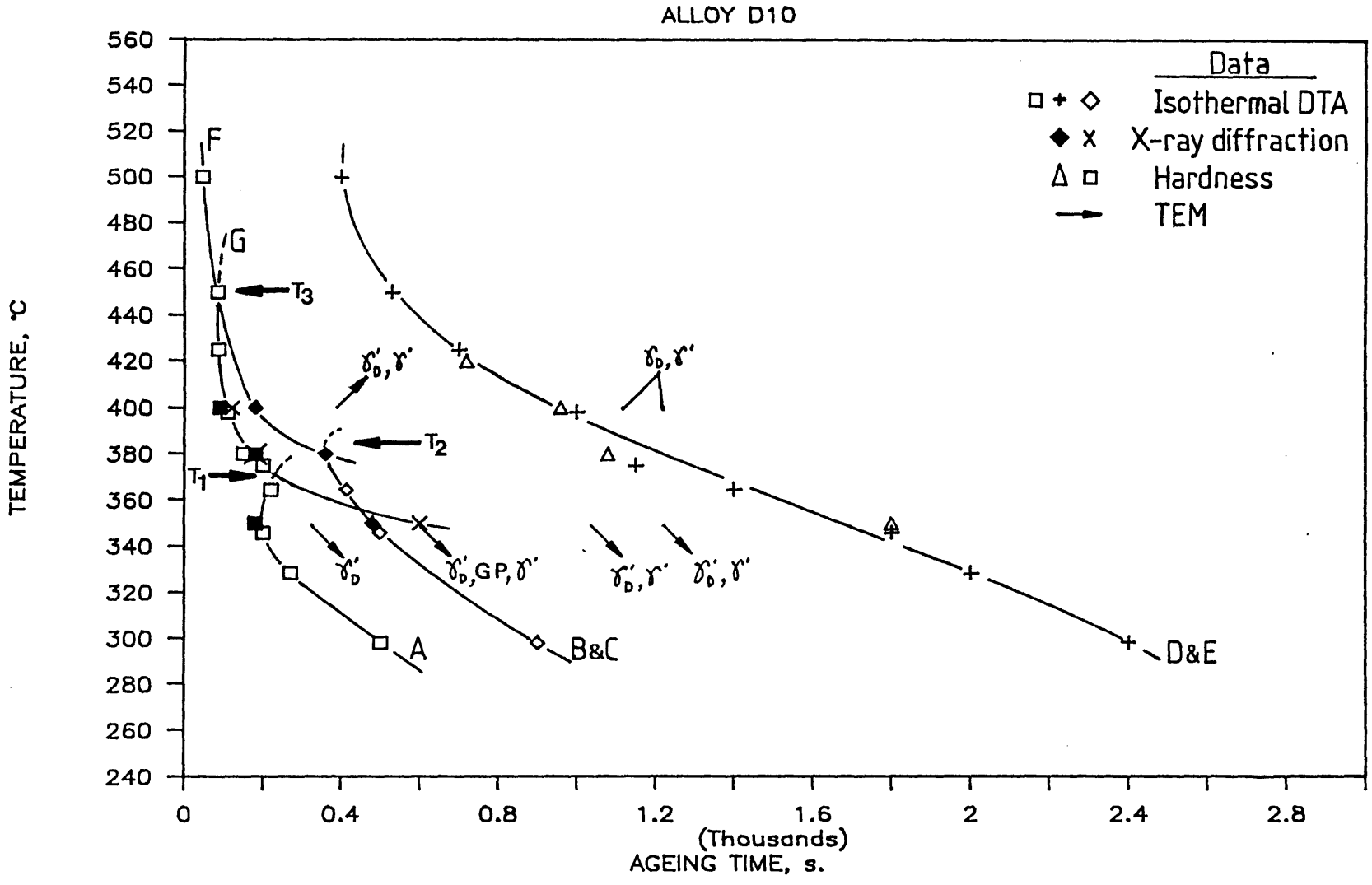


Figure 5.3- TTT diagrams for the 10% prior cold worked alloy (see Table 5.2 for details of symbols).

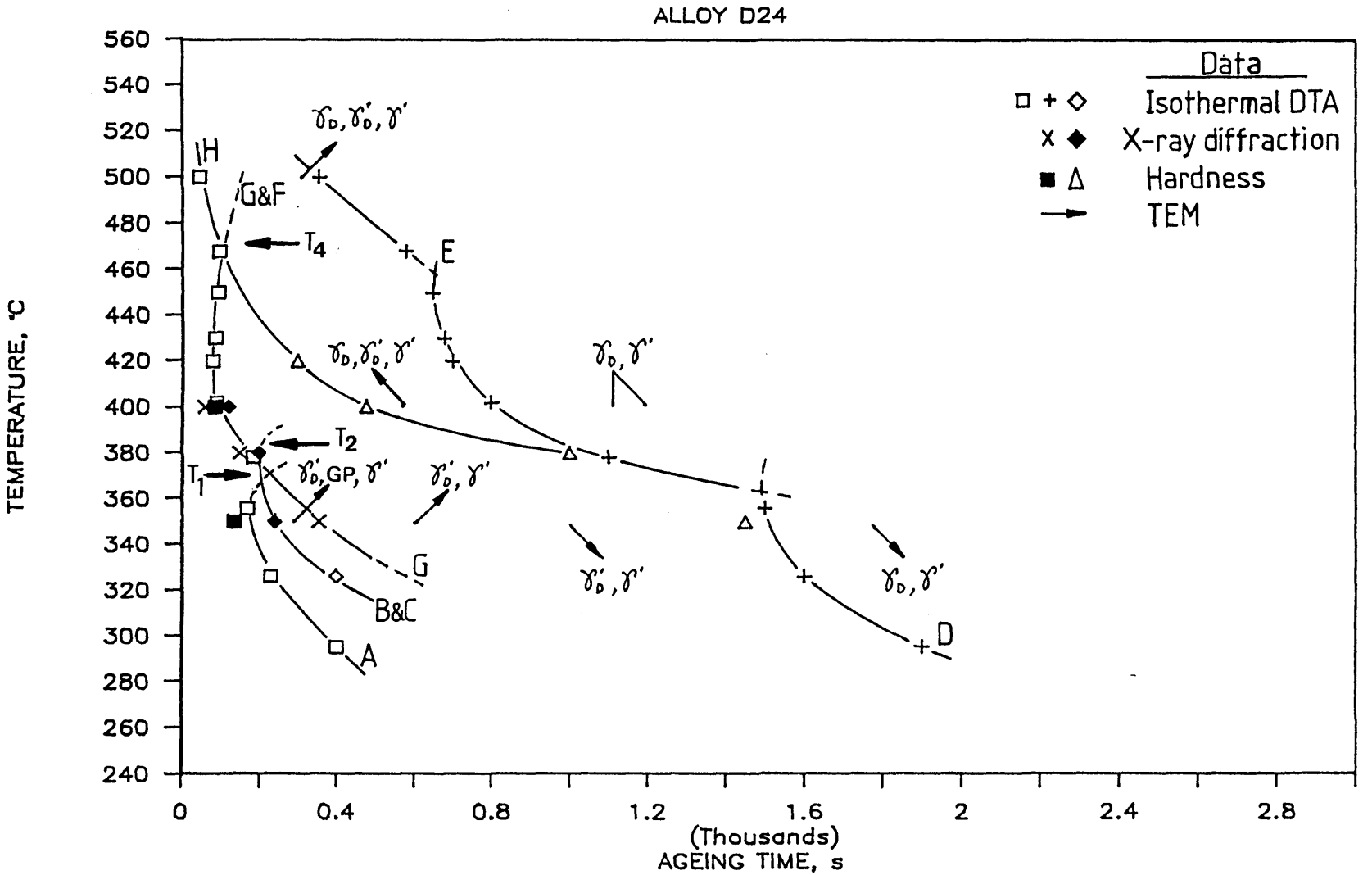


Figure 5.4- TTT diagrams for the 24% prior cold worked alloy (see Table 5.2 for details of symbols).

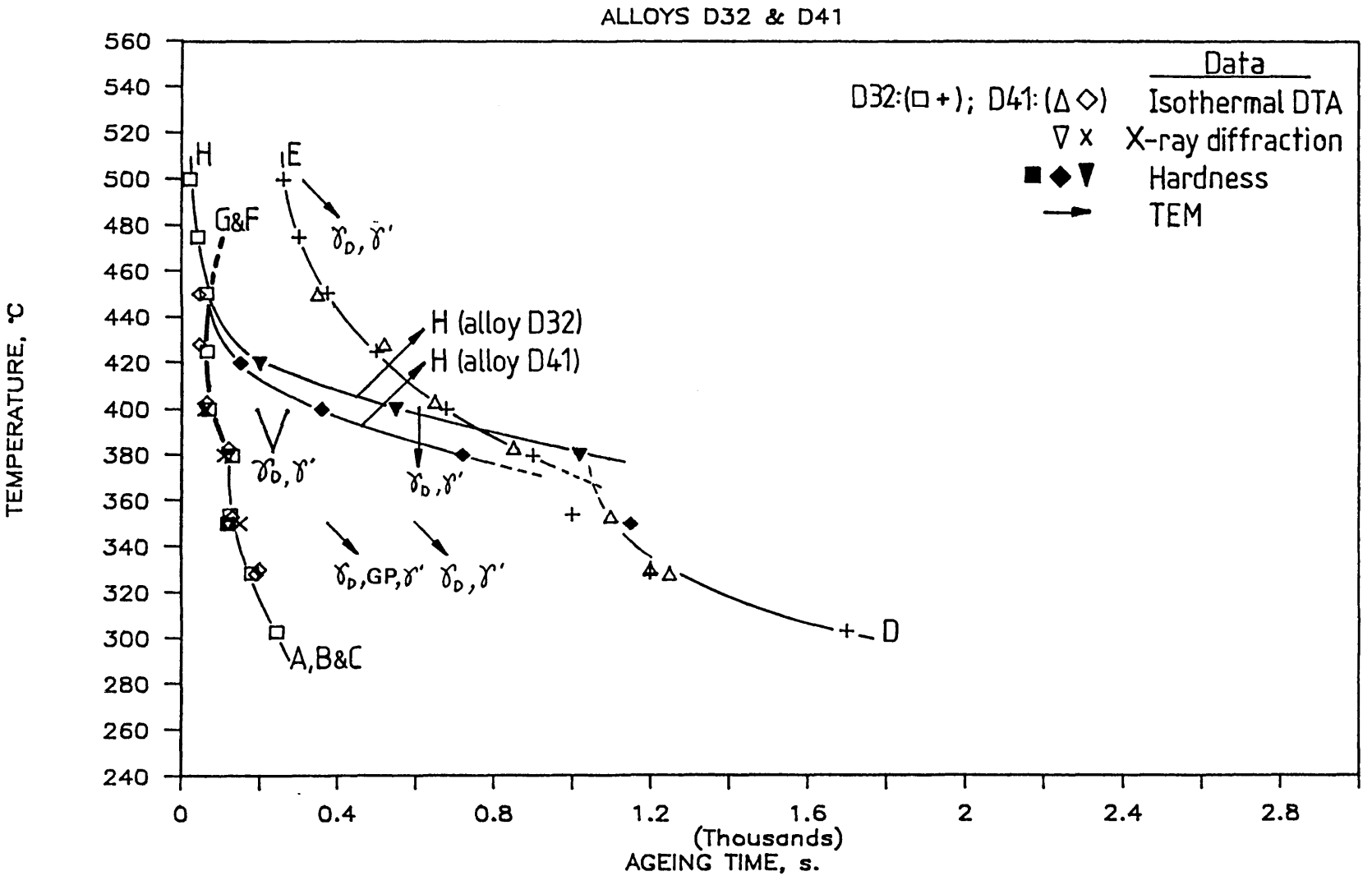


Figure 5.5- TTT diagrams for the 32 and 41% prior cold worked alloys (see Table 5.3 for details of symbols).

Table 5.2
Description of "C" curves for alloys D5, D10, and D24, given in Figures 5.2, 5.3, and 5.4, respectively

Curve	Temperature limit (°C)	Experimental evidence	Implication
A	$T \leq T_1 = 370$	(TEM) = γ'_D precipitation in puckered condition at G.B. (DTA) = (□) Onset of isothermal DTA peaks (Hardness) = (■) Onset of hardening	γ'_D precipitation at G.B.
B&C	$T \leq T_2 = 385$	(TEM) = Sequential formation of G.P. zones and γ' precipitates (DTA) = (◇) Onset of the sharp increase in the heat liberation during isothermal DTA runs (X-ray) = (◆) Onset of the increase in a_0	G.P. zone formation and subsequent γ'nucleation by the G.P. zones
D &E	$T \leq T_1$ $T > T_1$	(DTA) = (+) Completion of isothermal DTA peaks (Hardness) = (Δ) Time to attain peak hardness	Completion of γ' nucleation
F	$T > T_2$	(DTA) = (□) Onset of isothermal DTA peaks above T_3=450°C for alloys D5 and D10 and at $T_2 < T < T_3$ for alloy D24 (X-ray) = (◆) Onset of the increase in a_0 (TEM) = SSR on the SADP's of the matrix	γ' precipitation directly in the α_0-matrix
G	-	(DTA) = (□) Onset of isothermal DTA peaks below T_3=450-470°C (X-ray) = (X) Onset of the increase in the half breadth of the (111) diffraction lines (Hardness) = (■) Onset of hardening	γ'_D precipitation at G.B.
H	$T > T_2$ for alloy D24	(TEM) = Strain-free reoriented regions containing γ'_D and γ_D (DTA) = (□) Onset of isothermal DTA peaks above T_3=470°C (Hardness) = (Δ) Onset of the drop in hardness from the maxima	Onset of recrystallisation initiated at G.B.
K&L	not clear	(DTA) = (◇) Times to attain the peak position of isothermal DTA curves for only alloy D5	Curves reveal γ' precipita-tion in the α_0-matrix.

Table 5.3

Description of "C" curves for alloys D32 and D41, given in Figures 5.4

Curve	Temperature limit (°C)	Experimental evidence	Implication
A,B,&C	$T \leq T_2 = 380$	(DTA) = (□) Onset of isothermal DTA peaks (X-ray) = (◇) Onset of the increase in a_0 = (X) Onset of the increase in the half breadth of the (111) diffraction lines (Hardness)= (□) Onset of hardening (TEM) = See the notations in Figure 5.5	Formation of G.P. zones, which immediately nucleate the γ' precipitates, accompanying the nucleation of recrystallised grains at G.B, which also induce γ'_D precipitation
G&F	$T > T_2$	Same as these for curve A,B,&C	Same as above except that the G.P. zones cannot form, hence the γ' precipitates are nucleated directly in the matrix
D& E	not clear may be $\approx T > T_1$	(DTA) = (Δ,+) Completion of isothermal DTA peaks (Hardness)= (◆) Time to attain peak hardness	Completion of any type of nucleation event
H	$T > T_2$	(DTA) = (□) Onset of isothermal DTA peaks above $T_4 = 350°C$ (Hardness)= (◇,▼) Onset of the drop in hardness from the maxima (TEM) = See the notations in Figure 5.5	Recrystallisation inducing γ'_D precipitation that occurs mainly at G.B. and also in the matrix where polygonization and sub-grain formation had occurred

(ii) Beyond curve H, the recrystallisation and the continuous precipitation become competitive reactions. This is consistent with the findings of Bonfield and Edwards (1974) on ageing the 50% prior cold worked Cu 1.8wt% Be 0.28wt% Co alloy at 425°C. Above T_4 the recrystallisation seems to initiate slightly earlier than γ' precipitation in the matrix, but this needs further miscrostructural examinations to be confirmed.

Similar to previous TTT diagrams for less cold worked alloys, curves D and E represent the completion of any significant precipitation event. Any further precipita--tion or the growth of the existing precipitates, which might take place beyond curves E and D could not be detected by the present isothermal DTA method for the reasons described earlier in Section 5.1.5.

5.2.2 Hardening response of prior cold worked alloys during ageing

The microstructural information concerning the decomposition reactions in prior cold worked alloys show clearly that prior cold work lowers the supersaturation in the matrix in a short period of ageing by accelerating continuous precipitation. Therefore continuous precipita--tion in the matrix limits the discontinuous precipitation at grain boundaries in a more effective manner than that induced by continuous precipitation in the solution treated alloy. As discussed in above section, the continuous precipitation is responsible for the onset of hardening and the increase in hardness to the maxima. On the other hand, larger overall hardening was achieved by reducing the ageing temperature below 400°C. This is attributed to having a finer dispersion of the γ' precipitates since they are nucleated by the G.P. zones below $T_2 \approx 385$°C. Details of this process has been discussed in Section 5.1.3.

However, discontinuous precipitation results in lower hardness values of the alloy than those achieved by γ' precipitation in the matrix, and recrystallisation is known to reduce the hardness. Thus, increasing prior cold

work reduces the hardening increment on ageing as it promotes the recrystallisation process. As can be seen in Figure 4.5-b, on ageing above 350°C, the hardening increment increases up to 10% prior cold work and then reduces with further increase in prior cold work. The increase in the hardening increment up to 10% prior cold work is most probably aided by a considerable acceleration in the nucleation and growth of the γ' precipitates in the matrix and the consequent reduction in the kinetics of cellular precipitation. When prior cold work is increased above 10% RA, the promotion of the γ' precipitation in the matrix occurs to such extent that cellular precipitation is almost entirely retarded whilst the development of the strain-free regions and γ' precipitation in the matrix become two competing processes. In most cases, the nucleation of recrystallised grains is initiated at grain boundaries, whereas, when the prior cold work is increased above 32% RA, the recrystallisation is initiated in the matrix as well, due to the presence of a higher dislocation density that can induce polygonization and subgrain formation during recovery. This process has been well demonstrated by the shift of curve H towards shorter ageing times and lower temperatures on the TTT diagrams with the increase in prior cold work (see curve H in Figures 5.4 and 5.5). Therefore, the recrystallisation is believed to be the major factor in reducing the hardening increment as the amount of prior cold work increases. However, in less deformed alloys, recrystallisation has been shown not to occur extensively and the predominant γ' precipitation, lowering the kinetics of discontinuous precipitates seems to be responsible for the increase in overall hardening in alloys D5 and D10.

Moreover, it is evident from the continuous drop in the fractional change in resistivity, $\Delta\rho$, (Figure 4.55-b) during ageing at 380°C, even after the completion of γ' precipitation in the matrix, that recovery is still taking place, thus reducing the density of defects in the structure. Therefore, hardness should drop with prolonged ageing, whereas, there is an interruption in the hardness drop after the maxima when ageing above 350°C; this is

characterised by a plateau region on the hardness curves (Figures 4.2 to 4.4). This suggests that at the plateau region the growth of the γ' precipitates takes place. It is well known that the increase in the size of precipitates should increase the strength hence hardness until the precipitates reach a critical size at which they can not be sheared by gliding dislocations. It is therefore believed that, at the ageing stages that correspond to the plateau region on each hardness curve (Figures 4.2, 4.3, and 4.4), the growth of the γ' precipitates compensates the reduction in hardness, introduced by recrystallisation or discontinu--ous precipitation, as well as reducing the kinetics of these reactions. Therefore, there is a discontinuity in the drop of hardness at the plateau. However, it is not clear why a second drop in hardness initiates after the plateau. Nevertheless, the onset of the second drop may be approxi--mated to further recrystallisation, induced most probably by recovery in the matrix, as observed in the 41% deformed alloy on ageing at 500°C even after 18 min. (Figure 4.20).

5.2.3 Kinetic parameters determined by isothermal and non-isothermal DTA techniques

Various methods have been proposed for determining the devitrification kinetics in glasses, using the DTA and DSC techniques. The most common of these methods are summarised in Appendix A. However, the validity of these kinetic approaches for phase transformations in alloys has been debated and alternative methods have been proposed in the literature (Hirata and Matsuo, 1970; Cocks, 1969; Thompson, 1969; Augis and Bennett, 1978). The most common of the non-isothermal methods is the modified Kissinger method, which is also known as the Augis & Bennett method, ABM, details of which are summarised in Table A.2 in Appendix A. There is some merit in using the Augis & Bennett method for the DTA and DSC results of the present work, namely:

(i) The basic equation for ABM (equation [A.8] in Table A.2) does not require peak area measurements, which is the case for many other methods. The method involves only the measurement of the peak temperature, T_P, on the DSC and DTA curves, eliminating any error, which can arise from having overlapping peaks on area measurements, which is the case in the present work. Also, the value of the exponent n can be calculated directly according to the following equation:

$$n = \{(2.5/\Delta\tau_W)[T^2_P/(E/R)]\} \qquad [5.2]$$

where $\Delta\tau_W$ is the half breadth of the peak, E the calculated activation energy, and R the gas constant.

(ii) Equation [A.8] is independent of the value of the exponent n, and therefore gives an accurate estimate of the activation energy, E'=E/R, which is the slope of a straight line, obtained when $\ln\{\alpha/(T_P-T_0)\}$ is plotted against $1/T_P$, where T_0 is the starting temperature of a DTA or DSC run and α the heating rate.

In this respect, the non-isothermal DTA & DSC peaks (peak B in Figures 4.29, 4.32, and 4.33, and peak A in Figure 4.34) have been analysed according to both Augis & Bennett (ABM) and Kissinger (KM) methods. The plots of $\alpha/(T_P-T_0)$ vs. $1/T_P$ for ABM and α/T^2_P vs. $1/T_P$ for KM gave straight lines with a slope equal to E/R. Typical plots, obtained using the Augis & Bennett method, are given in Figure 5.6. As explained in Section 4.4, peak B for alloys UD, D5, and D10 corresponds to γ'_D precipitation in a cellular reaction, and peak A, which is the only peak for alloy D32, is for γ' precipitation in the matrix. Therefore, the slope of the straight lines for alloys UD, D5, and D10 yields E/R values for γ'_D precipitation and that of alloy D32 gives an E/R for γ' precipitation in the matrix, as described in Table 5.4. The time exponent, n, for each material was calculated according to equation [5.2] and the resultant values are also given in Table 5.4. The values of E for both γ' and γ'_D precipitation, obtained

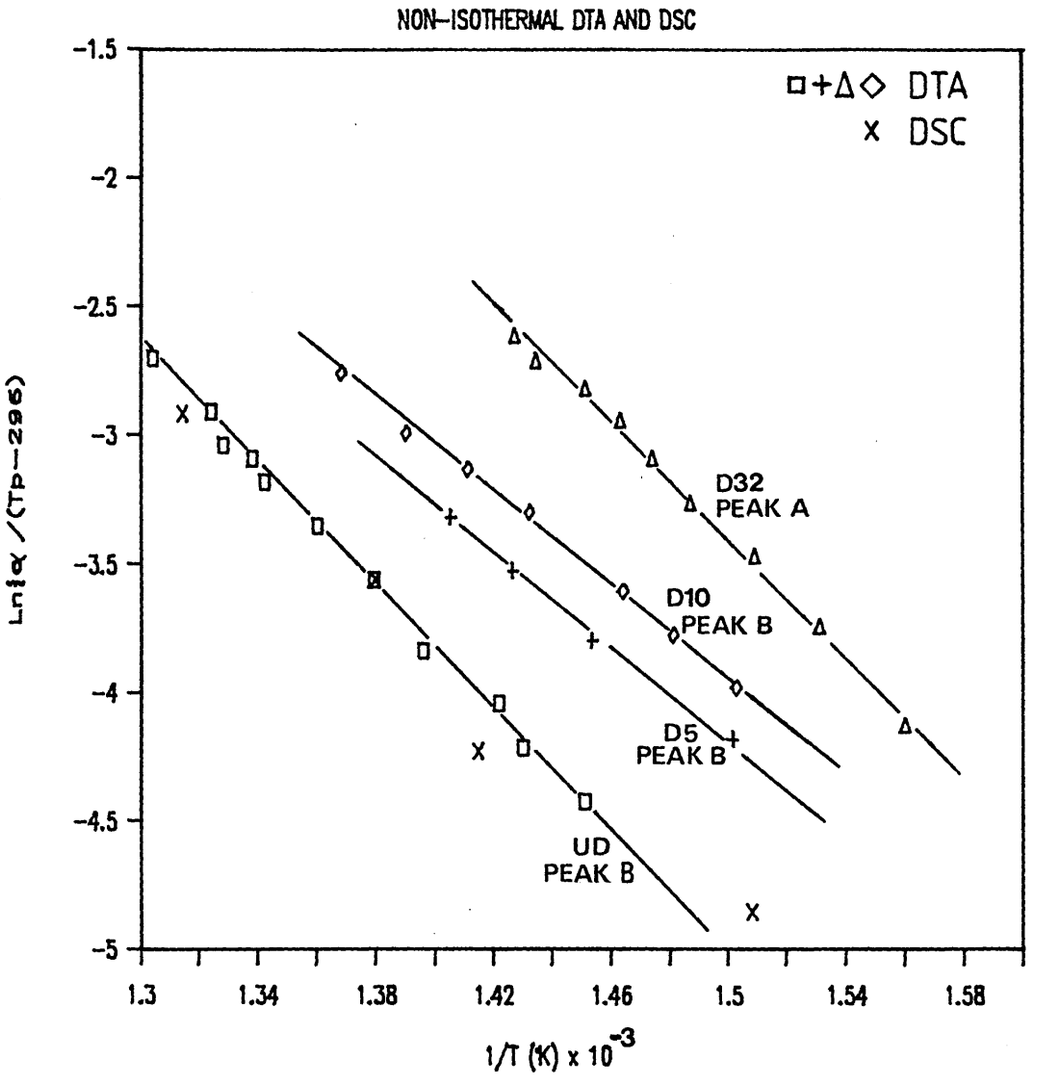


Figure 5.6- The plots of $\ln\{\alpha/(T_P-T_0)\}$ vs. $1/T_P$ for γ'_D precipitation in alloys UD,D5, and D10, and for γ' precipitation in alloy D32, according to the non-isothermal method of Augis and Bennett (1978); the data are from the non-isothermal DTA and DSC runs.

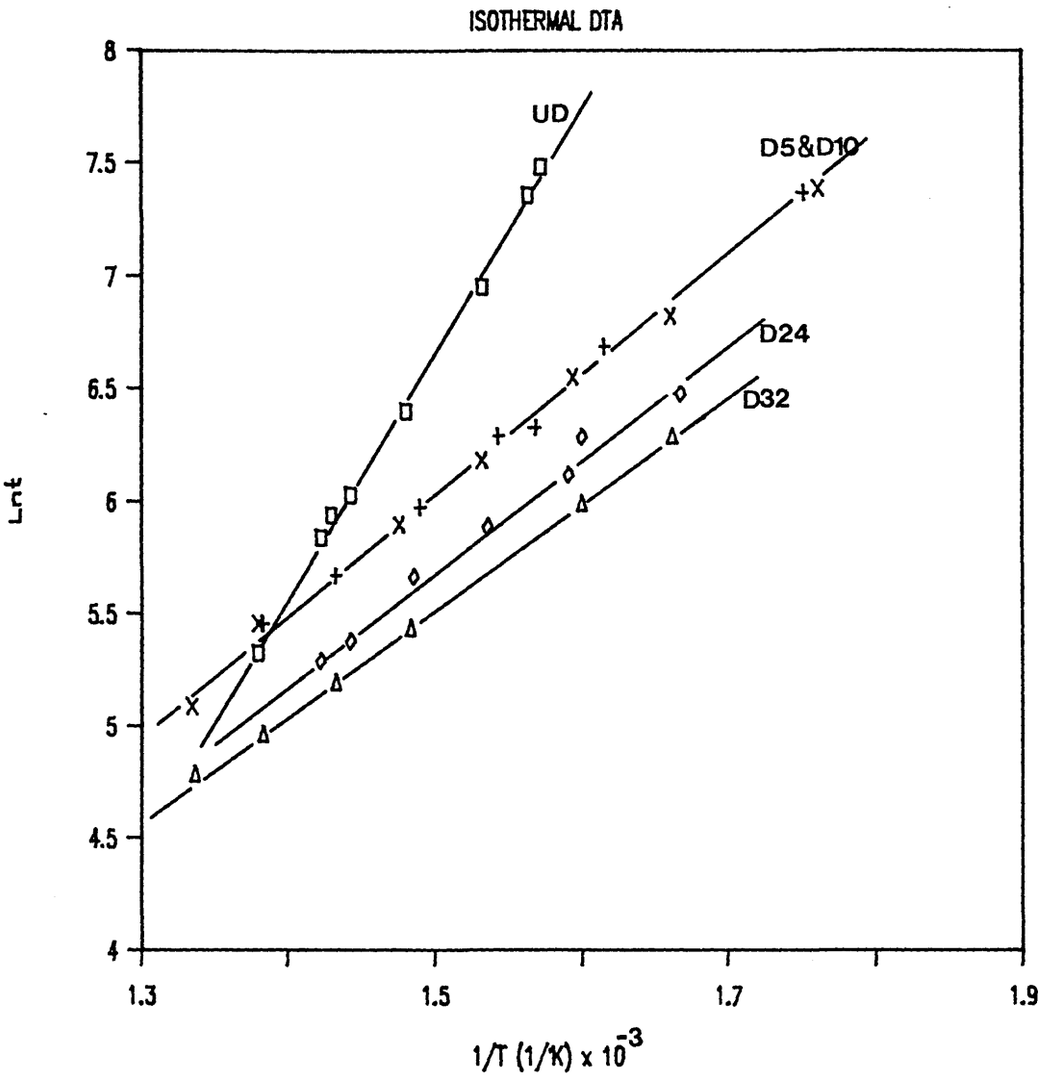


Figure 5.7- The plots of lnt vs. $1/T_P$ for γ' precipitation in alloys UD, D5, D10, D24, and D32, according to the isothermal DTA data.

using the Kissinger method, were 10% lower than those from the Augis & Bennett method. This is because the Kissinger method assumes that n=1 and hence the use of equation [A.9] for this method (see Table A.2 in Appendix A) to calculate the activation energy involves an error of 10%.

The relationship between the logarithm of the times (lnt) to attain the DTA peak, corresponding to γ' precipi-tation in the matrix, and the reciprocal absolute tempera-ture (1/T) of an isothermal DTA run may also be used to calculate the activation energy, $E_{\gamma'}$, for γ' precipitation in the matrix; this method has been described in Appendix A. For this method, the values to obtain the lnt vs. 1/T plots were resolved from the isothermal DTA peaks at $T \geq 380°C$, which is the temperature range in which the γ' precipitates are formed directly from the solid solution. As shown in Figure 5.7, the data points gave straight lines with the slopes, E/R, for continuous γ' precipitation in alloys UD, D5, D10, D24, and D32, and the calculated and the normalised values of $E_{\gamma'}$ for each alloy are given in Table 5.5.

5.2.4. Analysis of the kinetic parameters for deformed and undeformed states

Using the TEM data from the non-isothermally treated samples of alloys UD and D32 and the corresponding information, obtained from the nature of the DTA and DSC peaks, it has been established in previous sections that at high heating rates ($\alpha \geq 20°C$/min.) the predominant mode of reaction is the cellular γ'_D precipitation for alloys, deformed up to 24% RA. It is clear from Table 5.4 that the value of $E_{\gamma'D}$ for cellular precipitation reduces with prior cold work, e.g. the reduction in $E_{\gamma'D}$ after 10% prior cold work is about 28%. This may be attributed to the increase in the mobility of grain boundaries, or the interface of the cells, by the increase in the dislocation density inducing a localised high misorientation in certain regions of a given grain boundary. As can be seen in Figure 4.18, the grain boundary bows into the matrix, forming an "S"

Table 5.4

Kinetic parameters determined for solution treated and prior cold worked alloys according to non-isothermal DTA and DSC methods

Alloy	Phases	Augis & Bennett method		Kissinger method	E (kJ/mol) after Jovanovic et al.(1986)
		E (kJ/mol)	n (average)	E (kJ/mol)	
UD	γ'_D at G.B.	104.3	1.5 ±0.12	91.2	121.8-148.8
D5	" "	74.6	1.9 ±0.13	69.0	-
D10	" "	74.2	2.0 ±0.23	68.9	-
D32	G.P. & γ' in the matrix	93.8	1.0 ±0.04	84.5	-

Table 5.5

Activation energy for γ' precipitation in the matrix in solution treated and prior cold worked alloys according to isothermal DTA method

Alloy	$E_{\gamma'}$ (kJ/mol)	Normalised $E_{\gamma'}$
Alloy UD	90.8	1.00
Alloy D5	43.5	0.48
Alloy D10	43.5	0.48
Alloy D24	41.4	0.45
Alloy D32	38.3	0.42

shape by one part of the boundary moving into a highly deformed region. The presence of highly deformed regions may be explained by the deformation bands, providing a high dislocation population in some regions of grain boundaries. Also, the grain boundary movement into the grain, which possesses higher deformation than the neighboring grain can be followed by Figure 4.41-a. This type of mechanism may be analogous to that observed in various Al and Ag based alloys that has been explained by heterogeneity of deformation in the same grain (Pawlowski, 1979) or in neighboring grains (Bailey, 1960). However, as soon as the γ' precipitates form in the matrix, they induce a dragging force for cellular precipitation by reducing the solute content in the matrix and/or pinning the advancing cell-boundary.

For non-isothermal conditions that result in predominantly continuous γ' precipitation for 24% prior cold work and above, the activation energy for γ' precipi--tation in the matrix has been calculated to $E_{\gamma'}$=93.8 kJ/mol for alloy D32 (see Table 5.4); this may be compared with the previously reported value of $E_{\gamma'}$=148.84 kJ/mol for an undeformed Cu 1.8%Be 0.2%Co alloy by Jovanovic et al. (1986). If the latter is a correct value of $E_{\gamma'}$, there is about 40% reduction in $E_{\gamma'}$ as a result of introducing 32% prior cold work. However, $E_{\gamma'}$=90.8 kJ/mol, determined for the solution treated alloy in the present work by the isothermal DTA method (see Table 5.5), is also low compared with the value, reported by Jovanovic et al. (1986). Nevertheless, the reduction in $E_{\gamma'}$ values, determined by the same method, with increasing prior cold work demon--strates an acceleration of the kinetics of γ' precipita--tion in the matrix (see the normalised $E_{\gamma'}$ values in Table 5.5). Using $E_{\gamma'}$ values in Table 5.5, about 58% reduction in $E_{\gamma'}$ value after 32% prior cold work was determined. This is also comparable with ≈40% reduction, according to the result of the non-isothermal DTA method, given above.

The values for the percentage reduction in $E_{\gamma'}$ and $E_{\gamma'D}$ at different grades of prior cold work are compared in Table 5.6. By using the data in Table 5.6, it may be

reasonable to conclude that γ' precipitation in the matrix is accelerated by prior cold work more effectively than γ'_D precipitation at grain boundaries. For example, after 10% prior cold work, there is a reduction of ≈30% in the activation energy of γ'_D precipitation; this is considerably less than the reduction in the activation energy of γ' precipitation in the matrix (≈50%) as given in Table 5.6. The data in Tables 5.4 and 5.5 imply that the activation energy for γ'_D precipitation ($E_{\gamma'_D}$) is always less than that of γ' precipitation even after a more marked reduction in $E_{\gamma'}$ is introduced by prior cold work. However, the prior cold work reduces the amount of γ'_D precipitation at grain boundaries since the greater the degree of prior cold work, the more marked is the acceleration in γ' preci--pitation and the greater the reduction in Be content in the matrix that limits the growth of the γ'_D precipitation.

The above approach is consistent with the "C" curves in Figures 5.1 to 5.5, where the shift of curves A and G to shorter times for discontinuous precipitation with

Table 5.6

Percentage of reduction in $E_{\gamma'_D}$ and $E_{\gamma'}$ by increasing prior cold work

Alloy	Prior cold work (%RA)	% reduction in $E_{\gamma'_D}$(§)	% reduction in $E_{\gamma'}$(§)
D5	5	28.5	52
D10	10	28.8	52
D24	24	-	54.4
D32	32	-	57.9

(§) percentage reduction in $E_{\gamma'_D}$ or $E_{\gamma'}$ of the solution treated alloy by prior cold work.

increasing prior cold work is less than that of curves B and F for continuous precipitation, with the result that both types of "C" curves overlap after 24% prior cold work. Therefore, in agreement with the previously obtained results from Al-Cu alloys (Tavassoli, 1974) and the binary Cu-Be alloys (Nutting, 1971; Armitage, 1963; Kreye, 1971) it may be concluded that the dislocations, introduced by prior cold work, accelerate the rate of γ' precipitation in the matrix by accommodating the misfit strain and/or reducing the activation energy for the diffusion of solute atoms.

The values of the time exponent, n, given in Table 5.4, can also be used to explain the type of precipitation in the material. According to the criteria, given in Table A.1 in Appendix A, the values of n for grain boundary and grain edge nucleation are 1 and 2, respectively. Having $n \approx 1.5$ for γ'_D precipitation in alloy UD suggests that the cellular precipitation occurs at both grain boundaries and edges, whereas, there is an increase in n value to about 2 after 5% and 10% prior cold work (see Table 5.4). The obvious interpretation is that in prior cold worked alloys (up to 24% RA), grain edges become energetically more favourable for cellular precipitation than grain boundaries. The comparison of the TEM micrographs in Figure 4.15-a and c supports this view. A similar analysis has been made to explain the temperature dependency of n values for γ'_D precipitation in undeformed Cu 2wt%Be alloys by Tsubakino et al. (1981). They found that the value of n for γ'_D precipitation is 1.4 on ageing below 350°C and 2.2 above 350°C (see Table 2.2). They interpreted these n values as grain boundary precipitation below 350°C and grain edge precipitation above 350°C on the basis of the kinetic theory of nucleation and growth (see Section 2.6.2).

On the other hand, from the previous sections, prior cold work above 24% RA is known to suppress almost entirely γ'_D precipitation in a cellular reaction. Therefore, the n values of 1 obtained from the non-isothermal DTA data for the 32% prior cold worked alloy corresponds to the continu-ous precipitation of both G.P. zones and γ' precipitates,

nucleated by the G.P. zones (see Table 5.4). The value of unity for n is typical for the nucleation of needles and plates of finite long dimensions (see also Table A.1). It has been shown in previous sections that the formation of the G.P. zones and the γ' precipitates is a continuous ordering process and the the TEM micrographs of the specimens, tested non-isothermally in the DTA furnace at α=20°C/min, revealed the formation of both phases at the DTA peak. Therefore, it may be concluded that the nuclei of the γ' precipitates are the G.P. zones and the nucleation process is described by n=1.

5.3 Textural Changes in Cu-Be-Co Alloys

Most metallic materials in the deformed state are anisotropic in that their properties vary with direction. For an alloy, the variation of its properties with direction may be attributed to two reasons, namely:

(i) crystallographic anisotropy, which is produced by the non-random arrangement of the crystals that induces the development of preferred orientations or texture, and

(ii) microstructural anisotropy, which arises from the variation of grain size or shape and the presence of the phases, arranged in a non-random way.

Various interpretations on the texture development in pure metals and alloys have been put forward in the literature and most of them are concerned with the effect of the stacking fault energy of the material. The type of the texture, which belongs to either recrystallised or deformed structure, has been found to change with respect to the stacking fault energy of the material, which effectively alters the deformation and recrystallisation mechanisms (Sevillona et al., 1981; Dillamore and Roberts, 1965). In the present work, particular emphasis has been given to the texture of the FCC materials with a low or medium to low stacking fault energy since the Cu-Be-Co

alloys have reasonably low stacking fault energy very close to that of brass (≈20 mJm^{-2}) (Gadalla, 1980).

Criteria for cold rolling to introduce a homogeneous deformation across the thickness of the material have been described by Hansen and Mecking (1975) as follows:

(a) rolling direction should be reversed after each pass, and

(b) in order to obtain a uniform penetration of the shear deformation through the thickness of the material, the coefficient of the rolling gap geometry, L/d, should be greater than 1, as described by:

$$L/d = [\sqrt{R}/(d_0-d)]/d_0 > 1 \qquad [5.3]$$

where L is the projected length of the contact between the roll and the material, d_0 and d are the entrance and the exit thickness of the sample, and R is the roll radius. The cold rolling process, introduced to the investigated materials before and after the solution treatment at the manufacturer meets these requirements.

The information available in the literature on the texture development of Cu-Be alloys is limited, and the available data are based on the textures at high rolling deformations, e.g. prior cold work greater than 50% RA (Alpas and Öztürk, 1984; Tofpenets et al., 1979), and hence not directly relevant to the present work.

In the following sections, in Cu-Be-Co alloys, the recrystallisation texture after solution treatment, the deformation texture after prior cold work in the range 10 to 41% RA, and the change in the texture during ageing the prior cold worked alloys will be discussed and compared with the texture of similar materials.

5.3.1 Texture after the solution treatment

The face centred cubic pure metals, which have the copper-type rolling textures, are well-known to have recrystallisation textures, characterised by the formation of a sharp (100)<001> or "cube" orientation. However, some

alloy additions or impurity elements, e.g. for copper alloys, Zn, Al, Ge, Sn, P, As, Sb (Dillamore and Roberts, 1965), have a very strong inhibiting effect on the development of the cube texture. These elements are effective in suppressing the cube texture by changing the deformation substructure and reducing the velocity of the high angle grain boundary migration.

On the other hand, alloying elements reduce the stacking fault energy of the material, and hence result in the transformation of the pure metal type deformation texture to that of the brass-type. Since the recrystall--isation texture depends first of all on the deformation texture, one would expect a considerable deviation in the recrystallisation texture orientations of a given alloy from the cube texture as the amount of alloying addition increases.

In addition to the above factors, the amount of prior cold work may well affect the recrystallisation texture, as it alters the prior deformation texture even if the stacking fault energy is low enough after alloying to produce the brass-type texture. For example, the deformation textures for pure copper and 70:30 brass have been found to be essentially the same up to 40-50% RA (both were Cu-type), whereas greater prior cold rolling resulted in a deviation in the texture of brass from that of copper towards ideal brass-type texture (Leffers and Grum-Jensen, 1968). In this respect, the textural rotations during deformation are related to how recrystallisation nucleus orientations change with respect to the change in the deformed microstructure, or the change in the oriented growth of the recrystallised grains. Thus, the interdependancy between the recrystallisation texture and the deformation texture may be established.

The commercial production of Cu-Be-Co alloys involves the solution treatment of the cold rolled material to produce a supersaturated solid solution with a recrys--tallised structure with many annealing twins. The alloys investigated in the present work are produced commercially and the deformation texture prior to solution treatment is

unknown to the author. Nevertheless, it is clear that large amounts of deformation (above 50% RA) had to be introduced so as to produce a homogeneously recrystallised structure, which is evident by the presence of brass-type recrystall--isation texture. The results of rolling texture, which will be discussed in the following section, support this view; the 41% prior cold work results in a brass-type texture with some intermediate orientations while lesser amounts of cold work produce an intermediate texture to brass-type, which is in agreement with the description of Lefters and Grum-Jensen (1968). Also, considering that the alloying elements, Be and Co, reduce the stacking fault energy of the alloy considerably, and they are likely to introduce a solute drag effect against migrating bound--aries, the resultant recrystallisation texture is expected to be of the brass-type.

Indeed, the recrystallisation texture of the solution treated alloy, identified using the (200) pole figure (Figure 4.52-a) with the indices (225)<73$\bar{4}$> plus (522)<$\bar{4}$55> and (210)<001>, confirms the presence of brass-type texture since the (225)<73$\bar{4}$> orientation can only be obtained if the rolling texture was clearly of the brass-type. However, because of the ambiguity in the interpreta--tion of the brass-type recrystallisation texture in the literature both indices, suggested in the present work, are worthy of further discussion separately in relation to the suggestions of previous authors for the texture of similar materials. It must be noted that there is unfortunately no available information about the microstructural changes during the solution treatment of the present alloys. Therefore it may not be strictly correct to apply the models proposed for the recrystallisation texture of various alloys in the literature to the results of this work; nevertheless they may be used for a comparison.

5.3.1.1 The (225)<73$\bar{4}$> plus (522)<$\bar{4}$55> orientations

The (225)<734> recrystallisation orientation was first suggested for 70:30 brass by Beck and Hu (1952) (as cited by Lücke and Schmidt, 1972). However, according to Lücke and Schmidt (1972) the texture may be better represented by the indices (326)<83$\bar{5}$>. On the other hand, preceding studies on the brass-type recrystallisation texture, which were summarised by Dillamore and Katoh (1974), suggested a texture, identified by the indices (113)<21$\bar{1}$>. Nevertheless, as can be seen in Figure 5.8, these orientations are situated close together on the (111) and (200) pole figures, having similar angular rotations with reference to the rolling plane and the rolling direction. The theoretical approach of Dillamore and Katoh (1974) to the recrystallisation texture in FCC metals in terms of crystal rotations in spherical co-ordinates demonstrates that the only possible way that the (113)<21$\bar{1}$> orientation can develop is by the contribution from twinning during recrystallisation, details of which may be found in their publication. For single crystals, this has been explained by relating any of these orientations to the rotation of the deformed structure about simple crystal directions during recrystallisation, in other words, to the brass-type deformation texture orientation, (110)<$\bar{1}$12>, by 30-40° rotations around <111>, which is the sheet normal (Schmidt et al., 1975).

Considering that all three orientations do not differ noticeably, and may be considered as the spread of a single orientation with a few degrees rotation, the model of Dillamore and Katoh (1974) may be valid for all orientations. Therefore, it is likely that the (225)<73$\bar{4}$> orientation is the twin component of the recrystallisation texture in the solution treated alloy.

The (522)<$\bar{4}$55> component, which is a few degrees away from (225)<73$\bar{4}$> (Figure 4.52-a), also describes the brass-type recrystallisation texture; this texture has only been noted previously in brass rolled to 65% reduction and annealed at 600°C (Lee, 1984). It seems that the

(522)<$\bar{4}$55> orientation is the spread orientation of the brass-type texture, (225)<73$\bar{4}$>.

5.3.1.2 The (210)<001> orientation

As explained above, a copper-type rolling texture, characterised mostly with the indices (113)<21$\bar{1}$>, leads only to the cube recrystallisation texture, (100)<001>, as a result of oriented growth of grains (Dillamore and Katoh, 1974). However, some alloying additions, e.g. Zn, Ge, P, etc. in copper and Co in nickel, reduce the stacking fault energy and also suppress the oriented growth of the cube grains that leads to the cube texture so that alternative nuclei of recrystallised grains are brought into operation (Hutchinson, 1974). This results in the weakening or disappearance of the sharp texture components (particularly the cube texture) and other <001> rolling direction orientations, which are usually denoted as the "tilted cube texture", such as (410)<001>, (310)<001>, (830)<001>, (520)<001>, (210)<001>, and (110)<001>, develop at the expense of the cube texture by a tilting mechanism (Lücke, 1981; Virnich and Lücke, 1981; Slakhorst and Verbraak, 1975; Brickenkamp and Lücke, 1981; Schmidt et al., 1975). The tilting of the cube orientation (100)<001> to the above orientations, e.g. in the present case tilting to (210)<001>, is represented by the rotations around the <111> rolling direction as can be seen in Figure 5.9. On this basis, the presence of the (210)<001> texture component after the solution treatment of Cu-Be-Co alloys consequently shows the occurrence of the tilted cube texture by the alloying addition of Be and Co into copper.

5.3.2 Texture after cold rolling

Deformation on rolling FCC materials occurs by normal slip on the (111)<110> systems, which is supposed to lead to the copper-type rolling texture. The transition to brass type texture is obtained by either alloying or lowering the rolling temperature of pure metals, e.g. rolling at -196

°C. However, pure copper and brass have been found to develop copper-type textures up to moderate rolling deformations < 40% RA, whereas greater amounts of deform- - ation lead to a difference in texture; namely, for brass a transition from copper to brass-type texture occurs (Leffers and Grum-Jensen, 1968). Thus, the transition of the texture in a material to brass-type is initiated by two co-operating processes, namely alloying additions in the pure metal and the increase in the rolling deformation.

In fact, most of the alloying additions to Cu reduce the stacking fault energy. According to Wassermann, (1963), for FCC alloys with low stacking fault energy, mechanical twinning at moderate strains accompanied by $(111)\langle 11\bar{2}\rangle$ slip of partial dislocations is responsible for the texture transition from copper type $(110)\langle 001\rangle$ to brass type $(110)\langle \bar{1}12\rangle$. Therefore, the final rolling texture is described by the ideal orientation $(110)\langle \bar{1}12\rangle$ with an orientation spread including $(110)\langle 001\rangle$.

On the other hand, Lücke (1981) described a transi- -tion texture with reference to the texture of Cu-Zn and Al-Si alloys, with the starting orientation $(11\ 4\ 4)\langle \bar{8}\ 11\ 11\rangle$ that transforms to $(110)\langle \bar{1}12\rangle$ through a third component, $(123)\langle 63\bar{4}\rangle$, which is the main component in high stacking fault energy-material, e.g. Al-Si alloy. Again, the reason for this texture transformation is attributed to the decrease in the stacking fault energy by alloying, as well as an increase in deformation that favours mechanical twinning, which leads ultimately to the brass-type texture.

The present results are in agreement with these of Leffers and Grum-Jensen (1968) in the sense that the rolling texture is transformed to brass-type texture by the increase in rolling deformation, and also confirm the intermediate and ideal orientations, suggested by Lücke (1981). In this respect, the starting orientation after 10% prior cold work is $(522)\langle \bar{4}55\rangle$ (see Figure 4.52-b), which is almost the same as $(11\ 4\ 4)\langle \bar{8}\ 11\ 11\rangle$. The following inter- -mediate orientations to the ideal $(110)\langle \bar{1}12\rangle$ orientation are (326)(634), which diminishes after 32% cold work, and $(123)\langle 63\bar{4}\rangle$ plus $(146)\langle 21\bar{1}\rangle$, which do not totally diminish

after 41% prior cold work, but contribute to a weak spread texture intensity, as observed on the (200) pole figures (see Figure 4.52-e). It must be noted that, to the author's knowledge, none of the intermediate orientations, proposed in the present work, has been previously reported for Cu-Be alloys. However, considering that the previously obtained results are from highly deformed alloys, i.e. above 50% RA, the intermediate orientations may have diminished totally as the prior cold work probably exceeded the critical level.

The occurrence of deformation twins in Cu-Be alloys, which are essential for the texture transition according to the model due to Wassermann (1963) and Heye and Wassermann (1968), at moderate rolling deformations are not well established in the literature. Nourbakhsh and Nutting (1982) reported the presence of deformation twins after prior cold work as low as 20% RA whilst Armitage (1963) observed deformation twins only after 90% cold rolling. However, Alpas and Öztürk (1984) proposed that at moderate to high (50% RA) or high (>70% RA) rolling deformations, shear bands are prevalent in the structure of the alloy.

The electron microscopy investigations of the present research revealed that deformation bands are the common features observed after prior cold work in the range 10 to 41% RA, but neither twinning nor the development of shear bands are in progress even after 41 % cold work. Therefore, the transition of the deformation texture from copper to brass-type after 41% prior cold work cannot be explained by the mechanical twinning model of Heye and Wassermann. The present results are not conclusive in rejecting or supporting the previous theories of the brass-type texture development. However, deformation bands, which were the only inhomogeneities observed in the prior cold worked alloys, may be related to the texture transi--tion from copper to brass-type. This is parly consistent with the model due to Heye and Wassermann (1968) who assume that the texture transition in FCC alloys with low stacking fault energy at lower deformations, e.g. below 50% RA, is initiated by the development of deformation bands.

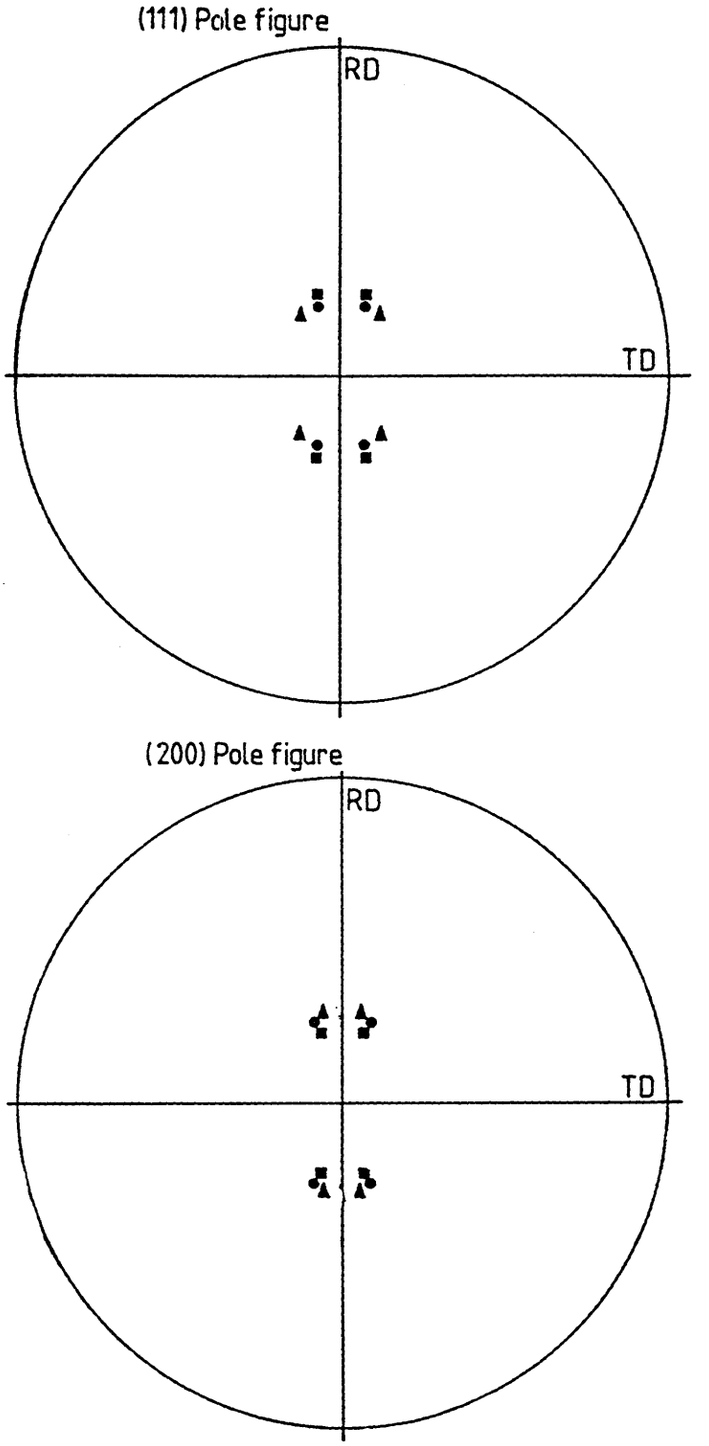


Figure 5.8- The (113)<21$\bar{1}$> (■), (326)<83$\bar{5}$> (▲), and (225)<73$\bar{4}$> (●) orientations on the (111) and (200) pole figures.

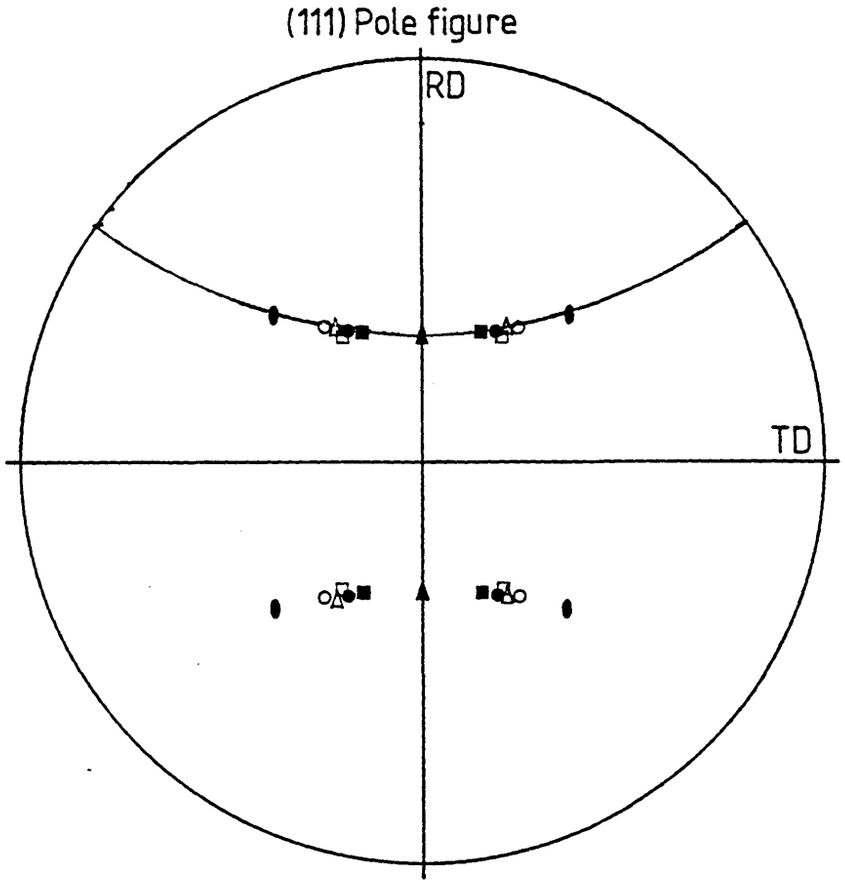


Figure 5.9- The tilting of the (110)<001> (●) orientation around the <111> rolling direction of the (111) pole figure towards other orientations, namely:

(■) (210)<001> (△) (310)<001>

(●) (520)<001) (○) (410)<001>

(□) (830)<001> (▲) (100)<001>

In fact, the texture on the (111) pole figure of the same material (Figure 4.52-e) suggests that the texture is not an ideal brass-type, but an intermediate texture. This is evident from the presence of a spread texture inten--sities on both (111) and (200) pole figures, contributed by the intermediate orientations although the ideal $(110)\langle\bar{1}12\rangle$ orientation is the main component of the texture. It is likely that mechanical twinning, followed by the development of shear bands, comes into operation at larger rolling deformations, e.g. after 50% cold work (Nourbakhsh and Nutting, 1982; Alpas and Öztürk, 1984; Tofpenets et al., 1979); this will consequently bring all the intermediate orientations to that of brass-type texture. This may be followed by the comparison of the experimental (111) pole figures (Figure 5.10-a and b) of the 41% cold rolled Cu 1.9% Be 0.25% Co alloy (the result of the present work) and the 93% cold rolled Cu 2% Be alloy (the result of Nourbakhsh and Nutting (1982)).

5.3.3 Texture after annealing cold worked alloys

The electron microscopy investigations on the decomposition reactions during ageing the prior cold worked alloys are limited to short ageing treatments (maximum 30 min.), and, although precipitation was quite advanced, at most temperatures the amount of recrystallisation was extremely limited. Only the 41% prior cold worked alloy, aged at 500°C, showed well-developed recrystallised grains both at grain boundaries and in the matrix, but even in this case the specimen was not fully recrystallised (see Figures 4.19 to 4.21).

The pole figures for the alloys D10, D21 and D32, given in Figure 4.53, show no change in the texture orientations during ageing at 400°C, whereas, there is an increase in the intensity of texture maxima on the (111) pole figures (see Figure 4.54). A similar but less increase in the texture maxima was also observed on the (200) pole figures. This corresponds to the ageing period in which continuous γ'' precipitation takes place in the matrix as a predominant

mode of reaction. It is therefore suggested that the elastic stresses, induced by γ' precipitation, and/or the dislocation accumulation at precipitates during recovery can be responsible for the increase in the intensity of the texture maxima. As suggested by Tofpenets et al. (1979) for a 50% prior cold worked Cu 1.9wt% Be alloy, the redistribution of dislocations by slip, which results in the cellular-type dislocation sub-structure, may be the process in 32 and 41% prior cold worked alloys that induces the intensification of the principal texture orientations, such as $(110)\langle\bar{1}12\rangle$. However, due to the limited extent of the TEM at long ageing times, a cell structure has not been observed in the present investigation.

On further ageing, the drop in the texture intensity to almost the initial intensity level is attributed to the extensive growth of the strain-free reoriented regions at grain boundaries in alloys D21, D32, and D41. It is believed that the growth of the reoriented regions does not contribute to any other type of texture, but results in a random texture. As a similar approach, Tofpenets et al. (1979) proposed that, after 50% prior cold work, ageing at 300°C results in the development and growth of sub-grains, from which the recrystallised grains are formed on prolonged ageing. They concluded that this process is responsible for the drop in the intensity of the principal texture orientations.

After ageing 41% deformed material at 400°C for 4 hours, there is a second increase in the intensity of the texture maxima on the (111) pole figure. The (200) pole figures for this material, aged at both 400 and 500°C for 4 hours, also reveal a second texture maxima, which are situated very close to the original deformation texture orientation, $(110)\langle\bar{1}12\rangle$. As the TEM micrographs (Figure 4.20) for the 41% cold worked alloy, aged at 500°C for 18 min., show well-developed recrystallised grains, it is suggested that these recrystallised grains are responsible for the second texture intensity on the (200) pole figure, and that they possess almost the same texture orientation as that introduced by the 41% prior cold work, showing the

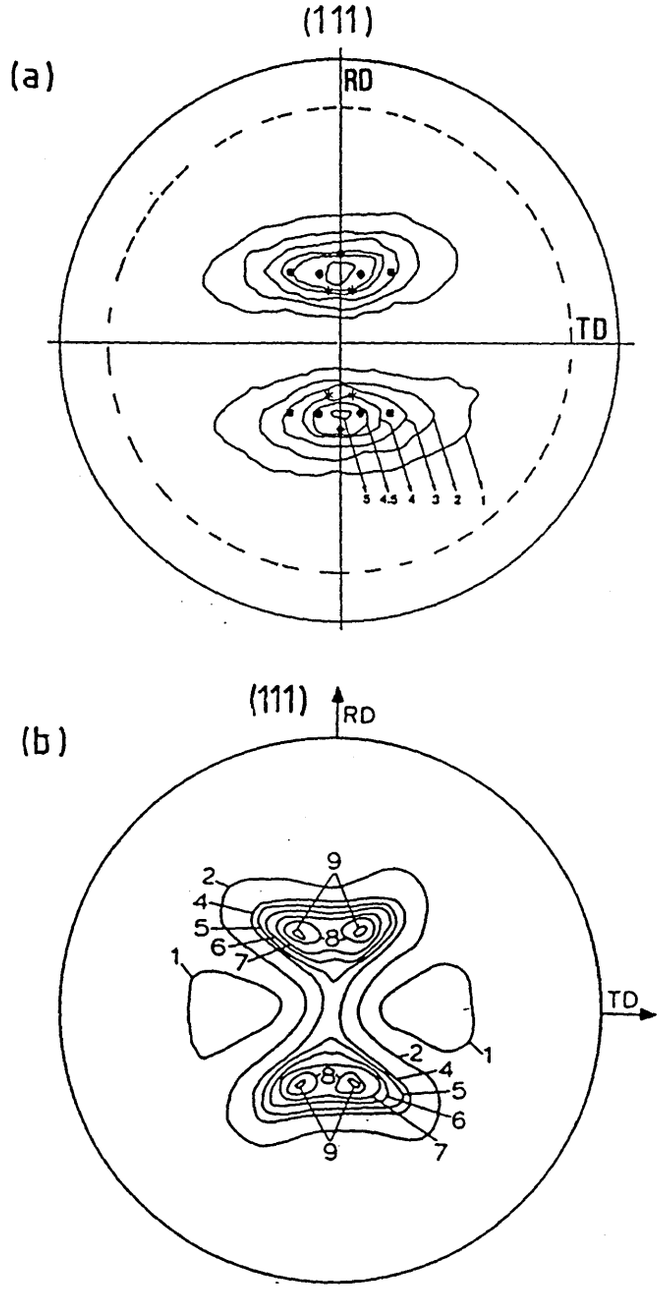


Figure 5.10- The comparison of the (111) pole figures of (a) the 41% prior cold worked alloy, studied in the present work, and (b) the 93% prior cold worked Cu 1.84wt% Be 0.3wt% Co alloy (after Nourbakhsh and Nutting, 1982).

dependency of primary recrystallisation at the initial stages on the prior deformation texture, as suggested by Bunge (1987). But, when the growth of recrystallised grains takes place extensively, the overall texture orientations are expected to shift towards the well-defined recrystall--isation texture orientations, such as (225)<73$\bar{4}$> (Lücke and Schmidt, 1972) or (113)<21$\bar{1}$> (Beck and Hu, 1952). This needs longer ageing treatments, and is not observed for ageing as long as 4 hours. Therefore, it is tentatively suggested that after ageing 4 hours at both 400 and 500°C the remaining deformation texture and the primary recrys--tallisation texture overlap; the overlapping is therefore represented by an increase in the texture intensities on the (111) pole figure.

5.4 Formability of Cu-Be-Co Strip Alloys

In the industry, several test methods are applied to specify the properties of a given material, obtained after various thermo-mechanical treatments, including the tensile test, hardness measurements, the cantilever bend test (ASTM D 747-70) for measuring the elastic contact force of the strip alloys, and the 90° bend test, based on ASTM B 194-81. However, each test method has its disadvantages and limitations when the formability of the alloys is the main concern. For example, the tensile test elongation is not a good predictor for the bend performance of a strip material because the overall strain in the gauge length of a tensile specimen is much less than that which occurs at the outer fibre of a bend sample when bending is performed on a reasonably sharp die. Hardness measurements may be a good predictor for the strength of the alloy, but the formability at different levels of strength remains unknown; a low hard--ness does not necessarily indicate a better formability.

In Section 4.6, the 90° bend tests have been shown not to be sensitive enough to follow the changes in formability of samples after different thermo-mechanical treatments. The experimental results (Figure 4.42) have also indicated that one of the short-comings of the

technique is that, because generally material is produced of a given thickness, only a limited number of R/t can be tested although a range of dies with different bend radii are available.

In the literature, the applicability of the cantilever bend tests to measure elastic spring back and the residual stress properties of spring materials has been demonstrated (Patrikh and Zarlingo, 1976; Brennemann et al., 1976). However, the technique is limited to only elastic deformation regimes, whereas, the cantilever-type bending used in the present study was designed to work at higher strains. Thus, the new cantilever-type bend test equipment in the present work made it possible to sensi--tively determine the bendability of a given material by a parameter "the maximum bendability angle", θ_M, at which cracks are initiated at the outer surface of the bend sample. Employing this technique, even small amounts of change in θ_M, introduced by changing the conditions of thermo-mechanical treatments, were succesfully detected.

As mentioned in Section 4.8.1, the only difficulty in this technique was that the value of θ_M is affected by the change in the thickness of the samples. Therefore, the values of θ_M for the materials of different thicknesses could not be compared from the raw data. Nevertheless, introducing a thickness correction factor, N_{COR}, eliminated any errors in the θ_M values due to thickness. In the following sections, the method of thickness correction, the the analytical modelling, and the corresponding experimen--tal results will be presented and discussed.

5.4.1 A thickness correction factor for cantilever-type bend tests

5.4.1.1 Analytical model

(1) Purely elastic bending

When a length of beam, which is initially straight (Figure 5.11-a), is bent elastically to a circular shape about the centre of curvature, O, (Figure 5.11-b), the plane AB rotates to A'B' and the length of the extreme fibre is changed by the amount δ. There is a neutral plane at the mid-thickness of the beam, and the stress and the strain across the thickness of the beam increase linearly from zero at the neutral plane to a maximum value at both surfaces, as shown in Figure 5.11-c.

In the theory of elastic bending, the following assumptions are made (Shanley, 1957; Murdi and McNabb, 1980):

(i) Plane cross sections before bending remain plane after bending.

(ii) Bending moment, M, is constant along the length and the stresses are uniform across the width of the beam.

(iii) The material obeys the Hooke's low, i.e. strain is proportional to stress, and the Youngs' modulus in tension is equal to that in compression.

(iv) All longitudinal fibres bend into circular arcs with the same centre of curvature, which is large compared to the cross sectional dimensions.

Following these assumptions, the strain at each fibre of length S_0 is given by

$$\epsilon = \delta / S_0 \qquad [5.4]$$

and direct comparison of triangles OEF and EA'A in Figure 5.11-a gives

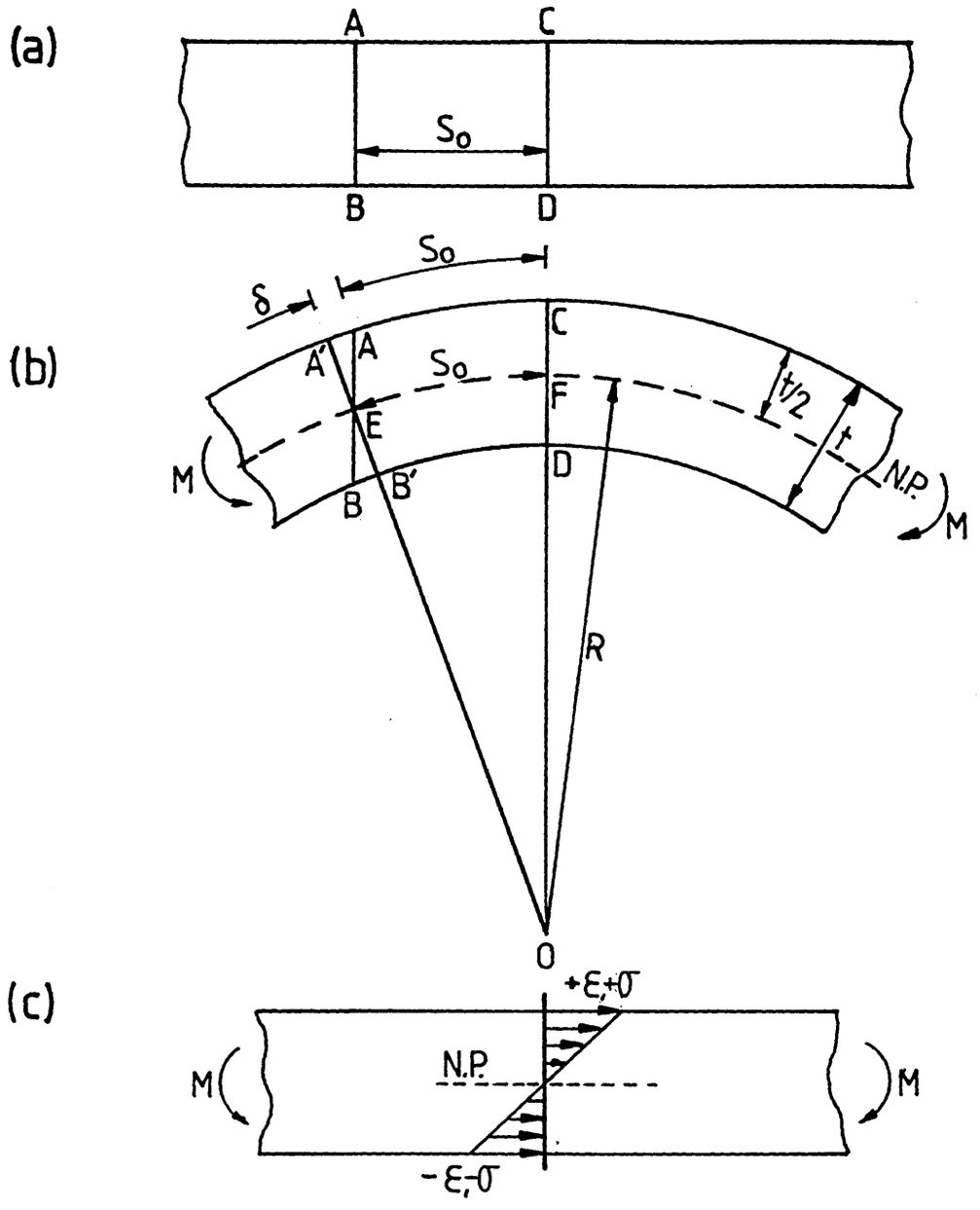


Figure 5.11- (a) A straight beam with a rectangular cross-section before bending.

(b) Strains in a beam after elastic bending; AB // CD.

(c) The elastic stress and strain distribution across the thickness of the bent beam of (b). NP shows the neutral plane.

$$\delta/S_0 = y/R$$

where y is the distance from the neutral plane. Therefore, from equation [5.4]

$$\epsilon = y/R \qquad [5.5]$$

where ϵ is the axial strain at a fibre and R the radius of curvature of the neutral plane.

Considering $\sigma = \epsilon E$ and equation [5.5], the stress at a given fibre, σ, is given by

$$\sigma = Ey/R \qquad [5.6]$$

Using equation [5.6], the bending moment, M = EI/R, becomes

$$M/I = \sigma/y = E/R \qquad [5.7]$$

where I is the momentum of inertia of cross section with respect to the neutral plane and E the Young's modulus.

(2) Inelastic bending

The theory of inelastic behaviour of bending beams makes the following assumptions (Shanley, 1957; Murdi and McNabb, 1980):

(i) A material has a relatively large elongation and a reasonably flat-topped stress-strain curve, which can be idealised as that shown in Figure 5.12 by neglecting strain hardening.

(ii) Tensile and compressive properties of the material are identical.

(iii) The effects of axial force and shear force are neglected in comparison to the effects of bending moments.

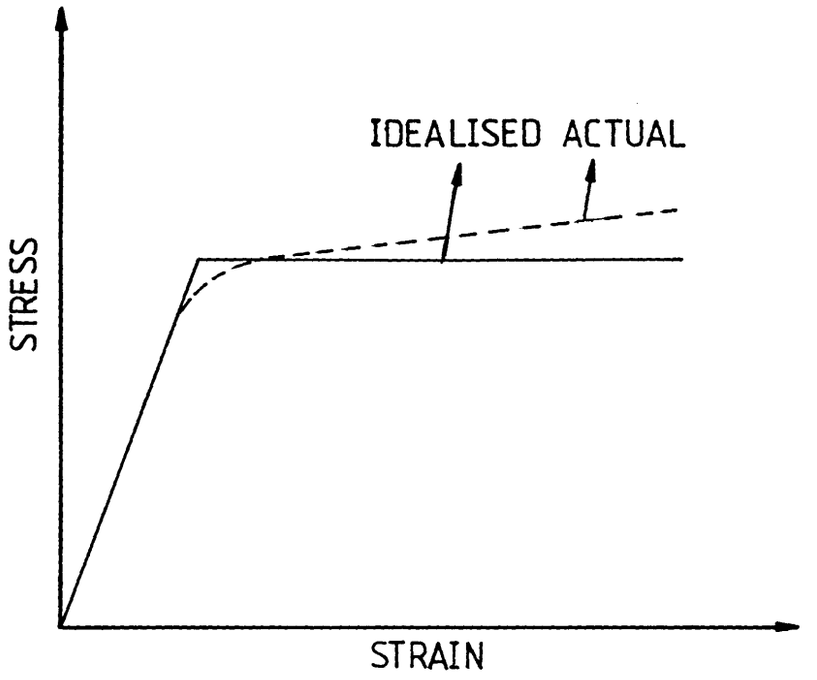


Figure 5.12- Idealised stress vs. strain diagram for inelastic bending.

Assuming that plane cross sections remain plane after bending, the moment associated with ideally plastic condition in which the entire cross section is at the plastic stress value , σ_P, as depicted in Figure 5.13-a, is given by (refer to equation [5.7]:

$$M_P = \sigma_P(I_P/y) \qquad [5.8]$$

For segments of the beam with areas A_1 and A_2 at a distance $y_1=y_2$ from the plastic neutral plane (PNP) (see Figure 5.13-a), the equilibrium of the stress σ_P may be related by:

$$\sigma_P/y_1 - \sigma_P/y_2 = 0 \qquad [5.9]$$

since

$$A_1 = A_2 \qquad [5.10]$$

For a beam with reasonably small width to thickness ratio, for example w/t=2, the deformation is in plane stress mode ($\sigma_X>0$, $\sigma_Y>0$, and $\sigma_Z=0$) and the cross sectional area above the neutral plane reduces as that below the neutral plane increases after applying the fully plastic moment M_P, as depicted in Figure 5.13-b. Therefore, equations [5.9] and [5.10] are not valid, i.e. $A_1 \neq A_2$, and the PNP should shift towards the centre of curvature until $\sigma_P/y_1-\sigma_P/y_2 = 0$; the amount of shift of PNP is equal to Δy.

Recently, Crafoord (1976) has shown analytically that during plastic bending a beam the magnitude of strain for a given fibre at λt distance from the outer surface of the beam (Figure 5.14-a) changes continuously. Crafoord proposed that the plot of strain ϵ vs. bending parameter K, where

$$\epsilon = 0.5\ln[(1-0.5K)^2 + 2\lambda K)]$$

$$K = t/R_1 \quad 0\leq K\leq 2$$

where t is the thickness of the beam and R_1 the radius of curvature of a given fibre for a given ϵ, shows that some fibres with $\lambda \geq 0.5$ have reversal in the strain direction as shown in Figure 5.14-b; the PNP is shifted to the fibres with increasing order of λ values as the bending radius R_1 increases.

As shown in Figure 5.13-b, the PNP is shifted towards the centre of curvature when w/t is small. Whereas, the cantilever-type bend samples in the present work have a w/t in the range 50 to 90, indicating that the samples are deformed in plane strain, as depicted in Figure 5.13-a ($\sigma_X>0$, $\sigma_Y>0$, and $\sigma_Z>0$). Also, it has been observed experimentally that the cross-sectional shape does not change during plastic bending to angles as large as 145°, suggesting that plane cross sections remain plane after bending. This confirms that the PNP remains in the centre of the cross section at any stage of the cantilever-type bending samples.

Having established that for cantilever-type bending samples the PNP does not shift and hence the distribution of stresses and strains above and below the PNP are identical, the effect of changing the thickness of a bend sample on the amount of strain, δ, at the extreme fibre may be determined. Considering that after plastic bending a sample with the thickness t_1 to an angle, θ_1, (Figure 5.15-a), AC and BD illustrate the limits of strains at the bend apex S_0 and S_1 the length of curvature at the neutral plane and the extreme fibre, and R_1 the radius of curvature at the neutral plane, the amount of strain, δ_1, at the extreme fibre can be determined as follows:

$$\begin{aligned} S_0 &= \theta_1 R1 \\ S_1 &= \theta_1 (R_1 + t_1/2) \\ \delta_1 &= S_1 - S_0 = \theta_1 (t_1/2) \end{aligned} \qquad [5.11]$$

where θ is measured in radians. Similarly, after plastic bending a sample with the thickness t_2 ($t_1>t_2$) to the same angle θ_1 as depicted in Figure 5.15-b, the amount of strain, δ_2, at the extreme fibre is given by:

$$\begin{aligned} \delta_2 &= S_2 - S'_0 \\ &= \theta_1 R_2 - \theta_1 (R_2 + t_2/2) \\ \delta_2 &= \theta_1 (t_1/2) \end{aligned} \qquad [5.12]$$

where the parameters are as shown in Figure 5.15-b. Note that even though the bend angles are the same (θ_1), δ_1 is

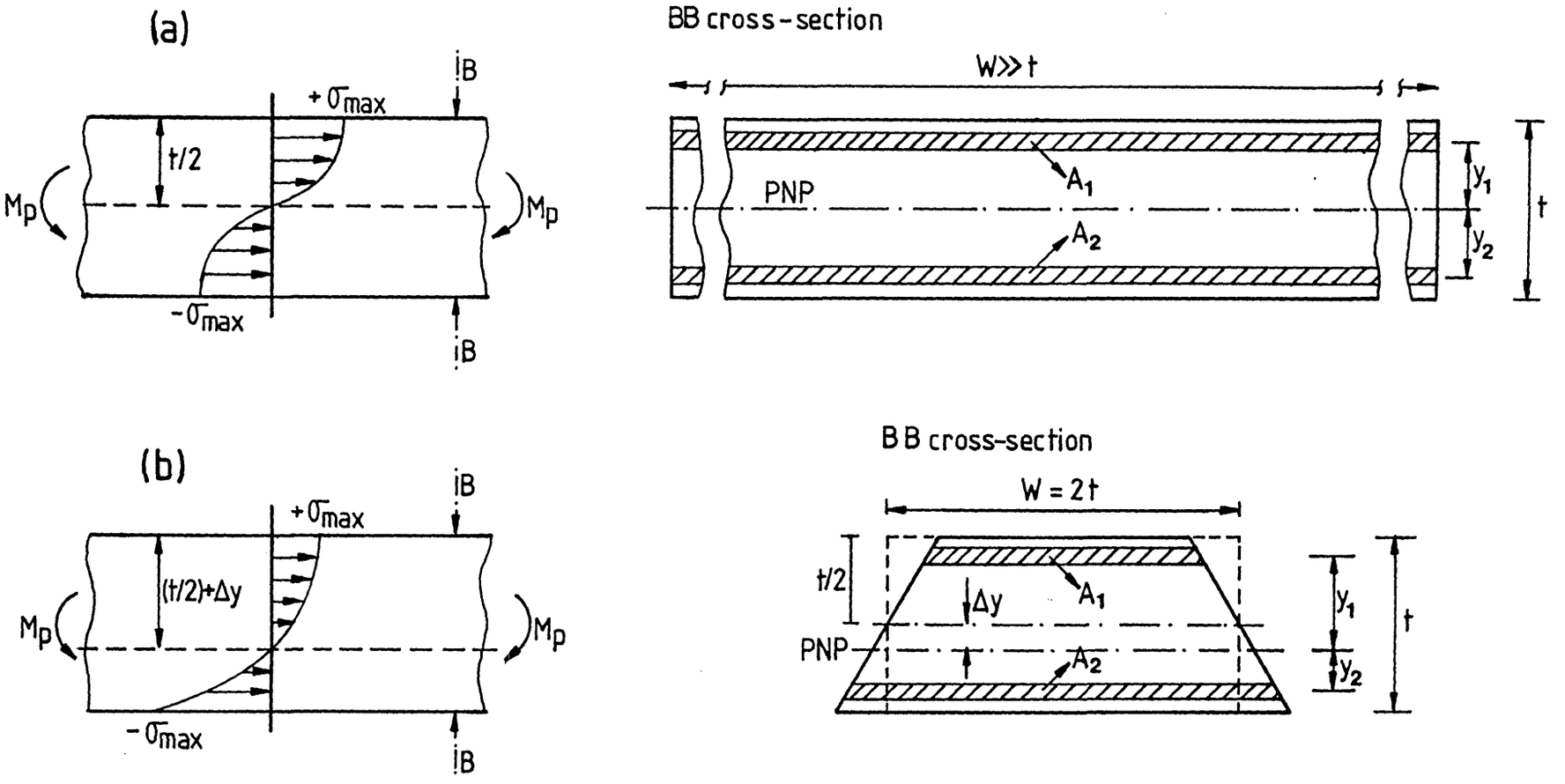


Figure 5.13- Simplified stress distribution and cross-sectional area after inelastic bending beams, which deform in (a) plane strain and (b) plane stress. PNP shows plastic neutral plane.

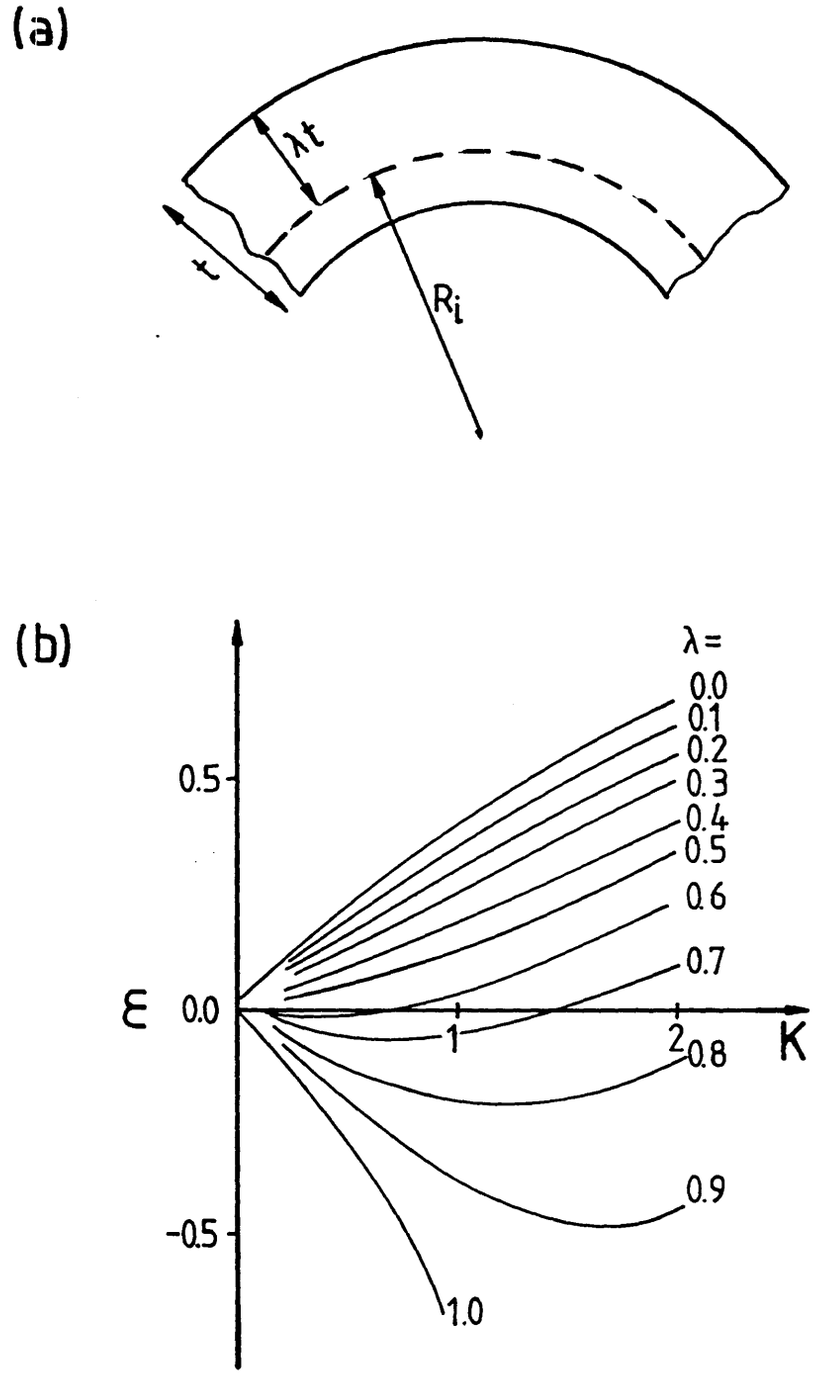


Figure 5.14- (a) A bent beam showing a fibre at λt distance from the outer surface and the corresponding radius of curvature, R_i.

(b) Distribution of bending strain at fibres with different λ ($0 \leq \lambda \leq 1$) as a function of a bending parameter, K (after Crafoord, 1976).

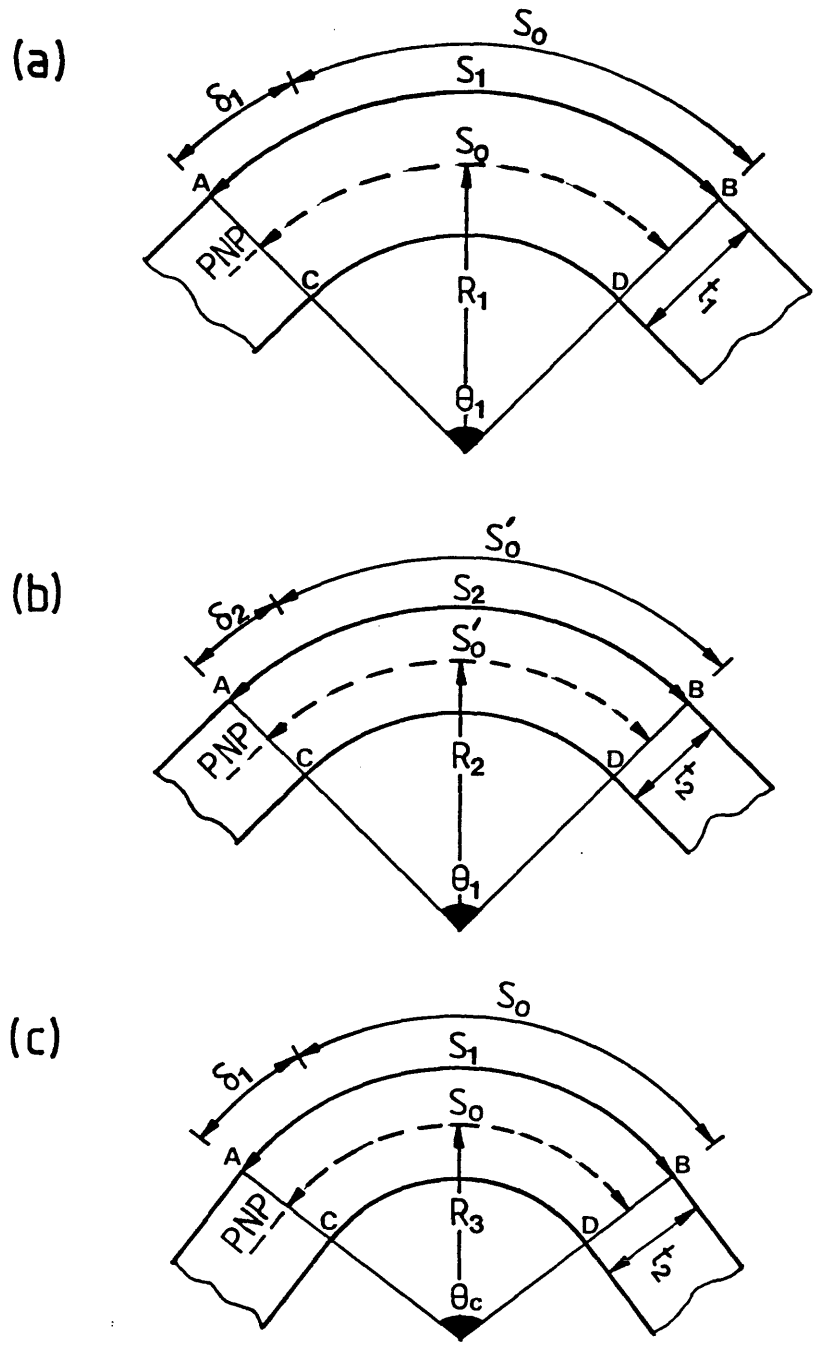


Figure 5.15- Strains during plastic bending

(a) a sample with the thickness t_1 to θ_1 angle,

(b) a sample with the thickness t_2 ($t_1 > t_2$) to θ_1 angle, and

(c) the sample of (a) to θ_c angle ($\theta_c > \theta_1$).

PNP indicates the plastic neutral plane at the mid-thickness of the sample.

larger than δ_2 since $R_1 > R_2$ and therefore the inequality in δ values for the samples with t_1 and t_2 arises only from the difference in thickness of the samples.

When the thinner sample with t_2 is further deformed in bending, there is a critical angle, θ_C, at which δ_1 becomes equal to δ_2, as shown in Figure 5.15-c. Assuming that the reduction in t_2 during bending from θ_1 to θ_C is very little and therefore can be ignored, θ_1 can be expressed by:

$$\delta_1 = \delta_2 = \theta_1(t_1/2) = \theta_C(t_2/2)$$

therefore

$$\theta_1 = \theta_C(t_2/t_1) \qquad [5.13]$$

Thus, the bend angle θ_C for the thinner sample of thickness t_2 can be corrected with respect to θ_2 by a correction factor:

$$N_{COR} = t_2/t_1 \qquad [5.14]$$

Therefore, the experimentally determined maximum bend-ability angle, θ_M, for samples of different thicknesses, obtained from the cantilever-type bend tests, can be corrected by using the following equation:

$$\theta_{COR} = \theta_M(t_1/t_M) \qquad [5.15]$$

where θ_{COR} is the corrected maximum bendability angle for a sample with the thickness t_1 and t_M is the thickness of the thickest sample among those tested.

5.4.1.2 Correlation of the analytical model by experimental results

(1) Sample preparation and testing

In order to investigate whether the correction factor, given in equation [5.14], is successful to elimin-ate the thickness effect on the experimental maximum bend-ability angle, the following experiment was carried out:

(i) Specimens with the same geometry as that of the cantilever bend tests were prepared from alloys UD and D5.

(ii) A number of samples from each alloy were ground on one surface to achieve smaller thicknesses; care was taken to obtain an even thickness through out the sample.

(iii) An original and a thinned sample were aged under identical conditions. This was repeated for six pairs of samples using different heat treatment conditions.

(iv) The aged samples were then tested on the cantilever-type bend test apparatus, following the procedure, described in Section 3.3.4.2.

(2) Analysis of the experimental data

The experimental values of the maximum bendability angle for each pair of the samples were classified as (i) θ_A of the samples with original thickness and (ii) θ_B of the thinned samples. The plot of θ_A vs. θ_B is given in Figure 5.16-a. As can be seen on this plot, the data point give a curved scatter band. In the absence of any experi--mental error, an ideal correction of θ_B with respect to θ_A should bring all the data points to the straight line (shown as broken line) with a slope equal to 1 (see Figure 5.16-a), whereas, at this stage the data points deviate from the straight line by about θ= 20 to 30°.

When θ_{COR} values for θ_B were obtained according to equation [5.15], the plot of θ_A vs. θ_{COR} revealed a good fit of the data points on the straight line with a standard deviation, θ ±3.12°, which is at the limits of the standard experimental error (Figure 5.16-b). It is now clear that N_{COR} can eliminate the thickness effect on the experimental θ_M values satisfactorily, and therefore θ_{COR} values becomes comparable without the interference of the error intro--duced by the change in the thickness of bend samples.

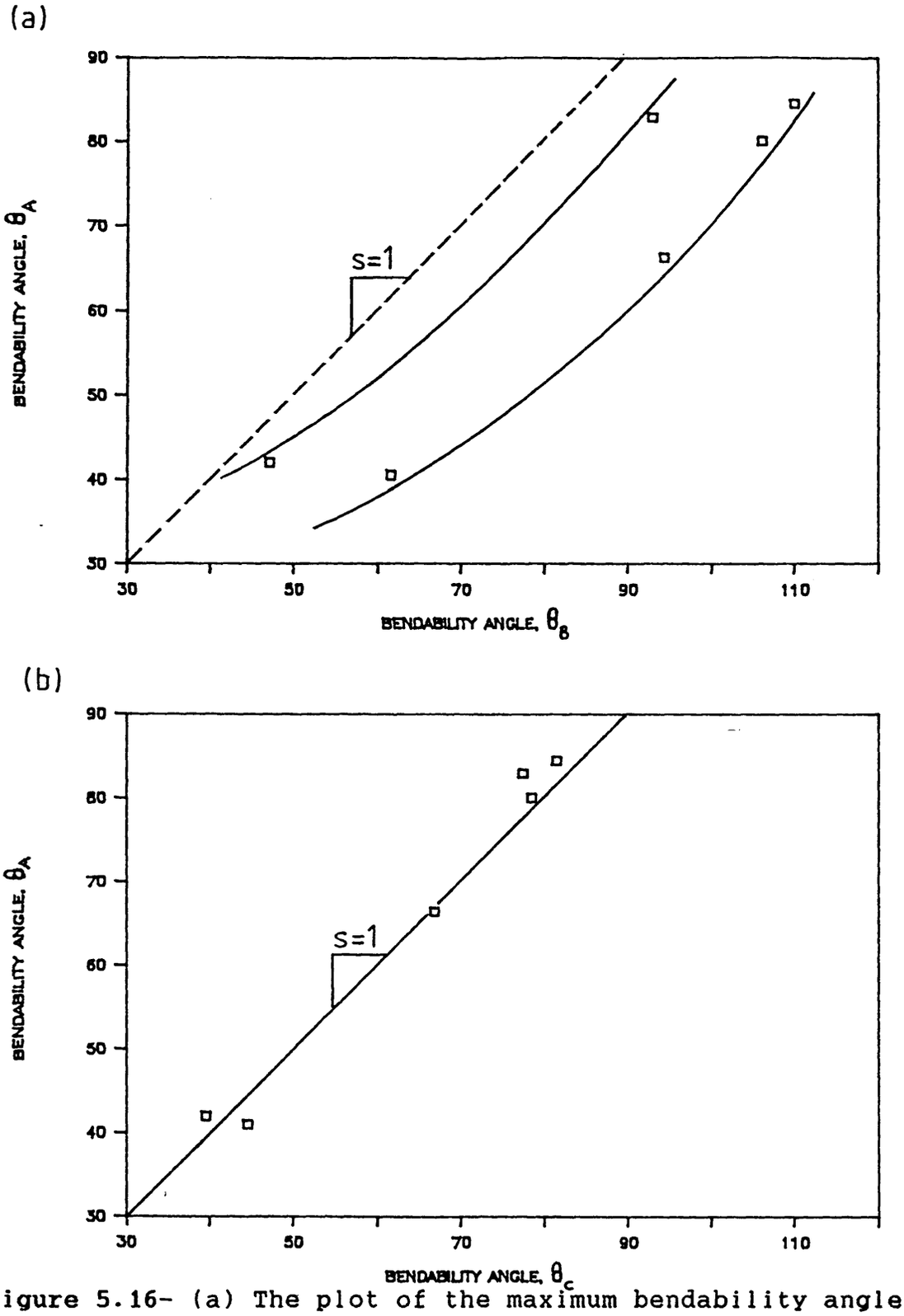


Figure 5.16- (a) The plot of the maximum bendability angle (θ_A) of an original sample vs. that (θ_B) of the thinned sample.

(b) The same plot of (a) after θ_B values are corrected using equation [5.13].

5.4.2 The use of three dimensional plots to follow changes in hardness and bendability

The criteria for determining the optimum properties of the alloy, which can be achieved after certain thermo-mechanical treatments, are (i) a better formability and (ii) a reasonably high hardness. Therefore, in order to facilitate determining the optimum formability and hardness values, from those achieved by various cold work-heat treatment regimes, three dimensional plots of the hardness and the maximum bendability angle vs. ageing time and temperature were obtained by computing the experimental data, given in Table B.1 in Appendix B, for a best fit on a three dimensional surface.

The plots of hardness vs. ageing time and tempera--ture and maximum bendability angle vs. ageing time and temperature for alloys UD, D5, D10, D18, D24, D32, and D41 are given in Figures 5.17 to 5.23 respectively. As can be seen on both 3D graphs of hardness and bendability in each figure, there seems to be a close symmetry in the shape of the surfaces. The change in the maximum bendability angle with ageing temperature and time and the amount of prior cold work has been described in Section 4.8.2. Using the 3D graphs, it is now clearer that the lower the ageing temperature and the higher the amount of prior cold work, the smaller the maximum bendability angle, θ_M, whilst the higher the ageing temperature, the greater the θ_M.

On the bendability plots the contour lines are marked by arbitrary numbers. Similar contour lines are also shown on the hardness plot of alloy UD (Figure 5.17-b) and the shape of the contour lines in the region of the initial hardness increase indicates similarity with these of "C" curves for this alloy. Following the contour lines, it was observed that an acceleration in hardening occurs above 380°C as indicated by an arrow. This is in agreement with T_2 value, at which curves G and F on the TTT diagram (see Figure 5.1) are separated. But, the contour lines of this type could not be resolved on the hardness plots of the prior cold worked alloys.

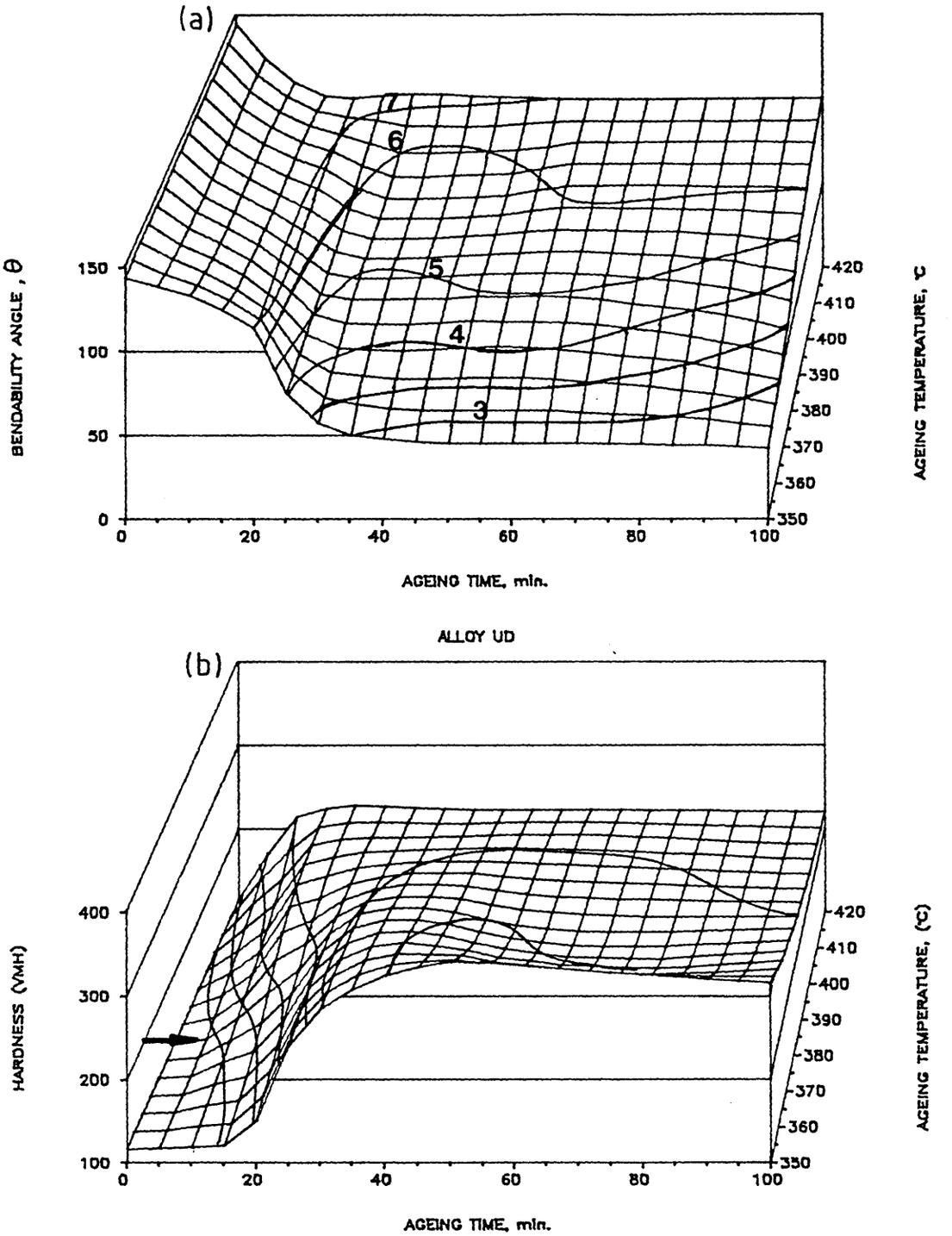


Figure 5.17- Three dimensional plots of (a) the maximum bendability angle vs. ageing temperature and time and (b) hardness vs. ageing temperature and time, for the solution treated alloy. The numbers 3 to 8 are arbitrary contour values.

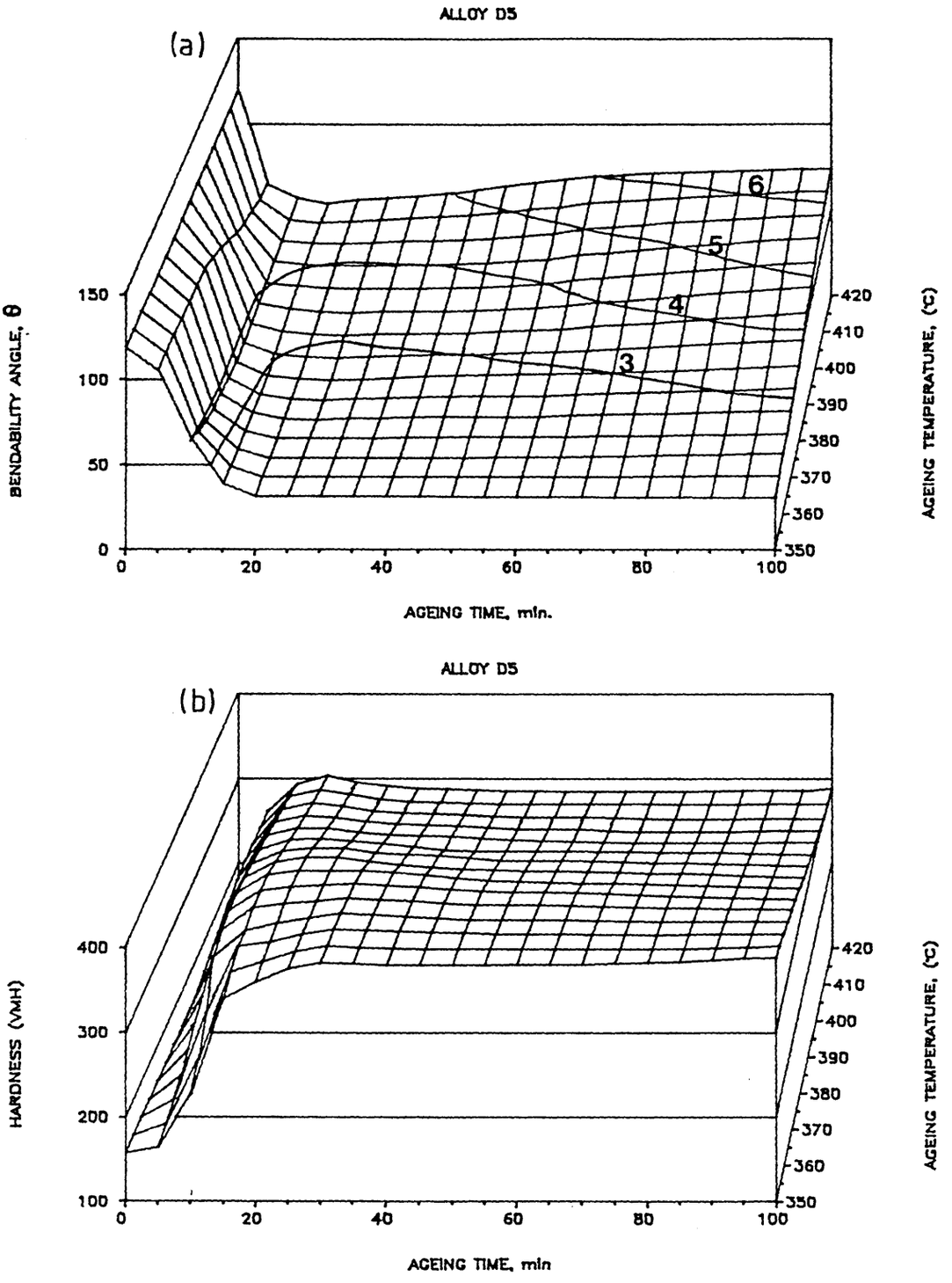


Figure 5.18- Three dimensional plots of (a) the maximum bendability angle vs. ageing temperature and time and (b) hardness vs. ageing temperature and time, for the 5% prior cold worked alloy. The numbers 3 to 6 are arbitrary contour values.

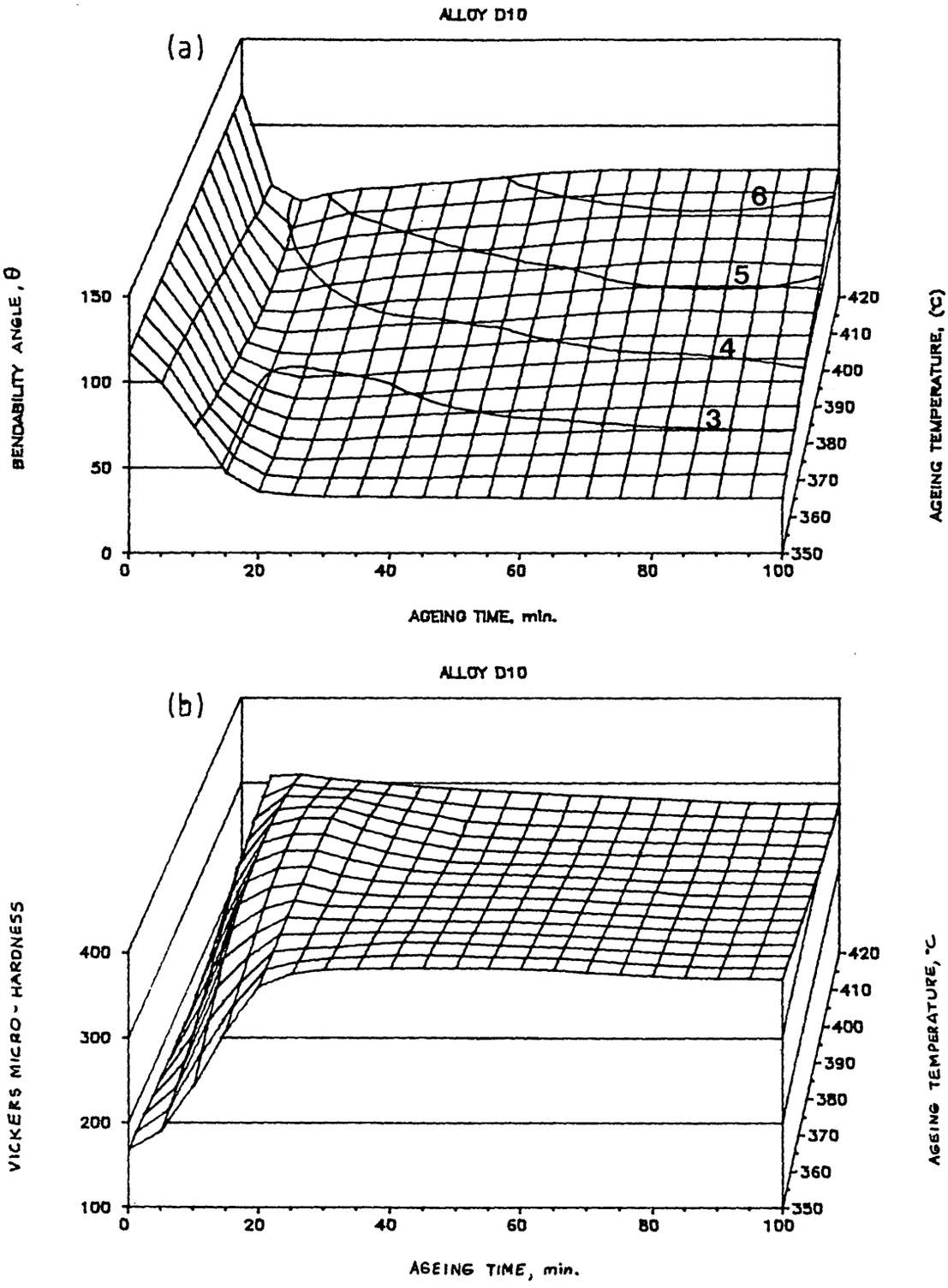


Figure 5.19- Three dimensional plots of (a) the maximum bendability angle vs. ageing temperature and time and (b) hardness vs. ageing temperature and time, for the 10% prior cold worked alloy. The numbers 3 to 6 are arbitrary contour values.

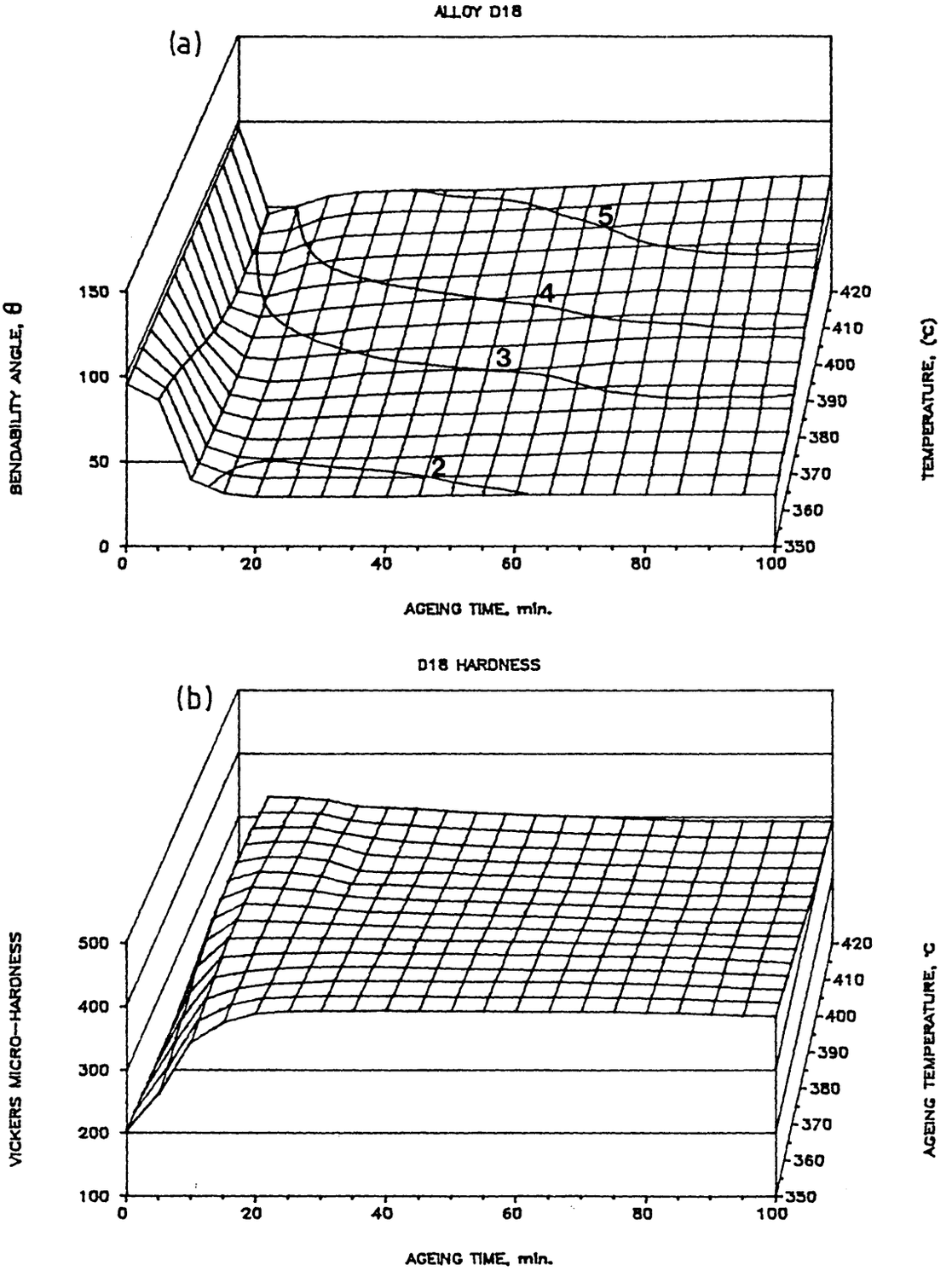


Figure 5.20- Three dimensional plots of (a) the maximum bendability angle vs. ageing temperature and time and (b) hardness vs. ageing temperature and time, for the 18% prior cold worked alloy. The numbers 3 to 5 are arbitrary contour values.

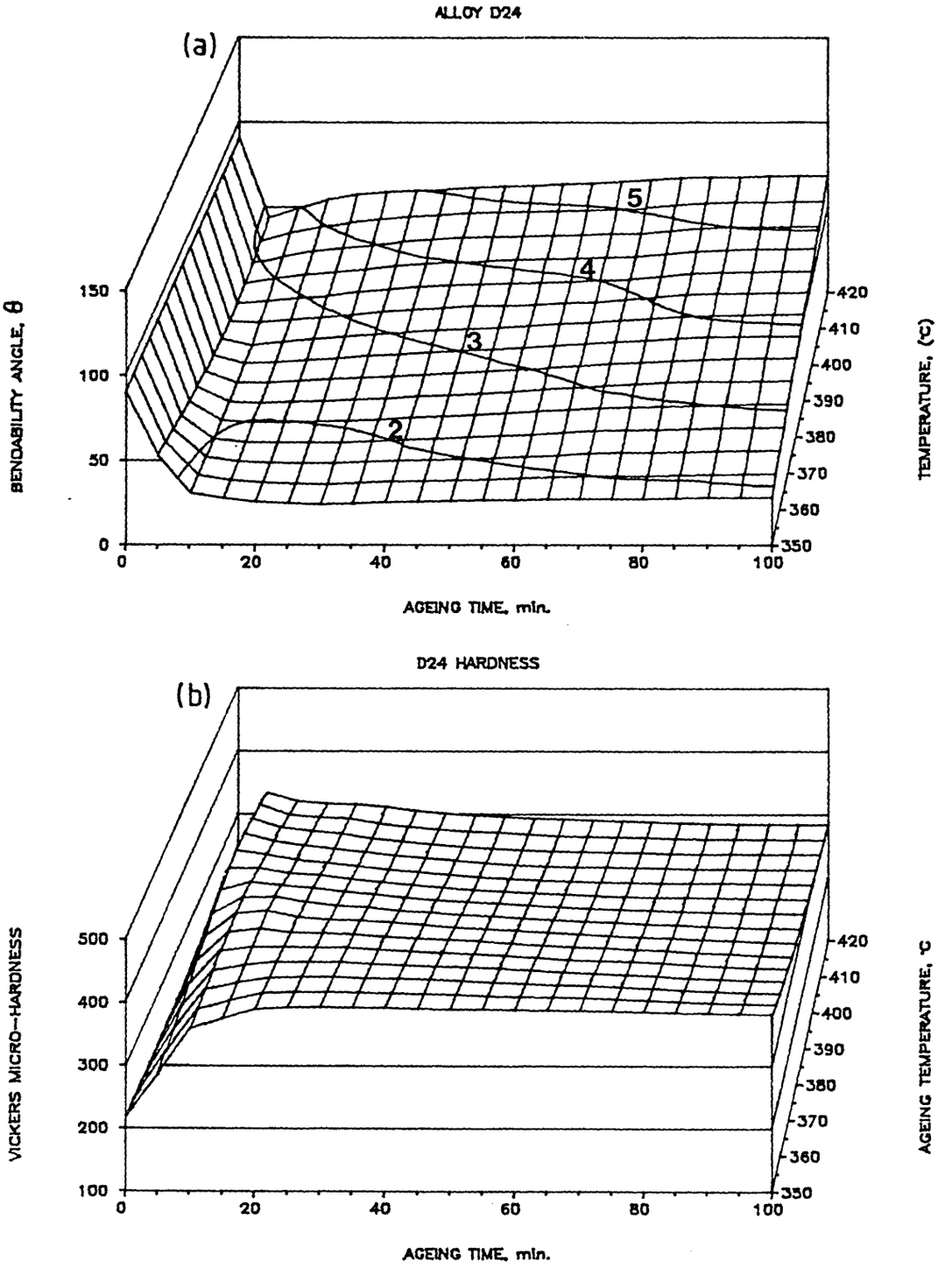


Figure 5.21- Three dimensional plots of (a) the maximum bendability angle vs. ageing temperature and time and (b) hardness vs. ageing temperature and time, for the 24% prior cold worked alloy. The numbers 3 to 5 are arbitrary contour values.

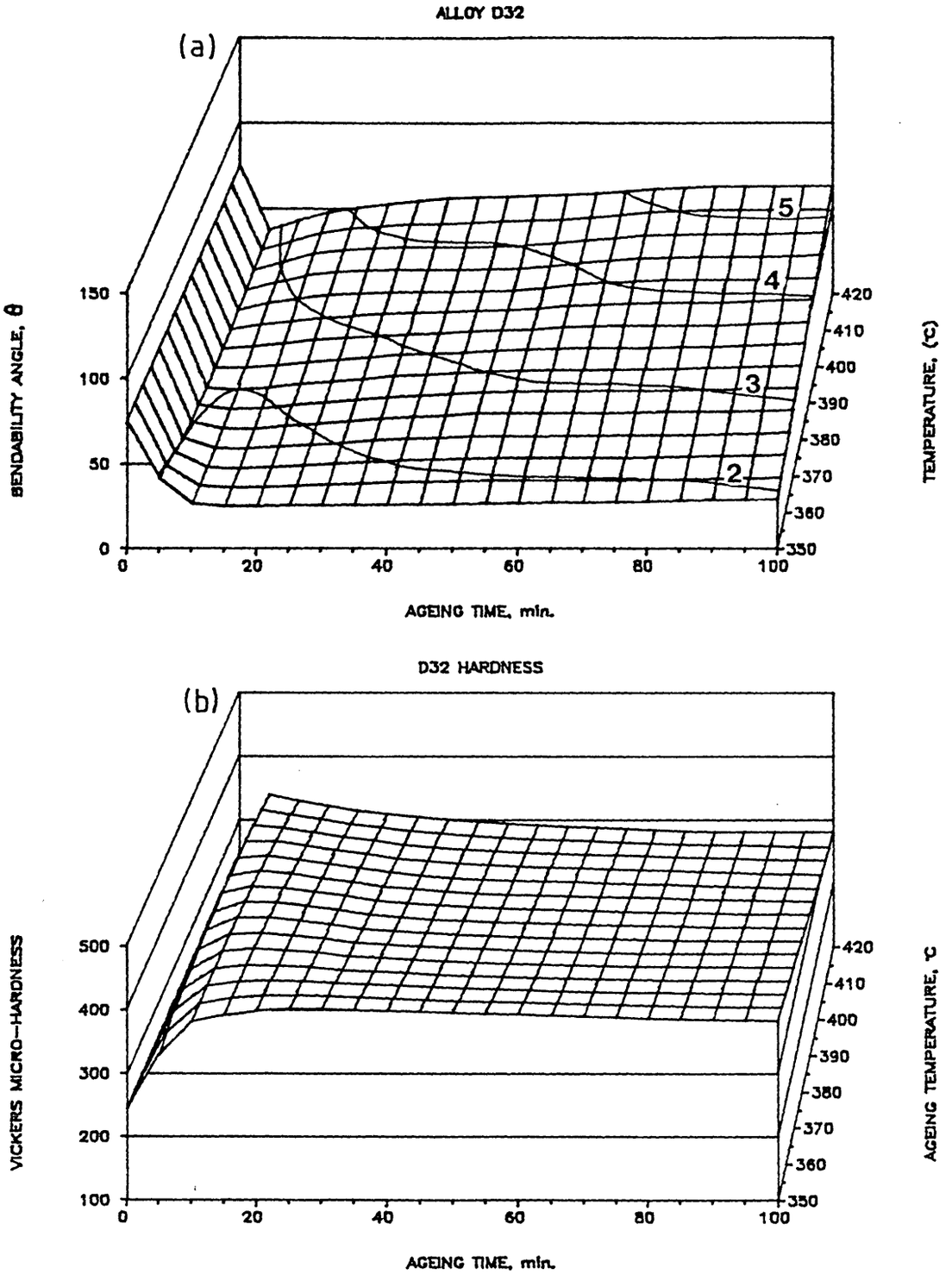


Figure 5.22- Three dimensional plots of (a) the maximum bendability angle vs. ageing temperature and time and (b) hardness vs. ageing temperature and time, for the 32% prior cold worked alloy. The numbers 3 to 5 are arbitrary contour values.

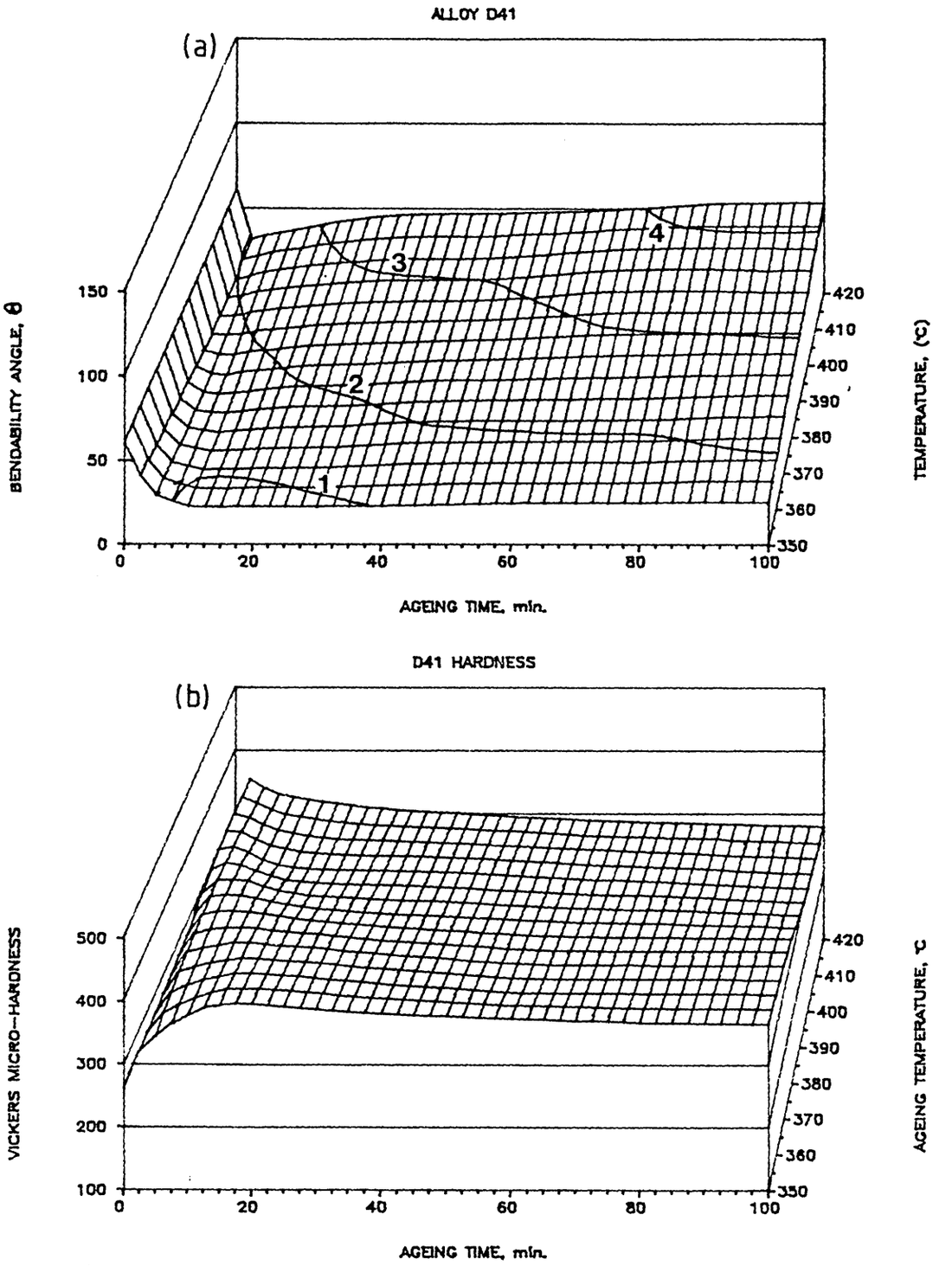


Figure 5.23- Three dimensional plots of (a) the maximum bendability angle vs. ageing temperature and time and (b) hardness vs. ageing temperature and time, for the 41% prior cold worked alloy. The numbers 3 to 5 are arbitrary contour values.

5.4.3 The combined 3D graphs of normalised bendability and normalised hardness

The 3D plots of bendability and hardness as a function of ageing time and temperature enable the selection of the optimum heat treatment conditions. However, two plots are required for each starting condition (UD, D5, D10, etc.) of the alloy and it is time consuming comparing the two plots. Therefore various attempts have been made to combine both types of plots into a single plot of a combined hardness and bendability parameter as a function of the studied ageing treatments. Among several normalisation methods, the following equation has been found to give the best result in combining the hardness and the bendability with equal weighing into a combined normalised parameter, F_{NORM}.

$$F_{NORM} = [(H_i - H_{min})/\Delta H_{max}] + [(\theta_i - \theta_{min})/\Delta\theta_{max}] \qquad [5.16]$$

where:

H_i and θ_i = Values of the hardness and the maximum bend--ability angle, respectively, measured after a given heat treatment of any alloy.

H_{min} and θ_{min} = The minimum value of the hardness and the maximum bendability angle, respectively, irrespective of degree of prior cold work and heat treatment. The values of H_{min} and θ_{min} were found to be 116 kg/mm^2 and 22°, respectively.

$\Delta H_{max} = H_{max} - H_{min}$ and $\Delta\theta_{max} = \theta_{max} - \theta_{min}$, where

H_{max} and θ_{max} = The maximum values of the hardness and the maximum bendability angle, respectively, irrespective of prior cold work and heat treatment. The values of H_{max} and θ_{max} obtained in the present investigations were 402 kg/mm^2 and 145°, respectively.

The data of hardness and bendability were computed using equation [5.16] to give the 3D plots of the F_{NORM} function for alloys UD, D5,D10, D18, D24, D32, and D41, presented in Figure 5.24-a to g. Also note that the scaling units on the axis of the F_{NORM} function graphs for all alloys are the same. Therefore, the F_{NORM} function graphs in Figure 5.24-a to g are comparable. The comparison of the F_{NORM} function graphs, using the contour lines, marked by arbitrary numbers from 1 to 18, clearly shows the following features:

(i) Only certain ageing treatments result in the optimum F_{NORM} fuction values and the contour lines with the greatest numbers on each graph represent these ageing conditions.

(ii) The highest contour regions correspond to the peak ageing and/or the overageing conditions.

(iii) The increasing prior cold work reduces the overall values of F_{NORM} function and the contour on the 3D surface.

In order to assess the reliability in using the F_{NORM} function graphs to select the best heat treatment conditions for the mill hardened Cu-Be-Co alloys, maximum bendability angle, θ_M, vs. hardness, H, plots were obtained for each alloy, using the experimental data in Table B.1 in Appendix B. The data points on these plots (Figure 5.25-a to g) reveal that the value of θ_M falls as the hardness increases. Also, the amount of scatter of the data points reduces with increasing prior cold work; this corre--sponds to the reduction in the contour range of the F_{NORM} function graphs (Figure 5.24-a to g) with prior cold work.

The data points, representing relatively high or the highest values of θ_M for different hardness values in Figure 5.25-a to g were found to correspond to the regions of higher contours on the F_{NORM} function graphs in Figure 5.24-a to g, respectively, or vice versa. For example, the data points, marked by A, B, C....N, for alloy UD in Figure

5.25-a, correspond to the same notations, marked on the F_{NORM} function graph of the same alloy in Figure 5.24-a. As can be seen on both graphs, data points A, H, I, J, K, and L indicate a good combination of θ_M and H values and high F_{NORM} values, whereas, B, C, D, E, F, G, M, and N reveal poor properties. For prior cold worked alloys, the same type of agreement of the data of Figure 5.24-b to g and these of Figure 5.25-b to g, respectively, has been observed, but for the sake of clarity on the graphs the notations are not indicated.

The agreement of the data points in both types of graphs in representing the properties clearly show that the F_{NORM} function and the related 3D graphs can be used safely for the selection of best heat treatment conditions.

As given in Table 1.1, the commercially produced mill-hardened Cu-Be-Co alloys, including the solution treated alloy, are classified by the grades, WM, W1/4HM, W1/2HM, etc., corresponding to different thermo-mechanical treatments. Additional grades intermediate to the standard grades are also proposed in the present work, as listed in Table 3.1. The alloys of each grade should possess a hardness within certain limits, as specified in Table 1.1. Therefore, the minimum limit of hardness for different grades will be used as a criterion to select the better heat treatments investigated in the present work. For this reason, the commercially used hardness limits for each grade are marked on the bendability vs. hardness plots in Figure 5.25-a to g.

5.4.4 Selection of the best thermal/thermo-mechanical treatments for optimum values of F_{NORM}

As presented in above sections, there is a distinct difference in hardness and bendability of the solution treated and the prior cold worked alloys. Therefore, in the following sections, the optimum properties and the corre--sponding heat treatments of the solution treated alloy will be examined and discussed separately from these of the prior cold worked alloys.

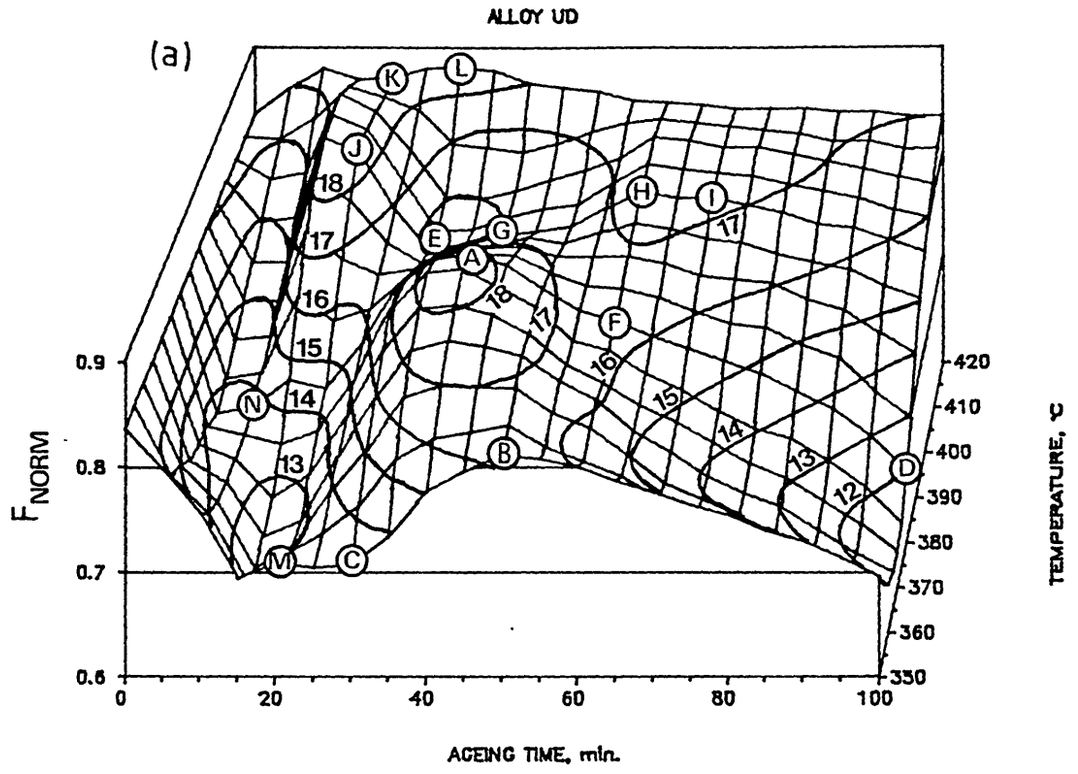


Figure 5.24- The combined plots of (a) and (b) in Figures 5.15, 5.16, 5.17, 5.18, 5.19, 5.20, and 5.21 for

(a) alloy UD,
(b) alloy D5,
(c) alloy D10,
(d) alloy D18,
(e) alloy D24,
(f) alloy D32, and
(g) alloy D41, respectively,

according to the computed values of F_{NORM} by using equation [5.14]. The numbers 1 to 18 are the contour values.

Figure 5.24

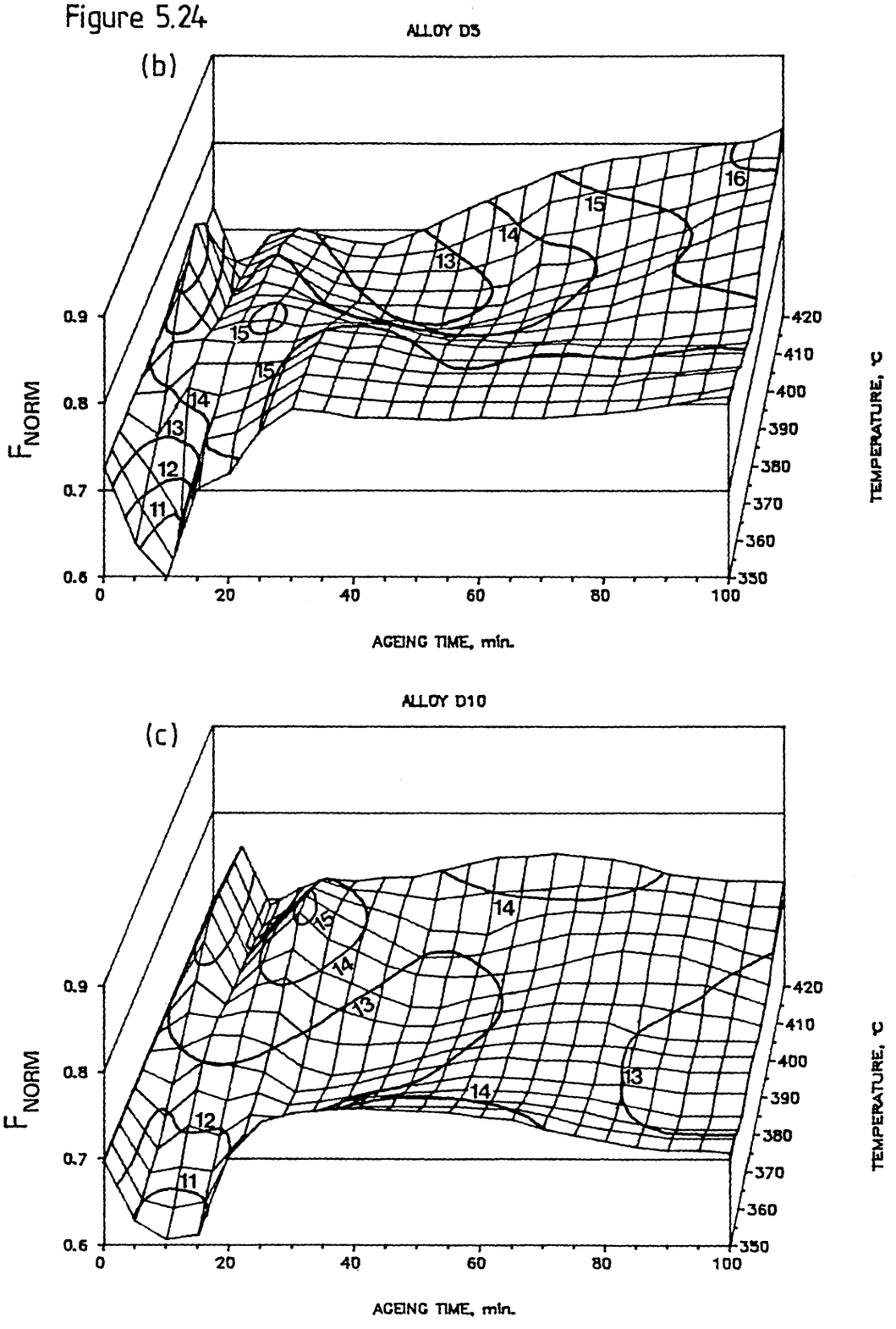

ALLOY D5
(b)
F_{NORM}
0.6
0.7
0.8
0.9
0
20
40
60
80
100
AGEING TIME, min.
350
360
370
380
390
400
410
420
TEMPERATURE, °C
11
12
13
14
15
16
ALLOY D10
(c)
F_{NORM}
0.6
0.7
0.8
0.9
0
20
40
60
80
100
AGEING TIME, min.
350
360
370
380
390
400
410
420
TEMPERATURE, °C
11
12
13
14

Figure 5.24

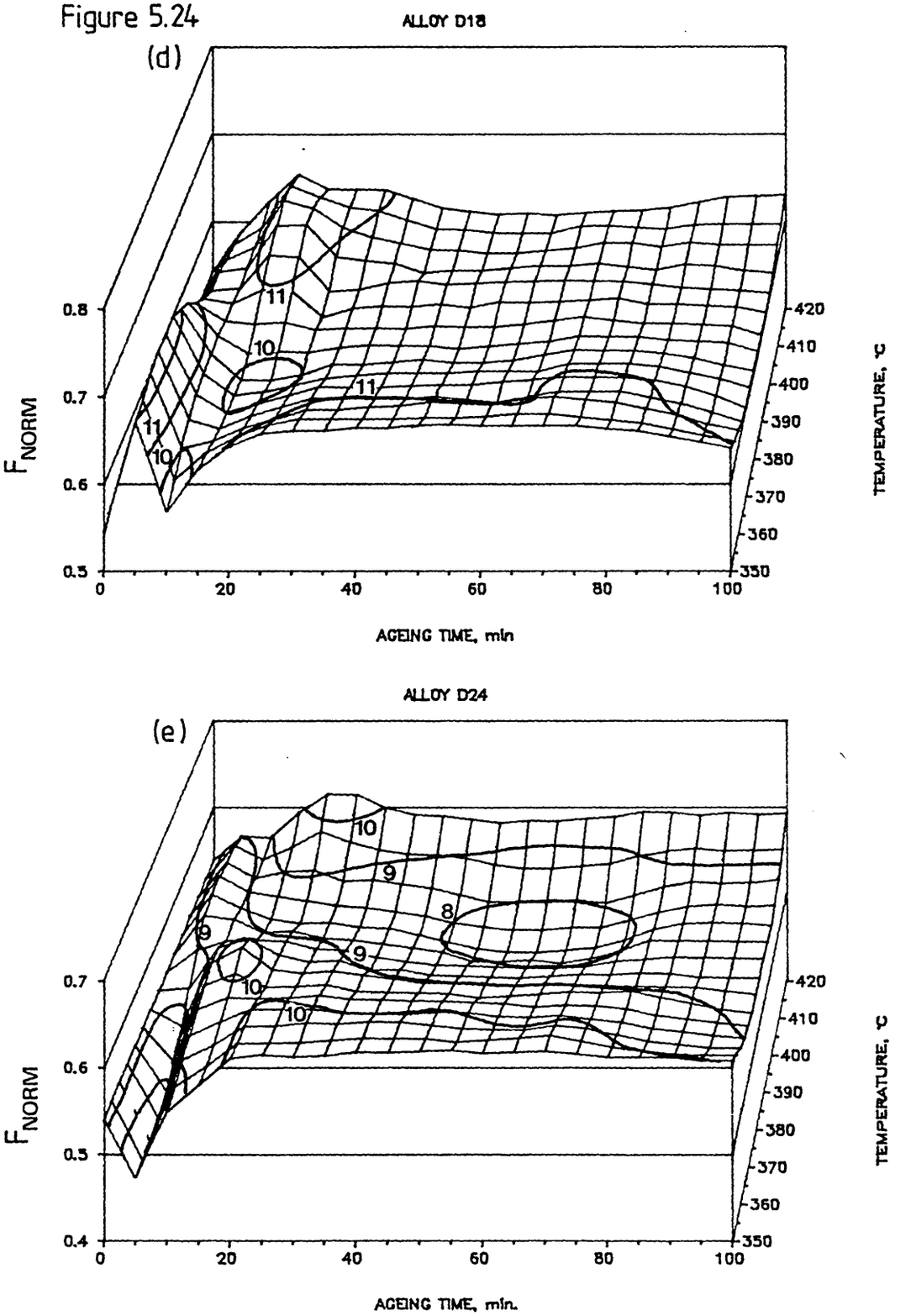
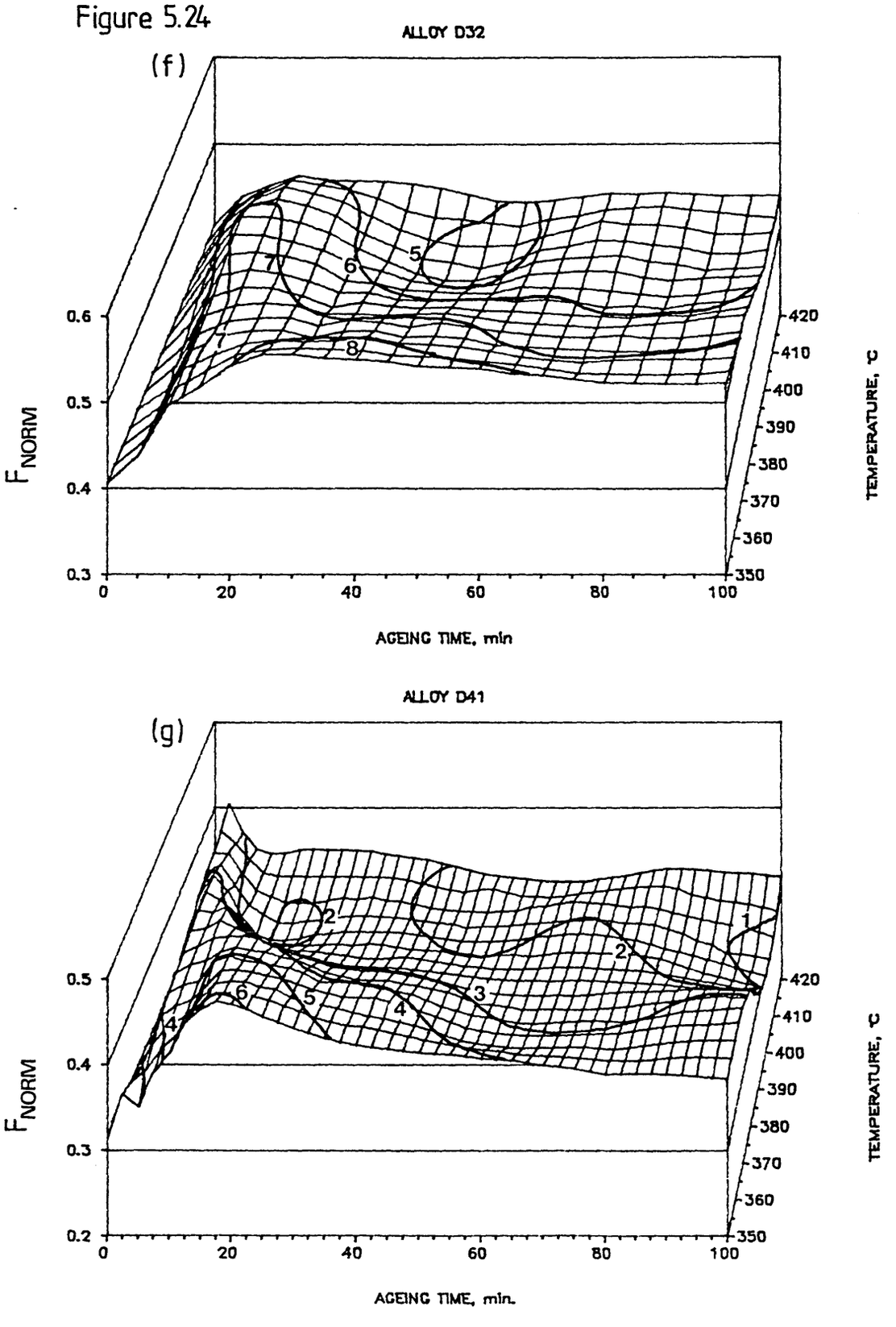

ALLOY D18
(d)
F_NORM
0.8
0.7
0.6
0.5
11
10
11
10
11
0
20
40
60
80
100
AGEING TIME, min
420
410
400
390
380
370
360
350
TEMPERATURE, °C
ALLOY D24
(e)
F_NORM
0.7
0.6
0.5
0.4
10
9
8
9
9
10
10
0
20
40
60
80
100
AGEING TIME, min.
420
410
400
390
380
370
360
350
TEMPERATURE, °C

Figure 5.24


ALLOY D32
(f)
F NORM
0.6
0.5
0.4
0.3
0
20
40
60
80
100
AGEING TIME, min
7
6
5
8
420
410
400
390
380
370
360
350
TEMPERATURE, °C
ALLOY D41
(g)
F NORM
0.5
0.4
0.3
0.2
0
20
40
60
80
100
AGEING TIME, min.
1
2
3
4
5
6
420
410
400
390
380
370
360
350
TEMPERATURE, °C

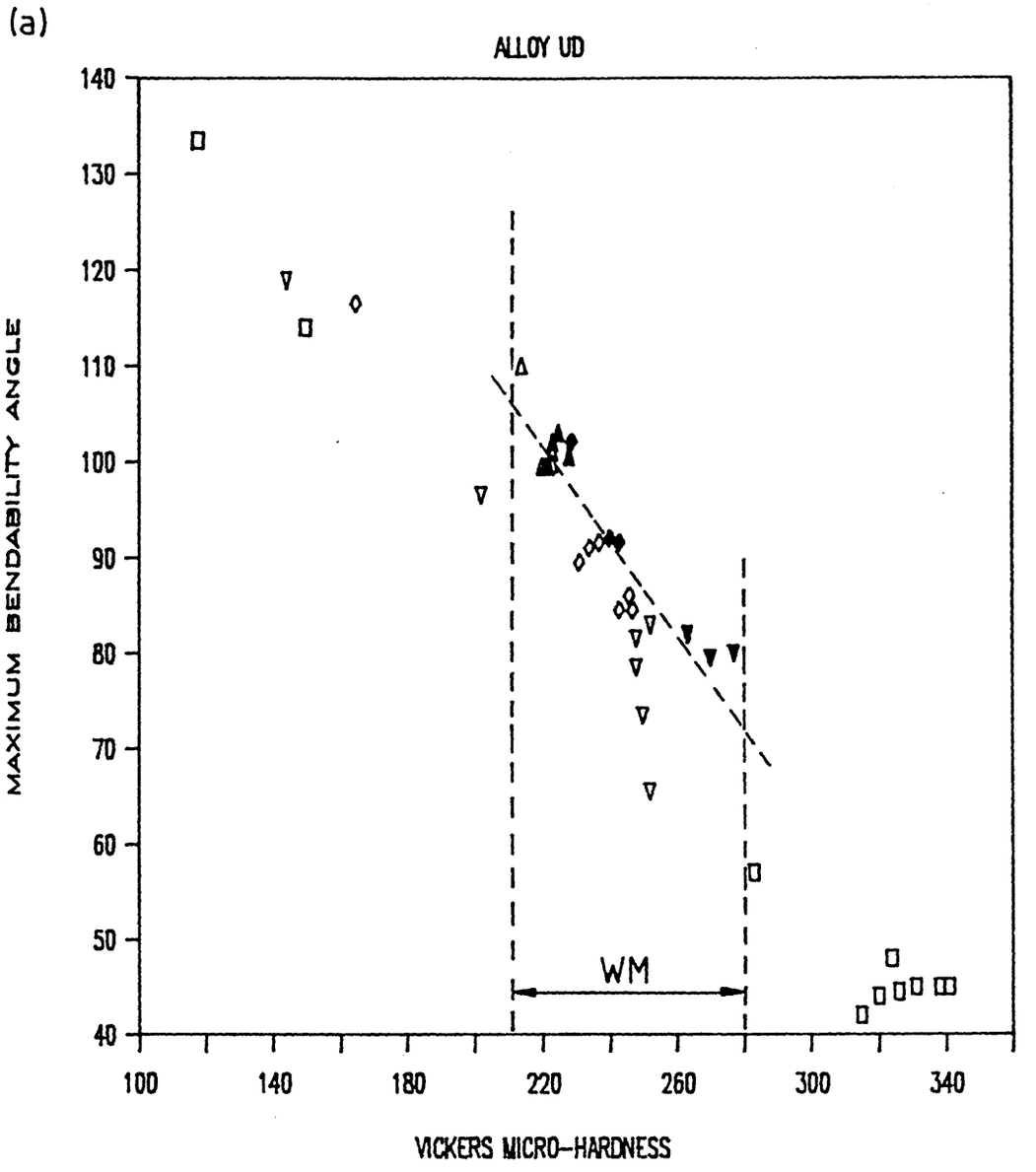


Figure 5.25- The plots of the maximum bendability angle vs. hardness for
(a) alloy UD,
(b) alloy D5,
(c) alloy D10,
(d) alloy D18,
(e) alloy D24,
(f) alloy D32, and
(g) alloy D41.
Note that full symbols correspond to the peak regions in the F_{NORM} function plots in Figure 5.24-a to g. Ageing temperatures are (□) 350°C, (▽) 380°C, (◇) 400°C, and (△) 420°C.

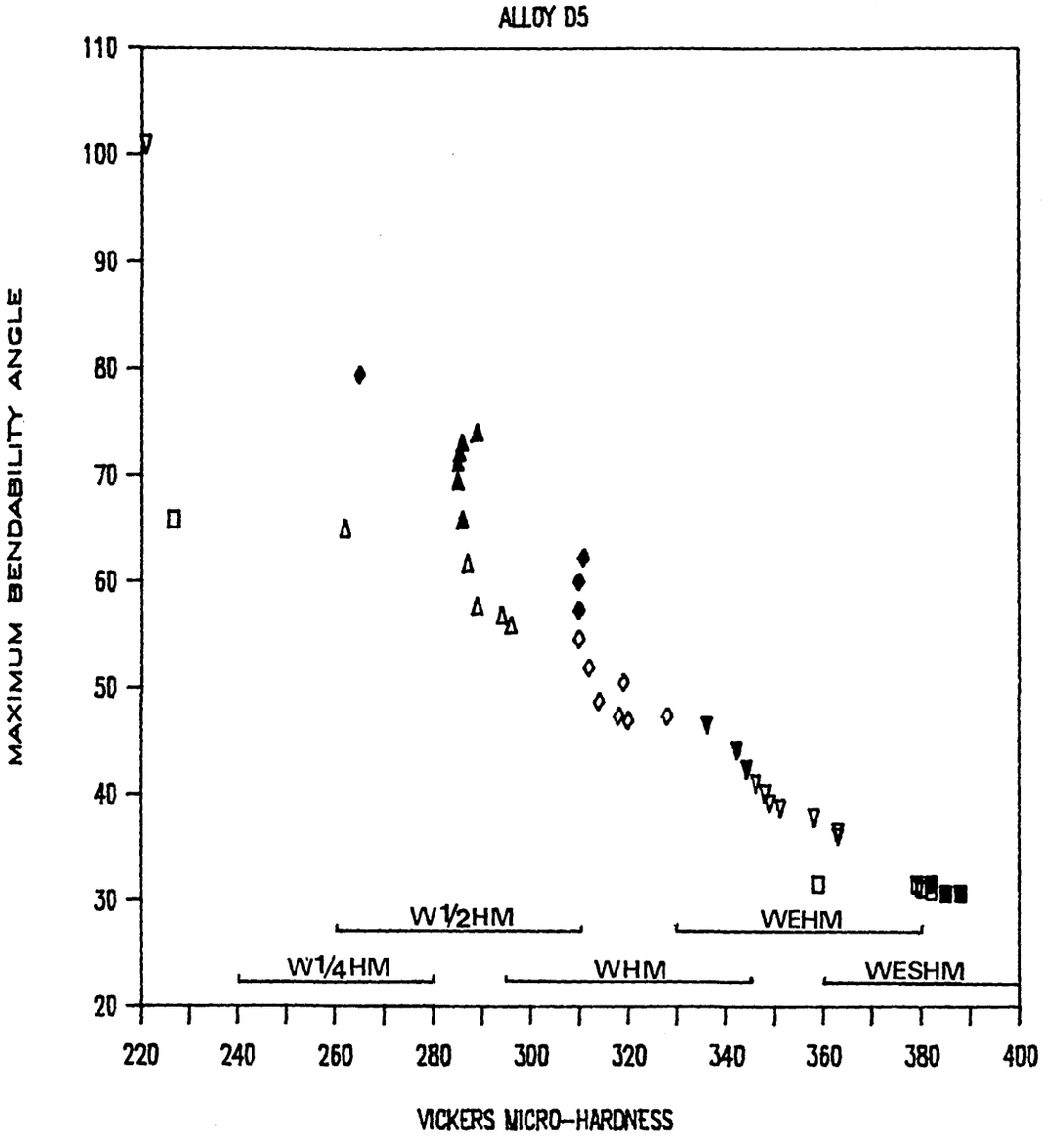

ALLOY D5
MAXIMUM BENDABILITY ANGLE
110
100
90
80
70
60
50
40
30
20
220
240
260
280
300
320
340
360
380
400
VICKERS MICRO-HARDNESS
W1/2HM
WEHM
W1/4HM
WHM
WESHM

Figure 5.25-b.

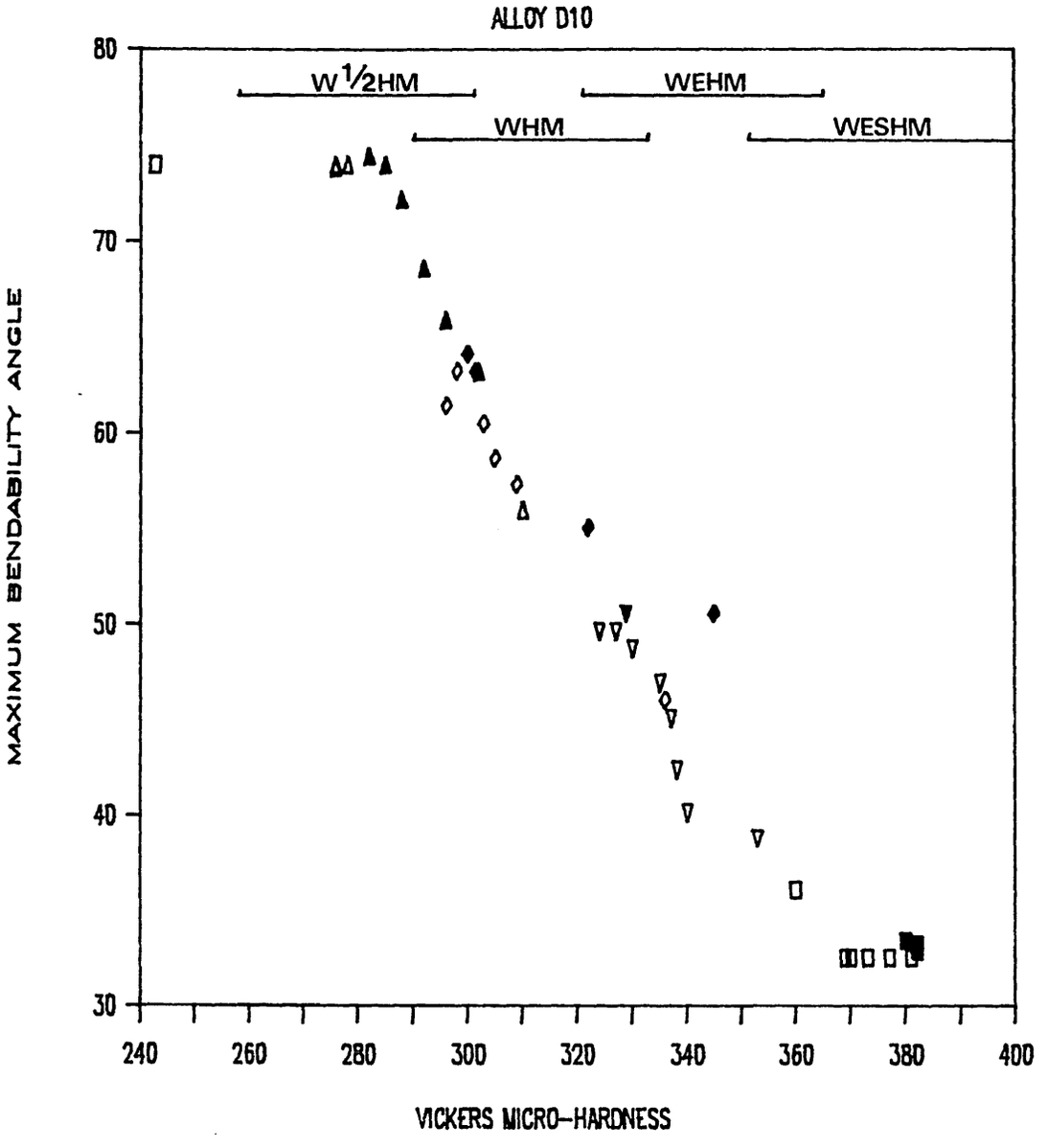

ALLOY D10
W1/2HM
WEHM
WHM
WESHM
MAXIMUM BENDABILITY ANGLE
80
70
60
50
40
30
240
260
280
300
320
340
360
380
400
VICKERS MICRO-HARDNESS

Figure 5.25-c.

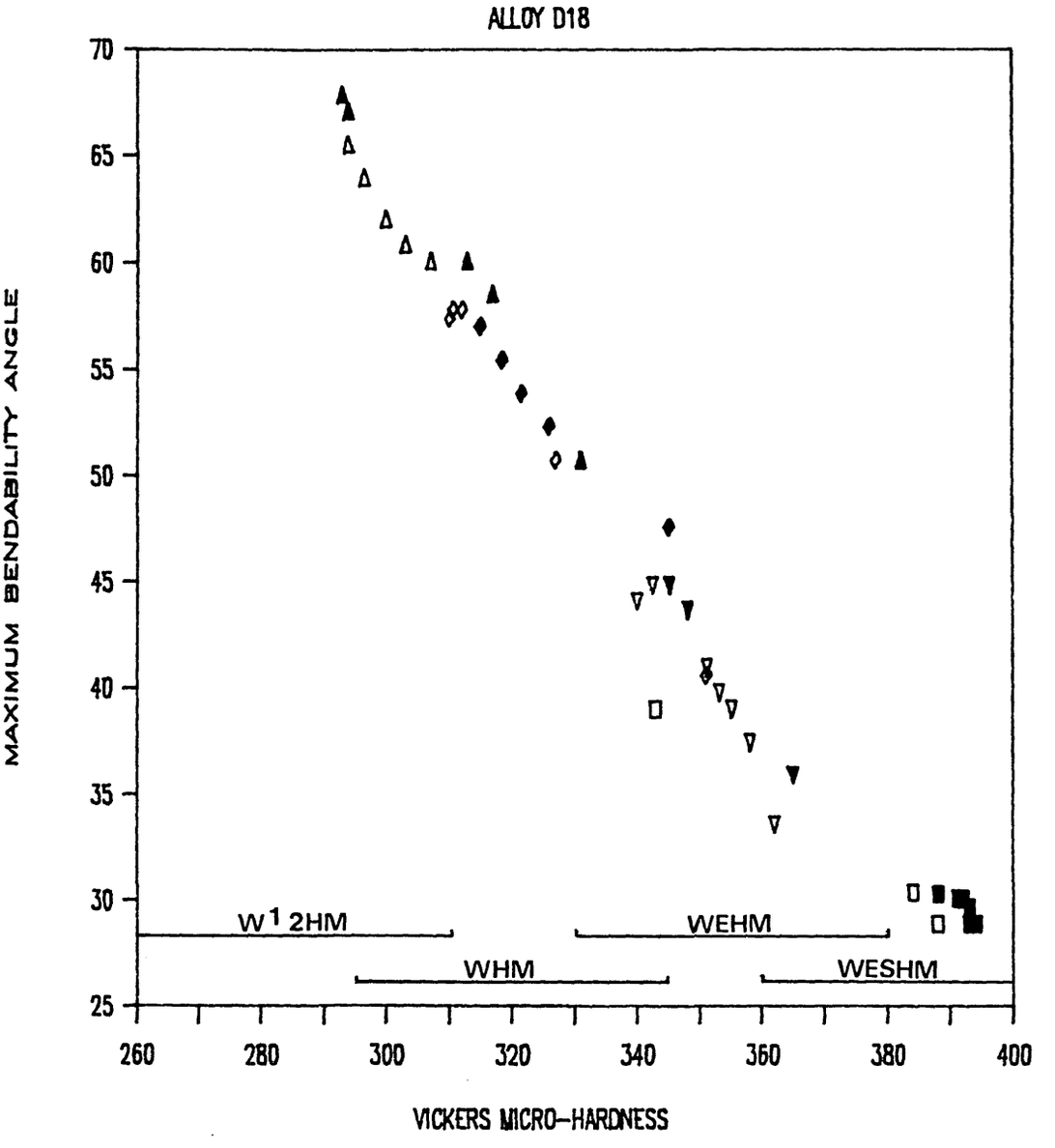

ALLOY D18
MAXIMUM BENDABILITY ANGLE
70
65
60
55
50
45
40
35
30
25
260
280
300
320
340
360
380
400
VICKERS MICRO-HARDNESS
W12HM
WHM
WEHM
WESHM

Figure 5.25-d.

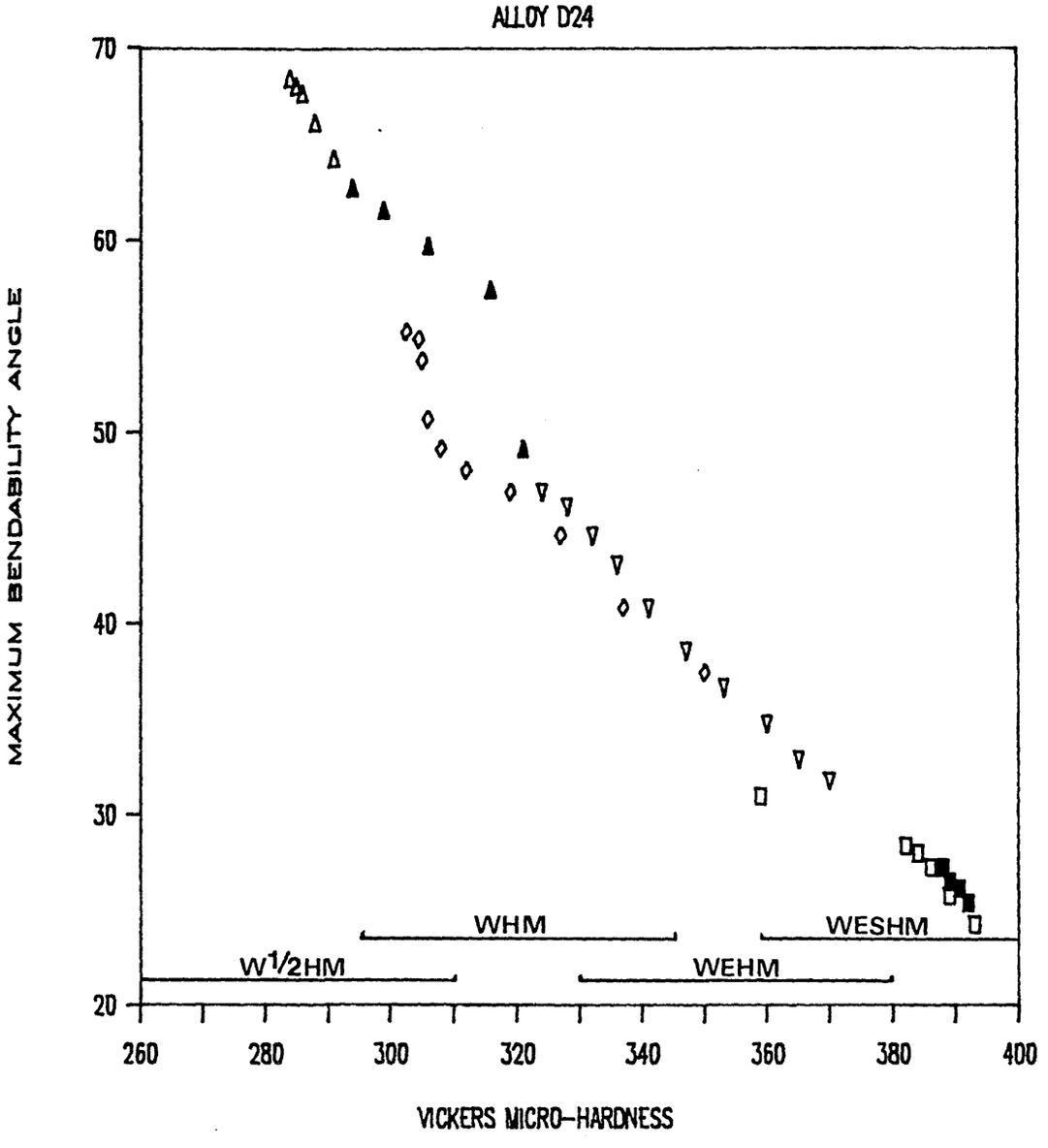

ALLOY D24
MAXIMUM BENDABILITY ANGLE
70
60
50
40
30
20
260
280
300
320
340
360
380
400
VICKERS MICRO-HARDNESS
W1/2HM
WHM
WEHM
WESHM

Figure 5.25-e.

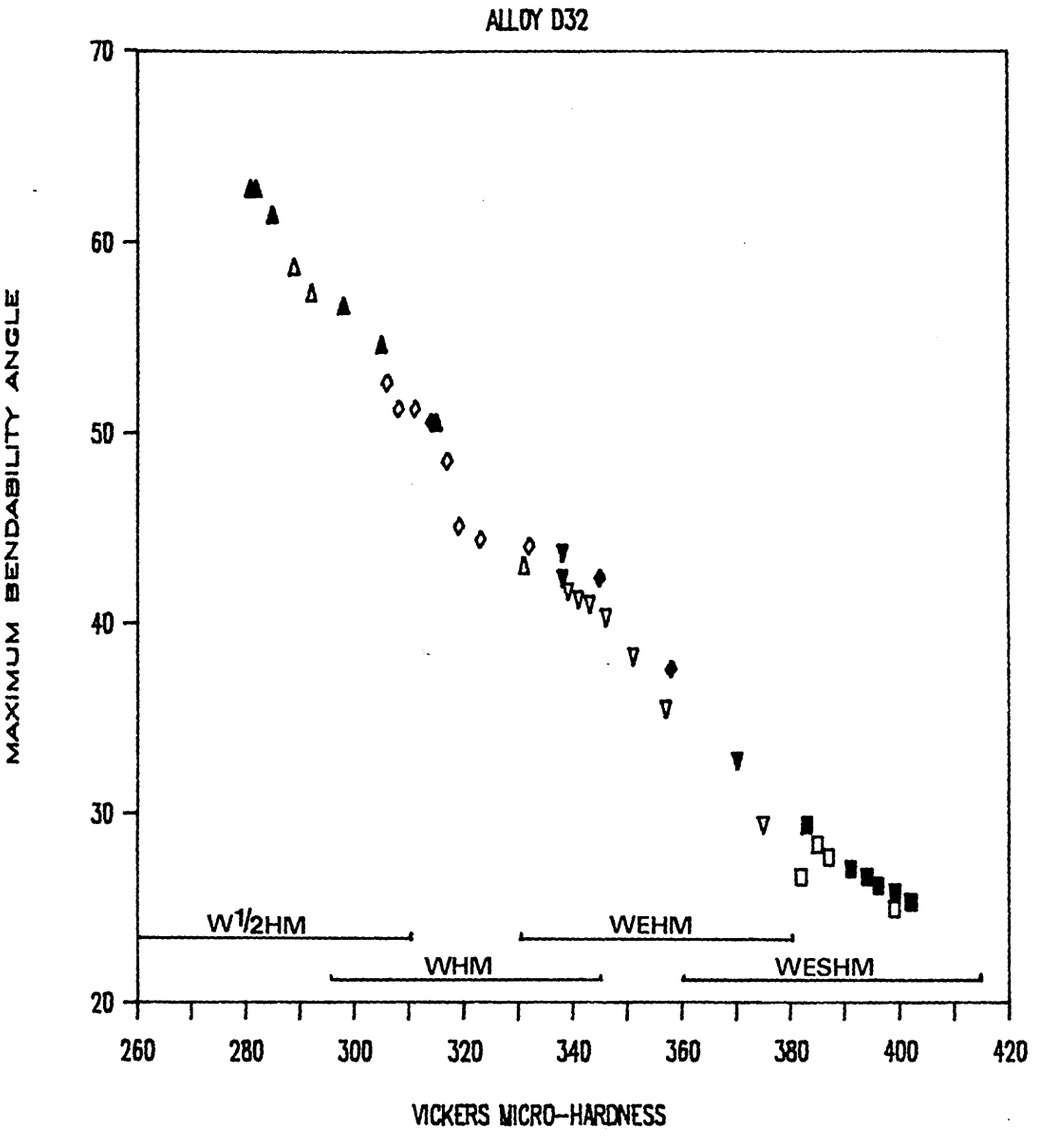

ALLOY D32
MAXIMUM BENDABILITY ANGLE
70
60
50
40
30
20
260
280
300
320
340
360
380
400
420
VICKERS MICRO-HARDNESS
W1/2HM
WEHM
WHM
WESHM

Figure 5.25-f

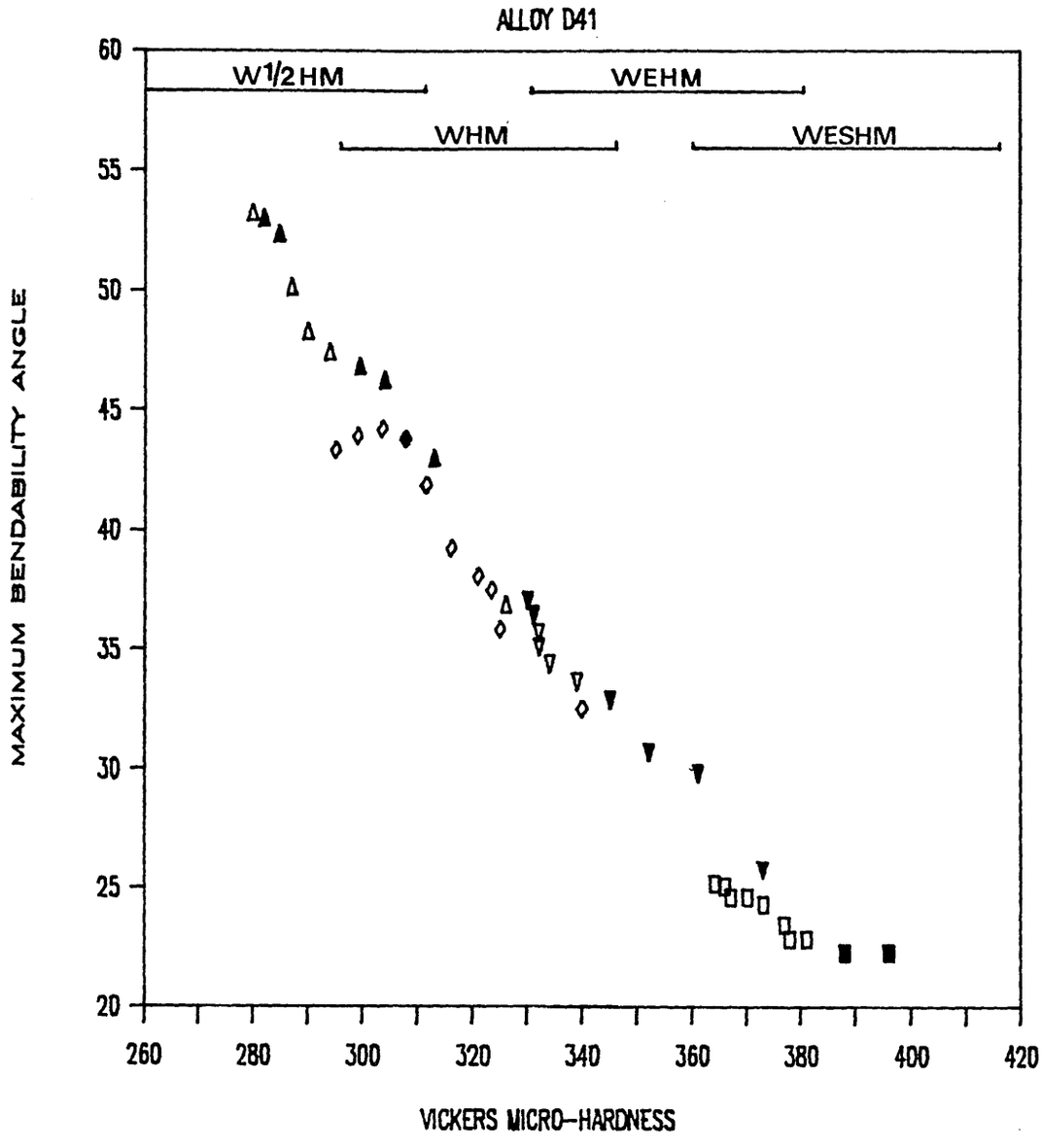

ALLOY D41
W1/2HM
WEHM
WHM
WESHM
MAXIMUM BENDABILITY ANGLE
VICKERS MICRO-HARDNESS
60
55
50
45
40
35
30
25
20
260
280
300
320
340
360
380
400
420

Figure 5.25-g.

5.4.4.1 The solution treated alloy

Having established that higher values of F_{NORM} correspond to the optimum hardness and bendability, the F_{NORM} function graphs can be used to select the best heat treatments that result in hardness values within the limits of WM grade for the solution treated alloy. In Figure 5.25-a, it has been shown that the data points, indicated by the full symbols, correspond to the peak regions in the F_{NORM} function graph (Figure 5.24-a). Therefore, a straight line, separating full symbols from the rest may be used as an acceptance/rejection criteria line. The combined analysis of the F_{NORM} function graph and the bendability vs. hardness plot have clearly shown that the best ageing treatments for the solution treated alloy correspond to the peak regions on the F_{NORM} function graph; these were either peak-ageing or over-ageing of the alloy, but under-ageing conditions produced considerably lower values of F_{NORM}. Therefore, the typical ageing conditions for the peak regions would be roughly the peak ageing at 380°C and the peak and over-ageing at 400 and 420°C. These ageing temperatures are not critical and may be relaxed into temperature ranges with reference to the contour line 17 on the F_{NORM} function graph (Figure 5.24-a), i.e. 380°C may be relaxed to 360-390°C and 400°C relaxed to 390-420°C.

In this respect, the best heat treatments for the solution treated alloy are determined by using the contour line 17, and the results are summarised in Table 5.7. Although the ageing conditions, listed in Table 5.7, are known to give the best bendability/hardness relationship, the attainable ranges of hardness and maximum bendability angle change from one ageing condition to another. Therefore, when applying one of these ageing conditions, the right selection of the ageing condition should be made for a required hardness and bend performance according to the corresponding values in Table 5.7.

The characteristic change in the contour of the F_{NORM} function graph also suggests that under-ageing and over-ageing treatments at temperatures below 400°C and

middle-ageing at temperatures in the range 390 to 410°C result in a sharp drop in the values of F_{NORM}; the middle-ageing is defined as ageing for a time slightly longer than that required for peak-ageing and which does not lead to significant fall in hardness. Therefore, in the commercial application of the proposed heat treatments in Table 5.7, care must be taken to ensure that the heat treatments are carried out within the proposed limits.

Table 5.7

Selected heat treatment conditions for the solution treated alloy giving optimum hardness and bendability

Ageing temperature range (°C)	Time (min)	Type of ageing	Data points in Fig.5.25-a	θ_M range (degrees)	Hardness range (VMH)
360-390	30-50	peak-ageing	▼	80-82	250-275
400-420	15-25	" "	◆▲	90-110	219-227
400	60-75	over-ageing	◆	90-92	238-243
420	25-50	middle-ageing	▲	100	223-227

5.4.4.2 Prior cold worked alloys

While it is of interest to determine the ageing conditions that give the highest F_{NORM} values for each prior cold worked alloy, it is also of importance to compare the highest F_{NORM} values, obtained from the alloys of different thermo-mechanical treatments, in order to be able to select the cold work and heat treatment regimes that give the best performance for different commercial grades, e.g. W1/4H, W1/2H...WESHM. The ageing conditions for each alloy, which result in the best bendability/ hardness relationship have already been determined by using the F_{NORM} function graphs (Figure 5.24-b to g) and the bendability vs. hardness plots (Figure 5.25-b to g). In an attempt to combine the selected overall data for different cold work levels, the maximum bendability angle vs. hardness plot was obtained (Figure 5.26), using the data points in Figure 5.25-b to g, which correspond to the peak regions on the F_{NORM} function graph. The desired limits of hardness for different grades are indicated on this plot. The data points are distributed in a scatter band, and the amount of scatter is measured by the difference in θ_M values ($\Delta\theta_M$) values at the upper and lower limits of the band for a given hardness, as shown in Figure 5.26; the magnitude of $\Delta\theta_M$ reduces with increasing hardness. Also, the greater the degree of prior cold work, the lower the optimum properties for a given grade; hence the data points within the hardness limits of a given grade in Figure 5.26 are situated at lower θ_M values.

In order to select the best ageing conditions and prior cold work levels for individual grades, a rejection curve was ploted in the scatter band at $1/3\Delta\theta_M$ distance from the top of the band, as shown in Figure 5.26. Naturally, the data points, representing a superior formability/hardness relationship, remain above the rejection curve, and hence are separated from these, which indicate a poor relationship. Using the selected data points, a variety of thermo-mechanical treatments may now be proposed as the best treatments for different grades of

the mill-hardened alloys. It must be noted that a number of data points above the rejection curve in Figure 5.26 are available for the individual grades in the range W1/2HM to WESHM. Whereas, for W1/HM grade there is no available data point above the rejection curve, demonstrating that none of the prior cold worked alloys can be employed for the W1/4HM grade after any heat treatment studied in the present work. This was attributed to the fact that the best ageing treatments for prior cold worked alloys result in the material having hardness values greater than those required for the W1/4HM grade, and therefore a softer material which possesses the required properties for W1/4HM grade is required. The solution treated alloy appears to be the only material that meets the requirements of the W1/4HM grade. Consequently, the same type of plot as that shown in Figure 5.26 was obtained for the solution treated alloy as shown in Figure 5.27. The presence of a number of data points above the rejection line on this plot shows that the solution treated alloy can be used as the W1/4HM and W1/2HM grade materials after ageing.

Finally, using the rejection line on both plots in Figures 5.26 and 5.27, the prior cold work and heat treatment regimes, which result in a superior bendability/hardness relationship, were determined for each grade and the overall results are summarised in Table 5.8. The general trend of the data in Table 5.8 demonstrates that the best properties are achieved by either peak ageing or middle-ageing and overageing, whereas, underageing always produced a poor bendability/hardness relationship. Also, it appears that there are alternative thermal and/or thermo-mechanical treatments for each grade that offer reasonably close values of optimum bendability and hardness. However, there is a range of attainable values of bendability and hardness within the limits of each grade, as can be seen by the values in Table 5.8. In fact, the multiplicity in these values seems to offer the convenience of producing a material with alternative hardness and bendability within the limits of a specific grade by a variety of routes. This is also valid for the results, obtained for the solution

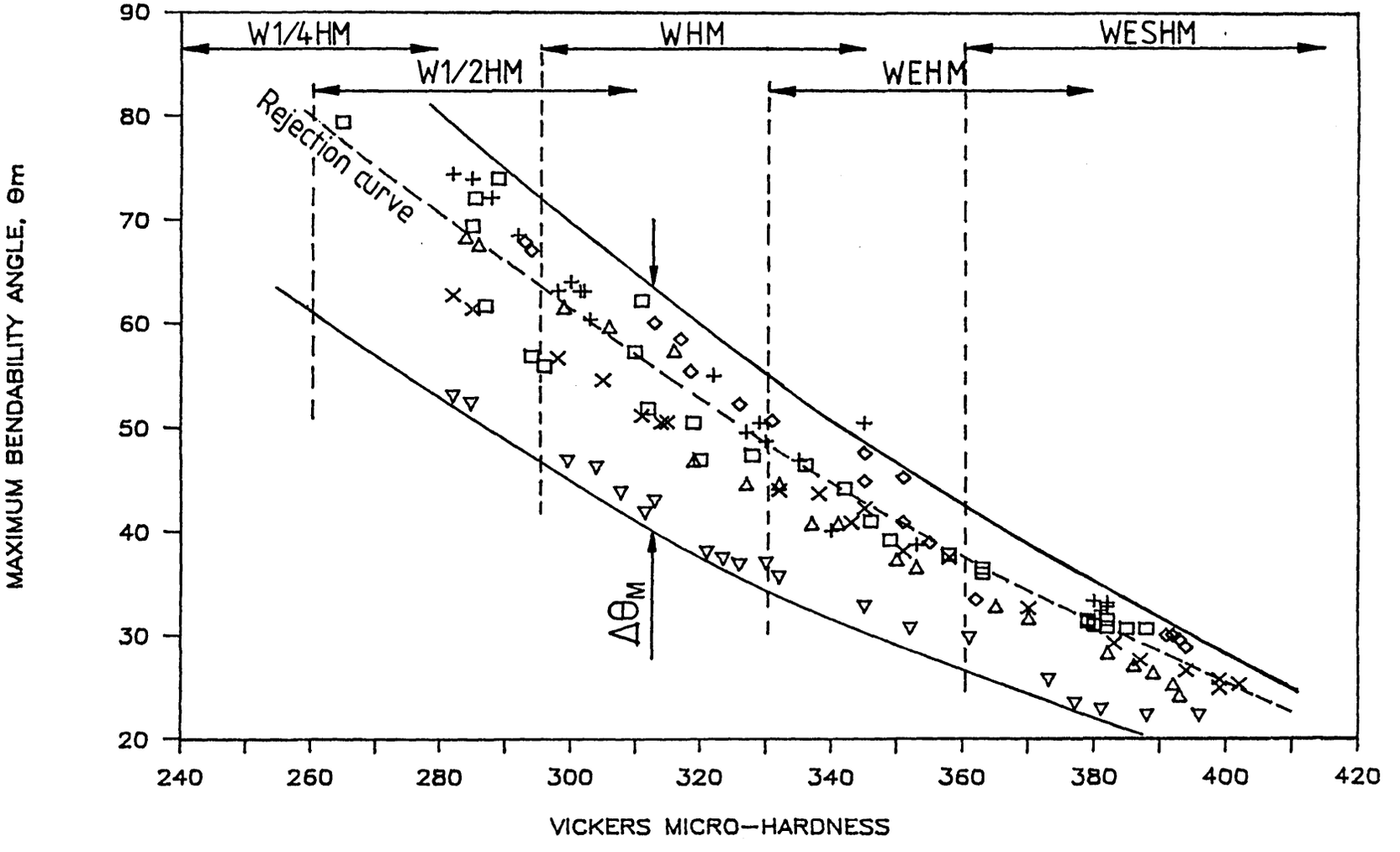


Figure 5.26- The maximum bendability angle vs. hardness plot of the selected data in Figure 5.25-b to g, which correspond to the peak regions of the FNORM function plots in Figure 5.24- a to g. The data points above the rejection curve (broken line) represent the best ageing treatments for the grades, indicated by scales on the hardness axis. All the data points are from the prior cold worked alloys.

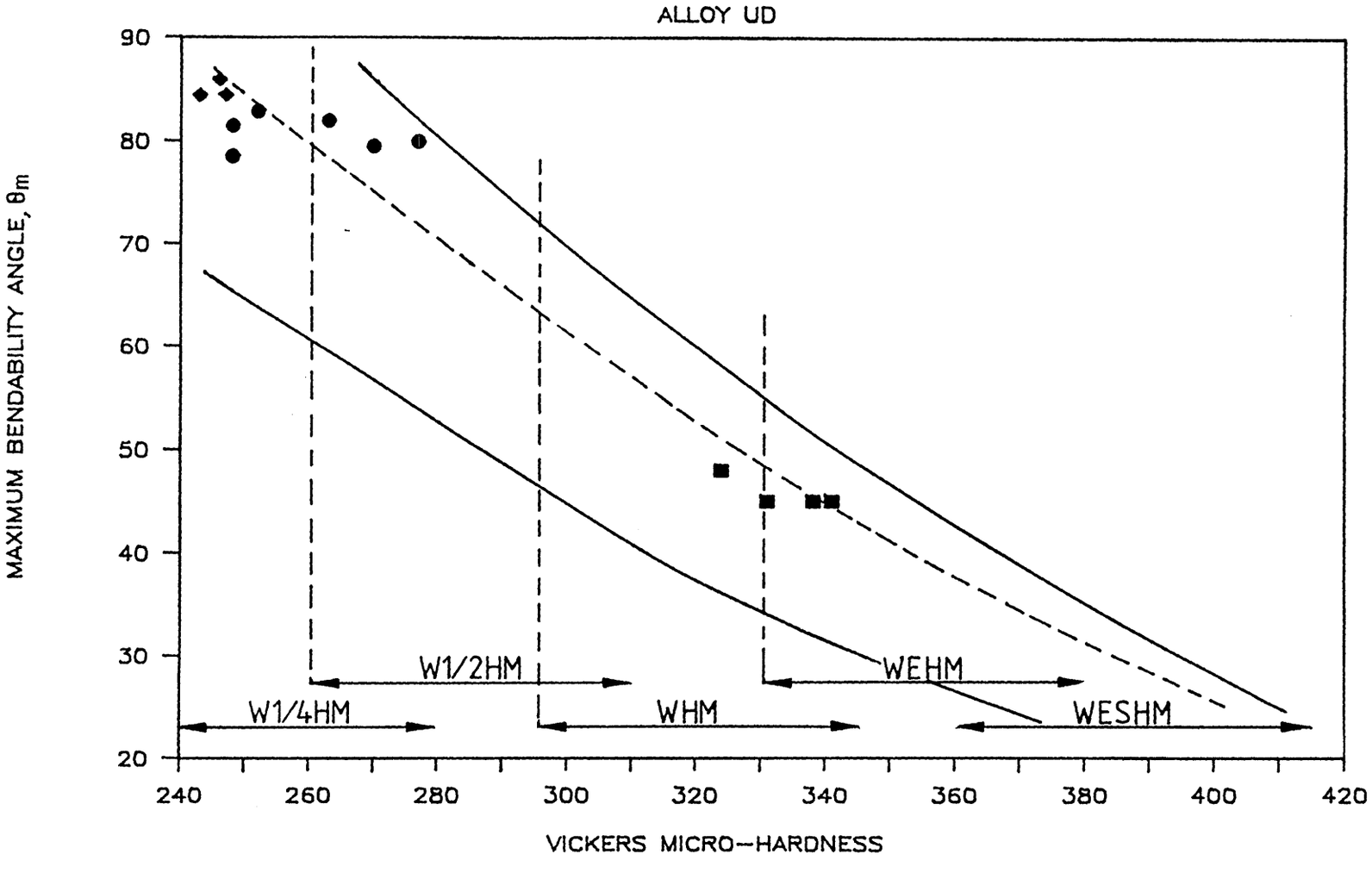


Figure 5.27- The same plot of Figure 5.24 for the solution treated alloy, showing the selected data points in Figure 5.25-a.

Table 5.8

Selected conditions of thermo-mechanical treatments for various grades of prior cold worked alloys

Grade	Alloy	Prior cold work (% RA)	Tempera-ture (°C)	Time (min.)	Type of ageing (•)	Data points (*)	Hardness range (VMH)	Bendablity angle range (degrees)
W1/4HM	UD	0	380	40-60	PA	●	252-277	80-83
W1/2HM	UD (§)	0	380	30-50	PA	●	263-270	79-82
	D5	5	420	60-100	OA	□	285-289	69-74
	D10	10	420	40-70	OA	+	282-292	69-74
	D18	18	420	90-100	OA	◇	293	67-68
WHM	D5 (x)	5	400	90-100	OA	□	310-311	60-62
	D10	10	400	25-30	MA	+	322-332	52-55
				60-90	OA		298-303	60-63
	D18	18	420	10-30	PA&MA	◇	313-331	51-60
	D24	24	420	20-30	MA	Δ	306-316	57-60
WEHM	D10	10	400	15-25	PA	+	332-345	47-52
	D18	18	380	80-100	OA	◇	340-345	44-45
			400	15-20	PA		345-351	45-48
WESHM	D5	5	350	30-100	PA&OA	□	379-388	30-32
	D10	10	350	30-60	PA	+	380-382	32-33
	D18	18	350	30-90	PA	◇	388-393	29-30
	D32	32	350	20-40	PA	X	399-402	25-26

(•) PA peak-ageing
MA middle-ageing
OA over-ageing

(*) data points in Figures 5.26 and 5.27
(§) overlapping the W1/4HM grade
(x) overlapping the W1/2HM grade

treated alloy (see Table 5.7).

As can be seen in Table 5.8, for grades up to WESHM the best results were achieved from alloys D5, D10, D18, and D24; note that the amount of cold work as percentage is given in these notations. This suggests that prior cold work greater than 24% RA is not advantageous in achieving a good bendability/hardness relationship; the bendability is too low for shaping process, which is evident from having noticeably low values of F_{NORM} (see the contour levels Figure 5.24-f and g). For the WESHM, grade there appears to be some use of alloy D32 on ageing in the regions of the highest contour (contour 8 in Figure 5.24-f). But, again the bendability of the alloy is considerably lower than those of alloys D18, and D10 for the same grade (see Table 5.8). Therefore, alloys D32 and D41 are not recommended if they have to be formed after ageing.

5.4.5 Microstructure for selected treatments

It is of interest to consider the microstructure resulting from the thermomechanical treatments that lead to a good combination of bendability and hardness. The TEM investigations of the decomposition reactions in Cu-Be-Co alloys are limited to ageing at 350, 400, and 500°C for a maximum of 30 minutes. Investigation of the microstructural changes at longer ageing times were precluded because of the limited time available. Therefore, the present TEM investigations provide information for only short ageing treatments and may be used only to predict the events, which take place in a given alloy on prolonged ageing.

Using the available information obtained from the TEM and the DTA investigations, the following deductions were made for microstructures corresponding to the selected prior cold work and heat treatment regimes proposed for various grades of the alloy:

(i) At 350 and 380°C: At these temperatures, it is peak ageing that gives good properties for most of the grades (see Tables 5.7 and 5.8). The predominant mode of the

decomposition reaction is the sequential precipitation of the G.P. zones and the γ' phase; only a limited amount of cellular precipitation or recrystallisation can take place at this temperature. The G.P. zones are finely dispersed platelets and result in a fine dispersion of the γ' precipitates since they act as the nuclei of the γ' phase. With reference to the TTT diagrams in Figures 5.1 to 5.5, it is clear that peak-ageing results in a microstructure containing newly nucleated γ' precipitates and this process is accelerated by both prior cold work and ageing temperature. It has been shown in Table 5.8 that only peak-ageing certain alloys, such as D5, D10, D18, and D32, at 350°C fulfils the requirement of the WESHM grade, i.e. a very high hardness and a reasonable bendability. Although the resultant bendability is very low in comparison with those for lower grades, a fine dispersion of the γ' precipitates results in a large overall hardening at the peak hardness that compensates the poor bendability and makes the material usable for the WESHM grade. Ageing prior cold worked alloys at 380°C does not seem to have much use for lower grades due to a very high hardness, achieved by a fine dispersion of the γ' precipitates, and consequently a very poor bendability. The only exception is that over-ageing alloy D18 at 380°C complies with the requirements of the WEHM grade. This may be due to the recrystallisation that can occur after long ageing treatments, and hence induce an increase in bendability without a considerable drop in hardness. The recrystallisation is known to occur in other alloys, but a better bendability is achieved in alloy D18 than the other alloys within the hardness limits of this grade. The undeformed alloy, UD, is an acceptable substitute for prior cold worked alloys for W1/4HM and W1/2HM grades when peak-aged at 380°C at 380°C. This is because the material is not deformed and therefore the finely dispersed γ' precipitates, formed by the G.P. zones, are in a soft matrix, thus providing a high maximum bend-bility angle and a reasonable hardness.

(ii) At 400 and 420°C: Although there are some examples in Table 5.8 of peak-aged alloys giving good properties at these temperatures, generally it is found that middle/over-ageing is more successful. It is clear that the G.P. zones cannot form and the γ' precipitates are nucleated directly in the matrix at these temperature. The presence of a higher thermal activation and the absence of the G.P. zones result in an increase in the particle size and spacing of the γ' precipitates and hence low flow stresses and relatively low work hardening rate, and thus a better bendability. However, the increase in prior cold work produces the opposite results, and therefore the alloys, cold worked greater than 24% RA has been found to be unusable for any grade (see Table 5.8). As stated earlier, the best results were achieved mostly after middle and over-ageing the prior cold worked alloys. Although the microstructure after over-ageing has not been studied in the present work, it is predicted from the TEM results obtained on short ageing treatments, and from the TTT curves (Figures 5.1 to 5.5) that the undeformed and lightly deformed overaged alloys will exhibit extensive cellular precipitation. It is somewhat surprising that the cellular growth did not lead to poor bendability results as it is generally assumed that the cellular growth is detrimental to formability. The cellular growth is of course associated with a reoriented (alloy UD) and recrystallised (alloys D5, D10, D18, etc) matrix, which may contribute to the good bendability.

5.5 Fracture Behaviour of Bend Samples

It has been described previously that during bending a sample on the cantilever-type bend test aparatus, the cross section of the sample is divided into two parts, namely the tension and compression regions above and below the neutral plane, respectively. During the plastic deform-ation the appearance of the localised wavy slip bands at the outer surface of the sample is followed by the develop-ment of the localised cracks where there is the highest stress concentration. The failure of the sample is then

governed by joining up of the localised cracks, producing slant fracture. Though the slant angle could not be measured on the samples, the plane stress condition implies that the fracture surfaces are slanted at 45° to the specimen surface since the maximum shear stress is on planes at this angle. The presence of the opposite slant surfaces (see Figure 4.50-b) suggests that the shear stresses at 45° to the surface of the sample are operative in opposite angles, producing the crossing shear bands, as depicted in Figure 5.28.

As can be seen in Figure 4.51-a, the sample at the outer fibre is sheared, forming fine shear dimples, which are elongated in the shear direction (see Figure 4.51-b). This process is limited to the region of the cross section from the outer surface to where mode I type deformation becomes favourable. The latter occurs by the nucleation and growth of the voids, most probably at precipitates, and results in the equiaxed dimple fracture. In the sheared part, the shear deformation occurs at a high rate, thus limiting voids growth and coalesce. However, in the region where the mode I type deformation occurs, a slower deformation rate due to the reduction in the distance from the neutral plane allows greater growth and the coalescence of the voids and consequently the material between the voids necks down until the ligament had no cross-sectional area.

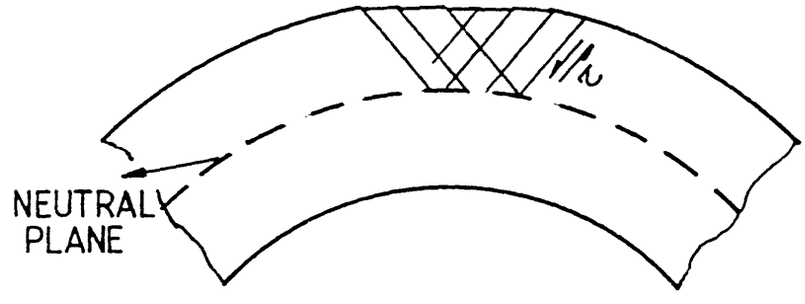


Figure 5.28- Schematic representation of the development of slip bands at the bend apex of a sample.

CHAPTER 6

CONCLUSIONS AND SUGGESTIONS FOR FURTHER WORK

6.1 Conclusions

6.1.1 Decomposition of the supersaturated solid solution

The decomposition reactions during ageing the alloys in deformed and undeformed states at temperatures in the range 300 to 500°C have been identified using the data from isothermal DTA curves, X-ray diffraction, hardness measure--ments, and TEM investigations. From these data TTT curves have been constructed. Using the characteristic "C" curves on the TTT diagrams and the information from the resistivity measurements and the non-isothermal DTA and DSC methods, the following conclusions have been made:

(i) Discontinuous precipitation: The γ'_D precipitates form initially at grain boundaries in a pucker-type process (stage I). The γ'_D precipitates have a BCC structure with a=0.27 nm and the crystallographic orientation relationship $(113)_\alpha$ // $(103)_{\gamma'_D}$; $[110]_\alpha$ // $[001]_{\gamma'_D}$. This is followed by the cellular precipitation (stage II), inducing the repeated nucleation and growth of the γ'_D precipitates at advancing interfaces of the cells and the equilibrium γ_D precipitation in the cells. There is a delay in the kinetics of γ'_D precipitation below T_1=370°C, which is attributed to the Co segregation at grain boundaries and the reduction in the solute content of the matrix by G.P. zone formation. Above T_1, the suppression mechanism on γ'_D precipitation does not seem to operate and the stage I precipitation is therefore followed immediately by the stage II in the absence of pre--cipitation in the matrix in the initial stages of ageing. In the undeformed alloy, γ'_D precipitation is governed by an activation energy, $E_{\gamma'_D}$=104.3 kJ/mol, which is reduced to 74.5 kJ/mol by 10% prior cold work; the reduction may be due to strain induced grain boundary movements facilitating γ'_D nucleation at grain boundaries. Prior cold

work reduces the amount of discontinuous precipitation by favouring continuous precipitation in the matrix more than γ'_D precipitation. Indeed, the γ'_D precipitates cannot form when prior cold work exceeds 24% RA. In addition, the greater the prior cold work, the more favoured is the recrystallisation that is initiated by the development of the strain-free reoriented regions at grain boundaries. For 24% prior cold work and above, the recrystallisation predominates at T_4=450-470°C and above.

(ii) Continuous precipitation: Below T_2=385°C, the decom--position reaction starts with G.P. zone formation on (100) habit planes of the matrix and the γ' precipitates are nucleated by the zones and, as the nuclei of γ' grow in size, their habit plane, $(100)_\alpha$, shifts towards $(112)_\alpha$. The structure of γ' is initially BCT with a=0.27-0.28 nm, c=0.258-0.2.62 mn, and a crystallographic orientation relationship, which is very close to $(112)_\alpha$ // $(120)_{\gamma'}$ and $[110]_\alpha$ // $[001]_{\gamma'}$. With prolonged ageing, the structure and the crystallography of the γ' precipitates become the same as these of γ'_D, formed at grain boundaries. Above T_2, the G.P. zones cannot form and the γ' precipitates are nucleated directly from the solid solution with the same structure and orientation relationship as these of γ'_D at grain boundaries. The role of prior cold work is to accele--rate γ' precipitation in the matrix, which is found to be more pronounced when ageing below T_2. The increase in the kinetics of γ' precipitation is associated with a reduction in the activation energy, $E_{\gamma'}$, with increasing prior cold work, e.g. 52% and 58% reductions in $E_{\gamma'}$ after 10 and 32% prior cold work respectively. In general, prolonged ageing treatments do not change the structure and the crystall--ography of the γ' precipitates, but they grow in size while retaining the same shape.

6.1.2 Hardening response of deformed and undeformed alloys

(i) The maximum hardness is attained when the γ' precipi-tates are nucleated in the matrix. Overageing of alloys occurs when the γ' precipitates grow to large sizes and the cellular precipitation in undeformed and lightly deformed alloys and the recrystallisation in highly deformed alloys advance into the matrix.

(ii) The maximum hardness is improved by increasing prior cold work whilst the amount of increment of hardening is reduced.

(iii) Onset of hardening and the hardness maxima are shifted towards shorter ageing times by increasing prior cold work and ageing temperature.

6.1.3 Texture of deformed and undeformed alloys

(i) The recrystallisation texture after the solution treatment is composed of a tilted cube texture, $(210)\langle 001\rangle$, and a twin component $(225)\langle 73\bar{4}\rangle$ plus $(522)\langle \bar{4}55\rangle$.

(ii) Prior cold rolling in the range 0 to 41% RA results in an intermediate texture, identified by the spread of orientations from the brass-type recrystallisation texture component $(225)\langle 73\bar{4}\rangle$ to the brass-type deformation texture orientation $(110)\langle \bar{1}12\rangle$. The intermediate orientations are $(326)\langle 63\bar{4}\rangle$, $(123)\langle 63\bar{4}\rangle$, and $(146)\langle 21\bar{1}\rangle$. As the degree of prior cold work increases, the intermediate orientations diminish in favour of the brass-type orientation $(110)\langle \bar{1}12\rangle$ due to increasing lattice rotations during cold rolling.

(iii) During ageing at 400 and 500°C, the intensity of the texture maxima is increased by the formation of intermedi-ate phases that induces the development of elastic stress fields in matrix. When the primary recrystallisation occurs, the recrystallised grains contribute to a texture, which is very close to the deformation texture orientations

revealing the dependancy of primary recrystallisation on the initial deformation texture.

6.1.4 The use of a cantilever-type bend test technique

(i) The design of a new cantilever-type bend test appar--atus made it possible to follow even very small changes in bendability of the alloys, introduced by altering the heat treatment conditions and the degree of prior cold work, which cannot be detected by any other relevant test method.

(ii) Bendability of a given alloy is assessed by the maximum bendability angle, θ_M, at which cracks are initi--ated at the bend apex of a sample and the load drops. The use of a correction factor, N_{COR}, to eliminate the error in θ_M introduced by variation in the thickness of the samples, has been shown to be feasible by an analytical model, which was proved by relevant experimental evidence.

6.1.5 Selection of the best heat treatments for different grades of Cu-Be-Co alloys

(i) Three dimensional plots of hardness and maximum bendability angle vs. ageing time and temperature have been introduced to assess the best thermal or thermo-mechanical treatments that give the optimum bendability and hardness for various grades of mill-hardened alloys, e.g. WM, W1/4HM ...WESHM, each grade having its own hardness limits. The combined 3D plots of bendability and hardness, obtained by using a normalisation function, F_{NORM}, have revealed charac--teristic peaks that correspond to the ageing treatments, which provide an optimum bendability/optimum hardness relationship for a given alloy. The use of the F_{NORM} function graphs for determining the best ageing treatments has been shown to be reliable by a cross-check of the data, in particular using plots of maximum bendability angle vs. hardness.

(ii) For WM and W1/4HM grades, the best ageing treatments that provide a hardness within the limitations of these grades have been found to be (a) peak ageing alloy UD at 360 to 390°C and peak-ageing and over-ageing at 400 to 420°C for WM grade and (b) peak ageing alloy UD at 380°C for W1/4HM grade. For higher grades in the range W1/2HM to WESHM, the optimum bendability/optimum hardness relation--ships have been obtained from a variety of alloys, including alloys D5, D10, D18, D24, and D32, after peak-ageing and/or over-ageing at temperatures from 350 to 420°C. In general, under-ageing at all temperatures and overageing below 380°C result in a poor bendability/ hardness relationship.

(iii) The greater the prior cold work, the poorer the optimum bendability/hardness relationship. Therefore, prior cold work greater than 24% RA is not recommended for any grade of mill hardened alloys with the exception of alloy D32, which is a promising material for the WESHM grade due to its very high hardness when peak aged at 350°C.

(iv) A fine dispersion of the γ' precipitates results in a high hardness but a very low bendability. Therefore, ageing below 380°C is limited to alloys for only WEHM grade. At higher temperatures, larger particle size and spacing of the γ' precipitates are obtained and consequent--ly there is an improvement in the optimum bendability/ optimum hardness relationship; hence the material becomes usable for a given grade, depending on its hardness and bendability. For undeformed alloys, the best properties are achieved before the extensive cellular precipitation occurs. The bend performance of prior cold worked alloys seems to improve, without a considerable drop in hardness when ageing results in the initial stages of the primary recrystallisation that is achieved on middle to over-ageing or over-ageing.

6.2 Suggestions for Further Work

(1) There is a need for a further detailed investigation of the microstructural changes in deformed and undeformed alloys during ageing at 380, 450, and 500°C, covering under ageing, peak ageing, and overageing conditions, in order to correlate the TTT diagrams and the findings of the the X-ray texture studies, proposed in the present work. In addition, it is of interest to investigate the microstruc--ture on over ageing alloys at 350 and 400°C, which is not covered by the TEM work of the present study, in order to correlate the hardness and the cantilever-type bend tests results of the present work as well as having a microstruc--tural interpretation of the best thermal and thermo-mechanical treatments, proposed for different grades of mill-hardened alloys for commercial application.

(2) For a better insight into the change in the optimum bendability/optimum hardness relationship with ageing temperature, further cantilever-type bend tests of samples aged above 420°C and below 350°C are required; the results should be correlated with the corresponding microstructural information.

(3) In order to explain the effect of various types of precipitates, degree of prior cold rolling, and recrystall--isation on the deformation mechanism during the cantilever-type bending a sample, a further investigation would include

(i) ageing the samples of both the solution treated and prior cold worked alloys to obtain the following structures (a) G.P. zones, (b) finely dispersed γ' precipitates, (c) coarse γ' precipitates, (d) γ' precipitates plus cellular structure, and (e) γ' precipitates plus recrystallised grains,

(ii) bending the samples with these specific structures on a cantilever-type bend rig, providing the similar test

conditions of the presented technique in this work, to achieve various degrees of plastic strains, and

(iii) TEM investigations of the plastically deformed structures.

(4) Determination of the orientation dependancy of the bend performance of the prior cold worked samples and the interrelation between the resulting changes in bendability of a given alloy with angular rotation from the rolling direction and the corresponding texture orientations, proposed in the present work.

(5) The use of the cantilever-type bend tests for different strip alloys, e.g. Al and other Cu based alloys, to prove the applicability of the proposed test method for determining the bend performance of a variety of alloys, which possess a wide range of mechanical properties.

APPENDIX A

KINETIC METHODS FOR DTA AND DSC ANALYSIS

There have been a variety of kinetic theories concerning the interpretation of the isothermal and non-isothermal DTA or DSC curves. In these theories, most of the equations are based on the formal theory of transformation kinetics, developed by Johnson and Mehl (1939) and Avrami (1941), which gives for the volume fraction X transformed at time t in a thermally activated growth reaction:

$$X = 1-\exp[-(kt)^n] \qquad [A.1]$$

where n is the time exponent, which reflects the nucleation rate and/or the growth morphology, and k is the effective overall reaction rate, which depends on temperature according to the equation:

$$k = v \exp(-E/RT) \qquad [A.2]$$

where E is the activation energy for overall transformation process, v is the frequency factor, and T and R have their usual meanings. Thermally activated growth reactions may be interface or diffusion controlled and in both cases, as mentioned previously, n depends on the nucleation rate (Table A.1). For both interface and diffusion controlled mechanisms, when the nucleation rate increases, n becomes higher than that for constant nucleation rate, and the decreasing nucleation rate results in an n value between those for constant and zero nucleation rate (De Bruijn et al., 1981).

The derivation of the theories, concerning the theoretical explanation of the DTA or DSC curves is unnecessary for the interpretation of the present work. Therefore, the most common of the equations and the method of application, together with assumptions made for the use of these equations, for isothermal and non-isothermal analysis will be summarised in the following sections.

Table A.1

The values of n for various transformations
(Christian, 1975)

(I) Discontinuous precipitation or interface controlled growth

Reaction mechanism	n
Increasing nucleation rate	>4
Constant " "	4
Decreasing " "	3-4
Zero nucleation rate (saturation of point sites)	3
Grain edge nucleation	2
Grain boundary nucleation	1

(II) Diffusion controlled growth

Reaction mechanism	n
All shapes growing from small dimensions with:	
(i) increasing nucleation rate	>2.5
(ii) constant nucleation rate	2.5
(iii) decreasing nucleation rate	1.5
(iv) zero nucleation rate	1-1.5
Needles and plates of finite long dimensions	1
Thickening of long cylinders or needles	1
Thickening of large plates	1.5
Precipitation on dislocations (very early stages)	≈2/3

A.1 Isothermal Transformation Kinetics

The equation generally used for describing isothermal reactions in solids, which consist of the nucleation and the growth processes, is obtained by taking the logarithm of equation [A.1] twice, which gives:

$$\ln[-\ln(1-X)] = n\ln k + n\ln t \qquad [A.3]$$

From typical DTA or DSC plots, k and n values at each temperature are determined from the least squares fit of $\ln[-\ln(1-X)]$ vs. $\ln t$. The values of X at various times are calculated from the ratio of the partial and total areas under the isothermal DTA curve. The activation energy, E, and the frequency factor, v, are then estimated from least squares fitting $\ln k$ vs. $1/T$, according to equation [A.2].

Alternatively, the value of E can also be calculated by determining the time, t_P, elapsed up to the maximum on the DTA or DSC peaks at temperature T. Then, the value of E is calculated from the slope, E/R, of a linear plot of $\ln t_P$ vs. $1/T$.

A.2 Non-Isothermal Transformation Kinetics

In the formal theory of the transformation kinetics, equations [A.1] and [A.2] strictly only apply to isothermal experiments, as presented above. However, these equations have been used to derive expressions describing non-isothermal transformations. The most commonly used treat-ments for non-isothermal transformations in the DTA and DSC experiments are summarised in Table A.2. All the methods assume a constant heating rate, α, in DTA and DSC experiments, which is expressed by the equation:

$$T = T_0 + \alpha t \qquad [A.4]$$

where T_0 is the temperature at the start of DTA or DSC experiments and α is the heating rate. The height of the DTA curve and that of the DSC curve at a temperature, T, as shown in Figure A.1, are measures of the difference in temperature, ΔT, between the sample and the reference, and the amount of heat evolved from the sample per unit time, respectively. Therefore, it is assumed (Borchardt and

Daniels, 1957) that the rate of heat generation, dH/dt, for either DTA or DSC is proportional to the transformation or the reaction rate, dX/dt, which is the differential of equation [A.1], which gives:

$$dX/dt = nknt^{n-1}(1-X) \qquad [A.5]$$

Thus, the area under the DTA or the DSC curves from the time t=0 to t_i (Figure A.1), which is the integration of dX/dt, is proportional to the fraction of the crystal--lisation at time t. Other assumptions, made for these methods, may be summarised as follows:

(i) a constant value of the heat capacity of sample,

(ii) a sample temperature, which is uniform during heating or cooling and equal to that of sample holder, and

(iii) heat transfer to the sample and the reference are identical.

The aim of all the methods is to determine two parameters (see Table A.2), and one of these parameters is plotted against the other, which will result in a straight line. Thus, the activation energy, E, and/or the time exponent, n, (the order of the reaction) are calculated from the slope of such straight lines.

As listed in Table A.2, the equations for all the approaches with the exception of the method proposed by Ozava (1971), were developed by either a differentiation of the equation [A.1] once or twice, or an integration of the differential equation, obtained after the first differen--tiation. These equations and the methods of analyzing experimental data differ from each other. Neverthless, the experimental data available in the literature on the crystallisation in various types of glasses suggest that the difference in the calculated E and n values for the same material by using different methods remain below 10%.

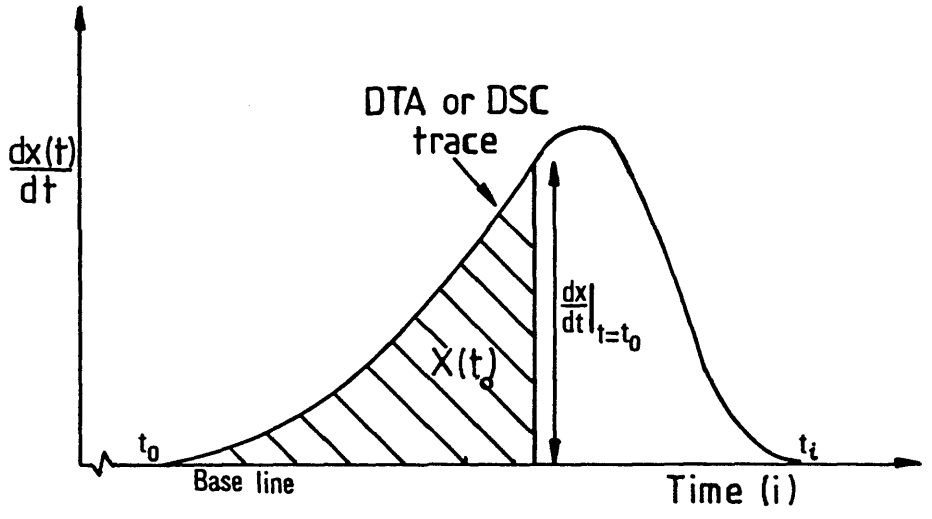


Figure A.1- Schematic drawing of DSC or DTA trace under constant scan rate conditions for a crystallisa-tion process which obeys the Johnson-Mehl-Avrami transformation rate equation (Henderson, 1979). The basic assumption is that ΔT (DTA) or dH/dT (DSC) are proportional to dx/dt.

Table A.2

Most common kinetic methods to calculate E and/or n employing DTA or DSC data

	Ozava (1971)	*Piloyan et al. (1966) and Borchardt & Daniels (1957)*
Equation	$\log[\ln(1-x)] = \log[K(T-T_0)] - n\log\alpha$ [A.6]	$\ln\Delta T = \ln[f(x)] + \ln K_0^n - E/RT]$ [A.7] where $f(x) = (1-x)[-\ln(1-x)]^{(n-1)/n}$
Assumption	-	(i) $x \propto \Delta T$, (ii) $f(x)$ = constant
Plot	$\log[\ln(1-x)]$ vs. $\log\alpha$	$\ln\Delta T$ vs. $1/T$
Type	measurement of x at the same temperature on peaks obtained at different heating rates	single peak scan
Slope	n	E/R
	Augis and Bennett (1978)	*Kissinger (1956)*
Equation	$\ln K_0 - E/RT_P + \ln(T_P-T_0)/\alpha = 0$ [A.8]	$\ln\alpha/T_P^2 = -E/RT_P + C$ [A.9]
Assumption	-	$[-\ln(1-x)]^{(n-1)/n}$ = constant
Plot	$\ln\alpha/(T_P - T_0)$ vs. $1/T_P$	$\ln\alpha/T_P^2$ vs. $1/T_P$
Type	heating rate dependence of reaction temperature, T_P.	
Slope	E/R	E/R

CONTD.....

Table A.2 Continued.

	Ozawa (1971) and Chen (1978)	*Takhor (1972)*
Equation	$\ln G(x') = \ln K_0 R/E + \ln T'^2/\alpha - E/RT$ [A.10]	$n\ln\alpha/(T_P-T_0) = \ln K_0^n/RT_P - nE/RT_P$ [A.11]
Assumption	$G(x') = \int_0^{x'} dx/(1-x)^n$ = constant regardless of α.	$\ln(T_P-T_0)$ = constant
Plot	$\ln T'^2/\alpha$ vs. $1/T'$	$\ln\alpha$ vs. $1/T_P$
Type	heating rate dependence of T'	heating rate dependence of T_P
Slope	E/R	E/R

Description of the parameters used in above equations:

C = a constant
E = activation energy
K_0 = frequency factor
n = the time exponent or the Avrami constant
R = gas constant
T_0 = the starting temperature of DTA or DSC runs
T_P = the peak temp erature of DTA or DSC curves
T' = the temperature at which the amount of the crystal volume fraction reached x'.
ΔT = the difference in temperatures of the sample and the reference
x = the crystal volume fraction transformed at T
α = heating rate

APPENDIX B

HARDNESS AND BENDABILITY RESULTS

The values of Vickers micro-hardness and the corrected maximum bendability angle, θM, obtained on ageing alloys UD, D5, D10, D18, D24, D32, and D41 at 350, 380, 400, and 420 °C are given in Table B.1. For some ageing treatments, the experimental hardness or bendability data were not available. The data for these ageing conditions were determined from the corresponding best-fit curves on the plots of hardness vs. ageing time and θ_M vs. ageing time (see Figures 4.1 to 4.5 for hardness plots and Figure 4.44-a to g for bendability plots). It was assumed that these values closely represent the actual hardness or bendability since the experimental data points did not show noticable deviation from the fitted curves.

Table B.1

Change in hardness and bendability angle of Cu-Be- Co alloys with various thermo-mechanical treatments.

Alloy	Prior cold work (% RA)	Ageing time (min.)	Maximum bendability angle (°)				Vickers micro-hardness			
			350°C	380°C	400°C	420°C	350°C	380°C	400°C	420°C
UD	0	0	144				116			
		5	139	130	127	125	118	120	139	164
		10	133	119	116	110	119	144	165	214
		15	120	109	109	102	125	175	219	224
		20	114	96	102	101	152	203	229	229
		25	84	83	90	102	242	222	238	228
		30	60	80	85	104	283	275	230	223
		35	47	76	84	102	304	277	238	223
		40	48	80	85	102	319	270	238	223
		50	45	82	85	101	321	256	237	224
		60	45	83	91	99	334	249	231	220
		70	44	83	92	100	330	244	232	220
		80	44	79	92	105	330	244	232	214
		100	42	70	90	99	324	243	231	227
D5	5	0	119				158			
		5	105	101	79	65	164	221	261	265
		10	66	46	50	57	227	337	320	291
		15	39	38	49	54	339	358	318	307
		20	32	36	47	56	354	351	328	294
		25	32	36	47	57	380	362	323	292
		30	32	36	47	57	383	365	319	290
		40	32	38	47	62	380	358	318	287
		50	31	39	49	66	380	342	314	286
		60	31	39	52	69	380	350	312	285
		80	31	41	57	72	380	346	305	286
		100	31	44	49	66	383	342	312	287

CONTD.....

Table B.1 Continued.

Alloy	Prior cold work (% RA)	Ageing time (min.)	Maximum bendability angle (°)				Vickers micro-hardness			
			350°C	380°C	400°C	420°C	350°C	380°C	400°C	420°C
D10	10	0	117				166			
		5	99	87	74	65	190	247	291	306
		10	74	50	46	56	243	329	337	310
		15	47	42	48	60	294	348	333	304
		20	36	39	50	63	360	354	345	302
		25	34	40	52	64	374	341	332	299
		30	33	40	55	66	380	335	321	300
		40	33	42	57	69	382	338	308	290
		50	33	45	59	72	383	335	305	288
		60	32	47	60	74	383	340	303	288
		80	32	49	64	74	370	325	300	278
		100	32	49	61	74	369	324	297	279
D18	18	0	95				203			
		5	86	56	44	46	262	330	344	331
		10	39	36	41	51	343	365	350	331
		15	31	33	45	56	375	363	352	328
		20	29	34	46	59	391	361	348	317
		25	29	35	49	59	390	360	330	315
		30	29	37	51	60	394	357	326	313
		40	29	39	52	60	394	355	327	308
		50	30	40	56	61	393	355	323	304
		60	30	41	55	62	397	348	318	301
		80	30	45	58	66	392	346	311	291
		100	30	44	57	68	382	339	312	293
D24	24	0	90				218			
		5	53	39	36	44	286	333	357	332
		10	31	32	37	49	358	370	352	319
		15	28	32	39	54	372	375	341	315
		20	26	33	41	57	389	361	348	319
		25	25	34	43	59	392	361	332	312
		30	24	35	45	60	393	360	327	306
		40	25	37	47	62	390	354	319	299
		50	26	39	48	63	390	345	312	295
		60	26	41	49	64	389	334	308	291
		80	27	45	54	68	385	332	305	285
		100	28	47	55	68	283	324	302	283
D32	32	0	74				244			
		2.5	48	38	35	37	290	318	340	348
		5	42	31	33	38	331	354	354	340
		10	27	29	38	43	382	370	358	331
		15	25	31	40	48	390	374	352	318
		20	25	33	42	51	399	369	346	315
		25	25	34	43	53	402	367	339	310
		30	25	36	44	55	391	356	331	305
		40	26	38	44	57	398	351	323	398
		60	27	41	48	59	396	340	317	289
		80	28	42	58	63	384	340	317	281
		100	29	44	53	63	383	338	301	281

CONTD....

Table B.1 Continued.

Alloy	Prior cold work (% RA)	Ageing time (min.)	Maximum bendability angle (°)				Vickers micro-hardness			
			350°C	380°C	400°C	420°C	350°C	380°C	400°C	420°C
D41	41	0	60				262			
		2.5	41	32	29	32	308	335	357	354
		5	29	26	29	34	345	366	361	338
		10	23	26	32	37	378	370	339	326
		15	22	28	34	40	395	369	327	318
		20	22	30	36	43	396	361	325	316
		25	22	30	37	45	392	356	324	308
		30	22	31	37	46	388	353	324	304
		40	23	33	38	47	381	344	321	299
		60	24	34	42	48	379	334	311	288
		80	25	36	44	52	365	330	304	286
		100	25	37	43	53	364	330	291	280

REFERENCES

Aaronson H.I. and Aaron H.B., Met. Trans. A, 3, (1972), 2743.

Alexander K.B., Steigerwald D.A., and Laughlin D.A., in "Solid- solid phase transformations", Proc. Int. Conf., (1982), 945, (edited by H.I. Aaranson, D.E. Laughlin, R.F. Sekerka, and C.M. Wayman), AIME.

Alpas A.T. and Öztürk T., in "Texture of materials", (1984), 211, Proc. Int. Conf., The Netherland, (edited by C.M. Brakman, P. Jongerburger, E.J. Mittemeijer).

Amano Y. and Koyama K., J. Jap. Inst. Met., 35, (3), (1971) 261

Armitage W.K., Ph.D. thesis, The Universiy of Leeds, (1963)

ASTM D 747-70, "Standard method of test for stiffness of plastics by means of a cantilever beam", Annual book of ASTM standards, Philadelphia, U.S.A., (1976).

ASTM B 194-81, "Standard specification for copper-beryllium alloy plate, sheet, strip, and rolled bar", Annual book of ASTM standards, Philadelphia, U.S.A, Part 6, (1982).

Augis J.A. and Bennett J.E., J. Thermal. Anal., 13, (1978), 283.

Avrami M., J. Chem. Phys., 9, (1941), 177, as cited by Christian (1975).

Baburaj E.G., Kulkarni U.D., Menon E.S.K., and Krishnan R., Phase Transi., 1, (1978), 171.

Bailey J.E., Phil. Mag., 5, (1960), 833.

Baumann S.F., Michael J., and Williams D.B., Acta Metall., 29, (1981), 1343.

Baumann S.F. and Williams D.B., Elec. Mic., 1, (1980), 194.

Beck P.A. and Hu H., Trans. AIME, 194, (1952), 83, as cited by Lücke and Schmidt (1972).

Bonfield W., Trans. AIME, 239, (1967), 99.

Bonfield W. and Edwards B.C., J. Mater. Sci., 9, (1974),398

Bonfield W. and Edwards B.C., ibid, 9, (1974), 409.

Bonfield W. and Edwards B.C., ibid, 9, (1974), 415.

Borchardt H. J. and Daniels F., J. Amer. Chem. Soc., 79, (1957), 41

Borchers H. and Schulz H., Acta Metall., 24, (1976), 639

Borchers H. and Schulz H., Z. Metallk., 66, (1975), 525.

Böhm H., Z. Metallk., 52, (1961), 564.

Brenneman W., Larson D.S., Shapiro E., and Tatum R., Bending moment-deflection testing and application of data, 12th annual connector symposium proceedings, 17 and 18 Oct., (1979), 283, published by Electronic Connector Study Group Inc. (USA).

Brickenkamp W. and Lücke K., in " The 6th international conference on texture of materials", vol.1, (1981), 570, The Iron and Steel Institute of Japan.

British Standard 2870-1980.

Bunge H.J., Int. Mater. Rev., 32, (6), (1987), 265

Butler E.P. and Swann P.R., Acta Metall., 24, (1976), 343.

Butler E.P. and Williams D.B., in "Solid-solid phase trans--formations", Proc. Int. Conf., (1982), 909, (edited by H.I. Aaronson D.E. Laughlin, R.F. Sekerka, and C.M. Wayman), AIME.

Cahn J.W., Acta Metall., 5 , (1957), 169.

Cahn J.W., ibid., 7, (1959), 18.

(1)* Chakrabarti D.J., Laughlin D.E., and Tanner L.E., Bull. Alloy Phase Diag., 8, (3), (1987), 269.

Chakrabarti D.J., Laughlin D.E., and Tanner L.E., Binary Alloy Phase Diagrams, vol. 1, ASM Metals Park, Ohio, USA, (1986), 449.

Chen H.S., J. Non-Crys. Sol., 27, (1978), 257.

Chernyakova L. Ye., Patseka R.F., Vorontsov N.M., Shugayenko W.K., and Drapiko P.Ye, Pys. Met. Metall. 48, (3), (1980), 105.

Christian J.W., The theory of transformations in metals and alloys, part I, 2nd edition, (1975), Pergamon Press.

Cocks F.H., Trans. ASM, 62, (1969), 805.

Copper and copper alloys data, vol.I, data sheet no:C5, (1972), Copper development assoc. of G.B.

(1)* Cahn R.W., "Recovery and Recrystallisation" in Physical Metallurgy (edited by R.W. Cahn and P. Haasen), part II, 3rd eddition,(1983), Elsevier Science Publishers.

Crafoord R., in "Sheet Metal Forming and Energy Conservation", [Proc. Conf.], 9th Annual Conference by BIENNAL, Congress of International Deep Drawing Research Group, Ann Arbor, Michigan, U.S.A., Oct. 13-14 1976, ASM (1976), 182.

De Druijn T.J.W, Jong W.A., and Van Den Berg, P.J., Thermochimica Acta, 45, (1981), 315.

Dillamore I.L. and Katoh H., Met. Sci., 8, (1974), 73.

Dillamore I.L. and Roberts W.T., Metallurg. Rev., 10,(1965) 271.

Djuric B., Jovanovic M., and Drobnjak D.J., Metallog., 13, (1980), 235.

Doherty R.D., "Diffusive phase transformations in the solid state" in Physical Metallurgy (edited by R.W. Cahn and P. Haasen), part I, 3rd eddition, (1983), 933, Elsevier Science Publishers.

Ecob R.C. and Ralph B., in "Solid-solid phase transform--ations", Proc. Int. Conf., (1982), 915, (edited by H.I. Aaronson D.E. Laughlin, R.F. Sekerka and C.M. Wayman), AIME.

Embury J.D. and Nicholson R.B., Acta Metall., 13, (1965), 403

Entwisle A.R. and Wynn J.K., J. Inst. Met., 89, (1960-1961) 24.

Esnault-Grosdemouge M.A., Matecki M., and Poulain M., Mater. Sci. Forum, 5, (1985), 241.

Fournelle R.A., Acta Metall., 27, (1979), 1135.

Fournelle R.A. and Clark J.B., Met. Trans., 3, (1972), 2757

Frebel M. and Schenk J., Z. Metallk., 70, (1979), 230.

Gadalla A.A., Ind. J. Pure & Appl. Phys., 18, (1980), 307.

Gavrilenko L.G., Mogutnov B.M., and Shvartsman L.A., Phys. Met. Metall., 26, (1969), 116.

Gavrilenko L.G., Gavrilova A.V., Mogutnow B.M., and Tyapkin Yu.D., ibid., 26, (1969), 179.

Geisler A.H., Mallery J.H., and Steigert F.E., Trans. Met. Soc. AIME, 194, (1952), 307.

Gitgarts M.I. and Tolstoy A.V., Phsy. Met. Metall., 45, (5) (1979), 133.

Gleiter H., Acta Metall., 18, (1970), 117.

Gleiter H., Phys. Stat. Sol., 45, (1971), 9.

Gordon P., Trans. AIME, 203, (1955), 1043.

Guinier A. and Jacquet P., Rev. Met., 41, (1944), 1, as cited by Guy A.G. et al., (1948)

Guy A.G., Barret C.H., and Mehl R.F., Trans. Met. Soc. AIME 175, (1948), 216.

Haessner F., "Systematic survey and fundamental problems of recrystallisation" in Recrystallisation in metallic materials (edited by F. Haessner), Seminar of the Institut fur Metallkunde of the University of Stuttgart, (1970), 5.

Hagel W.C. and Beattie, Jr, H.J., Trans. Met. Soc. AIME, 215, (1959), 967.

Hansen J. and Mecking H., in " Texture and the properties of materials", Proc. Int. Conf., (1975), 34, The Metals Society.

Hansen J., Pospiech J., and Lücke K., Tabels for Texture Analysis of Cubic Crystals, Springer Verlag, Berlin, (1978).

Harkness J.C., "Improved mill hardened beryllium copper strip for connector applications", 13th Annual Connector Symp. Proc., Electronic Connector Study Group, (1979), 130.

Hatherly M. and Dillamore I.L., J. Austr. Inst. Met., 20, (1975), 71.

Henderson D.W., J. Non-Crys. Sol., 30, (1979), 301.

Henmi Z. and Nagai T., Trans. Jap. Inst. Met., 10, (1969), 166.

Heye W. and Wassermann G., Z. Metallk., 59, (1968), 693.

Hillert M., Met. Trans., 3, (1972), 2729.

Hirata T. and Matsuo S., Trans. Jap. Inst. Met., 11, (1970) 200.

Hornbogen E., Met. Trans., 3, (1972), 2717.

Howard P., Pilkington R., Lorimer G.W., and Sale F.R., High Temp.-High Press., 17, (1985), 123.

Howell P.R. and Honeycombe R.W.K., in "Solid-solid phase transformations", Proc. Int. Conf., (1982), 399, (edited by H.I. Aaronson D.E. Laughlin, R.F. Sekerka and C.M. Wayman), AIME.

Hume-Rothery W., Smallman R.E., and Haworth C.W., The structure of metals and alloys, Institute of Metals, (1969), London.

Hutchinson W.B., Met. Sci., 8, (1974), 185

Johnson W.A. and Mehl R.F., Trans. AIME, 139, (1939), 416, as cited by Christian (1975).

Jovanovic M., Djuric B., Drobnjak D., Nesic O., and Kostic R., Mater. Sci. Tech., 2, (1986), 122.

Jovanovic M. and Drobnjak D., Script. Metall., 8, (1974), 1127.

Kainuma T. and Watanabe R., Jap. J. Inst. Met., 35, (2), (1971), 1126.

Kelly A. and Nicholson R.B., Prog. Mater. Sci., 10, (3), (1963), 151.

Kissinger H.E., J. Res. NBS, 57, (1956), 217.

Kreye H., Z. Metallk., 62, (1971), 556

Kunze G. and Wincierz K., Z.Metallk., 56, (1965), 421.

Laughlin D.E. and Tanner L.E., Bull. Alloy. Phase Diag., 2, (1), (1981), 28.

Lawley A., Lukens K.F., and Maddin R., Trans. ASM, 60, (1967), 517.

Lee D.N., in "Texture of materials", (1984), 101, Proc. Int. Conf., The Netherland, (edited by C.M. Brakman, P. Jongerburger, E.J. Mittemeijer).

Lee J.K., Barnett D.M., and Aar nson H.I., Met. Trans. A, 8, (1977), 963.

Leffers T. and Grum-Jensen A., Trans. AIME, 242,(1968),314.

Lorimer G.W., in "Solid-solid phase transformations", Proc. Int. Conf., (1982), 613, (edited by H.I. Aar nson D.E. Laughlin, R.F. Sekerka and C.M. Wayman), AIME.

Lloyd D.J. and Chaturvedi M.C., J. Mater. Sci., 17, (1982), 1819.

Lücke K., in "The sixth international conference on texture of materials", vol.1, (1981), 14, The Iron and Steel Institute of Japan.

Lücke K. and Schmidt U., J. Less-Comm. Met., 28,(1972),187.

Martin J.W., Micromechanisms in patricle-hardened alloys, Cambridge University Press, (1980).

Massalski T.B., "Structure of solid solutions" in Physical Metallurgy (edited by R.W. Cahn and P. Haasen), part I, 3rd eddition, (1983), 153, Elsevier Science Publishers.

Meyrick G., Scr. Metall., 10, (1976), 649.

Miki M., Hori S., and Amano Y., Trans. Jap. Inst. Met., 24, (10), (1983), 674.

Mishima Y., Okubo T., and Shiromizu R., Trans. Jap. Inst. Met., 10, (1969), 73.

Miyatani S., J. Phys. Soc. Jap., 4, (1949), 181, as cited by Armitage (1963).

Murakami Y., Yoshida H., and Yamamoto S., Trans Jap. Inst. Met., 9, (1968), 11.

Murdi B.B. and McNabb J.W., Engineering Mechanics of Materials, Macmillan Publ.Co., Inc., New York, U.S.A, (1980).

Nakagawa M., Jap. J. Appl. Phy., 4, (10), (1965), 760.

Nicholson R.B. and Nutting J., Acta Metall., 9, (1961), 332

Nishi Y., Aoyagi H., Suzuki K., and Yajima E., Trans. Jap. Inst. Met., 23, (1982), 703.

Nourbakhsh S. and Nutting J., J. Mater. Sci., 14, (1979), 2644.

Nutting J., Metall. Trans., 2, (1971), 45.

Okumura N, Venkatasubramanian T.V., Unvala B.A., and Baker T.J., Eng. Frac. Mech., 14, (1981), 617.

Ozawa T., Polymer, 12, (1971), 150.

Parikh P and Zarlingo S.P., in "Electronic study symposia" Proc. Conf., Oct. 1976, 435.

Pawlowski A., Scrip. Metall., 13, (1979), 785.

Persiano A.I.C., Ph.D. thesis, Imperial College of Science and Technology, London, (1986).

Pelletier J.M., Vigier G., Mai C., and Borrelly R., Acta Metall., 31, (10), (1983), 1491.

Pfeiffer I., Z. Metallk., 56, (1965), 465.

Philips V.A. and Tanner L.E., Acta Metall., 21, (1973), 441

Piloyan G.O., Ryabchiko I.D., and Novikova O.S., Nature, 10, (1966), 1229.

Pope M.I. and Judd M.D., Differential thermal analysis, Heyden & Son Ltd., Chatham in U.K., (1985)

Price R.J. and Kelly A., Acta Metall., 11, (1963), 915.

Pumphrey P.H., Scrip. Metall., 7, (1973), 1043.

Rakhshtadt A.G. and Tkhagapsoyev Kh.G., Russian Metall., 6, (1975), 150.

Rioja R.J. and Laughlin D.E., Acta Metall., 28, (1980),1301.

Rossiter P.L., Met. Forum, 8, (4), (1985), 204.

Rossiter P.L. and Wells P., Phil. Mag., 24, (1971), 425.

Russel K.C. and Aaronson H.I., J. Mater. Sci., 10, (1975), 1991.

Rutter J.W. and Aust K.T., Acta Metall., 13, (1965), 181.

Sachslehner F., Grogen V., and Stangler F., Met. Sci., 18, (1984), 153.

Schmidt U., Lücke K., and Pospiech J., in "Texture and the Properties of Materials" (edited by G.J. Davies, I.L. Dillamore, R.C. Hudd, and J.S. Kallend), Proc. Int. Conf., (1975), 147, The Metals Society.

Sestak J., Phs. Chem. Glass., 15, (6), (1974), 137.

Sevillona J.G., Houtte P., and Aernoudt E., Progr. Mater. Sci., 25, (1981), 69.

Shanley F.R., Strength of Materials, McGraw-Hill Book Co. Inc., New York, U.S.A., (1957).

Shimizu K., Mikami Y., Mitani H., and Otsuka K., Trans. Jap Inst. Met., 12, (1971), 206.

Shiromizu R. and Mishima Y., Jap. J. Inst. Met., 35, (3), (1971), 183.

Sivertsen J.M. and Nicholson M.E., Prog. Mater. Sci., 9, (1961), 305.

Slakhorst J.W.H.G and Verbraak C.A., in "Texture and the Properties of Materials" (edited by G.J. Davies, I.L. Dillamore, R.C. Hudd, and J.S. Kallend), Proc. Int. Conf., (1975), 160, The Metals Society.

Smallman R.E., Westmacott K.H., and Coiley J.H., J. Inst. Met., 88, (1959-1960), 127.

Sorokin L.M., Sov. Phys. Solid State, 8, (12), (1967), 2820

Sorokin L.M., ibid., 9, (6), (1967), 1353.

Stüve H.P., "Driving forcess for recrystallisation" in Recrystallisation in metallic materials (edited by F. Haessner), Seminar of the Institut`fur Metall--kunde of the University of Stuttgart, (1970), 21.

Tanaka K., Mannami M., Izumi K., and Marukawa K., Acta Metall., 11, (1963), 79.

Tanimura H. and Wassermann G., Z. Metallk., 25, (1933), 179, as cited by Chakrabarti et al. (1987).

Tanner L.E., Phil. Mag., 14, (1966), 111.

Tavassoli A.A., Met. Sci., 8, (1974), 424.

Thakur R.L., in "Advances in Nucleation and Crystallisation of Glasses" Ame. Ceram. Soc., Columbus, (1972), 166.

Thomas G., Phil. Mag., 4, (1959), 606.

Thomas G. and Whelan M.J., ibid., 4, (1959), 511.

Thomas H. and Wilke-Dorfurt U.,Z. Metallk., 50, (1959),466.

Thompson D.S., in "Thermal Analysis, Inorganic Materials & Phisical Chemistry", vol.2, edited by R.F. Schwenker and P.D. Garn, Academic Press, New York, (1969), 1147.

Toda T., Trans. Jap. Inst. Met., 11, (1970), 24.

Toda T, ibid., 11, (1970), 30.

Tofpenets R.L., Malashenko L.M., and Vasilyeva L.A., Phys. Met. Metall., 45, (4), (1979), 92.

Tsubakino H. and Nozato R., Bull. Univ. Osaka Prefecture Ser. A, 27, (2), (1978), 149.

Tsubakino H., Nozato R., and Mitani H., Jap. J. Inst. Met., 44, (10), (1980), 1122.

Tu K.N. and Turnbull D., Acta Metall., 15, (1967), 369.

Tu K.N. and Turnbull D., ibid., 15, (1967), 1317.

Turnbull D., Acta Metall., 3, (1955), 55.

Tyapkin Yu.D., Sov. Phys. Doklady, 9, (1), (1964), 95.

Tyapkin Yu.D., Sov. Phys. Crystallog., 10, (4), (1966), 418.

Tyapkin Yu.D. and Gavrilova A.V., ibid., 9, (2),(1964), 166

Uhlmann D.R., J. Amer. Cer. Soc., 66, (2), (1983), 95.

Unvala B.A., "Monitoring of crack lengths by AC potential drop technique" in Test and Transducer, The Inter-national Measurement Exhibition and Conference, Vol.1, Wembley conference centre, London on 28, 29, 30 Oct. (1986).

Unvin P.N.T. and Nicholson R.B., Acta Metall., 17, (1969), 1379.

Virnich K.H. and Lücke K., in "The sixth international conference on textures of materials", vol.1, (1981), 560, The Iron and Steel Institute of Japan.

Wassermann G., Z. Metallk., 54, (1963), 61.

Wendlandt Wesley WM., Thermal analysis, John Wiley & Sons, Inc., New York, (1986).

Wilkes P., Acta Metall., 16, (1968), 153.

Wilkes P. and Barrand P., ibid., 16, (1968), 159.

Wilkes P. and Jackson M.M., J. Met. Sci., 3, (1969), 130.

Williams D.B., "Analytical TEM of the discontinuous reac--tion in Cu-Be-Co alloys", 9th international congr. on Electron Microscopy, Toronto, 1, (1978), 506.

Williams D.B. and Butler E.P., Int. Met. Rev., 3, (1981), 153.

Williams D.B. and Edington J.W., Acta Metall., 24, (1976), 323.

Yamamoto S., Matsui M., and Murakami Y., Trans. Jap. Inst. Met., 12, (1971), 159.

Yamamoto S. and Murakami Y., Mem. Fac. Eng. (Koyoto University), 31, (1969), 576.

Yamamoto S., Yamamoto Y., and Murakami Y., J. Jap. Inst. Met., 37, (1973), 1268.

Zener C., Trans. AIME, 167, (1946), 550.

Zaryzcki J., in "Nucleation and Crystallisation of Glasses" the 83rd Annual meeting of the Amer. Cer. Soc. May 3-6 1981, printed in "Advances in Ceramics", Vol. 4, (Edd. by J.H. Simmons, D.R. Uhlmann, and G.H. Beall) Amer. Cer. Soc. (1982).

Zhu F., Mertens P., and Wollenberg H., Z. Metallk., 77, (1986), 1.